

Unmanned Autonomous Systems in Complex Environments 2021

Lead Guest Editor: Chenguang Yang

Guest Editors: Chao Zeng, Zhenyu Lu, and Chao Liu





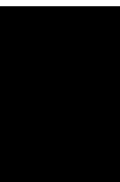
**Unmanned Autonomous Systems in Complex
Environments 2021**

Complexity

Unmanned Autonomous Systems in Complex Environments 2021

Lead Guest Editor: Chenguang Yang


Guest Editors: Chao Zeng, Zhenyu Lu, and Chao
Liu



Copyright © 2022 Hindawi Limited. All rights reserved.

This is a special issue published in "Complexity." All articles are open access articles distributed under the Creative Commons Attribution License, which permits unrestricted use, distribution, and reproduction in any medium, provided the original work is properly cited.

Chief Editor

Hiroki Sayama , USA

Associate Editors

Albert Diaz-Guilera , Spain
Carlos Gershenson , Mexico
Sergio Gómez , Spain
Sing Kiong Nguang , New Zealand
Yongping Pan , Singapore
Dimitrios Stamovlasis , Greece
Christos Volos , Greece
Yong Xu , China
Xinggang Yan , United Kingdom






Academic Editors

Andrew Adamatzky, United Kingdom
Marcus Aguiar , Brazil
Tarek Ahmed-Ali, France
Maia Angelova , Australia
David Arroyo, Spain
Tomaso Aste , United Kingdom
Shonak Bansal , India
George Bassel, United Kingdom
Mohamed Boutayeb, France
Dirk Brockmann, Germany
Seth Bullock, United Kingdom
Diyi Chen , China
Alan Dorin , Australia
Guilherme Ferraz de Arruda , Italy
Harish Garg , India
Sarangapani Jagannathan , USA
Mahdi Jalili, Australia
Jeffrey H. Johnson, United Kingdom
Jurgen Kurths, Germany
C. H. Lai , Singapore
Fredrik Liljeros, Sweden
Naoki Masuda, USA
Jose F. Mendes , Portugal
Christopher P. Monterola, Philippines
Marcin Mrugalski , Poland
Vincenzo Nicosia, United Kingdom
Nicola Perra , United Kingdom
Andrea Rapisarda, Italy
Céline Rozenblat, Switzerland
M. San Miguel, Spain
Enzo Pasquale Scilingo , Italy
Ana Teixeira de Melo, Portugal

Shahadat Uddin , Australia
Jose C. Valverde , Spain
Massimiliano Zanin , Spain






Contents

UAVs Protection and Countermeasures in a Complex Electromagnetic Environment

Anton O. Belousov , Yevgeniy S. Zhechev , Evgeniya B. Chernikova , Alexander V. Nosov , and Talgat R. Gazizov 

Research Article (16 pages), Article ID 8539326, Volume 2022 (2022)

A Novel Mining Approach for Data Analysis and Processing Using Unmanned Aerial Vehicles

Ali Alenezi , Ahmad Sawalmeh , Hazim Shakhatreh , Muhannad Almutiry , and Nasser Aedh Alreshidi 


Research Article (10 pages), Article ID 6795101, Volume 2022 (2022)

Flood Detection Based on Unmanned Aerial Vehicle System and Deep Learning

Kaixin Yang , Sujie Zhang , Xinran Yang , and Nan Wu 

Research Article (9 pages), Article ID 6155300, Volume 2022 (2022)

Super-Twisting Nonsingular Terminal Sliding Mode-Based Robust Impedance Control of Robots

Yixuan Wang, Tairen Sun , and Jiantao Yang

Research Article (6 pages), Article ID 9263699, Volume 2022 (2022)

Model-Based Design, HIL Testing, and Rapid Control Prototyping of a Low-Cost POC Quadcopter with Stability Analysis and Control

Abdullah Irfan , Muhammad Gufran Khan , Arslan Ahmed Amin, Syed Ali Mohsin, Muhammad Adnan , and Adil Zulfiqar 





Research Article (16 pages), Article ID 1492170, Volume 2022 (2022)

Event-Triggered Adaptive Dynamic Programming Consensus Tracking Control for Discrete-Time Multiagent Systems

Yuyang Zhao, Xiaolin Dai, Dawei Gong, Xinzhi Lv, and Yang Liu 



Research Article (14 pages), Article ID 6028054, Volume 2022 (2022)

Vibration Suppression of a Coupled Aircraft Wing with Finite-Time Convergence

Yiming Liu , Zhifeng Tan , Xiaofen Yang , and Xiaowei Wang 



Research Article (14 pages), Article ID 2417748, Volume 2022 (2022)

Higher-Order Iterative Learning Control with Optimal Control Gains Based on Evolutionary Algorithm for Nonlinear System

Yun-Shan Wei , Xiaofen Yang, Wenli Shang , and Ying-Yu Chen

Research Article (9 pages), Article ID 4281006, Volume 2021 (2021)

Multiscale Efficient Channel Attention for Fusion Lane Line Segmentation

Kang Liu  and Xin Gao 



Research Article (12 pages), Article ID 6791882, Volume 2021 (2021)

Cell on Wheels-Unmanned Aerial Vehicle System for Providing Wireless Coverage in Emergency Situations

Hazim Shakhatreh , Khaled Hayajneh , Khaled Bani-Hani , Ahmad Sawalmeh , and Muhammad Anan 

Research Article (9 pages), Article ID 8669824, Volume 2021 (2021)

Grasp Detection under Occlusions Using SIFT Features

Zhaojun Ye, Yi Guo , Chengguang Wang, Haohui Huang, and Genke Yang 

Research Article (12 pages), Article ID 7619794, Volume 2021 (2021)

A Deep-Learning-Inspired Person-Job Matching Model Based on Sentence Vectors and Subject-Term Graphs

Xiaowei Wang, Zhenhong Jiang, and Lingxi Peng 

Research Article (11 pages), Article ID 6206288, Volume 2021 (2021)

Research Article

UAVs Protection and Countermeasures in a Complex Electromagnetic Environment

Anton O. Belousov , **Yevgeniy S. Zhechev** , **Evgeniya B. Chernikova** ,
Alexander V. Nosov , and **Talgat R. Gazizov** 

Department of Television and Control, Tomsk State University of Control Systems and Radioelectronics, Tomsk, Russia

Correspondence should be addressed to Anton O. Belousov; ant1lafleur@gmail.com

Received 3 March 2022; Revised 30 April 2022; Accepted 17 June 2022; Published 13 July 2022

Academic Editor: Chao Liu

Copyright © 2022 Anton O. Belousov et al. This is an open access article distributed under the Creative Commons Attribution License, which permits unrestricted use, distribution, and reproduction in any medium, provided the original work is properly cited.

The study considers the problem of ensuring electromagnetic compatibility of EMI-based functional destruction means with other radioelectronic equipment as part of a complex for countering unmanned aerial vehicles. To solve this problem, it is proposed to create a methodology that combines a set of diverse approaches and methods. This study focuses on the use of hollow and thin passive conductors, the use of a magnetodielectric in a reflection symmetric modal filter, the use of reflection symmetric structures for decomposing the train of ultrashort pulses (USP), and the use of a meander line as a protective means against USPs. The main results that are expected to be obtained using the proposed approaches and methods are outlined.

1. Introduction

The last decade has been marked by intensification in the development of unmanned aerial vehicles (UAVs) because of their proliferation not only in the civilian but also in the military areas. UAVs make it possible to significantly reduce the cost of services related to remote and real-time monitoring of the environment and objects, compared with traditional space or aviation systems [1–3]. Meanwhile, this time also witnesses the appearance of improved medium and small UAVs, which makes the tasks of countering them in highly controlled areas particularly urgent [4, 5]. In addition, modern UAVs are used as one of the most important means of increasing the combat capabilities of the armed forces. Since UAVs have become widespread in military domain, intense research and development activities in this area has started, as can be seen from the works [6–10]. At the same time, this issue is relatively new, since the earliest work on the topic of countermeasures against UAVs [8] dates back to 2008, and the beginning of active scientific publications on this topic dates back to 2016–2017.

It is well-known that the task of countering UAVs (which arose in the early 2000) can be solved in various ways: from the use of fire weapons (i.e., air defense) and electronic countermeasures against critical UAV systems to direct physical interception of UAVs and the use of EMI-based functional destruction means. The latter method seems to be the most promising, since it is devoid of the most serious drawback of electronic countermeasures means—the lack of an unambiguous reaction of the UAV to successful suppression. However, the EMI-based functional destruction means operate using the generators of powerful microwave and laser radiation. The examples of such EMI generators can be electromagnetic installations (electromagnetic accelerators or simply guns), explosive magnetic generators, warheads of anti-aircraft guided missiles, and anti-aircraft artillery shells with emitters of powerful electromagnetic microwave pulses. Consequently, the high power of the generated EMI and the difficulty of ensuring its selectivity in relation to the affected radioelectronic equipment (REE) worsen the internal electromagnetic environment inside the UAV countermeasures complex. In particular, the difficulty in ensuring the selectivity of the EMI excitation can lead to

malfunctions of the elements of «friendly» REE (receiving and transmitting devices, signal generators, control, stabilization, command generation devices, and various electronic computers). The reason for such malfunctions can be as follows: excesses in useful signal amplitudes caused by crosstalk, the overlapping of useful signal spectra with interference ones, the overlapping of interference pulses in device circuits on generated useful signals and their superposition in time, and crosstalk in external and internal circuits. It raises the issue of ensuring electromagnetic compatibility (EMC) of the EMI-based functional destruction means with other REE as part of the UAV countermeasures complex. Another important issue is ensuring the EMC of «friendly» UAVs, which may be in the damage area of the EMI-based functional destruction means.

The reason why this issue has not been raised before is probably because the price of small UAVs is not high (in contrast to the prices of military equipment or ammunition). However, the additional «survivability» of UAVs can be of great help during real combat operations. Another reason is that ensuring the EMC of UAV countermeasures systems can be expensive. However, recently obtained investigation results for the first time can be exploited to find the ways to solve this problem. In addition, it could be possible without resorting to large financial costs.

Much attention is paid to the problem of UAV protection and countermeasures in complex electromagnetic environment. It is evidenced by the scientific work presented in the next section. However, the methodological aspects have not been studied enough. Hence, the authors are not aware of scientific works or standards devoted to the description of a unified methodology for ensuring the EMC of the UAV countermeasures complex that employs EMI-based functional destruction means. The aim of this work is to fill this gap by presenting preliminary results on such a methodology. To achieve this, several approaches and methods are discussed to create this methodology. In addition, the results that confirm the efficiency and applicability of some of them are presented. Thus, the overall contribution of this study in developing such a scientific direction has been motivated by new effective approaches to creating the methodology for ensuring EMC. These approaches are designed to eliminate significant shortcomings in the effectiveness of EMI-based functional destruction means that were mentioned earlier.

The article is divided into several sections. There are numbered, taking into account the sequence order, starting with section 2. Section 2 presents a brief review of scientific studies on the subject of the study. Section 3 highlights the proposed approaches and methods. In Sections 4–8, the feasibility of the proposed methods and approaches is demonstrated. Section 4 is devoted to modal filtration. Section 5 describes the method of hollow and thin passive conductors. Section 6 is devoted to the use of magnetodielectric in structures with modal reservation. Section 7 assesses the evaluation of ultrashort pulses (USP) train attenuation possibility. Section 8 considers the use of a meander lines (ML) as a mean of USP protection. The results are discussed in section 9 and summarized in section 10.

2. Brief Review of Related Scientific Works

There is a well-known work [11] that investigates the ultrawideband (UWB) electromagnetic pulse (EMP) effects on commercial DJI Phantom 3 Standard UAV. It was found that the UAV is vulnerable to UWB EMPs. The authors obtained the parameters of emitted pulses and classified the types of equipment faults. They also proposed the characteristics of UWB EMP emitter prototype used for UAV jamming. Since investigations of the influence of electromagnetic environment on UAVs have become relevant in recent years, a novel method is presented to test the susceptibility of UAVs to intentional electromagnetic interference [12]. Using this method, UAVs are tested on susceptibility to radiated continuous waves. The results show that even if the radiated electric field is lower than 1 V/m, the data link that is used by a UAV to communicate with the ground control station can be disrupted. It happens when the frequency of the radiated continuous wave is the same as, or close to, the UAVs data link. Some of the sensitive frequencies, such as 1/2, 1/3, 1/4, and 1/5 times of the working frequency, could lead to the disruption of the data link because of the harmonics produced by nonlinear units. Another study [13] describes a high-power microwave weapon that has many advantages to fight against UAVs. The basic concept of high-power pulse interference is introduced, and the feasibility of the EMI against UAVs is discussed. A change in the UAV normal operation mode was demonstrated with the help of simulation software. The work [14] presents a new model of the UAV datalink in different flight states. The relationship between the airborne operation signal, the induced interference, and the flight parameters is presented and compared in three typical flight states, i.e., the fixed angle state, dive state, and hover state. The article [10] deals with the issue of eliminating UAVs using nondestructive methods with the emphasis on possible electronic warfare applications. The results of the work summarize possible anti-UAV defense means and evaluate their potential defense potential. The article [15] proposes a warning technique in case a possible EMI appears near the UAV, which is based on semantic analysis. The data source for semantic analysis is collected based on the subtle changes of the UAV state parameters during the EMI interference process. The article [16] evaluates the effectiveness of the use of high power directed energy weapons as a method to neutralize civilian UAVs. In [17], various propulsion systems currently used in UAVs are analyzed. In doing so, special attention is paid to the characteristics that are essential to conduct a specific mission, including geological and photogrammetric ones. The book [18] details the aspects of countering a huge range of civil and military UAVs and their respective system components. The article [19] analyzes the EMI characteristics of the converter station equipment in the surrounding area and the EMI impact on the UAV communication circuits. The anti-EMI countermeasures strive to eliminate or reduce the EMI threats on the UAV hardware and its communication network. In [20], the latest accidents with medium and heavy UAVs in the past 10 years are analyzed. Combined with the performance and technical

characteristics of each device, the accident stages, causes, and rules are classified, summarized, and analyzed in detail, and the accident trend is predicted. In [21], various studies on the effect of intentional EMI on UAVs are considered. They are reviewed and classified on the basis of the power level, preset information, and frequency. The article [22] presents the results of the experimental tests of the pulse response of a UAV and its essential components. A standardized lightning pulse that is often used during equipment immunity tests in the aviation industry was applied. A model was built on the basis of the transmittance of the circuits that are most exposed to lightning surges. The article [23] presents the development and examination of genetic algorithms to solve the multicriteria problems of placing the onboard equipment inside UAV fuselage. In addition, the criteria for the EMC of onboard equipment with external, intersystem, and intrasystem electromagnetic effects are considered.

Meanwhile, since information technologies, especially wireless communications, are rapidly developing, the problem of EMC between systems is becoming more important. The article [24] reviews the literature on the EMC subject that is devoted to EMI that may affect data links operating between UAVs and ground stations. The study [25] describes the possibilities of developing innovative experimental and numerical approaches to assess the EMC of UAVs under high EMI intensity, such as lightning and nonnuclear electromagnetic pulses. The article [26] considers the electromagnetic environment of UAV systems and analyzes the features of the EMI impact. The numerical modeling of various EMIs, their experimental testing, and proposals on EMC are considered. In [27], the researchers investigate the influence of intentional EMI on the sensors of a UAV, which is a small serial quadcopter. The interfering signal is a narrowband high-power electromagnetic pulse characterized by frequencies between 100 MHz and 3.4 GHz and field strengths that are above the immunity levels required by EMC standards. In [28], the interference that occurs between the main UAV systems and the CDMA system is investigated using the Simulink software. The work [29] describes the measurements of potential interference spectra in a powerful electrical environment of a large UAV, which is viewed as a platform for installing equipment for measuring electromagnetic fields. The equipment includes an electromagnetically compatible transponder antenna for a tactical automatic landing system. The proposed repeater antenna has a monopole radiator designed for X-band operation in UAV guidance applications, and a protective metal cover to suppress unwanted RF interference. The mechanisms of electromagnetic coupling between the antenna and the neighboring conductive devices are also being studied to develop transponder antenna layout guidelines [30]. The measurements inside the UAV fuselage could also be carried out using a new loop probe with a double load, as described in [31].

The UAV EMC issues are presented in detail in two separate perspectives: radiation and noise immunity [32]. Small UAVs usually include satellite navigation, inertial navigation, and magnetic compass systems. Solid state inertial sensors are used to maintain the position of a UAV

during flight, and a compass can be used to determine the correct azimuth orientation. To study the effect of a powerful microwave pulse on the UAV data transmission channel during dynamic flight, it is proposed to use the interference tracking model for a powerful microwave pulse source in the direction of the UAV [33]. In addition, a dynamic flight model is being built to determine the reception of a powerful UAV microwave pulse. To predict the possible impact of a powerful microwave pulse on a data channel, tests on a certain type of UAV data link are carried out in the presence of a powerful microwave pulse with its carrier frequency in the L-, S-, and C-bands, respectively. The results show that EMI can easily enter the receiver through the antenna when the carrier frequency of a high-power microwave pulse falls within the operating bandwidth of the data link, causing permanent physical damage. Finally, the importance of the task of countering UAVs (and especially small UAVs) is confirmed by a large number of relevant works on this topic, for example, those presented in the book [34].

3. Suggested Approaches and Methods

The creation of any methodology implies the development of theoretical foundations, methods, basic principles, process, and means of their implementation, aimed at solving specific problems. In this case, the problem is to provide the EMC of EMI-based functional destruction means with other REE as part of the UAV countermeasures complex. To solve this sophisticated problem, a novel set of diverse approaches and methods are presented. They are given in Table 1.

In the following sections, the feasibility of the proposed methods and approaches is demonstrated on some examples, which are as follows: modal filtration, which is a method of hollow and thin passive conductors on the example of a 2-conductor MF based on a conventional microstrip line (MSL), a magnetodielectric for a reflection symmetric MF with a triple MR as a resource for increasing the attenuation of the interference signal, a reflection symmetric MF and an ML as a result of TRIZ application when they are exposed to a train of USPs, and an ML as a means of protection against USPs.

4. Modal Filtration

The level of the resulting voltage at the MF output is determined by various factors, namely the geometric configuration of the protective device, the number of conductors, the dielectric material used, and the length. Thus, a conventional MF based on a coupled transmission line is shown in Figure 1, where w is the width of the conductors, s is the distance between the conductors, t is the thickness of the conductors, h is the thickness of the dielectric, d is the distance from the edge of the structure to the conductors, and ϵ_r is the relative permittivity of the substrate (Figure 1(a)). The length (l) of the MF was taken equal to 1 m. As an excitation pulse, an EMF source with a USP in the form of a trapezoid was used with an amplitude of 1 V and the durations of the rise, fall, and flat top (at levels 0–1) of 100 ps, so that the total duration was 300 ps (Figure 1(b)).

TABLE 1: Suggested approaches and methods.

Title	Description
A priori awareness of «friendly» impact, possibly from a database (from open sources like [35]) of the characteristics of EMI-based functional destruction means	A priori knowledge of the specific parameters of the induced interference (for example, a dangerous USP) on numerous REE operating as a part of the UAV opens up the possibility of ensuring the operation of «friendly» UAVs after it being affected by EMI-based functional destruction means.
The use of the theory of inventive problem solving (TRIZ) as part of a diversionary approach [36]	TRIZ guarantees the discovery of hidden resources. The theoretical foundations of TRIZ are the laws of technical system development, formulated as a result of analyzing large arrays of patents, and studying the history and logic of technical system development. TRIZ is built as an exact science that has its own field of study, its own methods, its own language, and its own tools. In addition, TRIZ can be effectively used as part of a diversionary approach to identify weaknesses in case of deliberate impacts.
Modal filtration [37]	This method involves the protection of critical circuits of REE by means of the sequential decomposition of ultrashort pulses (USPs) into a sequence of pulses (because of the difference between mode delays in the transmission line) with much lower amplitudes. Devices based on this technique are called modal filters (MF).
The use of the method of hollow and thin passive conductors in an MF [38]	The method of hollow and thin passive conductors proposed in the Russian Foundation for Basic Research project for spacecraft reduces the mass of MF. In particular, UAV supporting structures can be employed. Placing transmission lines along them can form a protective structure.
Modal reservation (MR) of circuits [39, 40]	Complex reservation of UAV circuits at the level of components, boards, and cables ensures the survivability of the UAV using modal decomposition. A number of studies have been carried out directly on the hybridization of reservation and modal filtration into a single whole. They prove the possibility to successfully and efficiently apply MR. In this case, multicriteria optimization will be used to improve protection and reduce the mass of conductors and dielectrics.
Considering the possibility of dangerous USP impact bypassing protective means [41]	USP protection at a junction of the segments in coupled lines that have the opposite signs of the differences in per-unit-length delays of even and odd modes may be useless. The reason for this may be the USP decomposition into smaller amplitude pulses at this junction with its further recovery at the end of the structure.
The use of a spiral power bus [42]	A spiral power bus proposed for a spacecraft within the framework of the RFBR grant, which is used to protect the UAV, adds a minimum increase in the mass. This approach could reduce the mass and inductance of the bus at the same current load, utilize a minimum number of connectors, and shield (inside this bus) other conductors that are connected to critical nodes.
The use of a protective ML [43]	An ML in air dielectric filling (or an air ML) differs by a complete lack of a dielectric and a single frequency response in a wide frequency band. Nevertheless, it can decompose the USP of unlimited voltage into 2 main pulses of lower voltages. Microstrip MLs allow for USP decomposition into 3 or even 4 pulses.
Resonance shift in the body slots caused by their overlap with a thin magnetodielectric [44, 45]	New models that could set the values of the relative dielectric and magnetic permeability can be selected in accordance with the spectrum of the destructive impact for the masking or protective shift of resonances in the body slots because of their overlap with a thin magnetodielectric.
The use of software tools adapted for the goals of the work [46]	Software tools provide a complex estimation of how efficient the protection against arbitrary influences is according to the criterion of reducing 5 standard N -norms of the time response. They also enable optimization with any set of criteria using a genetic algorithm.

The resistance values (R) were chosen from the condition of matching the structure with the path (the signal amplitude at the beginning of the line (V_2) should be equal to half the EMF of the signal source (V_1) (Figure 1(c)) [47].

5. Method of Hollow and Thin Passive Conductors

UAVs performance could be improved by embedding REE elements or protective devices. At the same time, the minimum increase in mass is very important when developing new UAV designs or improving the existing ones. In this regard, it is effective to employ protective MFs that involve hollow and thin passive conductors. This approach reduces the mass of the final product while maintaining the protective characteristics. For clarity, it is demonstrated on MF prototypes with increased geometric dimensions

(relative to the designs used in real UAVs). What follows demonstrates the main results on the design and building these prototypes. The main structures with hollow and thin passive conductors and their geometric and circuit models are shown. A full-scale experiment on measuring the characteristics of the MF is described. The calculated and measured characteristics of the MF are compared.

The cross-sections and the equivalent circuit of the prototypes are shown in Figure 2. The cross-sections have the following parameters: $w = 10$ mm, $s = 0.5$ mm, $t = 10$ mm (in case of the MF with a thin passive conductor $t = 1$ mm), $h = 1.5$ mm, $g = 1$ mm (wall thickness of conductors), $\epsilon_r = 4.6$, and $tg\delta = 0.025$ (dielectric loss tangent). The parameters of the circuit are as follows: $R_G = R_L = 50 \Omega$, and $R = 10 \Omega$ for the MF with solid, hollow, and corner passive conductors; and $R = 13 \Omega$ for the MF with a thin passive conductor to approximate the values of the mean geometric

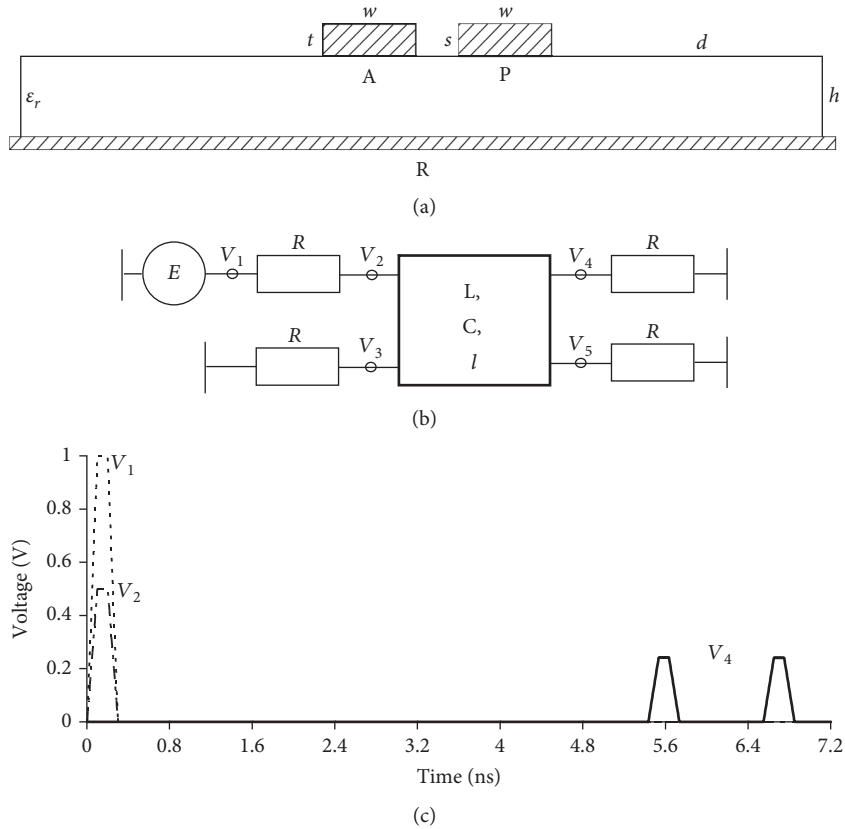


FIGURE 1: (a) Cross-section of the MF based on the coupled line, (b) its equivalent circuit, and (c) waveforms (V_1) of the EMF and voltages (V_2) at the input and (V_4) output of such an MF.

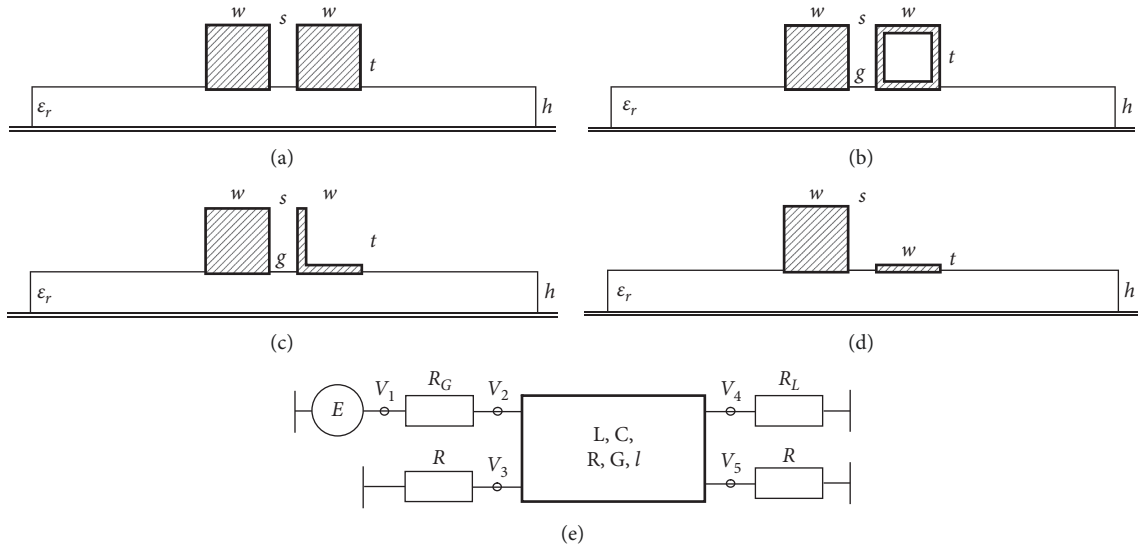


FIGURE 2: Cross-sections of the MF with passive conductors: (a) solid, (b) hollow, (c) corner, (d) thin, and their (e) equivalent circuit.

resistances of the even and odd MF modes. The lengths (l) of all MFs are 28 cm.

A full-scale experiment was conducted using the approach from [48]. In this case, the time and frequency characteristics were calculated in the ADS system based on the experimentally obtained S-parameters. After the MFs

under study were measured in the frequency domain, they were analyzed in the time domain in the ADS 2020 system. The device defined in the frequency domain was represented as an n -port device. It is described by equations that show the relation between the spectral variables of each port. Since the parameters of the scattering matrix (output format of the

S2P type) were determined for the MFs that are coupled MSLS, their circuit in ADS 2020 appeared to be a 2-port device.

The method of determining the time and frequency characteristics based on the measured S-parameters was used to describe the signal propagation through the MF so it is possible to use any form of influence. Therefore, an ideal trapezoidal pulse signal was used with an EMF amplitude of 1 V and the duration of the rise, fall, and flat top of 100 ps each (total duration was 200 ps at a level of 0.5).

The prototypes of the MFs are shown in Figure 3. To make the measurements more convenient, a single FR-4 dielectric substrate (obtained from a compound of 2 FR-4 substrates) was used. In this case, one of the conductors (active) is fixed, and the second is removable. Thus, the passive conductor in the MF can be replaced to measure the characteristics under the same conditions. To ensure the fixation and integrity of the structure, as well as the specified separation between the conductors, recesses were made in the substrate to accommodate the conductors. The recesses were 10 mm wide and 300 μm high. After fixing the conductors into the recesses, they were soldered along the edges for additional fixation and electrical contact (the active conductor was additionally placed on a thin layer of epoxy glue). SMA-connectors were installed at the ends of the active (solid) conductor.

The results of a full-scale experiment on measuring the MF characteristics with solid, hollow, corner, and thin passive conductors are considered in the time and frequency domains. The measuring setup with the MF prototype with a corner passive conductor is shown in Figure 4 (the rest of the passive conductors lie on the table). Figure 5 shows the frequency dependences of $|S_{21}|$ for each MF (measured by the vector network analyzer «Panorama» P4226).

It follows from the measurement results that the bandwidth of all MFs is 77–82 MHz. The frequency dependences of $|S_{21}|$ for the MF with solid, hollow, and corner passive conductors are very close. In this case, the frequency dependence of the MF with a thin passive conductor has significant differences from as high as 2.5 GHz.

$U(t)$ dependences at the output of all MFs, obtained by the experiment and the simulation that took into account losses, are shown in Figure 6. The values of the maximum output voltage for solid, hollow, corner, and thin passive conductors were 0.177, 0.178, 0.192, and 0.251 V during the measurements and 0.116, 0.117, 0.119, and 0.151 V during the simulation, respectively. The maximum deviation of the obtained values during the measurements and simulation was $\pm 25\%$ for the MF with a thin passive conductor. The measurements showed that the values of the maximum output voltage are 5.6, 5.61, 5.2, and 4 times less than the EMF amplitude.

It can be seen that the output signal arrives at approximately the same time with an average deviation of $\pm 3\%$ for the odd (early) mode. Unfortunately, because of the dispersion, it is impossible to accurately determine the arrival time of each pulse during measurements. In addition to dispersion, the voltage waveforms are affected by losses in conductors and dielectrics. It leads to an increase in the rise and fall times of each output pulse and to their partial

superposition, which is clearly observed for the MF with a thin passive conductor. In addition, the pulse amplitudes obtained by the simulation and experimentally differ (despite the fact that in both cases, the active conductor was loaded by 50 Ω and the passive conductor by 10 Ω for the MF with solid, hollow, and corner passive conductors, and 13 Ω for the MF with a thin passive conductor). The reason probably lies in the reflections caused by the mode mismatch, which are clearly manifested during the measurement. Thus, the first sequence of reflections is observed in the range of 3.4–7 ns (not shown in Figure 6 because it was important to detail the main output signal). Additionally, reflections caused by inhomogeneities that arrived at the end of the MF are superimposed on the main mode pulses (mainly on the even pulse (pulse 2)), leading to an increase in the resulting amplitude. It also explains the difference between the pulse amplitudes when simulating and measuring the MF with a thin passive conductor. Despite this, the modal filtration effect is seen to be preserved when the passive conductor of the MF is replaced. In general, there is consistency in the output voltage waveforms obtained experimentally and by the simulation.

Next, the mass of the developed MFs was estimated. Since the filters differ only in the passive conductor, its mass was estimated for various MF configurations.

With $w = 10$ mm, $t = 10$ mm, $g = 1$ mm, $l = 30$ cm, and aluminum density $\rho = 2.71$ g/cm³, the volume of a solid conductor is as follows:

$$V = lwt = 30 \text{ cm}^3, \quad (1)$$

and the mass is as follows:

$$m = V\rho = 81.3 \text{ g}. \quad (2)$$

The conductor cavity volume is as follows:

$$V_h = (l-2g)(w-2g)(t-2g) = 19.072 \text{ cm}^3, \quad (3)$$

and the mass of a hollow conductor is as follows:

$$m_h = (V - V_h)\rho = 29.615 \text{ g}, \quad (4)$$

which is almost 3 times less than the mass of a solid conductor.

The corner conductor mass is as follows:

$$m_C = \frac{m_h}{2} = 14.807 \text{ g}, \quad (5)$$

which is 5.5 times less than the mass of a solid conductor.

For a thin conductor, according to (1) and (2) at $t = 1$ mm, the volume will be 3 cm³, and the mass will be 8.13 g, which is 10 times less than the mass of a solid conductor.

6. Magnetodielectric in Structures with Modal Reservation

Redundancy is used to increase the reliability of REE. Engineers widely use cold redundancy because of the low complexity of its implementation. This approach provides

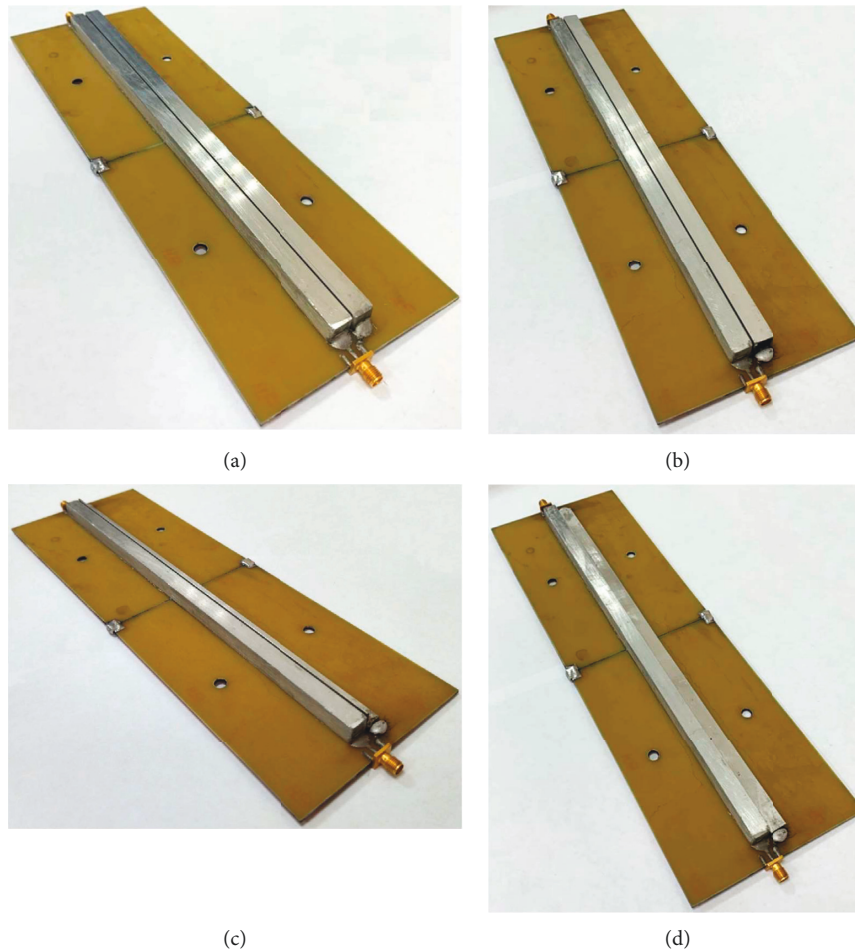


FIGURE 3: MF with a passive conductor: (a) solid, (b) hollow, (c) corner, and (d) thin.

the operation of redundant REE without failures. However, in regular situations, without failures, REE does not utilize the reserved units. Modal reservation (MR) is a type of cold redundancy that provides USP suppression by modal distortions [49]. Using MR to improve the reliability of vulnerable or critical units of UAVs also improves their interference immunity. There are many different structures with MR, which differ in application areas, the efficiency of USP suppression, and mass and size parameters [50, 51]. Of interest are reflection symmetric structures that provide the same USP suppression efficiency for each of the connected units [52]. They have good mass and size parameters, which allow their use in civil and military UAVs. Figure 7(a) shows a cross-section of the initial configuration of the proposed MR structure, which is a shielded four-layer printed circuit board. Figure 7(b) shows its connection diagram. In such a structure, internal conductors can connect power and ground circuits, while external conductors can be used for reserving particularly vulnerable or critical units of the UAV. The UAV enclosure can be used as a shielding surface. However, there may be apertures in the enclosure walls that reduce shielding effectiveness (SE). Shielding integrity can be provided by careful design, however, this task requires accurate solutions.



FIGURE 4: Vector network analyzer «Panorama» P4226 and an MF prototype with a corner passive conductor.

To reduce the resonance effects of the apertures, it is necessary to use TRIZ. By analyzing the existing methods of increasing SE, a technical solution was found. Thus, the space between the external conductors of the structure with a triple MR and the UAV enclosure can be filled with

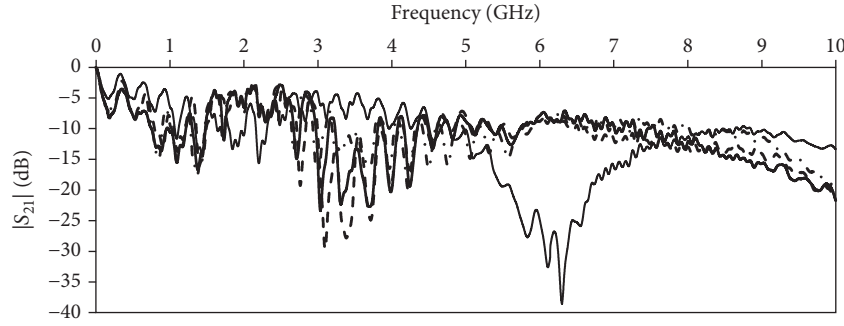


FIGURE 5: Measured frequency dependences $|S_{21}|$ of the MF with passive conductors: (—) solid, (---) hollow, (- · -) corner, and (-) thin.

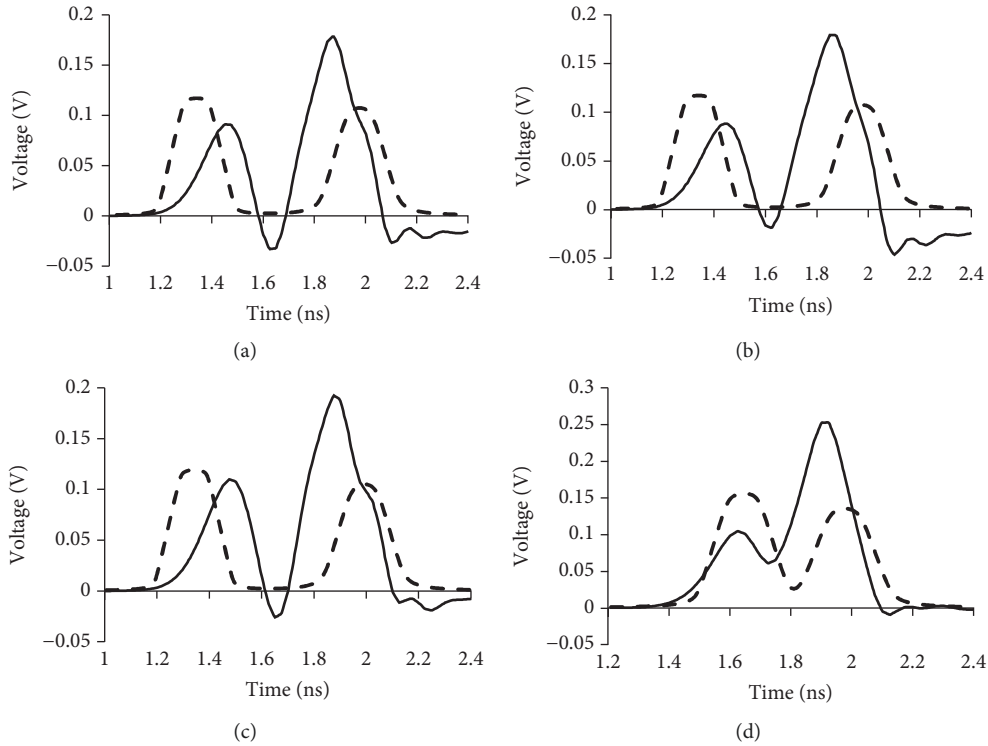


FIGURE 6: Voltage waveforms at the output of the MF with passive conductors: (a) solid, (b) hollow, (c) corner, and (d) thin, obtained by (---) lossy simulation and (—) experimentally.

broadband radio-absorbing materials (RAM), for example, magnetodielectric ZIPSIL RPM-P1, which can effectively be used as a resonance absorber. The high values of ϵ_{r1} and μ_{r1} can improve the USP suppression by increasing the differences in the per-unit-length delays. The electrodynamic simulations of the modified configuration with a triple MR and RAM were performed to evaluate its time and frequency characteristics. The structure was simulated with the following geometric parameters from [53]: $s = 700 \mu\text{m}$, $w = 1000 \mu\text{m}$, $t = 35 \mu\text{m}$, $H = 920 \mu\text{m}$, $H_1 = 2000 \mu\text{m}$, and $h = 510 \mu\text{m}$. The dielectric and magnetodielectric electrical parameters were the following: $\epsilon_r = 4.5$, $tg\delta = 0.025$, $\epsilon_{r1} = 20$, $tg\delta_{\epsilon_1} = 0.06$, $\mu_{r1} = 3$, and $tg\delta_{\mu_1} = 0.5$. To match the transmission line with the interference source U_s and the load, the resistances of all resistors (R) in the simulation were equal to 50Ω . Frequency characteristics were analyzed in the range

from 0 to 3 GHz. To analyze the time characteristics, two Gaussian pulses with a total duration of 0.8 and 2.4 ns were separately fed to the input of the reserved conductor (node V_1) (most of the energy is in the frequency range of 0 to 3 GHz and 0 to 1 GHz, respectively). To evaluate the effectiveness of suppressing such USPs, N -norms can be used [54]. They are also used to evaluate the possibility of dielectric electrical breakdown, and the burnout of connected elements. The analyzed norms and their characteristics from [55] are given in Table 2. The voltage waveforms of the decomposed pulses $U(t)$ are given as an argument in the equation.

Figure 8 shows the frequency dependences of $|S_{21}|$ and the voltage waveforms at the output of the reserved conductor (node V_2), which were obtained in the course of the electrodynamic simulation. The frequency characteristics

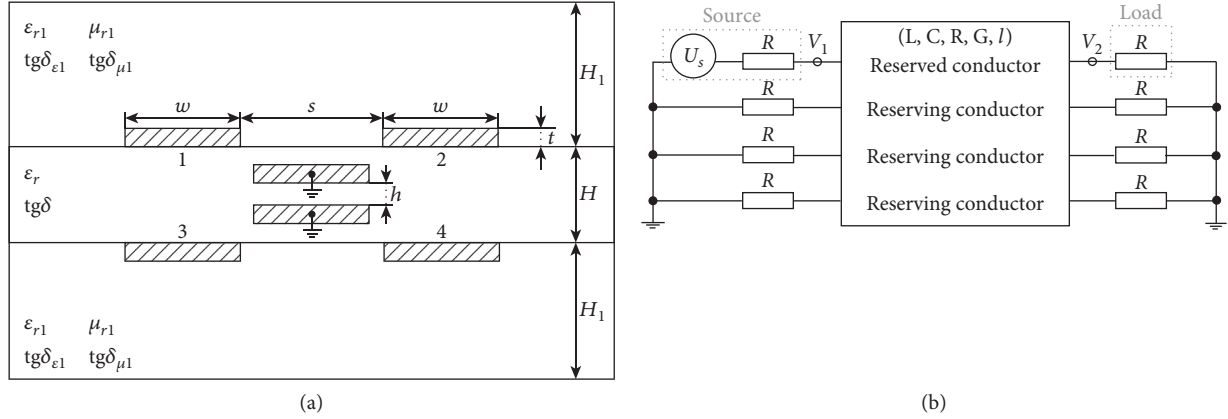


FIGURE 7: Reflection symmetric structure with triple MR: (a) cross-section and (b) connection diagram.

TABLE 2: N -norms description and application.

	N_1	N_2	N_3	N_4	N_5
Formula	$ U(t) _{\max}$	$ dU(t)/dt _{\max}$	$ \int_0^t U(t)dt _{\max}$	$\int_0^\infty U(t) dt$	$\{\int_0^\infty U(t) ^2 dt\}^{1/2}$
Name	The peak value (absolute)	The peak derivative (absolute)	The peak pulse (absolute)	Rectified general pulse	The square root of the action integral
Application	Circuit failure/electric breakdown/electric arc effects	Component sparking/circuit failure	Dielectric breakdown (if U means the E field)	Equipment damage	Component burnout

show that both configurations have the characteristics of a low-pass filter. The use of RAM reduced the cutoff and first resonance frequencies of the structure with MR. The frequency response of the configuration with RAM decreases monotonically with increasing the frequency because of the presence of heavy losses in the magnetodielectric. The time response shows that modal distortions and losses significantly influence the USP waveform. Thus, both configurations decomposed the input pulse into a sequence of 4 pulses. Because of heavy dispersion, complete modal decomposition is not observed. However, both configurations attenuated USPs by several times.

Table 3 provides the values of the cutoff and first resonance frequencies, as well as the maximum voltage at the output of the structure under investigation. The calculated N -norms for the two USPs are given in Table 4.

Table 3 provides that the f_c value decreased by 150 MHz and reached 40 MHz. It is also seen that the f_r value decreased by 490 MHz. Changing these two parameters indicates an increase in the duration of the maximum possible interference pulse, which will be decomposed in the structure with MR. Table 4 provides that both structures significantly attenuated both USPs, and using RAM reduced the values of all norms. Thus, in the case of N_1 , an additional attenuation of 1.87 times was obtained for USPs of 0.8 ns duration, and 2.51 times for USPs of 2.4 ns duration. Because of the strong dispersion, the N_2 value in the RAM configuration is much lower than that in the source configuration. At the same time, the maximum attenuation of the input excitation was 38 times for USPs with a duration of 0.8 ns. In the case of N_3 and N_4 , there is also a decrease in the input excitation. Since there are no negative components in the waveform, the two norms

will be identical. The use of RAM gives only a small advantage under these norms. In the case of N_5 , large differences are observed. Thus, the use of RAM reduced the values of the last norm by at least a factor of 1.74 for both USPs.

7. Evaluation of USP Train Attenuation Possibility

The progress of USP generators is steadily continuing. Their impact on the onboard equipment of the UAVs is more effective than the impact of other types of electromagnetic pulses at the same values of electric field strengths. It is explained by the fact that the duration of interference and information signals commensurate, which leads to an increase in the probability of violating the information processed by the UAV control system [56]. Thus, because of the rapid development of digital computing technology, the increase in the volume and speed of data transmission, and the ability to remotely control UAVs in real time, there appears a need to ensure the stable operation of UAVs under the conditions of possible USP impact. However, modern devices have a number of disadvantages that do not allow full USP protection (insufficient processing speed, parasitic parameters, complexity, and high cost), which urges the development of new devices.

Known are USP protection devices working on the principle of modal filtration. The principle lies in using coupled transmission lines with inhomogeneous dielectric filling to decompose the input USP of a large amplitude into several pulses of smaller amplitudes. As mentioned earlier, one of the devices where modal filtration is implemented is a reflection symmetric modal filter (MF) [57]. However, this

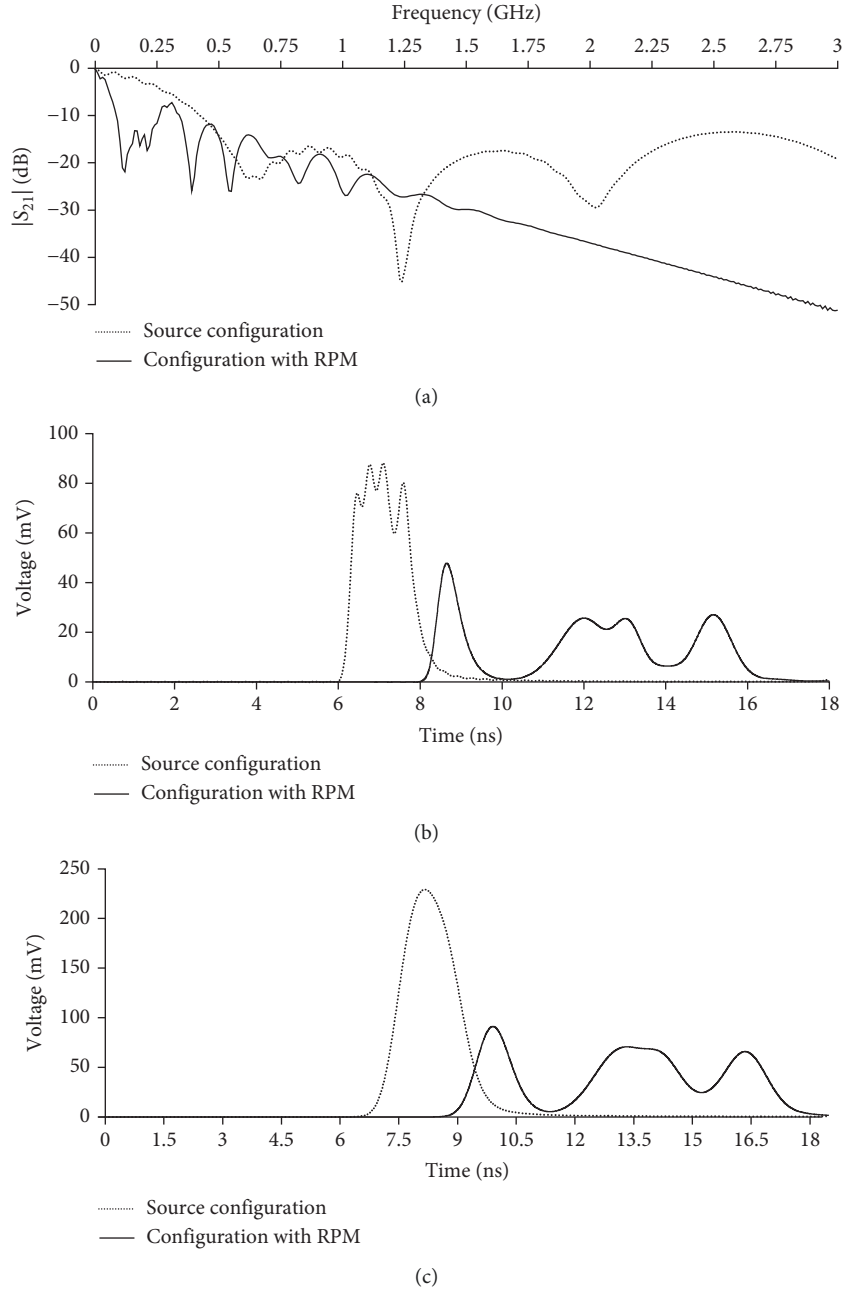


FIGURE 8: Characteristics of the two structures with MR: (a) frequency dependences of $|S_{21}|$, and output voltage waveforms for a USP with the duration of (b) 0.8 and (c) 2.4 ns.

TABLE 3: Cutoff and first resonance frequencies, as well as the maximum voltage at the output under the influence of USPs.

Parameters	f_c , MHz	f_r , MHz	U_{\max} , V (0.8 ns)	U_{\max} , V (2.4 ns)
Source configuration	190	610	0.088	0.229
Configuration with RAM	40	120	0.048	0.091

device has some disadvantages. An important parameter of the MF is the difference in modes' delays. The larger the difference, the longer the USP can be decomposed. Thus, the existing structure should be improved. In this case, it is effective to use TRIZ. By analyzing the existing methods of improving the MF, several solutions were found. One solution is to increase the value of the delay difference by

increasing the length. However, it will result in an increase in the MF size and weight. Another solution is to increase the ϵ_r value, however, the cost of the device will increase. The use of TRIZ led to the idea that there is no need to change the cross-section of the reflection symmetric MF but only its boundary conditions. It was proposed to obtain a reflection symmetric meander line (ML) from a reflection symmetric MF by

TABLE 4: N -norms for USPs of different durations.

Durations of the USP	Type of configuration	N_1	N_2	N_3	N_4	N_5
0.8 ns	Input excitation	1	$5.32 \cdot 10^9$	$285 \cdot 10^{-12}$	$285 \cdot 10^{-12}$	$14.2 \cdot 10^{-6}$
	Source configuration	0.088	$0.32 \cdot 10^9$	$136 \cdot 10^{-12}$	$136 \cdot 10^{-12}$	$2.95 \cdot 10^{-6}$
	Configuration with RAM	0.047	$0.14 \cdot 10^9$	$126 \cdot 10^{-12}$	$126 \cdot 10^{-12}$	$1.69 \cdot 10^{-6}$
2.4 ns	Input excitation	1	$1.77 \cdot 10^9$	$856 \cdot 10^{-12}$	$856 \cdot 10^{-12}$	$24.6 \cdot 10^{-6}$
	Source configuration	0.229	$0.28 \cdot 10^9$	$396 \cdot 10^{-12}$	$396 \cdot 10^{-12}$	$8.09 \cdot 10^{-6}$
	Configuration with RAM	0.091	$1.37 \cdot 10^9$	$375 \cdot 10^{-12}$	$375 \cdot 10^{-12}$	$4.56 \cdot 10^{-6}$

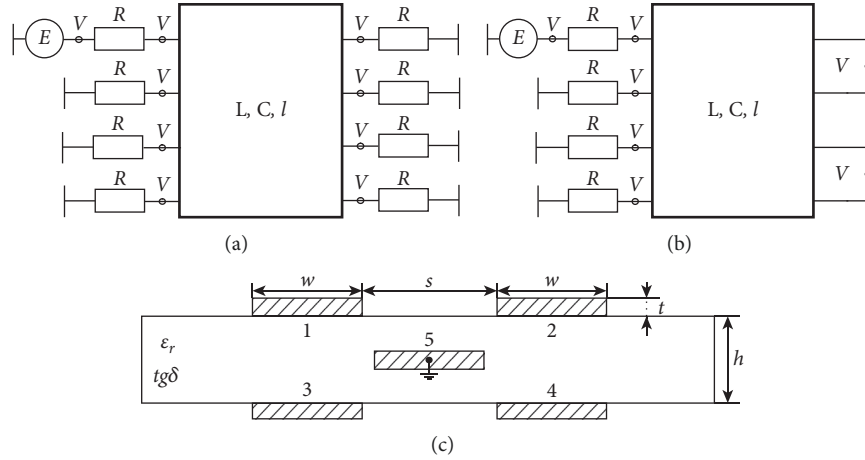


FIGURE 9: Equivalent circuits of reflection symmetric (a) MF, (b) ML, and their (c) cross-section.

electrically connecting the conductors at the ends of the line with bridges, instead of resistive ends to ground. In this case, the length and dimensions will remain unchanged, and the delay difference will increase by 2 times.

The main parameters of a USP are voltage amplitude, pulse duration, and steepness of its front, type, and width of the spectrum, as well as the number of consecutive pulses and the time intervals between them. In a real situation, USPs are generated in the form of a train with a certain frequency or repetition period. In this case, the effectiveness of the impact increases with an increase of its repetition frequency. In this regard, the analysis of the modal decomposition of USP train in reflection symmetric MFs and MLs is relevant.

The simulations were performed in the ADS 2020 software. The time characteristics were obtained using the inverse Fourier transform with the approach from [48]. Initially, S-parameters of the structures were measured with a vector network analyzer «Panorama» P4226 in the frequency range from 10 MHz to 20 GHz. Then, a two-port device was set in the ADS software, which was defined by the frequency characteristics obtained during the measurements. After that, the influence in the form of a train of USPs was applied to its input. Equivalent circuits of a reflection symmetric MF and an ML are shown in Figures 9(a) and 9(b), respectively. The cross-section is shown in Figure 9(c), where w and t are the width and thickness of the conductors (1075 and 35 μm), s is the distance between the conductors (700 μm), h is the dielectric thickness (1000 μm), and ϵ_r is the relative permittivity (4.5). The signal of 4 pulses with repetition periods (T) equal to 0.5, 1, and 2 ns was selected as an

excitation. The amplitude of each pulse is 1 V, the duration of the front, fall, and flat top are 50 ps each, and the total duration (t_Σ) is 150 ps.

Figure 10 shows the simulation results for the reflection symmetric MFs and MLs excited by a USP train, and Table 5 provides the amplitudes (U_{\max}) at the output of the structures.

It follows from Figure 10 that the superposition of the decomposition pulse sequences of individual USPs from the train increases the voltage amplitudes at the MF and ML outputs as the T value decreases. At $T=2$ ns, there is a division of each pulse from the USP train into a separate sequence of decomposition pulses. Therefore, with the fixed values of T and the duration of each pulse from the train, their complete decomposition is possible if the value of T is greater than or equal to the total duration of the sequence of decomposition pulses of one USP.

8. Using an ML as a USP Protection Means

Consider an ML to attenuate a USP amplitude. It is known that in one turn of an ML in air dielectric filling (or an air ML), the USP can be decomposed into 2 pulses (crosstalk and main signal) of smaller amplitudes [43], and in a turn of a microstrip ML, it is decomposed into 3 pulses (crosstalk and pulses of odd and even modes) of even smaller amplitudes [58]. Hence, for instance, the USP attenuation in the air ML was 1.6 times, and in the microstrip, it was 2.4 times. Moreover, the researchers managed to decompose a USP into as many as 4 pulses of smaller amplitudes [59]. The

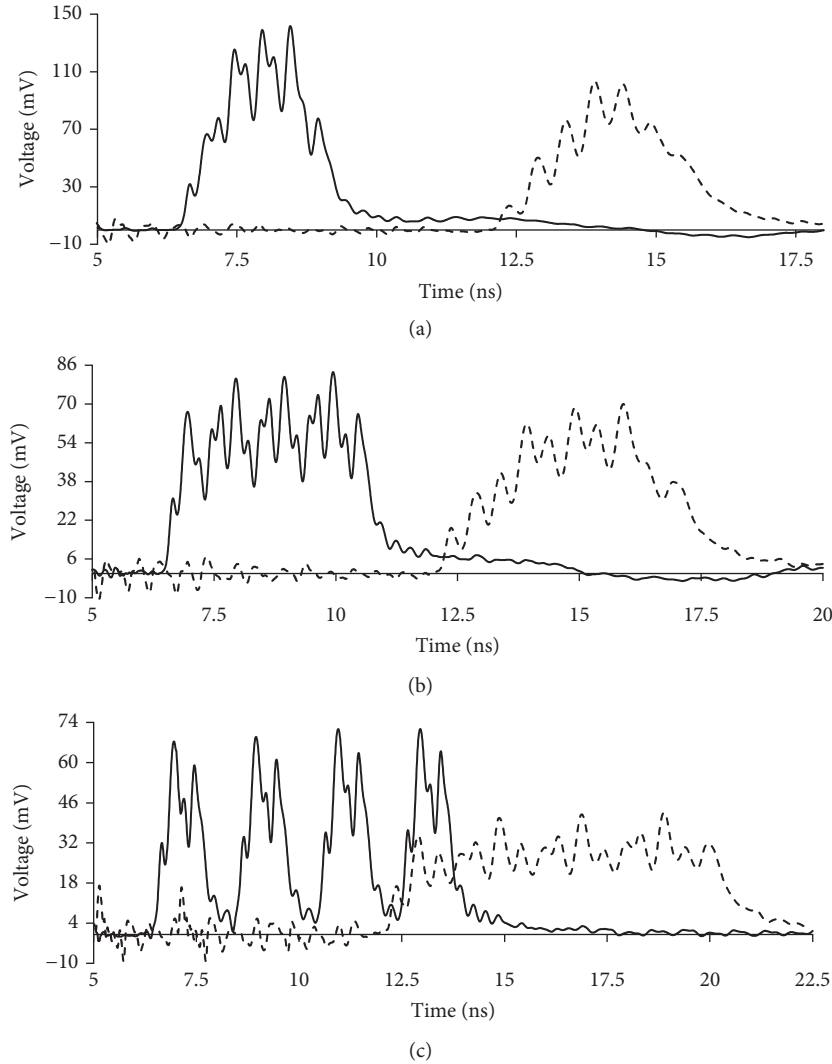


FIGURE 10: Voltage waveforms at the output of the reflection symmetric (—) MF and (---) ML when excited by a USP train with repetition periods of (a) 0.5, (b) 1, and (c) 2 ns.

TABLE 5: Amplitudes at the output of the structures.

Repetition period of pulses in the USP train (ns)	0.5	1	2
U_{\max} at the output of the reflection symmetric MF (mV)	141.39	82.27	69.45
U_{\max} at the output of the reflection symmetric ML (mV)	100.97	69.71	41.71

research on the ML application to protect against USPs proved the possibility to increase the USP attenuation in the line. Thus, because of the asymmetry in the cross-section of a microstrip ML and the addition of another passive conductor [60], the USP attenuation in the line was as much as 5.4 times. Another resource is ML cascading [61], which allowed for the 5-time USP attenuation in the MSL with 2 turns connected in the cascade. When the line had 3 turns, the attenuation was 8 times: 4 turns–20 times, and 5 turns–33 times. Finally, the ML and MF can form a hybrid device based on their cascade connection. Thus, the cascade

connection of a 3-conductor MF and a turn of a meander MSL allowed for the 10-time USP attenuation [62]. The structures based on a cascade connection of 3 and 4-conductor MF and the ML with a broadside coupling enabled as much as 12-time attenuation of the USP [63]. Note that these publications formulated conditions that allow complete USP decomposition for its maximum attenuation. These conditions are directly related to the matrices of the secondary parameters of the structures, which, in turn, are determined by their geometric parameters. These results were revealed with the help of TRIZ and previously developed approaches and methods.

9. Discussion

For the first time, the authors propose a set of diverse approaches and methods to solve the problem of providing the EMC of EMI-based functional destruction means with other REE as part of the UAV countermeasures complex. The

feasibility of the proposed approach has been demonstrated using some examples.

(1) Modal filtration

Modal filtration technology underlies a number of approaches aimed to solve the problem of ensuring EMC for both UAV countermeasure systems and «friendly» UAVs. At the same time, the very essence of the decomposition of conductive pulse excitations of short duration into a sequence of pulses with smaller amplitudes is valid for a wide range of MFs. However, an important factor is the possibility of using the available interconnects of a specific REE instead of a separate printed circuit board. For instance, such options that can be employed are as follows: the enclosure as a ground return plane, the free space on the printed circuit board, the existing cables and cable assemblies (replacement or modernization) as part of the REE, and the conventional printed conductors (with proper routing).

(2) Method of hollow and thin passive conductors

The measurement results confirm that the exciting pulse can be decomposed at the end of the active conductor of the MF when a solid passive conductor is replaced with a hollow, corner, or thin conductor. The consistency of the output voltage waveforms obtained experimentally and during the simulation was achieved. It was shown that the measured MFs had a bandwidth of about 77–82 MHz, and the values of the maximum output voltage were 5.6, 5.61, 5.2, and 4 times less than the EMF amplitude for the MFs with solid, hollow, corner, and thin passive conductors, respectively. Finally, it was estimated that when a solid passive conductor was replaced with a hollow one, it was possible to achieve a gain in mass by 3 times, with a corner conductor by 5.5 times, and with a thin conductor by 10 times. In this case, the decomposition of the USP into a sequence of pulses of smaller amplitudes is preserved.

(3) Magnetodielectric in structures with modal reservation

The application of TRIZ approach made it possible to design a device with a triple MR, which has improved interference protection characteristics. Using magnetodielectrics, it became possible to shift the resonant frequencies of the enclosure and suppress emissions. The N-norms of decomposed pulses were evaluated using two different durations of USPs and revealed the high efficiency of the investigated structure with MR in suppressing dangerous conducted interference.

(4) The evaluation of USP train attenuation possibility

In the considered example, the reflection symmetric MF attenuated the USP by 3, 6, and 7 times, and the ML by 5, 7, and 12 times at repetition periods of 0.5, 1, and 2 ns, respectively. More effective attenuation in the ML is explained by the fact that the time

intervals between the decomposition pulses of one USP is 2 times longer than that in the MF. The construction of such a device, which retains the dimensions of the original one and at the same time has improved characteristics, was possible, thanks to the use of the TRIZ approach in the development process.

(5) Using an ML as a USP protection means

A further increase in the attenuation of a USP in an ML (relative to the data in the main part of the study) and the applicability of MLs in UAVs will be carried out using verified approaches and methods, as well as, if necessary, new ones using the TRIZ approach. Now, it seems attractive to take advantage of an increase in the number of passive conductors, the use of asymmetry, cascading, as well as the hybridization of new structures based on MLs and MFs to increase USP attenuation. The approaches and methods discussed will allow for the synthesis of these devices while considering the requirements for the UAVs in which they will be used.

Thus, a careful study of the presented approaches and techniques resulted in a unified blended methodology that could further motivate the formulation of unique private methods. Their results will be represented by specific technical solutions aimed to ensure the EMC of specific UAV countermeasures systems, as well as «friendly» UAVs during potential military operations. As a result, there is a prospect of eliminating «enemy» UAVs (by means of EMI-based functional destruction means), without damaging «friendly» infrastructure and UAVs. On top of all, it can be done cost-effectively.

10. Conclusions

The study demonstrates the expediency of using a number of proposed approaches and methods exemplified by specific structures and under specific interference effects. A unique methodology was proposed for ensuring the EMC of UAV countermeasure systems that incorporate EMI-based functional destruction means. The obtained results are highly relevant and their use is incredibly broad because they imply additional protection (within the proposed methodology). It is true for REE operating as part of the UAV countermeasures complex and for «friendly» UAVs.

The next step is to create the valid design of the methodology, taking into account the proposed methods and approaches. For this purpose, it is important to make an extensive review and analysis of well-known methods for ensuring the EMC of critical components and systems. In addition, it is important to systematize the well-known means of EMI-based functional destruction means, as well as UAVs.

Data Availability

The data used to support this study are available from the corresponding author upon request.

Conflicts of Interest

The authors declare that there are no conflicts of interest.

Acknowledgments

The reported study was funded by the Russian Science Foundation (22-29-01331).

References

- [1] V. N. Zhuravlev and P. V. Zhuravlev, "Usage of unmanned aerial vehicles in general aviation: current situation and prospects," *Civil Aviation High Technologies (Nauchnyi Vestnik MGTU GA)*, vol. 4, pp. 156–164, 2016, in Russian.
- [2] S. A. Lyasheva, M. V. Medvedev, and M. P. Shleimovich, "Terrain object recognition in unmanned aerial vehicle control system," *izvestiya vysshikh uchebnykh zavedenii, Aviatsonnaya Tekhnika*, vol. 3, pp. 64–66, 2014, in Russian.
- [3] S. A. Lyasheva, M. V. Medvedev, and M. P. Shleymovich, "Image wavelet compression in unmanaged vehicle control systems," *Vestnik Kazanskogo gosudarstvennogo tekhnicheskogo universiteta im. A.N. Tupoleva*, vol. 4, pp. 218–222, 2013, in Russian.
- [4] M. Nuriev, "Physical simulation of an unmanned aerial vehicle electronic means noise immunity," *Trudy MAI*, vol. 102, no. 1–15, 2018, in Russian.
- [5] Z. M. Gizatullin, R. M. Gizatullin, and M. G. Nuriev, "Mathematical models for physical modeling problems of electromagnetic compatibility," *Power Engineering: Research, Equipment, Technology*, vol. 1–2, pp. 115–122, 2015, in Russian.
- [6] M. A. Holland, "Counter-drone systems," center for the study of the drone at bard college, *February*, vol. 20, p. 23, 2018.
- [7] C. rogue drones, *FICCI Committee on Drones*, p. 31, FICCI, New Delhi, India, 2018.
- [8] E. de Visser, M. S. Cohen, and M. LeGoullon, "A design methodology for controlling, monitoring, and allocating unmanned vehicles," in *Proceedings of the Third International Conference on Human Centered Processes (HCP-2008)*, pp. 1–5, Delft, The Netherlands, June 2008.
- [9] B. H. Sheu, C. C. Chiu, W. T. Lu, C. I. Huang, and W. P. Chen, "Development of UAV tracing and coordinate detection method using a dual-axis rotary platform for an anti-UAV system," *Applied Sciences*, vol. 9, no. 13, pp. 1–17, 2019.
- [10] M. Kratky and V. Minarik, "The non-destructive methods of fight against UAVs," in *Proceedings of the 2017 International Conference on Military Technologies (ICMT)*, pp. 690–694, Brno, Czech Republic, June 2017.
- [11] K. Y. Sakharov, A. V. Sukhov, V. L. Ugolev, and Y. M. Gurevich, "Study of UWB electromagnetic pulse impact on commercial unmanned aerial vehicle," in *Proceedings of the 2018 International Symposium on Electromagnetic Compatibility (EMC EUROPE)*, pp. 40–43, Amsterdam, Netherlands, August 2018.
- [12] Y. Chen, D. Zhang, E. Cheng, and X. Wang, "Investigation on susceptibility of UAV to radiated IEMI," in *Proceedings of the 2018 IEEE International Symposium on Electromagnetic Compatibility and 2018 IEEE Asia-Pacific Symposium on Electromagnetic Compatibility (EMC/APEMC)*, pp. 718–722, Suntec City, Singapore, May 2018.
- [13] C. Gao, Z. Xue, W. Li, and W. Ren, "The influence of electromagnetic interference of HPM on UAV," in *Proceedings of the 2021 International Conference on Microwave and Millimeter Wave Technology (ICMMT)*, pp. 1–3, Nanjing, China, May 2021.
- [14] D. Zhang, E. Cheng, H. Wan, X. Zhou, and Y. Chen, "Prediction of electromagnetic compatibility for dynamic datalink of UAV," *IEEE Transactions on Electromagnetic Compatibility*, vol. 61, no. 5, pp. 1474–1482, 2019.
- [15] X. Gao, H. Jia, Z. Chen, G. Yuan, and S. Yang, "UAV security situation awareness method based on semantic analysis," in *Proceedings of the 2020 IEEE International Conference on Power, Intelligent Computing and Systems (ICPICS)*, pp. 272–276, Shenyang, China, July 2020.
- [16] J. L. Esteves, E. Cottais, and C. Kasmi, "Unlocking the access to the effects induced by IEMI on a civilian UAV," in *Proceedings of the 2018 International Symposium on Electromagnetic Compatibility (EMC EUROPE)*, pp. 48–52, Amsterdam, Netherlands, August 2018.
- [17] M. Adamski, "Analysis of propulsion systems of unmanned aerial vehicles," *Journal of Marine Engineering & Technology*, vol. 16, no. 4, pp. 291–297, 2017.
- [18] A. Haider, "A comprehensive approach to countering unmanned aircraft systems," *Joint Air Power Competence Centre*, pp. 1–6, 2020, <https://www.japcc.org/books/a-comprehensiv-e-approach-to-countering-unmanned-aircraft-systems/>.
- [19] Y. Li, Q. Ding, K. Li, S. Valtchev, S. Li, and L. Yin, "A survey of electromagnetic influence on UAVs from an EHV power converter stations and possible countermeasures," *Electronics*, vol. 10, no. 6, p. 701, 2021.
- [20] P. Wang, C. Wu, Y. Wang, F. Xu, and J. Chen, "Statistics and analysis of foreign military medium and heavy UAV accidents," in *Proceedings of the SPIE 11562, AOPC 2020: Advanced Laser Technology and Application*, Beijing, China, November 2020.
- [21] S.-G. Kim, E. Lee, I.-P. Hong, and J.-G. Yook, "Review of intentional electromagnetic interference on UAV sensor modules and experimental study," *Sensors*, vol. 22, no. 6, p. 2384, 2022.
- [22] P. Szczupak and T. Kossowski, "Response of drone electronic systems to a standardized lightning pulse," *Energies*, vol. 14, no. 20, p. 6547, 2021.
- [23] I. V. Suzdaltsev, S. F. Chermoshencev, and N. Y. Bogula, "Genetic algorithm for onboard equipment placement inside the unmanned aerial vehicle fuselage," in *Proceedings of the 2016 XIX IEEE International Conference on Soft Computing and Measurements (SCM)*, pp. 262–264, St. Petersburg, Russia, May 2016.
- [24] I. Bennageh, H. Mahmoudi, and M. Labbadi, "Impact of the electromagnetic environment on UAV's datalink," *IOP Conference Series: Earth and Environmental Science*, vol. 785, pp. 1–6, 2021.
- [25] S. G. Garcia, "UAVEMI project: numerical and experimental EM immunity assessment of UAV for HIRF and lightning indirect effects," in *Proceedings of the 2016 ESA Workshop on Aerospace EMC (Aerospace EMC)*, pp. 1–5, Valencia, Spain, May 2016.
- [26] Y. Wu, Q. Ma, and P. Xu, "Progress of electromagnetic compatibility design for unmanned aerial vehicles," *MATEC Web of Conferences*, vol. 316, no. 11, Article ID 4008, 2020.
- [27] G. Lubkowski, M. Lanzrath, L. C. Lavau, and M. Suhrke, "Response of the UAV sensor system to HPEM attacks," in *Proceedings of the 2020 International Symposium on Electromagnetic Compatibility*, pp. 1–6, Rome, Italy, September 2020.
- [28] J. Junmin, S. Qijun, and G. Yougang, "The simulation of interference between the unmanned aerial vehicle (UAV)

- system and the CDMA system based on Simulink,” in *Proceedings of the The 2006 4th Asia-Pacific Conference on Environmental Electromagnetics*, pp. 750–754, Dalian, China, August 2006.
- [29] R. Geise, A. Weiss, T. Fritzel, R. Strauß, F. T. Faul, and T. F. Eibert, “Interference measurements of a high power cable-bound unmanned aerial vehicle,” in *Proceedings of the 2019 13th European Conference on Antennas and Propagation (EuCAP)*, pp. 1–5, Krakow, Poland, April 2019.
- [30] S. Lin, M. Cho, M. Lin, W. Hu, and J. Sun, “EMC considerations in transponder antenna design for tactical automatic landing systems,” in *Proceedings of the TENCON 2019 – 2019 IEEE Region 10 Conference (TENCON)*, pp. 235–237, Kochi, India, October 2019.
- [31] M. Pous, S. Fernández, M. Añón, M. R. Cabello, L. D. Angulo, and F. Silva, “Time domain double-loaded electromagnetic field probe applied to unmanned air vehicles,” in *Proceedings of the 2018 IEEE Symposium on Electromagnetic Compatibility, Signal Integrity and Power Integrity (EMC, SI & PI)*, pp. 30–35, Long Beach, CA, USA, August 2018.
- [32] R. J. Perez, “EMC considerations for unmanned aerial vehicles,” in *Handbook of Aerospace Electromagnetic Compatibility*, pp. 603–619, IEEE, 2019.
- [33] D. Zhang, X. Zhou, E. Cheng, H. Wan, and Y. Chen, “Investigation on effects of HPM pulse on UAV’s datalink,” *IEEE Transactions on Electromagnetic Compatibility*, vol. 62, no. 3, pp. 829–839, June 2020.
- [34] S. I. Makarenko, “Protivodejstvie Bepilotnym Letatel’nym apparatam. Monografiya,” *Naukoemkie tekhnologii*, vol. 204, 2020 in Russian.
- [35] N. Mora, F. Vega, G. Lugrin, R. Farhad, and R. Marcos, “Study and classification of potential IEMI sources,” *System and assessment notes*, *Note*, vol. 41, p. 92, 2014.
- [36] T. R. Gazizov, “Design of electronic systems protected from electromagnetic terrorism,” in *Proceedings of the 15-th Int. Wrocław Symp. on EMC*, pp. 469–472, Poland, Wrocław, June 2000.
- [37] A. T. Gazizov, A. M. Zabolotsky, and T. Rashitovich Gazizov, “UWB pulse decomposition in simple printed structures,” *IEEE Transactions on Electromagnetic Compatibility*, vol. 58, no. 4, p. 1136, 2016.
- [38] A. O. Belousov and T. R. Gazizov, “Method for tracing modal filter conductors,” 2750393, 2021.
- [39] T. R. Gazizov, P. E. Orlov, A. M. Zabolotsky, and S. P. Kuksenko, “New concept of critical infrastructure strengthening,” in *Proceedings of the 13th Int. Conf. of Numerical Analysis and Applied Mathematics*, pp. 1–3, Rhodes, Greece, September 2015.
- [40] A. O. Belousov, A. V. Medvedev, E. B. Chernikova, T. R. Gazizov, and Z. Alexander, “Switching order after failures in symmetric protective electrical circuits with triple modal reservation,” *Symmetry*, vol. 13, no. 6, pp. 1–22, Article ID 1074, 2021.
- [41] A. M. Zabolotsky, T. R. Gazizov, A. G. Bova, and W. A. Radasky, “Dangerous pulse excitation of coupled lines,” in *Proceedings of the 2006 17th International Zurich Symposium on Electromagnetic Compatibility*, pp. 164–167, Singapore, March 2006.
- [42] M. E. Komnatnov, T. R. Gazizov, I. I. Nikolaev, and A. A. Demakov, “Drozdova Method for manufacturing power transmission line with spiral cross-section and device based on its basis,” 2749558, 2021.
- [43] R. Surovtsev, T. Gazizov, and A. Zabolotsky, “Pulse decomposition in the turn of meander line as a new concept of protection against UWB pulses,” in *Proceedings of the 2015 International Siberian Conference on Control and Communications (SIBCON)*, pp. 1–5, Omsk, Russia, May 2015.
- [44] A. A. Ivanov, M. E. Komnatnov, and M. E. Komnatnov, “Semi-analytical method for evaluating shielding effectiveness of an enclosure with an aperture,” *Proceedings of Tomsk State University of Control Systems and Radioelectronics*, vol. 24, no. 1, pp. 16–23, 2021.
- [45] A. A. Ivanov, A. V. Demakov, and M. E. Komnatnov, “Semi-analytical approach for calculating shielding effectiveness of an enclosure with a filled aperture,” *Electrica*, vol. 22, no. 2, pp. 220–225, 2022.
- [46] S. P. Kuksenko, “Preliminary results of TUSUR University project for design of spacecraft power distribution network: EMC simulation,” *IOP Conference Series: Materials Science and Engineering*, vol. 560, pp. 1–7, Article ID 12110, 2019.
- [47] A. O. Belousov, E. B. Chernikova, and M. A. Samoylichenko, “From symmetry to asymmetry: the use of additional pulses to improve protection against ultrashort pulses based on modal filtration,” *Symmetry*, vol. 12, no. 7, pp. 1–38, 2020.
- [48] R. Vauché, “Experimental time-domain study for bandpass negative group delay analysis with lill-shape microstrip circuit,” *IEEE Access*, vol. 9, pp. 24155–24167, Article ID 24155, 2021.
- [49] T. R. Gazizov, P. E. Orlov, A. M. Zabolotsky, and S. P. Kuksenko, “New Concept of Critical Infrastructure Strengthening,” *AIP Conference Proceedings*, vol. 1738, Article ID 440007, Rhodes, Greece, 2016.
- [50] Y. S. Zhechev, A. V. Zhecheva, A. A. Kvasnikov, and A. M. Zabolotsky, “Using N-norms for analyzing symmetric protective electrical circuits with triple modal reservation,” *Symmetry*, vol. 13, no. 12, p. 2390, 2021.
- [51] P. E. Orlov, A. V. Medvedev, and V. R. Sharafutdinov, “Quasistatic simulation of ultrashort pulse propagation in the spacecraft autonomous navigation system power circuit with modal reservation,” in *Proceedings of the 2018 19th International Conference of Young Specialists on Micro/Nanotechnologies and Electron Devices (EDM)*, pp. 1–6, Erlagol, Russia, July 2018.
- [52] Y. S. Zhechev, E. B. Chernikova, and A. O. Belousov, “Research of the new structure of reflection symmetric modal filter,” in *Proceedings of the 2019 20th International Conference of Young Specialists on Micro/Nanotechnologies and Electron Devices (EDM)*, pp. 108–112, Erlagol, Altai Republic, July 2019.
- [53] Y. S. Zhechev, “Experimental study of the buried vias effect on reflection symmetric modal filter performance,” in *Proceedings of the 2020 21st International Conference of Young Specialists on Micro/Nanotechnologies and Electron Devices (EDM)*, pp. 200–204, Chermal, Russia, July 2020.
- [54] C. E. Baum, *Mathematics Notes. Note*, p. 63, 1979.
- [55] D. V. Giri, “High-Powered Electromagnetic Radiators: Nonlethal Weapons and Other Applications,” *Electromagnetics library*, Harvard University Press, Cambridge, MA, 2004.
- [56] Y. V. Yukhanov, T. Y. Privalova, A. Y. Yukhanov, V. I. Andrianov, A. G. Ostrovsky, and V. F. Los, “Peculiarities of videopulse scanning antenna array design,” in *Proceedings of the 2006 3rd International Conference on Ultrawideband and Ultrashort Impulse Signals*, pp. 85–89, Sevastopol, Ukraine, September 2006.
- [57] E. B. Chernikova and A. A. Ivanov, “Using composite insulating materials to improve modal filter performance,” in *Proceedings of the 2020 21st International Conference of Young*

- Specialists on Micro/Nanotechnologies and Electron Devices (EDM)*, pp. 187–190, Chernal, Russia, July 2020.
- [58] R. S. Surovtsev, A. V. Nosov, and A. M. Zabolotsky, “Simple method of protection against UWB pulses based on a turn of meander microstrip line,” in *Proceedings of the 2015 16th International Conference of Young Specialists on Micro/Nanotechnologies and Electron Devices*, pp. 175–177, Erlagol, Russia, July 2015.
- [59] A. V. Nosov and R. S. Surovtsev, “Revealing new possibilities of ultrashort pulse decomposition in a turn of asymmetrical meander delay line,” in *Proceedings of the 2020 21st International Conference of Young Specialists on Micro/Nanotechnologies and Electron Devices (EDM)*, pp. 149–153, Chernal, Russia, July 2020.
- [60] A. V. Nosov and R. S. Surovtsev, “Ultrashort pulse decomposition in the turn of a meander microstrip line with a passive conductor,” *Journal of Physics: Conference Series*, vol. 1862, pp. 1–6, 2021.
- [61] G. Y. Kim, A. V. Nosov, and R. S. Surovtsev, “Conditions for ultrashort pulse decomposition in multi-cascade protection devices based on meander microstrip lines,” *Journal of Physics: Conference Series*, vol. 1679, pp. 1–6, 2020.
- [62] A. V. Nosov, A. O. Belousov, and R. S. Surovtsev, “Simulating hybrid protection against ultrashort pulse based on its modal decomposition,” *Journal of Physics: Conference Series*, vol. 1353, pp. 1–6, 2019.
- [63] G. Kim, A. Nosov, and R. Surovtsev, “Ultrashort pulse decomposition in hybrid protection devices based on the cascade-connected modal filter and meander line with broad-side coupling,” in *Proceedings of the 2021 IEEE 22nd International Conference of Young Professionals in Electron Devices and Materials (EDM)*, pp. 163–166, Souzga, the Altai Republic, Russia, July 2021.

Research Article

A Novel Mining Approach for Data Analysis and Processing Using Unmanned Aerial Vehicles

Ali Alenezi ^{1,2} Ahmad Sawalmeh ^{2,3} Hazim Shakhatreh ⁴ Muhannad Almutiry ^{1,2}
and Nasser Aedh Alreshidi ⁵

¹Department of Electrical Engineering, Northern Border University, Arar, Saudi Arabia

²Remote Sensing Unit, Northern Border University, Arar, Saudi Arabia

³Computer Science Department, Northern Border University, Arar, Saudi Arabia

⁴Department of Telecommunications Engineering, Hijawi Faculty for Engineering Technology, Yarmouk University, Irbid, Jordan

⁵Department of Mathematics, College of Science, Northern Border University, Arar, Saudi Arabia

Correspondence should be addressed to Hazim Shakhatreh; hazim.s@yu.edu.jo

Received 2 March 2022; Revised 3 May 2022; Accepted 5 May 2022; Published 18 May 2022

Academic Editor: Chao Zeng

Copyright © 2022 Ali Alenezi et al. This is an open access article distributed under the Creative Commons Attribution License, which permits unrestricted use, distribution, and reproduction in any medium, provided the original work is properly cited.

In the mining industry, smart surveying and exploration operations for the minerals are essential during mining missions. Usually, these missions are performed in remote areas that do not have a wireless communications infrastructure. This paper proposes to use the unmanned aerial vehicle (UAV) as a relay communication node between the exploration team and the ground control station (GCS). UAV can act as a relay node to provide mobile, flexible, and reliable communication links in remote environments and complex topologies. In this work, the pathloss models in millimeter-wave technology are considered because they provide massive data rates for line of sight scenarios. The optimization problem of identifying a 3D location and trajectory of the UAV relay node is formulated to maximize the total team members' data rate. Because the problem is non-convex, the particle swarm optimization algorithm is used to solve it and determine an efficient location and trajectory of the UAV.

1. Introduction

Unmanned Aerial Vehicles (UAVs) have recently been employed in a variety of civilian applications, including real-time monitoring, infrastructure inspection, remote sensing, search and rescue operations, cargo delivery, surveillance, precision agriculture, and assisting with wireless coverage [1]. The UAV can be used for a variety of purposes in wireless communications, including providing coverage in the scenario of a base station failure during a disaster or temporary congestion in a specific geographic area [2–4].

On the one hand, numerous studies use UAVs as wireless communication relay nodes. For example, the analysis in [5] proposed employing a UAV as a relay to lower UAV transmission power. In addition, the team designed an energy-efficient relay UAV deployment in [6], which reduces backhaul link capacity and backhaul link latency. Kumar et al. [7] also addressed utilizing a UAV as a relay

communication node to guarantee the quality of service requirements was met. Furthermore, the authors devised a closed-form to discover the optimal position of the UAV acting as a relay in [8], to maximize network reliability. In [9], the authors study the problem of locating an aerial relay node efficiently that is presented as an optimization problem, with the goal of maximizing total wireless device throughput. When conventional base stations' capacity is suffering in some extreme scenarios, such as congestion inside the cell or a particular event, the authors of [10] propose an efficient three-dimensional placement of a single UAV-assisted wireless network. The goal of the research is to determine the 3D location of the UAV base station as well as the percentage of available bandwidth that must be allocated to the UAV in order to maximize the number of users serviced. The authors of [11] investigate a UAV-enabled uplink NOMA network in which the UAV receives data from ground users while flying at a predetermined altitude.

They study the topic of user pairing and provide a dynamic power allocation technique for calculating the user's power allocation coefficients, as well as a closed-form equation for the ergodic sum rate. In [12], the authors utilize a cell on wheels that cooperates with a single UAV in order to provide maximum wireless coverage to ground users.

On the other side, Zhan et al. proposed in [8] a multi-UAV relaying network between a group of users and a distant base station to establish a single-hop communication between ground users and the base station. In this work, a fixed-wing UAV relay communication node was used. Specifically, the communication link between the relay node and the ground users was described using free-space pathloss model. The authors concentrated on the physical communication layer, link efficiency, message error rate, and the ground device handoff mechanism for switching between relay nodes.

Moreover, the topic of relay selection for UAV-assisted vehicular ad hoc networks (VANETs) was investigated in [13]. They investigate multi-UAV collaboration, the network communication node motion model, and the quality of service for air-to-surface connections for UAV relaying in VANETs.

In [14], the authors take advantage of two sleep-scheduling policies for massive machine-type communication devices, namely, the multiple vacation policy and the start-up threshold policy, which are defined in the context by three different multiple access protocols: time-division multiple access, frequency-division multiple access, and non-orthogonal multiple access. Furthermore, under the constraints of energy harvesting power, status update rate, and stability conditions, they develop closed-form formulas for the massive machine-type communication devices system's peak age of information (AoI), which are formulated as the optimization objective. By fixing the status update rate, an exact linear search-based approach is proposed for finding the optimal solution. A low-complexity concave-convex technique is also proposed as a design alternative for finding a near-optimal solution by transforming the original problem into a form represented by the difference of two convex problems. The authors in [15] study an AoI-energy-aware data collection system for UAV-assisted Internet of Things (IoT) networks using age of information as a performance metric to assess the temporal correlation among data packets consecutively sampled by the Internet of Things devices. By optimizing the UAV flight speed, hovering sites, and bandwidth allocation for data collection, they aim to reduce the weighted sum of predicted average AoI, UAV propulsion energy, and transmission energy at IoT devices. By adding a deep neural network for feature extraction, they develop a twin-delayed deep deterministic policy gradient-based UAV trajectory planning algorithm to deal with the multidimensional action space. In [16], the authors study an energy-efficient computation offloading technique for UAV-mobile-edge computing (MEC) systems with a focus on physical-layer security. For secure UAV-MEC systems, they design a set of energy-efficiency challenges, which are subsequently transformed into convex problems. Finally, the

optimal solutions for both active and passive eavesdroppers are found.

Typically, in the exploration and search for minerals, the site to be analyzed in mining operations is first examined by the work team using geophysical equipment. This information is forwarded to the ground control station (GCs) for analysis, processing, and creating maps of the Earth's layers. Surveys are conducted in remote places where no telecommunication networks are available. As a result, the data acquired is kept and processed later at the GCs. Our research suggests a practical 3D placement of a dynamic UAV to operate as a relay node between the work team devices and the distant GCs over millimeter-wave frequencies in remote areas.

Because the surrounding environment in mining is typically harsh terrain, wireless communications network planning and enhancement is a challenging task. It differs from what communications engineers are used to when constructing wireless communications networks. In [17], they addressed the planning and optimization of broadband wireless networks in open-pit mines.

On the other hand, due to the constant change in topology and fleet in an open-pit mining environment, the study in [18] emphasizes the requirement for persistent wireless communication planning. Also, they provide an example of an LTE network that was planned and established in an open-pit mining site in 2007 to meet the needs of users and devices on the site, but in 2014 this network was no longer in service with only 34% of users; furthermore, the mine became more significant, and more areas needed to be connected by wireless communications.

Since working in an open-pit mine requires a collaborative system that includes mining people, sensors, and communications infrastructure. Rangan et al. discussed the possibility of a wireless emergency communications framework based on UAVs in deep open mines [19]. They found that, in open-pit mines, a UAV-based system has a viable communication method during an emergency and to bridge the coverage gap where there is no communication infrastructure. The rigorous performance evaluation of their proposed communications Skyhelp framework was implemented as a proof of concept.

1.1. Paper Contributions. The paper contributions are outlined as follows:

- 1 Two path losses models are utilized: The Air-to-Ground (ATG) pathloss model is utilized for the backhaul link. While, for the uplink, the Ground-to-Air pathloss model is used. These pathloss models are appropriate for 5G Aerial Millimeter Wave Networks.
- 2 The problem of determining the most efficient location and trajectory of a single UAV is addressed in order to optimize the total data rates of wireless devices in the scenario of uplink transmissions.
- 3 The RPGM mobility model is proposed and used to represent the users' movement inside the targeted

mining area and the PSO algorithm to find the efficient placements and trajectory for a UAV that maximizes the data rates of the wireless devices on uplink transmissions scenario.

The rest of this paper is structured as follows. In Section 2, the system model is presented. This section also includes the pathloss models for uplink and backhaul links. Section 3 presents the problem of determining an efficient UAV 3-D location and trajectory. Next, in Section 4, the Reference point group mobility model (RPGM) is presented. Then, Section 5 discusses the proposed UAV Placement and Trajectory Algorithm. After that, the simulation results are presented in Section 6. Finally, the conclusions are shown in Section 7.

2. System Model

Let the location of the aerial relay node is denoted by (x, y, z) and M wireless devices are assumed to be far away from the GCs. Due to the lack of line-of-sight linkages and substantial route losses caused by operating at high frequencies, these wireless devices are unable to communicate with the remote GCs. The drone, which works as an aerial relay node to convey information from the wireless devices to the GCs, must service the wireless devices, as illustrated in Figure 1. We assume an uplink situation in which the data is sent to the UAV using a frequency-division multiple access (FDMA) method with a signal-to-noise ratio (SNR) larger than or equal to SNR_{th} threshold.

This section considers a rectangular geographical region as a targeted mining area, $\mathbb{G} \subset \mathbb{R}^2$, this region is divided into n sub-regions $\mathcal{D} \in (n_1, n_2, \dots, n_k)$, where \mathcal{D} denoted as $(x_{\text{minimum}}, y_{\text{minimum}})$ and $(x_{\text{maximum}}, y_{\text{maximum}})$ as presented in Figure 2. More specifically, the users are distributed non-uniformly inside each sub-regions using beta random distribution and moving from sub-regions n to $n + 1$.

In this model, a single UAV serves and tracks mobile users during their movement inside the targeted region to accomplish the survey mission for mining. The UAV 3-D placement is represented by $(x_{uav}, y_{uav}, z_{uav})$ where (x_{uav}, y_{uav}) is the 2-D UAV placement and z_{uav} is the height of the UAV.

The mobile UAV can change its location to serve the ground users in the uplink scenario. We employ two mm wave pathloss models operating in 28 GHz in this scenario. The first model is the uplink model between users and UAV; the ground to air path model [20], and the second is between UAV and GCs [3]. Moreover, the RPGM mobility model represents the ground users' movement inside the targeted region.

2.1. Path Loss Models. Millimeter waves technology can support bandwidth up to 2 GHz since it operates in an extremely high frequency (EHF) band, ranging from 28 GB to 100 GB, allowing multiple gigabit data rates transmission. Millimeter-wave technology is unsuitable for non-line of sight (NLOS) communication link scenarios for a relatively large distance due to the high signal attenuation, not only

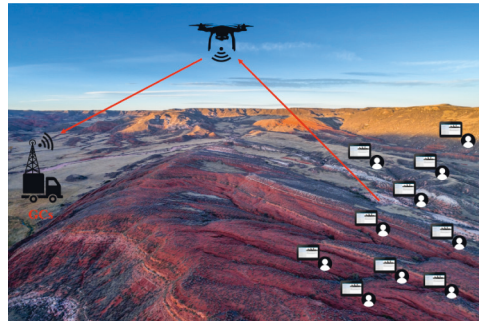


FIGURE 1: UAV acting as a relay node.

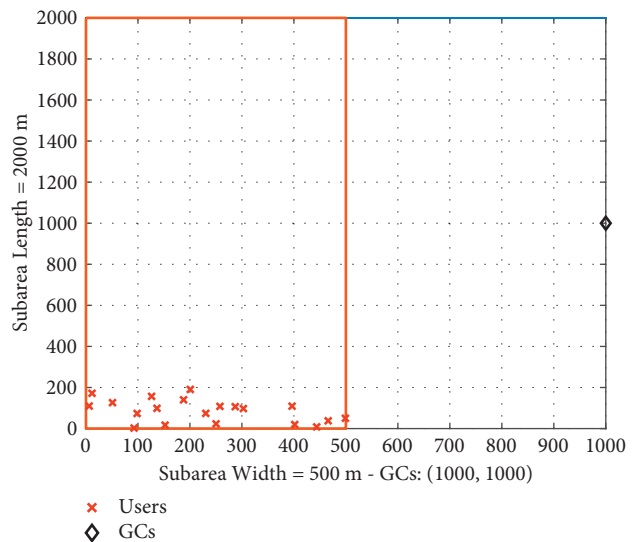


FIGURE 2: System settings of a coverage sub-area.

from buildings or barriers but also from being blocked by the human body [21]. But it is possible to use the millimeter-wave technique in cases where there are (NLOS) communication links at relatively small distances or in the LOS communication link for several kilometers.

In this research, we assume that a group of geologists are in the process of geological surveying and imaging the Earth's layers to detect minerals underground. There is a ground control station at a distance from them to process the data captured by exploration and prospecting devices. Since we use millimeter waves and do not have reliable LOS communication links with the ground control station, we use a UAV as a relay node between the wireless devices and the ground station. This study considers the uplink scenario between the ground users' devices and the UAV relay node.

2.2. Ground to Air Channel Model. We assume the survey team is working in semi-rugged terrain and providing data directly to the UAV relay node over millimeter waves in the case of uplink. To describe the channel between the ground users and the UAV relay node, we use the rural area route loss model. The mean pathloss between the i th user and UAV is given by [20, 22, 23].

$$L_{a,i} = P_L(r_i, z_u)L_{L,i} + [1 - P_L(r_i, z_u)]L_{N,i}, \quad (1)$$

where $L_{L,i}$ and $L_{N,i}$ are the pathlosses for LOS and NLOS links and they are given by

$$\begin{aligned} L_{L,i} &= A_L + 10B_L \log_{10}(d_i), \\ L_{N,i} &= A_N + 10B_N \log_{10}(d_i), \end{aligned} \quad (2)$$

where A_L , B_L , A_N , and B_N are the parameters of the line of sight (LOS) and non-line of sight (NLOS) pathloss models, and $d_i = \sqrt{(x_i - x_u)^2 + (y_i - y_u)^2 + (z_i - z_u)^2}$ is the 3D distance between the user and the UAV. Moreover, $P_L(r_i, z_u)$ represents the probability of human body blockage for the i th user and can be modeled as [23].

$$P_L(r_i, z_u) = \exp\left(-\lambda g_B \frac{r_i(h_B - h_R)}{(z_u - z_i)}\right), \quad (3)$$

where r_i is 2D distance between the i th user and the UAV, z_u is the height of the UAV, λ is the density of human blockers, g_B is the diameter of human blockers, h_B is the height of the human blocker, and z_i is the height of the user.

2.3. Air to Ground. Since we assumed the exploration and surveying operations take place in a remote area, we use the free space pathloss model to characterize communication channel between the UAV and the GCs. In free space pathloss model, L_{FS} the signal strength has a proportional relationship with the carrier frequency and the distance between the transmitter and the receiver, whereas the frequency or the distance increases, the pathloss will increase, as follows [3].

$$L_{\text{UAV-GC}}(d_{3D}) = 20\log_{10}(d_{3D}) + 20\log_{10}(f) + 92.45, \quad (4)$$

where $d_{3D} = \sqrt{(X_U - X_{GC})^2 + (Y_U - Y_{GC})^2 + (Z_U - Z_{GC})^2}$ is the 3D distance between the projection of the UAV and the GCs in Km , and f is the carrier frequency of the transmitted signal in GHz.

3. Problem Formulation

The problem of data rate maximization between ground users and the GCs via the UAV relay node is discussed in this work. As a result, we have two communication channels: one between ground users and the UAV and another between the UAV and the GCs. The data rate between a ground user i and the UAV can be calculated from Shannon's theorem as follows [24]:

$$C_{i\text{-UAV}} = B_{i\text{-UAV}} \log_2(1 + \text{SNR}_{i\text{-UAV}}), \quad (5)$$

where $B_{i\text{-UAV}}$ is the bandwidth assigned for ground user i , and $\text{SNR}_{i\text{-UAV}}$ is the signal-to-noise ratio of the received signal of ground user i at UAV relay node. However, the data rate between the UAV relay node and the GCs is given by

$$C_{\text{UAV-GCs}} = B_{\text{UAV-GCs}} \log_2(1 + \text{SNR}_{\text{UAV-GCs}}), \quad (6)$$

where $B_{\text{UAV-GCs}}$ is the bandwidth assigned for the communication channel between the UAV relay node and the GCs, and $\text{SNR}_{\text{UAV-GCs}}$ is the SNR of the UAV relay node transmitted signal at the GCs receiver.

This work aims to find an efficient placement and trajectory of a single UAV where the objective is to maximize the total data rate for ground nodes. The problem is formulated as follows:

$$x_u^t, y_u^t, z_u^t \sum_{i=1}^{|U|} \sum_{|T|} B_{i\text{-UAV}} \log_2(1 + \text{SNR}_{i\text{-UAV}}^t), \quad (7a)$$

$$\sum_{i=1}^{|U|} B_{i\text{-UAV}} \log_2(1 + \text{SNR}_{i\text{-UAV}}^t) \leq B_{\text{UAV-GCs}} \log_2(1 + \text{SNR}_{\text{UAV-GCs}}^t), \forall t \in T, \quad (7b)$$

$$\text{SNR}_{i\text{-UAV}}^t \geq \text{SNR}_{th}, \forall i \in U, \forall t \in T, \quad (7c)$$

$$p_i^t \leq p^{\max}, \forall i \in U, \forall t \in T, \quad (7d)$$

$$p_i^t \geq 0, \forall i \in U, \forall t \in T, \quad (7e)$$

$$x_{\min} \leq X_u^t \leq x_{\max}, \quad (7f)$$

$$y_{\min} \leq Y_u^t \leq y_{\max}, \quad (7g)$$

$$z_{\min} \leq Z_u^t \leq z_{\max}. \quad (7h)$$

Constraint (7b) is used to guarantee that the data rate for the connection between the drone and the ground wireless

devices is less than or equal to the data rate of the connection between the GCs and the drone. The constraint (7c) is to

ensure that the devices' SNR is greater than or equal to the threshold. Moreover, constraint (7d) is used to ensure that the power consumption for each ground device is less than the maximum power for this device. The constraint (7e) is to ensure that the power consumption for each device is greater than or equal to zero. The constraints from (7f)–(7h) present the maximum and minimum X_u^t , Y_u^t , and Z_u^t values.

4. Mobility Model

Mobility models describe mobile nodes and users' movement patterns and mobility behavior. Moreover, it describes the location, velocity, and acceleration changes for users over time. Mobility models are split into two classes; individual movement models like a Random-Walk, or Brownian motion, Probabilistic Random Walk [25], Random Waypoint [26], Weighted Waypoint [27], and Random Directions [28]. The second category is group movement models such as Reference Point Group Model (RPGM) [29], Column Mobility Model, Nomadic Mobility Model, and Pursue mobility model [25]. RPGM illustrates the users' mobility inside the targeted mining area in this paper.

In RPGM model [29], the users' cluster has a centroid point, namely, logical reference point (RP). Moreover, all cluster members track the RP movement. Group RP's motion represents its behavior, with additional movement parameters such as the user's velocity, locations, direction, and acceleration. Hence, the group's trajectory is defined according to the RP movement. The group members are distributed uniformly near the reference point center within the targeted mining region.

For every time slot, the users' are moved inside the targeted sub-region and move from one sub-region to another by tacking the RP. The sub-region members are distributed randomly near the RP.

The RPGM model describes the mobility of group members for numerous approaches, such as in battleground communications and during catastrophe scenarios in search and rescue missions. In these systems, group members progress towards a common objective and create all users' cooperative movement.

The RPGM consists of RP (group centroid) and all group members inside the sub-region. The main components of this model will be represented as:

- 1 Reference point (RP): The RP guides the group member's movement, representing the group's motion pattern. Vector $\overrightarrow{V}_{g(t)}$ denotes the RP mobility of the group member's at time t and velocity v . The vector's path $\overrightarrow{V}_{g(t)}$ will be selected based on a predefined path or in a random manner. In this study, a predefined path to represent the member's trajectory is considered.
- 2 Group nodes: The RP movement will impact the mobility of the cluster members. The movement of each member is associated with the RP movement, which lets the cluster members heed the model movement. The allocation of group members is randomly distributed around the RP.

Group members represent the nodes located inside the sub-region of the team members.

The motion vector $\overrightarrow{Vel}_{i(t)}$ for member i at time t described as the following equation [30]:

$$\overrightarrow{Vel}_{i(t)} = \overrightarrow{Vel}_{g(t)} + G_{MV_i}(t), \quad (8)$$

where $G_{MV_i}(t)$ is the group motion vector of member i , and $\overrightarrow{Vel}_{g(t)}$ is the motion vector of the reference point.

5. UAV Placement and Trajectory Algorithm

In this section, the PSO algorithm [31, 32] is utilized to find the efficient UAV placement and trajectory such that the total data rate for all wireless devices in the uplink connection between all users and UAV is less than or equal to the total data rate for the backhaul connection between UAV and GCs. Specifically, the PSO algorithm is utilized to locate an efficient solution for the formulated problem in Section 3. Moreover, the proposed algorithm pseudo-code is presented in this section.

5.1. Particle Swarm Optimization Algorithm (PSO). Eberhart, Russell, and Kennedy proposed in [33] the PSO algorithm in 1995. PSO is a heuristic algorithm works based on the paradigm of a swarm and animal social behavior such as schools of fish and swarm of birds. In this algorithm, the swarm consists of n particles, and the particles communicate with each other for finding an efficient output to the formulated problem. During every iteration, the location and velocity of all particles are updated to better positions. The update process occurred according to the particles cost and the cost of their neighbors.

PSO is initialized with a set of n possible solutions (particles/members). Then, PSO updates the best local location and velocity for all particles/members according to velocity and position equations (9) and (10). In addition, PSO updates the global best location.

$$\begin{aligned} V_j(t+1) = & V_j(t) + (k1 * rand) * (P_j^{\text{Best-Local}}(t) - P_j(t)) \\ & + (k2 * rand) * (P_j^{\text{G-Best}}(t) - P_j(t)). \end{aligned} \quad (9)$$

Here, $V_j(t+1)$ is the speed at $t+1$, $k1$ is the acceleration coefficients for best local solution. While, $k2$ is the acceleration coefficients global best solution. $rand$ is a function used to generate a random number between 0 and 1, $P_j(t)$ is the location of the j_{th} particle/member, $P_j^{\text{Best-Local}}(t)$ is the best location of the j_{th} particle/member at time t , and $P_j^{\text{G-Best}}(t)$ is the global best location of the problem.

The following equation presents the positions update for particle/member:

$$P_j(t+1) = P_j(t) + V_j(t+1). \quad (10)$$

The PSO algorithm is considered one of the most popular meta-heuristic algorithms. It can be used for finding or choosing a near-optimal solution to the optimization problem. PSO employs a global search method to locate the

```

1 Efficient UAV 3-D Placement
2 Input:
3  $(h_{\min}, h_{\max})$ : min. and max. UAV height.  $(x_{\min}, x_{\max}), (y_{\min}, y_{\max})$ : MIN. and MAX. dimensionalities of the 2-D region.
4 Initialization:  $z1 = \text{total\_pathloss from users to UAV}$ ;  $z2 = \text{total\_pathloss from UAV to GCs}$ ;
5 For  $(h = h_{\min} : h_{\max}, x = x_{\min} : x_{\max}, y = y_{\min} : y_{\max})$ 
6 for All users (U): a) Apply PSO to find 3-D UAV placement that minimizes  $z$  1; b) Find  $z2$ ;
7 end
8 If  $z1 \leq z2$ , then  $x_{\min} = x_{\min} + 1$ ;
9 Go to Step 3
10 else
11 Efficient 3-D UAV placement =  $(x, y, h)$ 
12 end
13  $(x, y, h)$  is the efficient 3-D UAV placement at minimum pathloss between users and UAV that satisfying the constraint in (7a).

```

ALGORITHM 1: Proposed algorithm for efficient UAV 3-D placement.

global optimal point instead of being stuck in a local minimum solution. Thus, the employment of the global search approach in PSO can overcome the problem of the local search methods that converges optimal local solutions. Moreover, it can converge to the efficient solution faster than other meta-heuristic algorithms [11].

5.2. Meta-Heuristic Algorithms Complexity. In this section, we present the computation complexity of two meta-heuristic algorithms, the PSO and the genetic algorithm GA. For PSO, the complexity depends on the following steps: a- Initialization of the population. b- Fitness function evaluation which requires t iterations. c- Performs N_{it} iterations for step b. d- Performs p_{it} iterations to update velocity and position for each particle. The worst-case complexity of these steps can be expressed as $\mathcal{O}(tp_{it}N_{it})$. For constant N_{it} the algorithm complexity is $\mathcal{O}(tp_{it})$.

On the other hand, the performance of the PSO-based approach is compared and evaluated against the GA algorithm. The computation complexity of the GA algorithm is discussed in detail in [30]. In GA, the fitness function of each particle of n population will be evaluated, then, the tournament selection to select m individuals that have the best fitness score, to become parents of the new generation of m individuals using the crossover and mutation process, will be evaluated. Specifically, in the tournament selection, it takes $\mathcal{O}(\log(m))$ operations, after building the initial tournament in $\mathcal{O}(m)$. Thus, considering the worst-case scenario, the computational complexity of the GA algorithm can be denoted as $\mathcal{O}(n.m \log(m))$.

The simulation results section presents the results for both PSO and GA algorithms, and we show that the PSO requires less computational complexity and less execution time.

5.3. Efficient UAV Placement Approach. This section discusses the proposed approach to find the efficient 3D UAV placement and trajectory such that the total group members throughput is maximized and satisfies the backhaul link throughput. Algorithm 1 presents the proposed approach. In this algorithm, we apply the PSO to solve the optimization

problem and find the 3-D UAV placement that minimizes the total path losses between ground users and the UAV; then, we compare this pathloss with the backhaul pathloss between UAV and GCs. Here, we aim to guarantee that the total throughput between all users and UAV does not exceed the backhaul link throughput, specifically, to satisfy constraint 8a in the problem formulation. If the total pathloss between users and UAV is less than the backhaul link pathloss, then we move UAV 1 meter towards the GCs as in Step 5 in the proposed algorithm. These steps will be repeated until this constraint is satisfied.

6. Simulation Results and Discussion

In this section, the results of the proposed approach are presented. PSO is employed to find a UAV trajectory considering the mobility of the mining team, where their movement follows the RPGM models. In this paper, we aim to maximize the throughput of the mining team's members, satisfying the constraints in the problem formulation (7a)–(7h). The simulation parameters used in this work are presented in Table 1.

In this work, the dimension of the targeted mining region, \mathbb{D} is 500 m \times 2000 m. Moreover, the team members are uniformly distributed inside the sub-region and moving in a group based on RPGM model. In this scenario, the total number of team members is 20.

The total required time to finish the mining mission in each targeted area \mathbb{G} is defined as T . Then, the targeted area \mathbb{G} is split into n sub-areas, with dimensions of 500 m \times 2000 m, where the 200 m is the sub-area length $\in \mathbb{D}$. The average movement speed of the team members is 0.41 m/s [30].

Figure 3 illustrates the movement of the mining team members from one sub-area to another at a speed of 0.41 m/s. Here, the worst-case distribution scenario for the mining team members inside sub-region k_n is considered. In this scenario, the users are distributed inside the whole k_n . Then, we find an efficient UAV placement, where the total path-losses between team members and the UAV are minimized, and guarantees that the total throughput between users and UAV does not exceed the backhaul link

TABLE 1: Simulation and system parameters.

Simulation and System Parameters					
Targeted mining area, \mathbb{G}	(x_{\max}, y_{\max})	(500 m, 2000 m)	Frequency	f	28 GHz
Min UAV height	h_{\min}	100 m	$(\alpha, \beta, \zeta \sim \mathcal{N}(0, \sigma^2))$	NLOS	(113.63, 1.16, 2.58)
Number of teams members	U	20	$(\alpha, \beta, \zeta \sim \mathcal{N}(0, \sigma^2))$	LOS	(84.64, 1.55, 0.12)
GCs location	(x_{GCs}, y_{GCs})	(1000, 1000)	PSO max # of iterations	N_{it}	100
Mining mission period	T	≈ 80 min	PSO population size	N_{pop}	50
Users velocity	V_i	≈ 0.41 m/sec	Height of GCs	hGCs	6 m
# Of sub-regions inside each \mathcal{E}	k	10	Noise power	N_p	-100 dBm

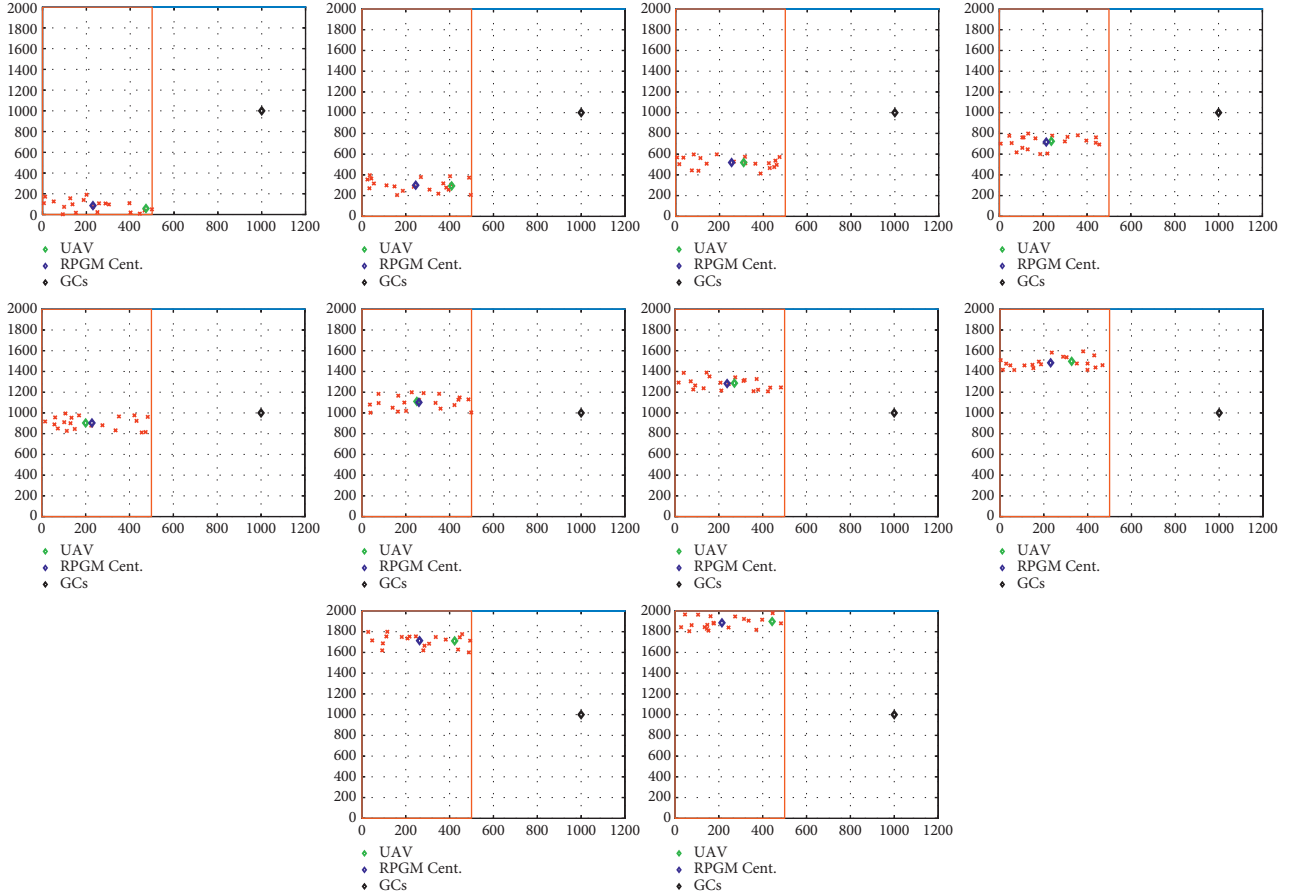


FIGURE 3: Users movement and trajectory based on RPGM inside the sub-area from T1 to T10. The dimensionalities of the axes are meters.

throughput. Specifically, this figure shows the users distribution, reference point for RPGM model, GCs, and the efficient 3-D UAV placement for each sub-region from T1 to T10.

As we can see in Figures 3–1, the sub-region dimensions (0, 0) to (500, 200), the mining team members starts forward movement from the beginning of the trajectory between (0, 500) with velocity 0.41 m/s. The reference point for this sub-region is (230, 86) as shown in Figures 3–1. The mining team members are distributed uniformly around this point. The time required to survey this sub-region is 8.1 minutes. Moreover, an efficient 3D UAV placement using PSO is (472, 58.38, 100). This figure also presents the UAV 3-D placement and the reference point for the RPGM model for all time steps from T1 to T10.

Table 2 depicts the dimension of the sub-regions, the reference point of the RPGM model, the efficient 3-D UAV placement using two different heuristic algorithms PSO and GA. This table also presents the average pathloss for the uplink between team members and the aerial UAV; and the pathloss between UAV and the GCs for all time steps.

Moreover, from this table, it can be clearly seen that the PSO and GA algorithms converge to the same efficient placement. As a result, to compare these two meta-heuristic algorithms, we consider the execution time and the computational complexity for the worst-case scenario. On the other hand, the required time to find the efficient placement using GA is 1.9644 sec. Moreover, the PSO requires, on average, 1.6417 sec. Therefore, the PSO algorithm outperforms the GA in terms of execution time. The PSO reduces

TABLE 2: Simulation results for mining mission inside a subarea.

Time	Alg.	Sub-region	Efficient UAV 3-D	Reference RPGM	Average pathloss	Pathloss
Step (T_n)		(m)	Placement	Model placement	Usr-UAV	UAV-GCs
T1	PSO	0–200	(472, 58.379, 100)	(230.81, 86.72, 0)	122.1563	122.094
	GA		(470.22, 56.01, 102.74)		122.1650	
T2	PSO	200–400	(409, 293.248, 100)	(245.38, 300.45, 0)	120.7329	120.7300
	GA		(409.3761, 293.6445, 100)		120.7400	
T3	PSO	400–600	(310, 518.708, 100)	(255.06, 519.13, 0)	120.0709	119.9504
	GA		(312.42, 520.07, 100)		120.0714	
T4	PSO	600–800	(237, 723.795, 100)	(213.89, 716.78, 0)	119.8564	119.641
	GA		(239.10, 702.38, 100)		119.700	
T5	PSO	800–1000	(200, 903.039, 100)	(228.72, 903.46, 0)	119.6643	119.5821
	GA		(203.88, 908.61, 100.06)		119.6856	
T6	PSO	1000–1200	(250, 1.1112e+03, 100)	(260, 1101.8, 0)	119.6257	119.0550
	GA		(251.42 1.1112e+03 100)		119.6258	
T7	PSO	1200–1400	(271, 1.2872e+03, 100)	(237.8, 1283.5, 0)	119.3638	119.3418
	GA		(272.6354, 1.2923e+03, 101.3710)		119.4084	
T8	PSO	1400–1600	(327, 1.4976e+03, 100)	(231.2, 1483.5, 0)	120.0784	119.9063
	GA		(328.40 1.4974e+03 100)		120.0877	
T9	PSO	1600–1800	423, 1.7112e+03, 100)	(262.9, 1713.5, 0)	120.7655]	120.6787
	GA		(428.29 1.7084e+03 100.54)		120.8518	
T10	PSO	1800–2000	(443, 1.8982e+03, 100)	(214.1, 1885.6, 0)	122.0125	121.9112
	GA		(454.91 1.8977e+03 101.68)		122.2650	

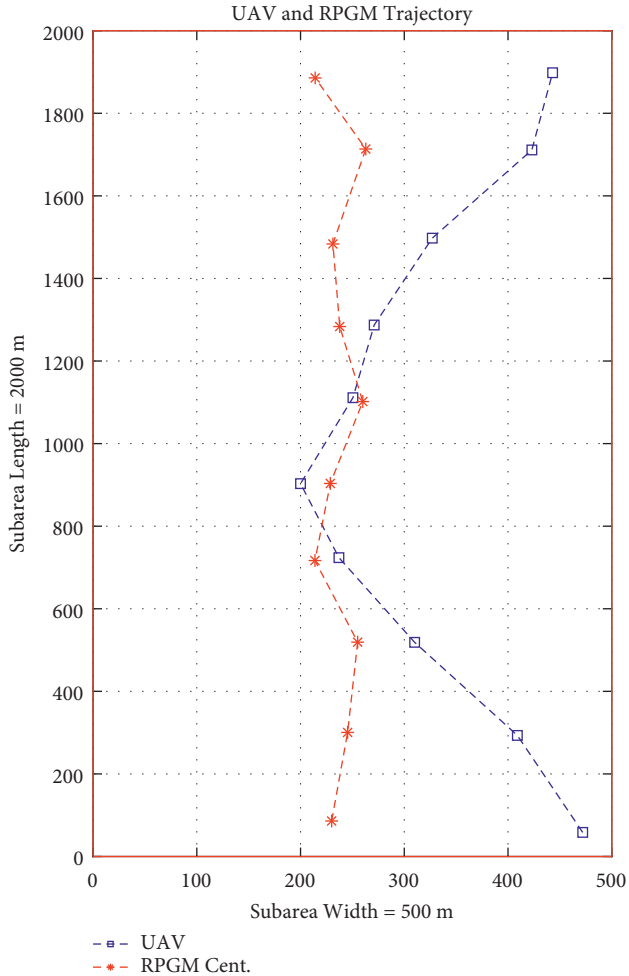


FIGURE 4: Efficient UAV and RPGM trajectories from T1 to T10.

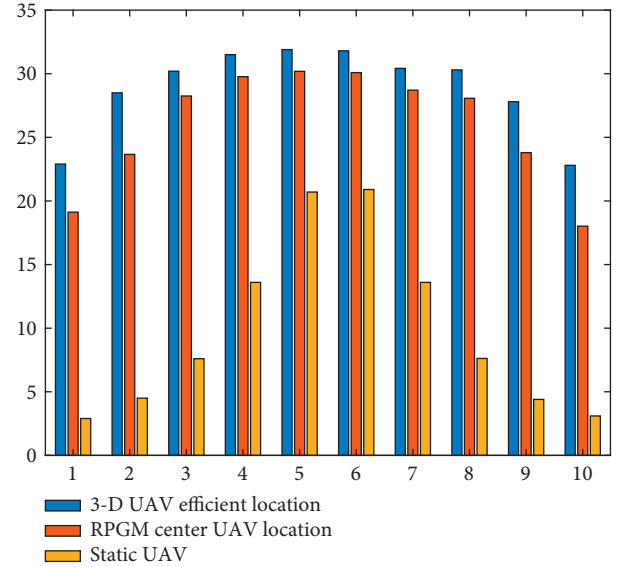


FIGURE 5: Users average sum rate over different time slots for 3 UAV placement approaches efficient, RPGM center and static.

the execution time by 16% compared to GA. In this paper, the minimum height of the aerial drone is 100 m for safety and collision avoidance. References [34, 35].

On the other hand, Figure 4 presents an efficient trajectory for the UAV during mining surveying operations from T_1 to T_{10} using the proposed algorithm. Moreover, this figure shows the trajectory of the reference point for the RPGM model during team members' movement for all time slots.

Figure 5 shows the average sum rate of ground users for three different UAV placement scenarios, namely, dynamic, RPGM center, and static. Specifically, in the dynamic UAV

TABLE 3: Average sum rate for dynamic and static UAV locations.

Time step (T_n)	Sub-region (m)	Dynamic UAV sum rate (bits/sec/Hz)	RPGM UAV sum rate (bits/sec/Hz)	Static UAV sum rate (bits/sec/Hz)
T1	(0–200)	22.9	19.12	2.9
T2	(200–400)	28.5	23.66	4.5
T3	(400–600)	30.2	28.25	7.6
T4	(600–800)	31.5	29.77	13.6
T5	(800–1000)	31.9	30.19	20.7
T6	(1000–1200)	31.8	30.09	20.9
T7	(1200–1400)	33.2	28.71	13.6
T8	(1400–1600)	30.3	28.07	7.6
T9	(1600–1800)	27.8	23.80	4.4
T10	(1800–2000)	22.8	18.02	3.1

placement scenario, the PSO algorithm is used to find the efficient trajectory of the UAV satisfying the constraints from (7b) to (7h). Then, in the static UAV placement, we consider the center of the coverage region (500, 1000) as a location of the UAV. Moreover, for the third scenario, we use the center of the RPGM as a UAV placement from T1 to T10. In the second and third scenarios, the UAV height is set to 100 m. These two scenarios are employed as a benchmarking for comparison with the dynamic approach. As shown in Figure 5, the sum rate of team members in the dynamic UAV scenario outperforms both RPGM centers and static UAV scenarios for all time slots. Moreover, Table 3 presents the values of the average sum data rate for optimized dynamic UAV, RPGM centers, and static UAV locations [36].

7. Conclusion

UAVs in wireless communication networks have a great value on the mining industry. In this paper, a single UAV was used in the mining mission; specifically, UAV acted as a relay node between the exploration team and the GCs using millimeter-wave technologies. Two pathloss models were used to present the communication channel; the first is the ground to air pathloss to describe the uplink communication channel between the team members and the UAV that acts as a relay node. The second model is the free space pathloss, which is used to represent the downlink communication channel between the UAV and the GCs. The optimization problem was formulated with an objective function to find the 3-D location and trajectory of the UAV such that it maximizes the data rate of team members. Since the formulated problem is non-convex, we have used the PSO to find the UAV relay node's efficient 3D location and trajectory.

Data Availability

Data are available from the corresponding author upon request.

Conflicts of Interest

The authors declare that they have no conflicts of interest.

Acknowledgments

This work was supported by the Deputyship for Research and Innovation, Ministry of Education in Saudi Arabia, project no. 6864 2020 IF.

References

- [1] H. Shakhathreh, A. H. Sawalmeh, A. Al-Fuqaha et al., "Unmanned aerial vehicles (uavs): a survey on civil applications and key research challenges," *IEEE Access*, vol. 7, no. 48, pp. 48572–48634, 2019.
- [2] Y. Zeng, Q. Wu, and R. Zhang, "Accessing from the sky: a tutorial on uav communications for 5g and beyond," *Proceedings of the IEEE*, vol. 107, no. 12, pp. 2327–2375, 2019.
- [3] L. Zhang, H. Zhao, S. Hou et al., "A survey on 5g millimeter wave communications for uav-assisted wireless networks," *IEEE Access*, vol. 7, no. 117, pp. 460–117 504, 2019.
- [4] H. Ullah, N. G. Nair, A. Moore, C. Nugent, P. Muschamp, and M. Cuevas, "5g communication: an overview of vehicle-to-everything, drones, and healthcare use-cases," *IEEE Access*, vol. 7, no. 37, pp. 37251–37268, 2019.
- [5] S. Yin, Z. Qu, and L. Li, "Uplink resource allocation in cellular networks with energy-constrained uav relay," in *Proceedings of the 2018 IEEE 87th Vehicular Technology Conference (VTC Spring)*, pp. 1–5, IEEE, Porto, Portugal, June 2018.
- [6] U. Demir, C. Toker, and Ö. Ekici, "Energy-efficient deployment of uav in v2x network considering latency and backhaul issues," in *Proceedings of the 2020 IEEE International Black Sea Conference on Communications and Networking (Black-SeaCom)*, pp. 1–6, IEEE, Odessa, Ukraine, May 2020.
- [7] S. Kumar, S. Suman, and S. De, "Backhaul and delay-aware placement of uav-enabled base station," in *Proceedings of the IEEE INFOCOM 2018-IEEE Conference on Computer Communications Workshops (INFOCOM WKSHPS)*, pp. 634–639, IEEE, Honolulu, HI, USA, May 2018.
- [8] Y. Chen, W. Feng, and G. Zheng, "Optimum placement of uav as relays," *IEEE Communications Letters*, vol. 22, no. 2, pp. 248–251, 2017.
- [9] H. Shakhathreh, A. Alenezi, A. Sawalmeh, M. Almutiry, and W. Malkawi, "Efficient placement of an aerial relay drone for throughput maximization," *Wireless Communications and Mobile Computing*, vol. 2021, Article ID 5589605, 11 pages, 2021.
- [10] K. F. Hayajneh, K. Bani-Hani, H. Shakhathreh, M. Anan, and A. Sawalmeh, "3d deployment of unmanned aerial vehicle-base station assisting ground-base station," *Wireless*

- Communications and Mobile Computing*, vol. 2021, Article ID 2937224, 11 pages, 2021.
- [11] S. Abdel-Razeq, H. Shakhathreh, A. Alenezi, A. Sawalmeh, M. Anan, and M. Almutiry, "Pso-based uav deployment and dynamic power allocation for uav-enabled uplink noma network," *Wireless Communications and Mobile Computing*, vol. 2021, Article ID 2722887, 17 pages, 2021.
 - [12] H. Shakhathreh, K. Hayajneh, K. Bani-Hani, A. Sawalmeh, and M. Anan, "Cell on wheels-unmanned aerial vehicle system for providing wireless coverage in emergency situations," *Complexity*, vol. 2021, Article ID 8669824, 9 pages, 2021.
 - [13] Y. He, D. Zhai, D. Wang, X. Tang, and R. Zhang, "A relay selection protocol for uav-assisted vanets," *Applied Sciences*, vol. 10, no. 23, p. 8762, 2020.
 - [14] Z. Fang, J. Wang, Y. Ren, Z. Han, H. V. Poor, and L. Hanzo, "Age of information in energy harvesting aided massive multiple access networks," *IEEE Journal on Selected Areas in Communications*, vol. 40, 2022.
 - [15] M. Sun, X. Xu, X. Qin, and P. Zhang, "Aoi-energy-aware uav-assisted data collection for iot networks: a deep reinforcement learning method," *IEEE Internet of Things Journal*, vol. 8, no. 24, pp. 17275–17289, 2021.
 - [16] T. Bai, J. Wang, Y. Ren, and L. Hanzo, "Energy-efficient computation offloading for secure uav-edge-computing systems," *IEEE Transactions on Vehicular Technology*, vol. 68, no. 6, pp. 6074–6087, 2019.
 - [17] L. G. U. Garcia, E. P. L. Almeida, V. S. B. Barbosa et al., "Mission-critical mobile broadband communications in open-pit mines," *IEEE Communications Magazine*, vol. 54, no. 4, pp. 62–69, 2016.
 - [18] V. S. Barbosa, L. G. Garcia, G. Caldwell et al., "The challenge of wireless connectivity to support intelligent mines," in *Proceedings of the 24th World Mining Congress 2016. IBRAM*, pp. 105–116, Brasilia, Brazil, October 2016.
 - [19] A. Ranjan, B. Panigrahi, H. B. Sahu, and P. Misra, "Skyhelp: uav assisted emergency communication in deep open pit mines," in *Proceedings of the 1st International Workshop on Internet of People, Assistive Robots and Things*, pp. 31–36, Munich, Germany, June 2018.
 - [20] H. Shakhathreh, W. Malkawi, A. Sawalmeh, M. Almutiry, and A. Alenezi, "Modeling ground-to-air path loss for millimeter wave uav networks," 2021, <https://arxiv.org/abs/2101.12024>.
 - [21] X. Wang, L. Kong, F. Kong et al., "Millimeter wave communication: a comprehensive survey," *IEEE Communications Surveys & Tutorials*, vol. 20, no. 3, pp. 1616–1653, 2018.
 - [22] M. R. Akdeniz, Y. Liu, M. K. Samimi et al., "Millimeter wave channel modeling and cellular capacity evaluation," *IEEE Journal on Selected Areas in Communications*, vol. 32, no. 6, pp. 1164–1179, 2014.
 - [23] M. Gapeyenko, I. Bor-Yaliniz, S. Andreev, H. Yanikomeroglu, and Y. Koucheryavy, "Effects of blockage in deploying mmwave drone base stations for 5g networks and beyond," in *Proceedings of the 2018 IEEE international conference on communications workshops (icc workshops)*, pp. 1–6, IEEE, Kansas, MO, USA, May 2018.
 - [24] D. Tse and P. Viswanath, *Fundamentals of Wireless Communication*, Cambridge University Press, Cambridge, England, UK, 2005.
 - [25] T. Camp, J. Boleng, and V. Davies, "A survey of mobility models for ad hoc network research," *Wireless Communications and Mobile Computing*, vol. 2, no. 5, pp. 483–502, 2002.
 - [26] J. Broch, D. A. Maltz, D. B. Johnson, Y.-C. Hu, and J. Jetcheva, "A performance comparison of multi-hop wireless ad hoc network routing protocols," in *Proceedings of the 4th annual ACM/IEEE international conference on Mobile computing and networking*, pp. 85–97, ACM, Dallas, TX, USA, October 1998.
 - [27] W.-j. Hsu, K. Merchant, H.-w. Shu, C.-h. Hsu, and A. Helmy, "Weighted waypoint mobility model and its impact on ad hoc networks," *ACM SIGMOBILE - Mobile Computing and Communications Review*, vol. 9, no. 1, pp. 59–63, 2005.
 - [28] P. Nain, D. Towsley, B. Liu, and Z. Liu, "Properties of random direction models," in *Proceedings of the IEEE 24th Annual Joint Conference of the IEEE Computer and Communications Societies*, vol. 3, pp. 1897–1907, Miami, FL, USA, March 2005.
 - [29] K. H. Wang and B. Li, "Group mobility and partition prediction in wireless ad-hoc networks," in *Proceedings of the 2002 IEEE International Conference on Communications. Conference Proceedings. ICC 2002 (Cat. No.02CH37333)*, vol. 2, pp. 1017–1021, Philadelphia, Pennsylvania, April 2002.
 - [30] A. H. Sawalmeh, N. S. Othman, H. Shakhathreh, and A. Khreishah, "Wireless coverage for mobile users in dynamic environments using uav," *IEEE Access*, vol. 7, pp. 126 376–126 390, 2019.
 - [31] J. Kennedy and R. Eberhart, "Particle swarm optimization," vol. 4, pp. 1942–1948, in *Proceedings of the ICNN'95-International Conference on Neural Networks*, vol. 4, pp. 1942–1948, IEEE, Perth, WA, Australia, November 1995.
 - [32] M. Clerc and J. Kennedy, "The particle swarm - explosion, stability, and convergence in a multidimensional complex space," *IEEE Transactions on Evolutionary Computation*, vol. 6, no. 1, pp. 58–73, 2002.
 - [33] R. Eberhart and J. Kennedy, "A new optimizer using particle swarm theory," in *Micro Machine and Human Science*, in *Proceedings of the 6th International Symposium on 1995 MHS'95*, pp. 39–43, IEEE, Lugano, Switzerland, October 1995.
 - [34] A. Sawalmeh and N. S. Othman, "An overview of collision avoidance approaches and network architecture of unmanned aerial vehicles (UAVs)," *International Journal of Engineering and Technology*, vol. 7, no. 4, p. 35, 2018.
 - [35] M. A. Jasim, H. Shakhathreh, N. Siasi, A. Sawalmeh, A. Aldalbahi, and A. Al-Fuqaha, "A survey on spectrum management for unmanned aerial vehicles (uavs)," *IEEE Access*, vol. 10, 2021.
 - [36] M. Anam, K. P. Rane, A. Alenezi, R. Mishra, S. Ramamurthy, and F. J. J. Joseph, "Content classification tasks with data preprocessing manifestations," *Webology*, vol. 19, no. 1, 2022.

Research Article

Flood Detection Based on Unmanned Aerial Vehicle System and Deep Learning

Kaixin Yang ¹, Sujie Zhang ¹, Xinran Yang ², and Nan Wu ¹

¹Tianjin College, University of Science and Technology Beijing, Beijing, China

²Tianjin University of Science and Technology, Tianjin, China

Correspondence should be addressed to Kaixin Yang; kxyang@163.com

Received 20 February 2022; Revised 28 March 2022; Accepted 16 April 2022; Published 5 May 2022

Academic Editor: Chao Liu

Copyright © 2022 Kaixin Yang et al. This is an open access article distributed under the Creative Commons Attribution License, which permits unrestricted use, distribution, and reproduction in any medium, provided the original work is properly cited.

Floods are one of the main natural disasters, which cause huge damage to property, infrastructure, and economic losses every year. There is a need to develop an approach that could instantly detect flooded extent. Satellite remote sensing has been useful in emergency responses; however, with significant weakness due to long revisit period and unavailability during rainy/cloudy weather conditions. In recent years, unmanned aerial vehicle (UAV) systems have been widely used, especially in the fields of disaster monitoring and complex environments. This study employs deep learning models to develop an automated detection of flooded buildings with UAV aerial images. The method was explored in a case study for the Kangshan levee of Poyang Lake. Experimental results show that the inundation for the focal buildings and vegetation can be detected from the images with 88% and 85% accuracy, respectively. And further, we can estimate the buildings' inundation area according to the UAV images and flight parameters. The result of this study shows promising value of the accuracy and timely visualization of the spatial distribution of inundation at the object level for the end users from flood emergency response sector.

1. Introduction

Floods are the most frequently occurring and damaging natural disasters in the world. The average annual deaths and economic losses caused by floods are 1354.9 people and US \$32.847 billion in China, ranked 4th and 2nd in the world, respectively [1]. Traditional flood monitoring uses hydrological processes simulation with precipitation data from surface hydrological stations, satellite observations, re-analysis data based on numerical models, and assimilation. These data have certain limitations in terms of temporal resolution, spatial resolution, and accuracy [2]. This signifies the need to quickly detect flood-affected areas with advanced technologies so that efficiently rescue activities can be initiated as soon as possible.

Satellite remote-sensing techniques have been widely used when nature disasters occurred. The main advantages of satellite data are its time and cost effectiveness, since satellite data of large areas can be gathered quickly and economically [3, 4]. The application of space borne remote

sensing in flood detection varies across the large variety of spatial and temporal scales, as well as multisensor, operating in several platforms [5]. Numerous studies have been carried out for flood monitoring, inundation mapping, and loss assessment. However, the quality of satellite images is greatly affected by weather conditions such as clouds' cover and shadow effect. Another important consideration is the long revisit time of most satellites that might be useful for long-term and large-scale floods monitoring [6].

In recent years, the UAV remote-sensing system has been used in disaster detection due to the advantages of real-time data acquisition and full-time observation [7]. This makes UAVs to be an efficient way to investigate high-risk areas that are unreachable by humans during disaster events. Flood rescue agencies can use UAV to quickly collect data and visualize flooded regions and grasp the state of the disaster. Some studies have investigated the applications of the UAV system for flood hazard modeling [8–10]. Lei used UAV remote sensing to investigate and monitor the severe cold rain, snow, and freezing disasters in southern of China

in 2008 [11]. Schumann et al. evaluated the accuracy of a UAV-derived Digital Elevation Model (DEM) and assessed its reliability on flood mapping operation [12]. Annis et al. demonstrated the performances of the UAV data in simulating flood extension and depth [13]. Hashemi-Beni et al. adopted the UAV system for spatial flood assessment mapping and evaluating the extent of a flood event [14]. Most of the related works focus on the large-scale flood model integrated with DEM and GIS data. However, when flood occurred, transferring the trapped people in time is the focus of rescue work. Detection of submerged buildings would provide timely information for rescue efforts. To our knowledge, the applications of UAV to retrieve flood information at the object level are usually less investigated.

Flooded object recognition such as the buildings, crops, and infrastructures from aerial images can be analyzed to make disaster response decisions. UAV can obtain a large amount of image data when flood occurred. Remondino, Han, and other scholars have carried out research in flood data acquisition and disaster assessment using UAV remote-sensing technology [15–19]. The pertinent literature shows that image processing such as edge detection, segmentation, and machine learning have been widely utilized for flood detection, but deep learning techniques are rare and not well investigated with for this purposes [20].

The images acquired with UAV have the characteristics of small picture format and image distortion, which increase the difficulty in image processing and information extraction [21]. In recent years, major breakthroughs have been made in the field of computer vision based on deep learning technology. In 2012, Hinton proposed a deep convolutional neural network algorithm and won the ImageNet competition champion in the field of computer vision [22]. Since then, companies such as Microsoft, Facebook, Google, and Baidu have successfully applied deep learning in image recognition and voice identification. In flood research, Chang utilized artificial neural network (ANN) to create a flood inundation forecast model [23]. Abbot optimized rainfall forecasting using ANNs [24]. Jiménez-Jiménez proposed an object-based approach for flood damage assessment [25].

This study proposes a method to detect flooded buildings and vegetation by integrating deep learning and UAV image processing. We use the YOLOv3 algorithm as a deep learning model on aerial images and estimate the area of submerged buildings through the relationship among the UAV flight parameters. The case study is the flood area of the Kangshan Levee of Poyang Lake. This study aims to estimate the affected area and potential trapped people by detecting the inundated buildings, analyze the disaster intensity, and provide real-time data for flood rescue departments to make decision.

The study is organized as follows. Section 2 introduces the study area, the Kangshan levee of Poyang Lake. Section 3 focusses on the research methodology, and the process of image acquisition is also elaborated. Section 4 illustrates data processing and experimental results. Finally, the overall achievements and limitations of the proposed approach are presented. The main contribution of this study is to combine

UAV image data and deep learning algorithm for flood detection at the object level and provide timely visualization of the spatial distribution of inundation for flood emergency response sector.

2. Study Area

Poyang Lake is located at the north of Jiangxi Province, China. It is the largest freshwater lake in China and one of the main tributaries of the middle and lower Yangtze River. The lake is about 3,150 square kilometers, supplied by the Ganjiang River, Xiuhe River, Xinjiang River, Raohe River, and other water sources. It flows into the Yangtze River in Jiujiang City from south to north. The geographical location of Poyang Lake is shown in Figure 1.

In late June 2020, most of Jiangxi Province continued to rain heavily. Affected by heavy rainfall and upstream water, the total rainfall in northern Jiangxi was more than three times that of normal years. The area of the main body of Poyang Lake expanded by 352 square kilometers on July 8 compared with that on July 2. On July 14, the area expanded to 4,403 square kilometers, which was 2.5% larger than the historical average (3,510 square kilometers) during the same time period. The flood disaster has affected 499,000 people in 36 counties in Jiangxi. The flood control pressure of the local government is increasing along with the flooding area of Poyang Lake.

From July 2 to July 8, 2020, high-resolution satellite images with a spatial resolution of 10 meters were used for remote sensing monitoring by National Satellite Meteorological Center. The flooded areas of Poyang Lake are shown in Figure 2. The blue in the figure indicates the unchanged water body, the red indicates the expanded water body, and the green box is the study area, which is located at Kangshan Dike of Poyang Lake.

3. Data and Methodology

3.1. Data Acquisition. In response to the emergency floods in the Poyang Lake area, the aerial images were captured by Feima F200 UAV system. A total of 10 sorties were flown, covering an area of more than 50 square kilometers in total, and more than 3000 images were captured by the UAV platform. The forward overlap of the aerial image is 70%, and the lateral overlap is 65%.

The F200 UAV platform is a light fixed-wing UAV with a wingspan of 1.9 meters and a maximum flight time of 1.5 hours. The system has high stability and can repeat high-precision flight operations. It can be thrown off by hand, landed by parachute, easy to control, and can be operated by one person. Due to the limited load of the UAV, the size and weight of the sensor are limited. The UAV carries a miniature Sony ILCE-5100 camera. Its effective pixels are about 24.3 million, and the focal length is 20 mm. Figure 3 shows part of the trajectory planning of the F200 UAV equipped with a Sony ILCE-5100 camera to obtain flood image data. Table 1 shows the parameters of the Sony camera.

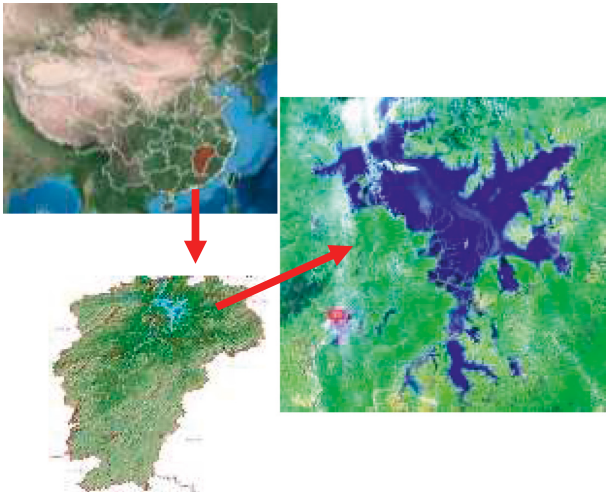


FIGURE 1: Geographical location of Poyang Lake.

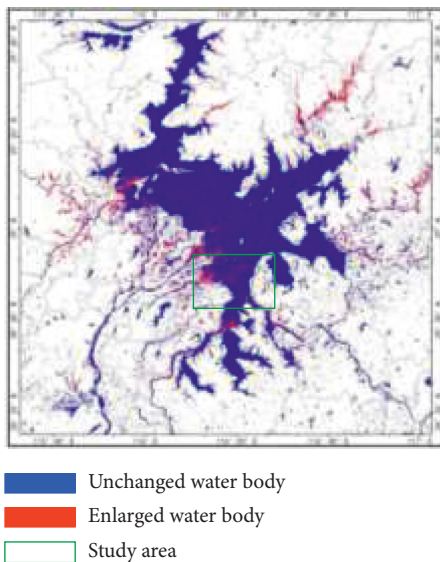


FIGURE 2: Flood change monitoring in Poyang Lake area.

3.2. *Methodology.* This study uses the UAV image data and deep learning method to conduct flood automatic detection and estimation. The proposed methodology is shown in Figure 4. The methodology consists of three main steps.

3.2.1. *Flood Image Dataset Construction.* The purpose is to extract buildings and vegetation submerged by floods. Therefore, the flood images obtained by the UAV system need to be filtered out which contains buildings and vegetation submerged scenes. Since the forward and lateral overlap of the acquired images by UAV is as high as 65% to 75% of a single image and a large number of images are completely flooded areas, about 600 images have been screened as flood image samples for training and testing. We choose 500 images as the training data and 100 images as the test data. The dataset sample is shown in Figure 5 (Section 4).

The construction of the training dataset includes the collection of flood images and object labeling. At present,

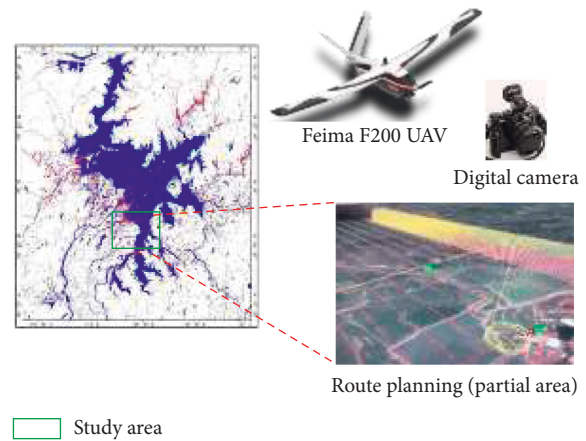


FIGURE 3: Flood image data acquired by UAV in the study area.

TABLE 1: Camera parameters of Sony ILCE-5100.

Name	Parameters
Pixel	6000*4000
Sensor	CMOS (23.4*15.6)
Shutter speed	1/1600s
Pixel size	6.41 μm
Focal length	20 mm

there are still no public datasets consist of aerial flood images, and image search engines such as Google and Baidu are used to collect aerial flood images. Totally, there are about 500 aerial flood images collected through the Internet, together with the images obtained by the UAV system, which form a training dataset. After that, the training samples are labeled and input into the deep learning model for feature learning.

3.2.2. *Deep Learning Model.* The research conducts the object detection based on YOLOv3 algorithm with Tensorflow framework. The model learns the characteristics of the buildings and vegetation inundated by flood through data labeling and training. Then, the inundated objects could be extracted using the trained model.

The deep learning framework Tensorflow has very powerful versatility. This study chooses Tensorflow as the operating environment. The experimental platform chooses the YOLOv3 algorithm to conduct object detection. YOLOv3 is a new peak in target recognition after the emergence of R-CNN series models. The object detection method with YOLOv3 [26] is shown in Figure 6.

The YOLOv3 algorithm divides the input images into $S \times S$ grids; for each object and grid, it calculates the probability that the center of the objects falls within the grids. If the probability exceeds a threshold value, it is determined that there is an object in the grid. The boundary boxes are built for the grids with objects, and the confidence level of each box is computed simultaneously. Each bounding box contains five parameters: center of bounding box relative to the bounds of the tile (x, y) , the width and height related to the entire image (w, h) , and confidence level.

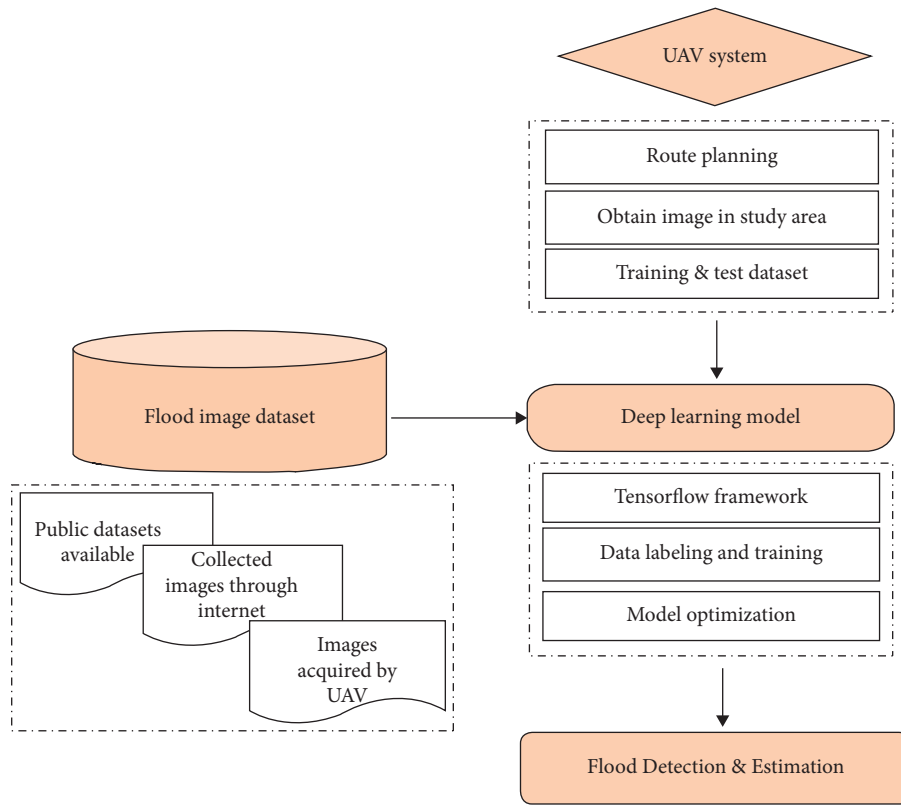


FIGURE 4: Proposed methodology.

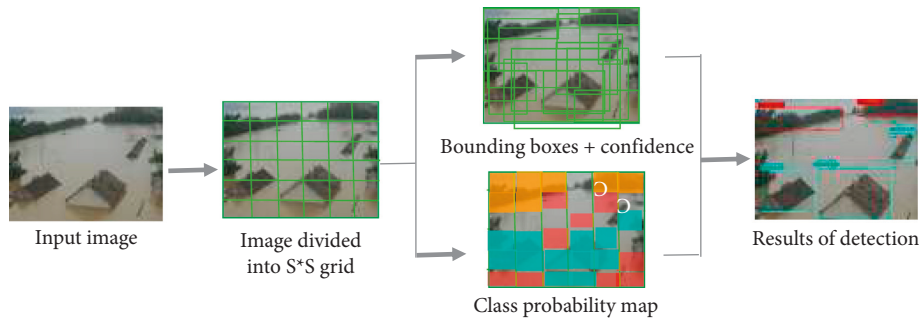


FIGURE 5: The relationship of UAV flight parameters.

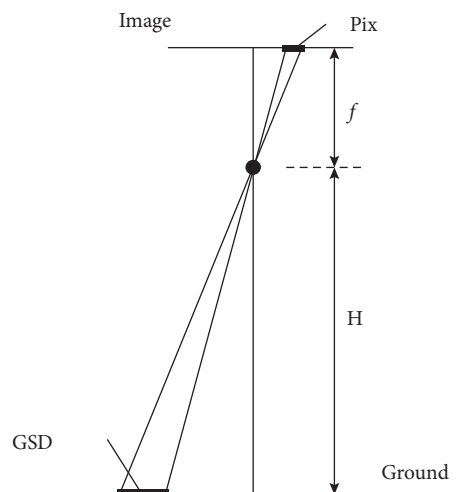


FIGURE 6: Dataset sample.

The output of each grid includes the position information, the confidence level of the boundary box, and the class probabilities. Thus, the loss function consists of three parts: the coordinate error ($Error_{coord}$), the intersection-over-union error ($Error_{iou}$), and the classification error ($Error_{class}$) [27]. The loss function is defined as follows:

$$\text{Loss} = \sum_{i=0}^{S^2} (\lambda_{coord} \text{Error}_{coord} + \lambda_{noobj} \text{Error}_{iou} + \text{Error}_{class}), \quad (1)$$

$$\begin{aligned} \text{loss} = & \lambda_{coord} \sum_{i=0}^{S^2} \sum_{j=0}^B I_{ij}^{obj} (2 - w_i * h_i) [(-\hat{x} * \log(x_i) - (1 - x_i) * \log(1 - x_i)) + (-\hat{y}_i * \log(y_i) - (1 - y_i) * \log(1 - y_i))] \\ & + \lambda_{coord} \sum_{i=0}^{S^2} \sum_{j=0}^B I_{ij}^{obj} (2 - w_i * h_i) [(w_i - \hat{w}_i)^2 + (h_i - \hat{h}_i)^2] \\ & - \sum_{i=0}^{S^2} \sum_{j=0}^B I_{ij}^{obj} [\hat{C}_i^j \log(C_i^j) + (1 - \hat{C}_i^j) \log(1 - C_i^j)] \\ & - \lambda_{noobj} \sum_{i=0}^{S^2} \sum_{j=0}^B I_{ij}^{noobj} [\hat{C}_i^j \log(C_i^j) + (1 - \hat{C}_i^j) \log(1 - C_i^j)] - \sum_{i=0}^{S^2} I_i^{obj} \sum_{c \in \text{classes}} [\hat{p}_i(c) \log(p_i(c)) + (1 - \hat{p}_i(c)) \log(1 - p_i(c))], \end{aligned} \quad (2)$$

where S is the number of grid that input images are divided into, B is the number of bounding boxes predicted for each tile, I_i^{obj} denotes if the target appears in tile i and I_{ij}^{obj} denotes that the j th bounding box predictor in tile i is responsible for that prediction, and λ_{coord} and λ_{noobj} are hyperparameters that separate the loss to loss from bounding box coordinate predictions and that from confidence predictions for boxes that do not contain targets. During the deep learning training process, when looking for the optimal parameters in the model, it is to find the parameters that make the value of the loss function as small as possible [28].

3.2.3. Flooded Buildings' Estimation. The deep learning model could detect flooded object; after that, we can estimate the area of the flooded object. The flying height of the UAV is mainly related to the focal length (f) of the camera, the pixel size, and the image ground sampling distance (GSD). The relationship of the UAV flight parameters is shown in Figure 7 and the following equation:

$$\frac{f}{H} = \frac{\text{pix}}{GSD}, \quad (3)$$

The formula for calculating the area corresponding to a single pixel is as follows:

$$\text{Area of the pixel} = GSD^2 = \left(\frac{\text{pix} * H}{f} \right)^2, \quad (4)$$

where GSD is the ground sample distance, H is the UAV flight altitude relative to the ground level, f is the focal length of

digital camera, and pix is the size of one single pixel on the CCD of the digital camera. Thus, the area of flooded buildings is the product of the pixel area and the number of pixels.

where $Error_{coord}$ represents the sum of the squared errors of the position information, $Error_{iou}$ is the sum of the squared errors of the confidence level, and $Error_{class}$ represents the sum of squared errors of the classes. The formula of loss function is as follows:

4. Flood Automated Detection Method

4.1. Data Preparation. Currently, there is no flood-related image data in the public datasets. The research in this study uses the Internet to search for aerial images of flooded houses and vegetation, together with the data obtained by UAV in the Poyang Lake flood area. The software Labelimg is used for labeling to create the training sample dataset. When UAVs perform more flood monitoring missions in the future, the acquired images can continuously fill the sample database to improve the accuracy and reliability of the model. Figure 7 shows part of the flood sample data.

4.2. Training Data Labeling. Deep learning methods need to train the model through a large amount of data. An important step is to label the data in the training dataset. In this study, the software Labelimg is used to label the training data.

Figure 8 shows the software Labelimg operation interface. Select the create-RectBox button to mark the flooded houses and vegetation on the right side. The green border in the picture is the effect after marking. If an image has multiple targets, repeat the above steps. After an image is marked, it would be saved as xml file.

The training data selected in this study contain about 1,000 images of houses and vegetation submerged by floods.

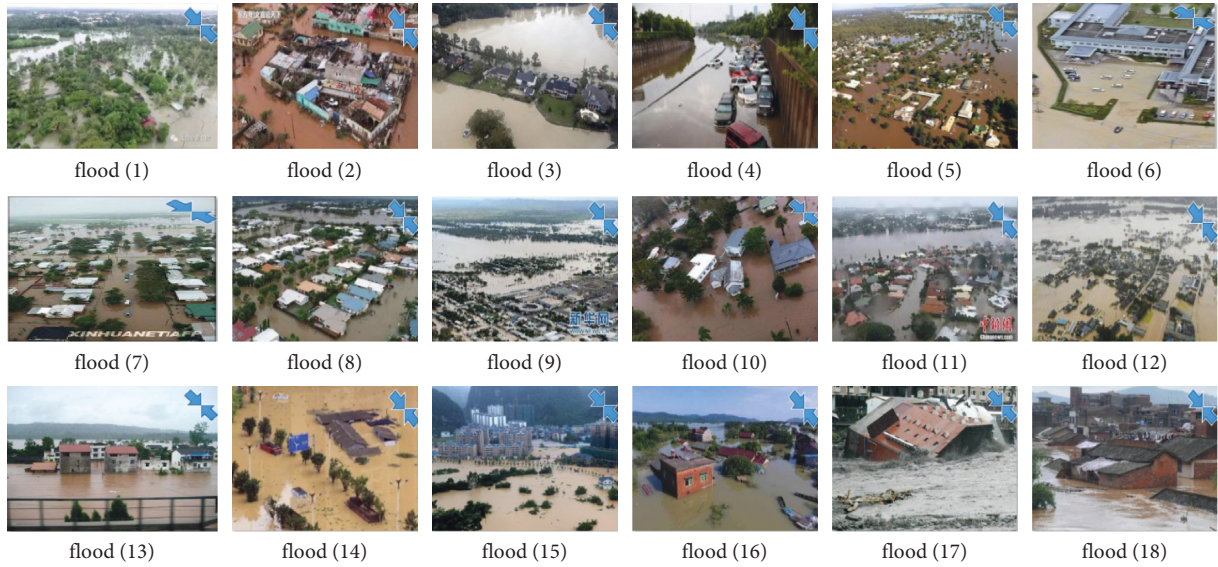


FIGURE 7: The YOLOv3 object detection method.

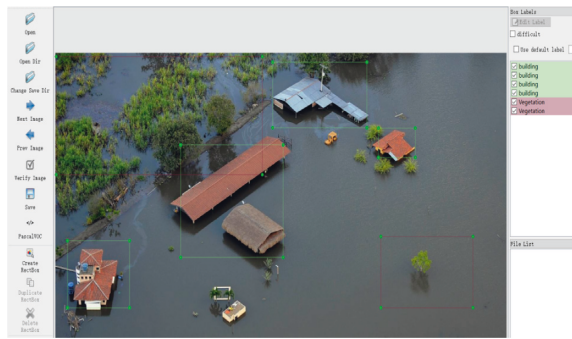


FIGURE 8: Training data labeling.

In total, the identifiers are marked as building and vegetation. Table 2 shows the training data statistics.

4.3. Model Training and Optimization. Object detection based on deep learning is different from traditional methods. It no longer requires time-consuming steps such as feature selection and extraction; effective feature discovery can be made through deep learning networks. The main factors affecting the accuracy of the model are the richness and connotation of the training dataset. Figure 9 shows the training process.

The model is trained using YOLOv3 algorithm, and it took about 60 hours to get the parameters optimization. If the learning rate is appropriate, it should be ensured that the loss after each round of complete training is reduced and maintained at a small level after a period of training. During the training process, loss will continue to decline at the beginning and drop quickly; after a period of time, it will begin to converge, and finally, it will gradually stabilize. Figure 10 shows the loss curve of the model that when the number of iterations reaches about 5000 times, it starts to converge and gradually stabilizes and fluctuates around a fixed value.

TABLE 2: Training data statistics.

Class name	Building	Vegetation
Total number	1623	2190

```
./darknet_detector train cfg/voc.data cfg/yolov3-voc.cfg darknet53.conv.74
Region 82 Avg IOU: 0.727443, Class: 0.199634, Obj: 0.827442, No Obj: 0.002739, SR: 1.000000, 75R: 0.500000, count: 2
Region 94 Avg IOU: -nan, Class: -nan, Obj: -nan, No Obj: 0.000088, SR: -nan, 75R: -nan, count: 0
Region 106 Avg IOU: -nan, Class: -nan, Obj: -nan, No Obj: 0.000038, SR: -nan, 75R: -nan, count: 0
Region 82 Avg IOU: 0.855029, Class: 0.095664, Obj: 0.677242, No Obj: 0.000090, SR: -nan, 75R: -nan, count: 0
Region 94 Avg IOU: -nan, Class: -nan, Obj: -nan, No Obj: 0.000036, SR: -nan, 75R: -nan, count: 0
Region 106 Avg IOU: 0.498990, Class: 0.136265, Obj: 0.968725, No Obj: 0.002454, SR: 0.500000, 75R: 0.000000, count: 2
Region 94 Avg IOU: -nan, Class: -nan, Obj: -nan, No Obj: 0.000087, SR: -nan, 75R: -nan, count: 0
Region 106 Avg IOU: -nan, Class: -nan, Obj: -nan, No Obj: 0.000035, SR: -nan, 75R: -nan, count: 0
Region 82 Avg IOU: 0.773964, Class: 0.226081, Obj: 0.685679, No Obj: 0.002542, SR: 1.000000, 75R: 1.000000, count: 2
Region 94 Avg IOU: -nan, Class: -nan, Obj: -nan, No Obj: 0.000088, SR: -nan, 75R: -nan, count: 0
Region 106 Avg IOU: -nan, Class: -nan, Obj: -nan, No Obj: 0.000038, SR: -nan, 75R: -nan, count: 0
646: 0.476303, 0.584737 avg, 0.000174 rate, 2.031312 seconds, 500 images
```

FIGURE 9: Training process.

5. Experimental Results and Discussion

5.1. Experimental Results. After the model training is completed, the model can perform target recognition on the test images. We select flood images from different scenes to verify the recognition effect of submerged buildings and vegetation. Figure 11 shows the detect effect of different scenes include images with good quality and illumination condition, images under insufficient light, images under occlusion, and only the building roof is exposed. The blue box represents building recognition, and the red box represents vegetation recognition.

Approximately 100 flood images were used for testing. For images with good quality and illumination condition, the recognition results are satisfactory. When the images are captured under insufficient light, the recognition accuracy is unsatisfactory for long-distance objects. In the case of images

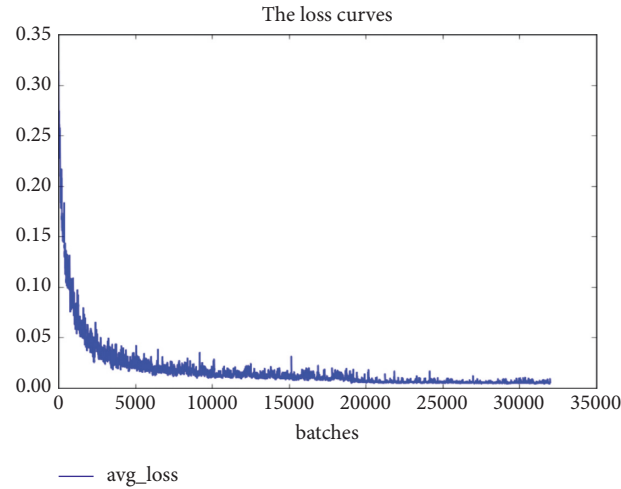


FIGURE 10: Loss function curve.

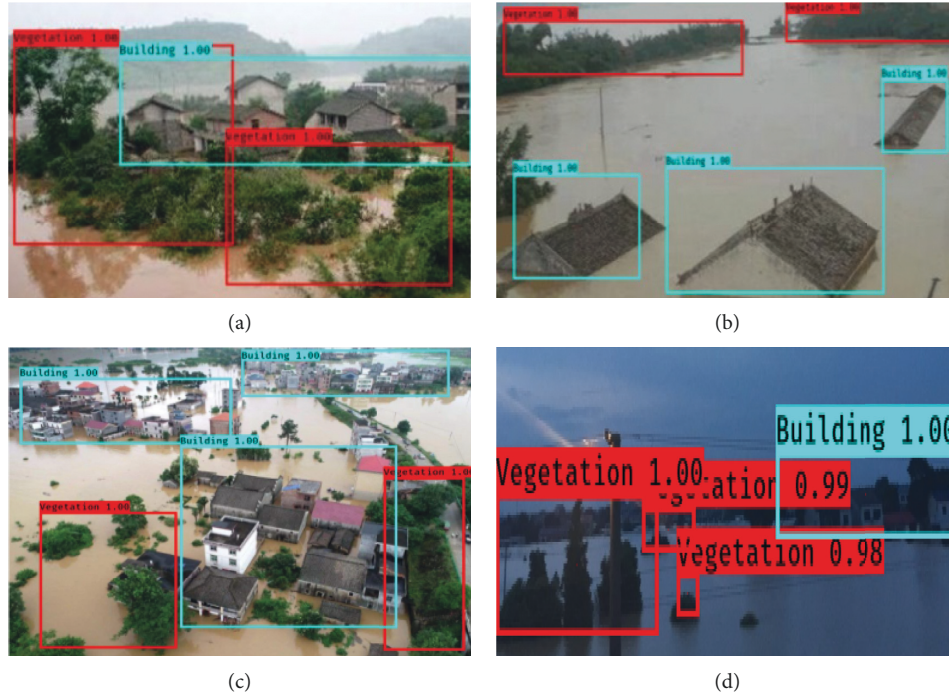


FIGURE 11: Examples of the recognition effect. (a) Good quality and illumination condition. (b) Image under insufficient light. (c) Image under occlusion. (d) Only the building roof is exposed.

under occlusion, as long as the main features of the recognized object can be captured, it can be recognized. If the objects are severely occluded, it is difficult to identify the target. For images only the building roof is exposed, there are few test data that cannot be recognized due to incomplete features. However, in general, the detection and recognition rate are satisfactory.

5.2. Recognition Result Evaluation. The model was evaluated with the test results. There are 120 buildings and 230 vegetation in 100 test images, as shown in Table 3. The results show the model can effectively identify the

inundated objects in the images from different scenes. The overall recognition rate can reach more than 85%. In terms of recognition speed, the detection time of each image only needs 2–4s. Experiments show that the UAV system can obtain flood data in time, and the proposed method can identify submerged buildings and vegetation effectively.

5.3. Inundated Building Area Estimation. We chose one flood image as an example to estimate the inundated building area. The pixel number of the example image is

TABLE 3: Objects' recognition rate.

Class name	Number	Recognition number	Recognition rate (%)	Recognition speed
Building	120	106	88	2-4s
Vegetation	230	195	85	2-4s



FIGURE 12: Example of flooded building area estimation.

1080*810, and the pixel number of the flooded building area includes three sky blue labeling boxes, as shown in Figure 12, which is calculated as 44,3159 pixels.

The formula for calculating the area corresponding to a single pixel is shown in formula (4). In this example, the parameters are shown in Table 1:

$$H = 500 \text{ m}, f = 20 \text{ mm}, pix = 6.41 \mu\text{m}. \quad (5)$$

After unifying the measure units, we can get the result of the pixel is 0.025 square meters, and the area of inundated buildings in the example image is 11078.98 square meters, which is shown in equation (5):

$$\begin{aligned} \text{Area} &= \text{Area of the pixel} * \text{Number of pixels}, \\ &= \left(\frac{pix * H}{f} \right)^2 * \text{Number of pixels}, \\ &= 0.025 * 443159, \\ &= 11078.98. \end{aligned} \quad (6)$$

According to the area of buildings inundated by flood, the affected people and economic losses can be estimated, and scientific decisions can be made for evacuation and rescue work.

6. Conclusions

Floods cause great damage to the infrastructure and property, resulting in huge economic losses. Due to the lack of technologies that could automatically detect the flood affected at the object level, recovery services sometimes cannot be provided on time. Traditional remote-sensing satellites have demonstrated delayed response due to orbital period. At present, the UAV system has been widely used in the fields of natural disasters due to ideal for acquiring

high-resolution images in a short period. The pertinent literature shows that UAV and deep learning techniques have been used for flood simulation model, but are rare and not well experimented with flooded object detection.

In this study, we introduce the deployed UAV remote-sensing system, deep learning method, and procedures for flood detection. The case study is adopted where the flood-prone area of Poyang Lake. We use YOLOv3 algorithm as a deep learning model on aerial images to detect the inundated buildings and vegetation. Experimental results show that flooded buildings and vegetation can be detected from the images with 88% and 85% accuracy, respectively. And then, we can estimate the inundated buildings area through the relationship among the UAV flight parameters. The experiment results have proved the feasibility and effectiveness of applying the UAV system for flooded region detection. Such timely flood inundation detection can provide visual disaster information in time and is crucial to efficiently rescue activities. For areas with severe floods, the rescue department will allocate resources according to the flooded buildings to ensure the safety of people's lives and property.

Nevertheless, there are still some items for improvement. For instance, we were unable to acquire more information such as the depth of floodwater and the destroyed degree of the buildings. For future work, we may employ UAV oblique photography or Light Detection and Ranging (LiDAR) equipment which could generate the three-dimensional (3D) model. More effort should be made to perform in-depth analyses by expanding the 3D image dataset using the UAV system. Considering the disaster scene, we would use lightweight algorithms such as YOLOv3_tiny and MobileNet to carry out future work. And furthermore, we try to integrate lightweight algorithms into the UAV flight control board for real-time target detection instead of data post-processing. This may improve the efficiency of the flooded objects detection and provide timely information for disaster emergency response and rescue.

Data Availability

The data used to support the findings of this study are available from the corresponding author upon request.

Conflicts of Interest

The authors declare that there are no conflicts of interest regarding the publication of this paper.

Acknowledgments

The work was supported by the Scientific Research Project of Tianjin Education Commission (Grant no. 2019KJ143).

References

- [1] K. Sönke, D. Eckstein, and I. Melchior, *Global Climate Risk Index*, 2017, <https://germanwatch.org/en/download/16411.pdf>.
- [2] H. Wu, R. F. Adler, Y. Tian, G. J. Huffman, H. Li, and J. Wang, "Real-time global flood estimation using satellite-based precipitation and a coupled land surface and routing model," *Water Resources Research*, vol. 50, no. 3, pp. 2693–2717, 2014.
- [3] H. S. Munawar, F. Ullah, S. Qayyum, and A. Heravi, "Application of deep learning on UAV-based aerial images for flood detection," *Smart Cities*, vol. 4, no. 3, pp. 1220–1243, 2021.
- [4] E. Opolot, "Application of remote sensing and geographical information systems in flood management: a review," *Research Journal of Applied Sciences, Engineering and Technology*, vol. 6, no. 10, pp. 1884–1894, 2013.
- [5] H. Taubenböck, M. Wurm, M. Netzband, H. Zwenzner, A. Roth, and A. S. Rahman, "Flood risks in urbanized areas - multi-sensoral approaches using remotely sensed data for risk assessment," *Natural Hazards and Earth System Sciences*, vol. 11, no. 2, pp. 431–444, 2011.
- [6] M. S. Rahman and L. Di, "The state of the art of spaceborne remote sensing in flood management," *Natural Hazards*, vol. 85, no. 2, pp. 1223–1248, 2016.
- [7] D. Li, "Earth observation and earthquake," *Science Surveying and Mapping*, vol. 34, no. 1, pp. 8–10, 2009.
- [8] J. P. Leitão, M. Moy de Vitry, A. Scheidegger, and J. Rieckermann, "Assessing the quality of digital elevation models obtained from mini unmanned aerial vehicles for overland flow modelling in urban areas," *Hydrology and Earth System Sciences*, vol. 20, no. 4, pp. 1637–1653, 2016.
- [9] J. Langhammer, J. Bernsteinová, and J. Miřijovský, "Building a high-precision 2D hydrodynamic flood model using UAV photogrammetry and sensor network monitoring," *Water*, vol. 9, no. 11, p. 861, 2017.
- [10] D. Backes, G. Schumann, F. N. Teferle, and J. Boehm, "Towards a high-resolution drone-based 3D mapping dataset to optimise flood hazard modelling," *The International Archives of the Photogrammetry, Remote Sensing and Spatial Information Sciences*, vol. XLII-2/W13, no. 13, pp. 181–187, 2019.
- [11] T. Lei, C. Li, and X. He, "Application of UAV aerial remote sensing system in disaster emergency rescue," *Journal of Natural Disasters*, vol. 20, no. 1, pp. 178–183, 2011.
- [12] G. Schumann, J. Muhlhausen, and K. Andreadis, "Rapid mapping of small-scale river-floodplain environments using UAV SfM supports classical theory," *Remote Sensing*, vol. 11, no. 8, p. 982, 2019.
- [13] A. Annis, F. Nardi, A. Petroselli et al., "UAV-DEMs for small-scale flood hazard mapping," *Water*, vol. 12, no. 6, p. 1717, 2020.
- [14] L. Hashemi-Beni, J. Jones, G. Thompson, C. Johnson, and A. Gebrehiwot, "Challenges and opportunities for UAV-based digital elevation model generation for flood-risk management: a case of princeville, North Carolina," *Sensors*, North Carolina, vol. 18, no. 11, p. 3843, 2018.
- [15] F. Remondino, L. Barazzetti, F. Nex, M. Scaioni, and D. Sarazzi, "UAV photogrammetry for mapping and 3D modeling—current status and future perspectives," *The International Archives of the Photogrammetry, Remote Sensing and Spatial Information Sciences*, vol. 38, no. 1, 2011.
- [16] W. Han, Y. Ren, and S. Zhao, "The main application of UAV remote sensing in flood disaster response," *Geospatial Information*, vol. 9, no. 5, pp. 6–8, 2011.
- [17] J. Langhammer and T. Vacková, "Detection and mapping of the geomorphic effects of flooding using UAV photogrammetry," *Pure and Applied Geophysics*, vol. 175, no. 9, pp. 3223–3245, 2018.
- [18] Q. Feng, J. Liu, and J. Gong, "Urban flood mapping based on unmanned aerial vehicle remote sensing and random forest classifier—A case of yuyao, China," *Water*, vol. 7, no. 12, pp. 1437–1455, 2015.
- [19] S. Li, W. Yuan, and H. Gong, "The application of UAV remote sensing system in disaster loss assessment," *Science Surveying and Mapping*, vol. 38, no. 6, pp. 76–78+81, 2013.
- [20] M. J. Chang, H. K. Chang, Y. C. Chen, G. F. Lin, and P.-A. Chen, "A support vector machine forecasting model for typhoon flood inundation mapping and early flood warning systems," *Water*, vol. 10, no. 12, p. 1734, 2018.
- [21] I. Colomina and P. Molina, "Unmanned aerial systems for photogrammetry and remote sensing: a review," *ISPRS Journal of Photogrammetry and Remote Sensing*, vol. 92, pp. 79–97, 2014.
- [22] A. Krizhevsky, I. Sutskever, and G. Hinton, "Imagenet classification with deep convolutional neural networks," *Advances in Neural Information Processing Systems*, vol. 25, 2012.
- [23] L. C. Chang, M. Amin, S. N. Yang, and F. J. Chang, "Building ANN-based regional multi-step-ahead flood inundation forecast models," *Water*, vol. 10, no. 9, p. 1283, 2018.
- [24] J. Abbot and J. Marohasy, "Input selection and optimisation for monthly rainfall forecasting in Queensland, Australia, using artificial neural networks," *Atmospheric Research*, vol. 138, pp. 166–178, 2014.
- [25] S. Jiménez-Jiménez, W. Ojeda-Bustamante, R. Ontiveros-Capurata, and M. Marcial-Pablo, "Rapid urban flood damage assessment using high resolution remote sensing data and an object-based approach," *Geomatics, Natural Hazards and Risk*, vol. 11, no. 1, pp. 906–927, 2020.
- [26] L. Pang, H. Liu, Y. Chen, and J. Miao, "Real-time concealed object detection from passive millimeter wave images based on the YOLOv3 algorithm," *Sensors*, vol. 20, no. 6, p. 1678, 2020.
- [27] S. Lu, B. Wang, H. Wang, L. Chen, M. Linjian, and X. Zhang, "A real-time object detection algorithm for video," *Computers & Electrical Engineering*, vol. 77, pp. 398–408, 2019.
- [28] M. Liu, X. Wang, A. Zhou, X. Fu, Y. Ma, and Uav-Yolo, "Small object detection on unmanned aerial vehicle perspective," *Sensors*, vol. 20, no. 8, 2020.

Research Article

Super-Twisting Nonsingular Terminal Sliding Mode-Based Robust Impedance Control of Robots

Yixuan Wang, Tairen Sun , and Jiantao Yang

School of Health Science and Engineering, University of Shanghai for Science and Technology, Shanghai 200093, China

Correspondence should be addressed to Tairen Sun; suntren@gmail.com

Received 21 January 2022; Accepted 4 April 2022; Published 16 April 2022

Academic Editor: Chao Zeng

Copyright © 2022 Yixuan Wang et al. This is an open access article distributed under the Creative Commons Attribution License, which permits unrestricted use, distribution, and reproduction in any medium, provided the original work is properly cited.

This paper proposes a super-twisting terminal sliding mode-based robust impedance controller to improve the compliance and robustness in robot-environment interaction. Based on the desired impedance dynamics, an impedance reference trajectory is constructed. Then, based on a super-twisting terminal sliding-mode, the robust impedance controller is designed to guarantee the achievement of the desired impedance dynamics in finite-time through the finite-time convergence of an impedance error. The main contribution of this paper is that the proposed control improves impedance control robustness by using the super-twisting nonsingular terminal sliding-mode without causing the chattering problem. The finite-time stability of the closed-loop control system is validated by theoretical analysis based on the Lyapunov theory, and the control effectiveness is illustrated by simulations on a two-link robot manipulator.

1. Introduction

Compliant behavior of a robot is required in its interaction with its environment to ensure safe interaction [1] but cannot be provided by traditional position control of rigid-link robots. Impedance control proposed by Hogan in 1980s is one of the most popular used active compliance control approaches [2]. In this approach, the desired spring-damping dynamics between robot positions and interaction forces is constructed to improve interaction compliance. This active compliance control has been applied in service robots and industrial robots. In applications, one difficulty in impedance control design comes from robot modeling uncertainties, which hinders the convergence of impedance errors to zero or its small neighborhood and affects the control stability and control robustness. How to improve impedance control robustness has always been a significant research topic.

In the last decades, varieties of robust impedance control approaches including iterative learning impedance control [3–5], adaptive impedance control [6–9], neural network impedance control [10–15], and fuzzy impedance control [16] were proposed to improve impedance control

robustness. However, these control strategies have the following deficiencies. (i) The desired impedance dynamics requires to be factorized in the real space, which restricts the application ranges. (ii) Iterative learning impedance control is mainly applied in repetitive motions, adaptive impedance control requires linear factorization of robot dynamics, while neural/fuzzy impedance control only obtains finiteness of impedance errors and cannot get the convergence of impedance errors to zero.

Sliding-mode control is well known for its strong robust. In [17], a sliding-mode impedance control strategy was proposed based on robust passivity. However, the inherent chattering problem in sliding-mode control severely affects the impedance control performances. To alleviate the chattering problem, a dead-zone strategy was used in designing sliding-mode impedance control [18]. However, this strategy may not effectively decrease chattering. What is worse, the used dead-zone strategy may hinder arriving at the desired sliding surface, which further affects the impedance control performances.

By traditional sliding-mode control, tracking errors asymptotically converge to zero after related variables arriving at the desired sliding surfaces. Terminal sliding mode

control with a nonlinear sliding-mode can guarantee the finite-time convergence of tracking errors, which is better than the asymptotic convergence to some extent [19]. Super-twisting algorithm considered as second-order sliding-mode control has strong control robustness to modeling uncertainties without causing chattering problems [20]. This paper proposes a robust impedance control approach for robots by exploiting the advantages of super-twisting terminal sliding mode. Based on the desired impedance dynamics, an impedance trajectory is constructed. Then, based on a super-twisting sliding mode, a robust impedance controller is designed to guarantee the achievement of the desired impedance through the finite-time convergence of an impedance error. This proposed control approach improves the impedance control robustness using the super-twisting sliding-mode without causing the chattering. The finite-time control stability and the control effectiveness are validated by theoretical analysis and simulation results.

2. Robot Dynamics

Consider the robot arm with the following dynamics:

$$\ddot{q} = f(q, \dot{q}) + \Delta(q, \dot{q}) + M^{-1}(q)(\tau + \tau_e), \quad (1)$$

where q and \dot{q} denote the robot angular vector and velocity vector, respectively; $M(q)$ denotes the inertial matrix; $f(q, \dot{q})$ denotes a known robot function; $\Delta(q, \dot{q})$ denotes robot modeling uncertainties; τ is the control input; and $\tau_e = J^T f_e$ is the interaction force in joint space with J being the Jacobian matrix and f_e the interaction force in work space.

Assumption 1. The desired trajectory q_d and its first- and second-order time derivative are bounded.

Assumption 2. On a compact set Ω , the uncertainty term $\Delta(q, \dot{q})$ satisfies $d_\Delta = [d_{\Delta 1}, \dots, d_{\Delta n}]^T = \hat{\Delta}$, where $|d_{\Delta i}| \leq d_{\max}$, $i = 1, 2, \dots, n$ and d_{\max} is a positive constant.

The objective of this paper is to design a robust impedance controller for (1) based on a super-twisting non-singular terminal sliding-mode control approach to achieve the following desired impedance dynamics:

$$-\tau_e = M_d(\ddot{q}_d - \ddot{q}) + D_d(\dot{q}_d - \dot{q}) + K_d(q_d - q), \quad (2)$$

where M_d, D_d , and K_d denote the desired inertial matrix, the desired damping matrix, and the desired stiffness matrix, respectively.

3. Super-Twisting Terminal Sliding-Mode Impedance Control

Passing τ_e through the following filter:

$$M_d \ddot{q}_e + D_d \dot{q}_e + K_d q_e = \tau_e, \quad (3)$$

then the desired impedance dynamics in (2) can be expressed as

$$M_d(\ddot{q}_r - \ddot{q}) + D_d(\dot{q}_r - \dot{q}) + K_d(q_r - q) = 0, \quad (4)$$

where $q_r = q_d + q_e$ is the constructed impedance trajectory.

Remark 1. In (2), M_d, D_d , and K_d are usually chosen as positive definite diagonal matrices that guarantees the following: (i) $q_d - q$ in (2) converges to zero when τ_e equals to zero; (ii) given $\tau_e \in L_\infty$, q, \dot{q} , and \ddot{q} in (2) are bounded and q_e, \dot{q}_e , and \ddot{q}_e in (3) are bounded. Combining $q_e, \dot{q}_e, \ddot{q}_e \in L_\infty$ and Assumption 1, one can obtain $q_r, \dot{q}_r, \ddot{q}_r \in L_\infty$.

Define $e_1 = q_r - q$, $e_2 = \dot{q}_r - \dot{q}$. The impedance error has the following form:

$$\begin{aligned} e_{im} &= M_d(\ddot{q}_d - \ddot{q}) + D_d(\dot{q}_d - \dot{q}) + K_d(q_d - q) + \tau_e, \\ &= M_d(\ddot{q}_r - \ddot{q}) + D_d(\dot{q}_r - \dot{q}) + K_d(q_r - q). \end{aligned} \quad (5)$$

From (5), the desired impedance dynamics in (2) can be realized through the convergence of e_{im} , if e_1, e_2, \dot{e}_2 converge to zero. In the following, super-twisting-based robust control is designed to make e_1, e_2, \dot{e}_2 converge to zero.

Define the following terminal mode:

$$s = \gamma e_1^{\alpha_1/\alpha_2} + e_2, \quad (6)$$

where $s = [s_1, \dots, s_n]^T$ and α_1, α_2 are odd and satisfy $1 < \alpha_1/\alpha_2 < 2$. Based on the dynamics in (1), the dynamics of s satisfies

$$\dot{s} = \gamma \frac{\alpha_1}{\alpha_2} e_1^{\alpha_1/\alpha_2 - 1} e_2 - f(q, \dot{q}) - \Delta - M^{-1}(q)(\tau + \tau_e) + \ddot{q}_r. \quad (7)$$

Design the following super-twisting mode control:

$$\begin{aligned} \tau &= -\tau_e + M(q) \left[\gamma \frac{\alpha_1}{\alpha_2} e_1^{\alpha_1/\alpha_2 - 1} e_2 + \ddot{q}_r + k_1 |s|^{1/2} \text{sgn}(s) \right. \\ &\quad \left. + k_2 \int_0^t \text{sgn}(s(\tau)) d\tau - f(q, \dot{q}) \right]. \end{aligned} \quad (8)$$

where k_1 and k_2 are positive constants and satisfy $k_1^2 > 4k_2$, $k_2 > d_{\max}$. Substituting (8) into (7) yields

$$\dot{s} = -k_1 |s|^{1/2} \text{sgn}(s) - k_2 \int_0^t \text{sgn}(s(\tau)) d\tau - \Delta. \quad (9)$$

Theorem 1. *Design the super-twisting sliding-mode controller in (8) for the robot with dynamics (1). Then, the errors e_1, e_2, \dot{e}_2 converge to zero in finite-time, which further guarantees the finite-time convergence of e_{im} and the realization of the impedance dynamics in (2).*

Proof. Define

$$\begin{aligned} z_{1i} &= s_i, \\ z_{2i} &= k_2 \int_0^t \text{sgn}(s_i(\tau)) d\tau + \Delta_i, \\ x &= [x_1, x_2]^T = [|z_{1i}| \text{sgn}(z_{1i}), z_{2i}]^T. \end{aligned} \quad (10)$$

From (9), the dynamics of x satisfies

$$\dot{x} = \frac{1}{|x_1|} (Ax + B\bar{d}_\Delta), \quad (11)$$

where $\bar{d}_\Delta = |x_1| d_\Delta$ and satisfies $|\bar{d}_\Delta| \leq d_{\max} |x_1|$, and matrices A and B are defined by

$$A = \begin{bmatrix} \frac{-k_1}{2} & \frac{1}{2} \\ -k_2 & 0 \end{bmatrix}, B = \begin{bmatrix} 0 \\ 1 \end{bmatrix}. \quad (12)$$

Define $C = [1, 0]$. Then, $d_{\max}^2 x^T C^T C x - \bar{d}_{\Delta}^T \bar{d}_{\Delta} \geq 0$, and there exist a positive matrix P and a positive constant ϵ , such that

$$\begin{bmatrix} A^T P + PA + d_{\max}^2 C^T C + \epsilon P & PB \\ B^T P & -1 \end{bmatrix} \langle 0. \quad (13)$$

Consider the following Lyapunov function:

$$V = x^T P x. \quad (14)$$

Taking the time derivative of V with respect to the time t and substituting (13) and (15) into it yields

$$\begin{aligned} \dot{V} &= \frac{1}{|x_1|} \begin{bmatrix} x^T & \bar{d}_{\Delta}^T \end{bmatrix} \begin{bmatrix} A^T P + PA & PB \\ B^T P & 0 \end{bmatrix} \begin{bmatrix} x^T & \bar{d}_{\Delta}^T \end{bmatrix}^T, \\ &\leq \frac{1}{|x_1|} \begin{bmatrix} x^T & \bar{d}_{\Delta}^T \end{bmatrix} \begin{bmatrix} A^T P + PA & PB \\ B^T P & 0 \end{bmatrix} \begin{bmatrix} x^T & \bar{d}_{\Delta}^T \end{bmatrix}^T \\ &\quad + d_{\max}^2 x^T C^T C x - \bar{d}_{\Delta}^T \bar{d}_{\Delta}, \\ &= \frac{1}{|x_1|} \begin{bmatrix} x^T & \bar{d}_{\Delta}^T \end{bmatrix} \begin{bmatrix} A^T P + PA + d_{\max}^2 C^T C & PB \\ B^T P & -1 \end{bmatrix} \begin{bmatrix} x^T & \bar{d}_{\Delta}^T \end{bmatrix}^T, \\ &\leq \frac{-\epsilon}{|x_1|} x^T P x = \frac{-\epsilon}{|x_1|} V. \end{aligned} \quad (15)$$

Since $|x| \leq V^{1/2} / \lambda_{\min}^{1/2}(P)$, then

$$\frac{-1}{|x|} \leq -\frac{\lambda_{\min}^{1/2}(P)}{V^{1/2}}. \quad (16)$$

From (15) and (16), one can obtain

$$\dot{V} \leq -\epsilon \lambda_{\min}^2(P) V^2. \quad (17)$$

Based on (17), V converges to zero in finite-time T_0 which is defined by

$$T_0 = \frac{2V^{1/2}(x(0))}{\epsilon \lambda_{\min}^{1/2}(P)}. \quad (18)$$

From the finite-time convergence of $V(x)$, $x, s_i, z_{2i}, i = 1, 2, \dots, n$ converge to zero in finite-time. From the definitions of s_i and s , we can further obtain the finite-time convergence of e_1, e_2 in the finite-time T_0 . The dynamics of e_2 can be expressed as

$$\dot{e}_2 = \gamma \frac{\alpha_1}{\alpha_2} e_1^{\alpha_2 - 1} e_2 - k_1 |s|^2 \text{sgn}(s) - k_2 \int_0^t \text{sgn}(s(\tau)) d\tau - \Delta. \quad (19)$$

As e_1, e_2, s, z_{2i} converge to zero in the finite-time T_0 , from (19), \dot{e}_2 converges to zero in the finite-time T_0 . The finite-time convergence of e_1, e_2 , and \dot{e}_2 implies the finite-time convergence of the impedance error which guarantees the achievement of the dynamics in (2). \square

Remark 2. If $x_{1i} = 0$, then $z_{1i} = s_i = 0$ and $\dot{s}_i = 0$ which imply $e_1 = 0, e_2 = 0$, and $\dot{e}_2 = 0$. Then, the desired impedance dynamics is achieved.

Remark 3. In comparison with nonfinite-time control, finite-time control can make the robot converge to the desired signal in finite-time. It has been illustrated that finite-time control has faster convergence, better robust, and anti-disturbance performances.

Remark 4. Neural networks (NNs), fuzzy logic (FL), and sliding-mode control can be applied to improve impedance control robustness. However, neural networks- and fuzzy logic-based control typically only achieves infinite-time uniformly ultimately bounded stability owing to the inherent approximation errors of NNs and FL. Compared with NNs- and FL-based impedance control, the proposed super-twisting impedance control can obtain finite-time control stability and has better control robustness.

4. Simulation Results

To show the control effectiveness, simulations are conducted on a two-link robot manipulator (see Figure 1) with the dynamics in (1), where $f(q, \dot{q}) = 0$,

$$\begin{aligned} \Delta(q, \dot{q}) &= M^{-1}(q) (C(q, \dot{q})\dot{q} + G(q) + F\dot{q}), \\ M(q) &= \begin{bmatrix} M_{11} & M_{12} \\ M_{21} & M_{22} \end{bmatrix}, \\ C(q, \dot{q}) &= \begin{bmatrix} -w_3 \sin(q_2) \dot{q}_2 & -w_3 \sin(q_2) (\dot{q}_1 + \dot{q}_2) \\ w_3 \sin(q_2) \dot{q}_1 & 0 \end{bmatrix}, \\ G &= \begin{bmatrix} g_1 \\ g_2 \end{bmatrix}, F = \begin{bmatrix} v_1 & 0 \\ 0 & v_2 \end{bmatrix}, \\ J &= \begin{bmatrix} -l_1 \sin(q_1) - l_2 \sin(q_1 + q_2) & -l_2 \sin(q_1 + q_2) \\ l_1 \cos(q_1) + l_2 \cos(q_1 + q_2) & l_2 \cos(q_1 + q_2) \end{bmatrix}, \\ M_{11} &= w_1 + 2w_3 \cos(q_2), \\ M_{22} &= w_2, \\ M_{12} &= w_3 \cos(q_2) + w_2, M_{21} = M_{12}, \\ g_1 &= w_4 g \cos(q_1) + w_5 g \cos(q_1 + q_2), g_2 = w_5 g \cos(q_1 + q_2). \end{aligned} \quad (20)$$

The related parameters in the above equations are defined by

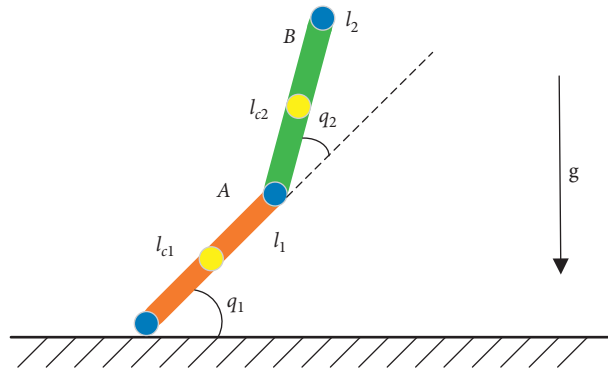


FIGURE 1: Two-link robot arm.

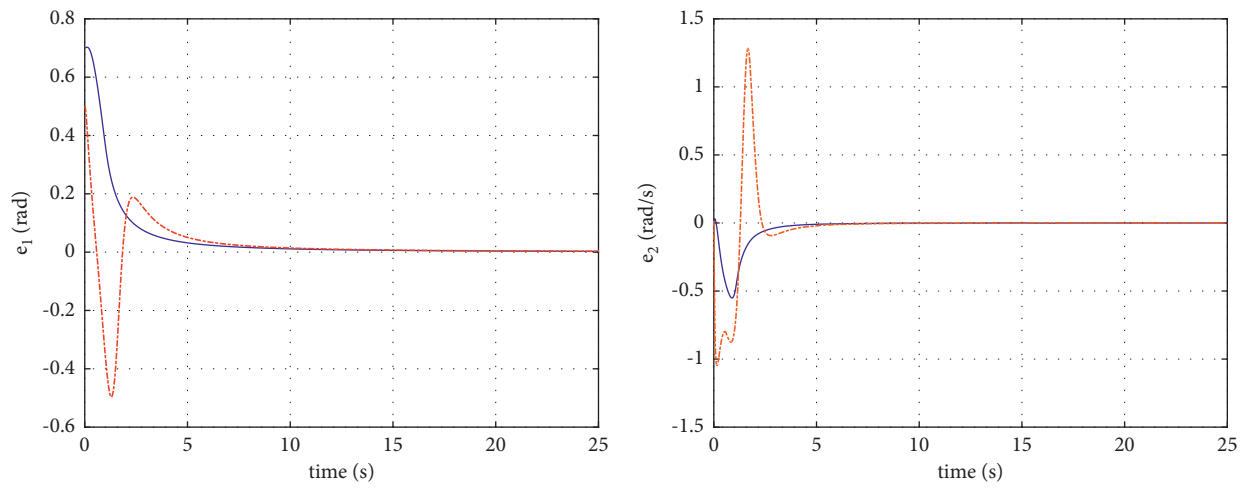
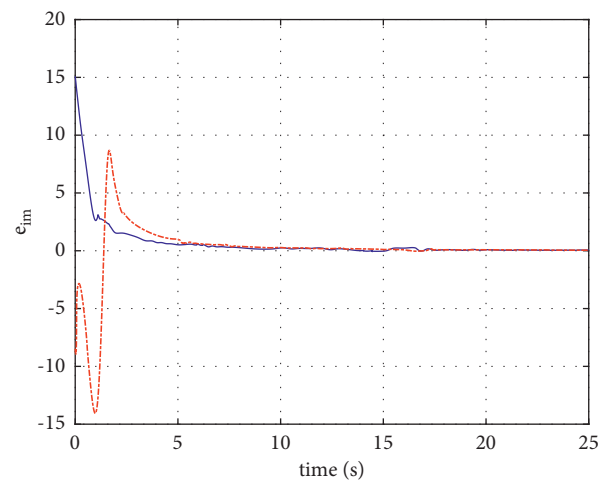
FIGURE 2: Performances of auxiliary errors e_1 and e_2 .

FIGURE 3: Performances of the impedance error.

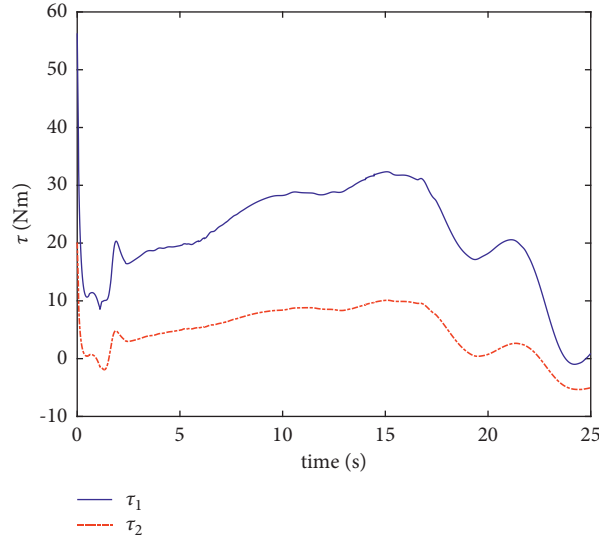


FIGURE 4: The super-twisting terminal sliding-mode impedance control.

$$\begin{aligned}
 w_1 &= I_1 + I_2 + m_1 l_{c1}^2 + m_2 l_1^2 + m_2 l_{c2}^2, w_2 = m_2 l_{c2}^2 + I_2, w_3 = m_2 l_1 l_{c2}, w_4 = m_1 l_{c1} + m_2 l_1, w_5 = m_2 l_{c2}, w_6 = v_1, w_7 = v_2, \\
 m_1 &= m_2 = 1.5 \text{ kg}, l_1 = l_2 = 0.8 \text{ m}, l_{c1} = l_{c2} = 0.4 \text{ m}, I_1 = I_2 = 0.3 \text{ kg} \cdot \text{m}^2, \\
 v_1 &= v_2 = 0.3 \text{ N} \cdot \text{m} \cdot \text{s}, g = 9.8 \frac{\text{m}}{\text{s}^2}.
 \end{aligned} \tag{21}$$

Choose the interaction force $f_e = [5 \sin(0.2t), 5 \cos(0.2t)]^T$, the robot initial position $q(0) = \dot{q}(0) = [0, 0]^T$, the desired trajectory $q_d = [0.5 + 0.2 \cos(\pi t/3)]^T$, and the desired inertial matrix, the desired damping, the desired stiffness as I , $10I$, and $20I$, respectively. Design the control parameters as $\gamma = 3$, $\alpha_1 = 5$, $\alpha_2 = 3$, $k_1 = 8$, and $k_2 = 10$. Figures 2 and 3 depict the performances of tracking errors e_1, e_2 and the impedance error e_{im} by the proposed super-twisting sliding-mode impedance control in Figure 4. Under the proposed robust impedance controller, the auxiliary tracking errors e_1 and e_2 converge to zero after 10 second, which guarantees the convergence of the impedance error e_{im} . From the simulation results, the super-twisting terminal sliding-mode impedance control effectively improves the impedance control robustness without causing the chattering problem in sliding-mode control.

5. Conclusions

This paper proposes a super-twisting terminal sliding-mode impedance controller for robots to improve the compliance and robustness of robot-environment interaction.

By finite-time control theory, we validate the finite-time control stability and the impedance control robustness by theoretical analysis. The control effectiveness is illustrated by simulations on a two-link robot arm. The main contribution and innovation of this paper lie in the super-twisting terminal sliding-mode impedance controller which improves the impedance control robustness without causing chattering.

The desired impedance dynamics in (2) has infinite-time stability. In the near coming future, we will construct finite-time impedance dynamics and design robust impedance control to achieve the desired finite-time impedance dynamics using sliding-mode control or sliding-mode observer.

Data Availability

The raw/processed data required to reproduce these findings cannot be shared at this time as the data also form part of an ongoing study.

Conflicts of Interest

The authors declare that there are no conflicts of interest regarding the publication of this paper.

Acknowledgments

This work was supported in part by the National Key Research and Development Project (No. 2019YFB1312500) and in part by the National Natural Science Foundation of China (Nos. 62073156 and 62103280), and in part by Shanghai Engineering Research Center of Assistive Devices.

References

- [1] C. Zeng, Y. Li, J. Guo, Z. Huang, N. Wang, and C. Yang, "A unified parametric representation for robotic compliant skills

- with adaptation of impedance and force,” *IEEE/ASME Transactions on Mechatronics*, pp. 1–11, 2021.
- [2] N. Hogan, “Impedance control: an approach to manipulation: part i-theory,” *Journal of Dynamic Systems, Measurement, and Control*, vol. 107, no. 1, pp. 1–7, 1985.
 - [3] C. C. Cheah and D. W. Wang, “Learning impedance control for robotic manipulators,” *IEEE Transactions on Robotics and Automation*, vol. 14, no. 3, pp. 452–465, 1998.
 - [4] X. Li, Y.-H. Liu, and H. Yu, “Iterative learning impedance control for rehabilitation robots driven by series elastic actuators,” *Automatica*, vol. 90, pp. 1–7, 2018.
 - [5] X. Q. Liang, H. Zhao, X. F. Li, and H. Ding, “Force tracking impedance control with unknown environment via an iterative learning algorithm,” *Science China Information Sciences*, vol. 62, Article ID 050215, 2019.
 - [6] Y. Li and S. S. Ge, “Human-robot collaboration based on motion intention estimation,” *IEEE*, vol. 19, no. 3, pp. 1007–1014, 2014.
 - [7] Z. Li, Z. Huang, W. He, and C.-Y. Su, “Adaptive impedance control for an upper limb robotic exoskeleton using biological signals,” *IEEE Transactions on Industrial Electronics*, vol. 64, no. 2, pp. 1664–1674, 2017.
 - [8] T. Sun, L. Peng, L. Cheng, Z.-G. Hou, and Y. Pan, “Composite learning enhanced robot impedance control,” *IEEE Transactions on Neural Networks and Learning Systems*, vol. 31, no. 3, pp. 1052–1059, 2020.
 - [9] M. Sharifi, S. Behzadipour, H. Salarieh, and M. Tavakoli, “Cooperative modalities in robotic tele-rehabilitation using nonlinear bilateral impedance control,” *Control Engineering Practice*, vol. 67, pp. 52–63, 2017.
 - [10] W. He, Y. Dong, and C. Sun, “Adaptive neural impedance control of a robotic manipulator with input saturation,” *IEEE Transactions on Systems, Man, and Cybernetics: Systems*, vol. 46, no. 3, pp. 334–344, 2016.
 - [11] C. Yang, G. Peng, Y. Li, R. Cui, L. Cheng, and Z. Li, “Neural networks enhanced adaptive admittance control of optimized robot-environment interaction,” *IEEE Transactions on Cybernetics*, vol. 49, no. 7, pp. 2568–2579, 2019.
 - [12] S. Seul Jung and T. C. Hsia, “Neural network impedance force control of robot manipulator,” *IEEE Transactions on Industrial Electronics*, vol. 45, no. 3, pp. 451–461, 1998.
 - [13] W. He and Y. Dong, “Adaptive fuzzy neural network control for a constrained robot using impedance learning,” *IEEE Transactions on Neural Networks and Learning Systems*, vol. 29, no. 4, pp. 1174–1186, 2018.
 - [14] C. Yang, C. Chen, W. He, R. Cui, and Z. Li, “Robot learning system based on adaptive neural control and dynamic movement primitives,” *IEEE Transactions on Neural Networks and Learning Systems*, vol. 30, no. 3, pp. 777–787, 2019.
 - [15] C. Yang, G. Peng, L. Cheng, J. Na, and Z. Li, “Force sensorless admittance control for teleoperation of uncertain robot manipulator using neural networks,” *IEEE Transactions on Systems, Man, and Cybernetics: Systems*, vol. 51, no. 5, pp. 3282–3292, 2021.
 - [16] L. Roveda, S. Haghshenas, A. Prini, T. Dinon, and N. Pedrocchi, “Fuzzy impedance control for enhancing capabilities of humans in onerous tasks execution,” in *Proceedings of the 2018 5th International Conference on Ubiquitous robots*, pp. 406–411, Honolulu, Hawaii, June 2018.
 - [17] S. P. Chan, B. Yao, W. B. Gao, and M. Cheng, “Robust impedance control of robot manipulators,” *International Journal of Robotics and Automation*, vol. 6, pp. 220–227, 1991.
 - [18] H. Mohammadi and H. Richter, “Robust tracking/impedance control: application to prosthetics,” in *Proceedings of the American Control Conference*, pp. 2673–2678, Chicago, Illinois, July 2015.
 - [19] C. Yang, Y. Jiang, J. Na, Z. Li, L. Cheng, and C.-Y. Su, “Finite-time convergence adaptive fuzzy control for dual-arm robot with unknown kinematics and dynamics,” *IEEE Transactions on Fuzzy Systems*, vol. 27, no. 3, pp. 574–588, 2019.
 - [20] D. Fu, X. Zhao, and J. Zhu, “A novel robust super-twisting nonsingular terminal sliding mode controller for permanent magnet linear synchronous motors,” *IEEE Transactions on Power Electronics*, vol. 37, no. 3, pp. 2936–2945, 2022.

Research Article

Model-Based Design, HIL Testing, and Rapid Control Prototyping of a Low-Cost POC Quadcopter with Stability Analysis and Control

Abdullah Irfan , Muhammad Gufran Khan , Arslan Ahmed Amin, Syed Ali Mohsin, Muhammad Adnan , and Adil Zulfiqar 

Department of Electrical Engineering, National University of Computer and Emerging Sciences, Chiniot-Faisalabad Campus, Islamabad 44000, Pakistan

Correspondence should be addressed to Abdullah Irfan; f180868@nu.edu.pk

Received 15 October 2021; Revised 29 January 2022; Accepted 22 February 2022; Published 28 March 2022

Academic Editor: Chao Liu

Copyright © 2022 Abdullah Irfan et al. This is an open access article distributed under the Creative Commons Attribution License, which permits unrestricted use, distribution, and reproduction in any medium, provided the original work is properly cited.

Unmanned aerial vehicles (UAVs), particularly quadcopters, have several medical, agriculture, surveillance, and security applications. However, the use of this innovative technology for civilian applications is still very limited in low-income countries due to the high cost, whereas low-cost controllers available in the market are often tuned using the hit and trial approach and are limited for specific applications. This paper addresses this issue and presents a novel proof of concept (POC) low-cost quadcopter UAV design approach using a systematic Model-Based Design (MBD) method for mathematical modeling, simulation, real-time testing, and prototyping. The quadcopter dynamic model is developed, and controllers are designed using Proportional Integral, and Derivative (PID), Pole Placement, and Linear Quadratic Regulator (LQR) control strategies. The stability of the controllers is also checked using Lyapunov stability analysis. For verification and validation (V&V) of the design, Software-in-the-Loop, Processor-in-the-Loop, Hardware-in-the-loop testing, and Rapid Control Prototyping have been performed. The V&V methods of the MBD approach showed practically valid results with a stable flight of the quadcopter prototype. The proposed low-cost POC quadcopter design approach can be easily modified to have enhanced features, and quadcopters with different design parameters can be assembled using this approach for a diverse range of applications.

1. Introduction

Unmanned aerial vehicles (UAVs) are quite popular as they are small and can be flown without a pilot, either remotely or through autonomous algorithms. UAVs have applications in several domains like agriculture, military, rescue missions, etc. [1]. Several types of UAVs have been introduced; their classification can be done according to size and payload, aerodynamic configuration, applications, level of autonomy, or their range of action [2].

The quadcopter/quadrotor is a type of UAV compact and possesses diverse capabilities like better maneuverability, stationary hovering, and vertical takeoff and landing (VTOL) [3]. A quadcopter consists of a frame/skeleton responsible for supporting its components. It has four

propellers attached to Brushless DC (BLDC) motors to control the motion of the quadcopter [4]; each motor speed varies according to the control strategy to maintain its stability. It also contains electronic speed controllers (ESCs), which provide PWM signals to the motors, a flight controller, and a battery. The rotation of the motors is paired as clockwise and anticlockwise to keep the total angular momentum zero.

During the flight, the quadcopter experiences external forces like gravity, viscous friction, propellers, thrust and drag forces, etc. and thus makes the gyroscope output of the quadcopter nonlinear [5]. Such nonlinear behavior and the mechanical structure of the system make the quadcopter quite complex to control [6]. To counter these challenges, the controller must be designed in such a way that it can keep the

quadcopter stabilized under different real-world conditions. Among other control techniques, Linear Quadratic Regulator (LQR), Model Predictive Control, Proportional Integral, and Derivative (PID), backstepping, and neural network are quite prominent [7] in this field.

Many researchers have proposed different design techniques to develop mathematical models of the quadcopter. A dynamic control model is proposed by [8], using linear and nonlinear control techniques combined to create algorithms that stabilize the altitude, attitude, heading, and position in space. The proposed model includes the effects of rotor and aerodynamics with two control techniques, i.e., PD and nonlinear sliding mode controller. A limitation of this work is that the designed Multiple Input Multiple Output (MIMO) system is not controllable, so a proper MIMO controller for this model could not be developed. Reference [9] developed a dynamic model using Euler and Newton equations, and the modeling for the environmental effects was done with high accuracy to validate the model under different circumstances. The model performance results are quite good and show quite realistic results. Still, the designed model is not suitable to be used for MIMO controller design since the nonlinearities in the model are not dealt with efficiently.

Reference [10] has introduced a mathematical design for the quadcopter and developed a simulation environment to validate the software development. The developed model performed exceptionally well, but the approach used to validate the model had hardware limitations. Reference [11] proposed a sliding mode controller technique with state estimation through linear observer by employing the residual-based method for control configuration. The model can also distinguish between disturbances and faults, thus theoretically making it quite suitable for use. However, the processing cost of the proposed technique is quite extensive, thus making it nonfeasible for practical use. Reference [12] proposed dynamic modeling of the system in the MathWorks Simulink environment. PID control strategy is built for single-axis control, and STM32 is used for practical validation of the system, which showed promising results. Reference [13] proposed a cascaded PID control strategy and compared classical and cascaded PID controller performances. However, the conventional hit and trial method is employed to get PID gains rather than designing a proper autotuning setup for the system.

Apart from this, reference [14] proposed a tiltrotor model with H-configuration, which allowed relatively the undefined weight to be pulled easily theoretically. Reference [15] proposed a variable pitch-based quadrotor model, which showed disturbance compensation during a wind gust. Reference [16] proposed a model with the capability to change shape during flight by compensating for the dynamic center of gravity and continuous variation in a moment of inertia.

The Model-Based Design (MBD) approach has become quite popular in recent years due to its ability to design and test plant and controller models iteratively and detect errors early in the design process. Software In Loop (SIL) and

Processor In Loop (PIL) simulations are an essential part of the MBD approach [17]. It integrates visual and mathematical methods to address the complex problems related to signal processing, communication systems, and embedded software. It provides a mutual design environment that helps in data analysis, general communication, and system verification. It lets engineers locate and remove early errors in the system, minimizing the time and financial impact of the system [18]. The HIL-based model and testing have been proposed in [19], in which a quadcopter model setup is developed, and indoor testing for hardware is done.

Moreover, the designed system can be upgraded/modified easily as per the requirements due to the modular approach. After successfully validating SIL and PIL simulations, Hardware In Loop (HIL) testing is adopted by deploying an actual controller to identify real-world problems and issues. After the successful real-time HIL testing, rapid control prototyping is done using plant and controller hardware, and the complete system is validated in the real world. MBD has become a standard approach for system design in many industries such as aerospace, automotive, and industrial equipment manufacturing. The designed model can also be utilized for wireless-powered communication to improve energy efficiency in a distributed nonorthogonal multiple access PSN [20].

This paper presents a novel end-to-end approach of quadcopter system design through systematic design and implementation strategy, mathematical modeling, control algorithm, and real-time testing of a low-cost quadcopter by employing the MBD approach. Previously, this kind of system design and prototyping approach having similar features with low-cost components is not available in the literature to the best of our knowledge. The following are the key contributions of the paper:

- (1) Mathematical modeling a quadcopter with multiple control techniques using a model-based design approach
- (2) Defining criteria for practical implementation of the validated theoretical system
- (3) Validation of proposed system by practical testing of the prototype.

Apart from these, the controllers can be efficiently designed and adapted according to required tasks; e.g., a controller designed for speed can be modified to carry heavy loads without moving to any hit and trial approach. This increases work efficiency and cost optimization by adopting the system as per requirements.

The remainder of the paper is organized as follows: Section 2 comprises mathematical modeling of the plant, while the mathematical modeling of the controller is presented in Section 3. Section 4 discusses the results obtained from SIL and PIL simulations. Section 5 presents HIL testing on different microcontrollers, while Section 6 comprises rapid control prototyping of the proposed system, Section 7 discusses the cost and computational complexity of the system, and finally, Section 8 concludes the paper.

2. System Modelling

In system modeling, the mathematical models of the system through transfer functions or state-space equations are derived and developed. Primarily derived systems are nonlinear, and to design a controller for them, they need to be linearized. Newton Euler equations are used for quadcopter dynamic modeling to develop the quadcopter frames. To limit the variable constraints, some assumptions are made as follows:

- (1) The body of the quadcopter is rigid and symmetrical
- (2) The center of gravity of the quadcopter is in the center of the body
- (3) Quadcopter rotors are inflexible

$$R_{xyz} = \begin{bmatrix} \cos \theta \cos \psi & \sin \phi \sin \theta \cos \psi & \cos \phi \sin \theta \cos \psi + \sin \phi \sin \psi \\ \cos \theta \sin \psi & \sin \phi \sin \theta \sin \psi + \cos \theta \cos \psi & \cos \phi \sin \theta \sin \psi + \sin \theta \cos \psi \\ -\sin \theta & \sin \phi \cos \theta & \cos \phi \cos \theta \end{bmatrix}. \quad (1)$$

Quadcopter motion velocities are generated from the Inertial Measurement Unit (IMU) sensor model (embedded in the equation), and the body coordinated (Euler) rates (η) are converted into angular rates (ω) by using the following relation:

$$\omega = R_T \dot{\eta}. \quad (2)$$

Here, R_T is given as

$$R_T = \begin{bmatrix} 1 & 0 & -\sin \theta \\ 0 & \cos \phi & \sin \phi \cos \theta \\ 0 & -\sin \phi \cos \theta & \cos \phi \cos \theta \end{bmatrix}. \quad (3)$$

The system is decomposed into two parts to generate a dynamic mathematical model of the quadcopter. One is rotational (along ϕ , θ , and ψ axes), and the other is the translation (along x , y , and z axes). Here, the rotational part is actuated; however, the translational part is underactuated. Gyroscopic moments derive rotational equations of motions because the desired inertial matrix should be independent of time. The rotational equation of motion for the system is given as

$$J\dot{\omega} + \omega \times J\omega + \omega [0 \ 0 \ J_r \ \omega_r]^T. \quad (4)$$

Here, J_r is rotor inertia, J is quadcopter's diagonal inertia matrix, ω is angular body rate, and ω_r is rotors speed ($\omega_r = \omega_2 - \omega_1 + \omega_4 - \omega_3$). As quadcopter is in symmetry, so inertia matrix is a diagonal matrix given by

$$J = \begin{bmatrix} I_x & 0 & 0 \\ 0 & I_y & 0 \\ 0 & 0 & I_z \end{bmatrix}, \quad (5)$$

where I_x , I_y and I_z are the moment of inertial of the system along the three perpendicular axes.

Generally, two frame references are used to express the quadcopter position: one is Earth Frame Reference (EFR), presented as e_x, e_y, e_z and the other is body frame reference (BFR), presented as x, y, z . The lists of abbreviations and symbols with descriptions have been mentioned in Tables 1 and 2, respectively.

In EFR, an initial point on ground/plane/Earth is taken as a reference, while, in the case of BFR, the center of the quadcopter is treated as a reference point, where the z -axis points downwards/ground. Roll, pitch, and yaw are used to represent the quadcopter's orientation. EFR and BFR conversion is required for some states, so the rotation matrix, given below, is used:

Individual axis moments are derived and combined using the right-hand rule. The forces impacting the quadcopter are derived to estimate each motor rotation impact on the system. After adding these two forces, the obtained equations are

$$B_M = \begin{bmatrix} F_A l (\omega_4^2 - \omega_2^2) \\ F_A l (\omega_3^2 - \omega_1^2) \\ F_M (\omega_2^2 - \omega_1^2 + \omega_4^2 - \omega_3^2) \end{bmatrix}. \quad (6)$$

where B_M is turning force acting on a quadcopter with respect to its body frame, F_M is moment acting on quadcopter model (it is the constant derived from the product of the quadcopter's air density, propeller area, and the radius of the propeller [21]), F_A is aerodynamic force, and l is propeller length, which can be modified as per the available system.

Quadcopter in hovering state exerts force in a downward direction only, which is equal to the thrust force generated by the system, i.e., against the gravitational force. The x - and y -axis movements will be zero in the hovering state because pitch and yaw angles are zero. The hovering state forces are given by

$$B_F = \begin{bmatrix} 0 \\ 0 \\ F_A (\omega_1^2 + \omega_2^2 + \omega_3^2 + \omega_4^2) \end{bmatrix}. \quad (7)$$

The air friction causes drag forces given by D_F and their impact is in the opposite direction to the moment of quadcopter body, i.e., $B_M - D_F$.

State-space modeling of the system helps in MIMO controller design. Quadcopter degrees of freedom (DOF) are mapped into state vector X presented as

TABLE 1: List of abbreviations.

Abbreviations	Description
EFR	Earth frame reference
BFR	Body frame reference
IMU	Inertial measurement unit
MIMO	Multiple input multiple output
LQR	Linear quadratic regulator
SIL	Software in the loop
COG	Center of gravity
MBD	Model based design
HIL	Hardware in the loop
RCP	Rapid control prototyping
ESC	Electronic speed controller
BLDC	Brushless DC motor
PPM	Pulse position modulation

TABLE 2: List of symbols.

Symbols	Description
e_x	X position w.r.t BFR
e_y	Y position w.r.t BFR
e_z	Z position w.r.t BFR
x	X position w.r.t EFR
Y	Y position w.r.t EFR
Z	Z position w.r.t EFR
ϕ	Angular position phi
θ	Angular position theta
ψ	Angular position psi
η	Eta - viscosity
R_T	Rotation matrix
J_r	Rotor inertia
J	Diagonal inertia matrix
ω	Angular rate
I_x	Moment of inertial along the x -axis
I_y	Moment of inertial along the y -axis
I_z	Moment of inertial along the z -axis
I_{xx}, I_{yy}, I_{zz}	Moment of inertia for body frame principle axes
A_x, A_y, A_z	Drag coefficients
F_A	Aerodynamic force
F_M	Moment force
B_M	Quadcopter moment
D_F	Drag force
k_M	Moment constant
k_f	Aerodynamic force constant
P	Pitch
T	Thrust
D	Diameter
$Kv_{require d}$	Required Kv
$V_{battery}$	Battery voltage
$Kv_{nominal}$	Nominal Kv
P_{out}	Output power
B_C	Battery capacity
$I_{nominal}$	Nominal current
E	Endurance
e	Efficiency

$$X = [\phi \dot{\phi} \theta \dot{\theta} \psi \dot{\psi} x \dot{x} y \dot{y} z \dot{z}]' \quad (8)$$

$$= [x_1 x_2 x_3 x_4 x_5 x_6 x_7 x_8 x_9 x_{10} x_{11} x_{12}]'$$

Input vectors are presented as $u = [u_1 u_2 u_3 u_4]$. Moment constant as k_M and aerodynamic force constant as

k_f are considered for the derivation of frame forces. Thus, the system state-space model becomes

$$\begin{aligned} \dot{x}_1 &= x_2 \\ \dot{x}_2 &= \frac{k_f(\omega_4^2 - \omega_2^2)}{I_{xx}} \\ \dot{x}_3 &= x_4 \\ \dot{x}_4 &= \frac{k_f(\omega_3^2 - \omega_1^2)}{I_{yy}} \\ \dot{x}_5 &= x_6 \\ \dot{x}_6 &= \frac{k_M(\omega_1^2 - \omega_2^2 + \omega_3^2 - \omega_4^2)}{I_{zz}} \\ \dot{x}_7 &= x_8 \\ \dot{x}_8 &= A_x x_1 \\ \dot{x}_9 &= x_{10} \\ \dot{x}_{10} &= A_y x_3 \\ \dot{x}_{11} &= x_{12} \\ \dot{x}_{12} &= A_z x_5 - g + \left(\frac{1}{m}(\omega_1^2 + \omega_2^2 + \omega_3^2 + \omega_4^2)\right) \end{aligned} \quad (9)$$

where I_{xx} , I_{yy} , and I_{zz} are the area moments of inertia about the principal axes of quadcopter body frame, m is mass, and g is the gravitational force. A_x , A_y , and A_z are the drag coefficients taken from the dynamic behavior of the system of [22].

The developed state-space model is then transformed into A , B , and C matrices and used for controller design. However, a nonlinear model is used as a plant model for testing purposes. One significant benefit of this design is that m variable can be varied as per load requirements.

3. Controller Design

The main objective of the state-space modeling of the quadcopter is to minimize the complexity of control strategies as MIMO systems can be efficiently dealt with in this form. Three control strategies are designed in this work: PID that is capable of altitude control, pole placement controller (designed through full state feedback), and LQR technique that offers position control of quadcopter.

3.1. PID Controller Design. A PID controller combines three actions to control the signal. They are responsible for delivering zero error between the feedback signal (process variable) and the desired output (setpoint). Proportional (P) control calculates error and multiplies with P constant to generate output. P-controller provides stable operation but

never reaches steady-state; thus, it needs a manual reset or basing. I-controller holds error value time until error becomes zero; this resolves the P-controller steady-state problem. A nonlinear plant can cause integral output to increase event at zero error state, also known as an integral windup condition, so a limiter is required at the output of integral action. Also, I-controller cannot predict future errors and only operates when the setpoint is changed. D-controller can predict future system behavior by considering the rate of change of error with time. If the controller observes any rate change, it acts on output increasing system response [23]. A general PID can be presented using

$$u(t) = K_p \left[e(t) + \frac{1}{T_i} \int_0^t e(\tau) d\tau + T_d \frac{de(t)}{dt} \right], \quad (10)$$

where K_p is the gain.

A PID can only do Single Input Single Output (SISO) operation. A quadcopter has at least four controllable states (orientation with altitude control), so individual PID is required for each state. Before placing in the system, all four PIDs are tuned separately using the LabVIEW PID tuning module. PID controller in the proposed model is only designed for position control. System states are defined using LabVIEW subVIs, and indicators show results.

3.2. Full State Feedback Control Design. A system can have multiple degrees of freedom. A closed-loop characteristic equation for a system can be expressed as

$$s^n + a_{n-1}s^{n-1} + \dots + a_1s + a_0 = 0. \quad (11)$$

Poles in the closed-loop system can be set at the desired location by selecting the n value. A typical feedback control

system has its output y fed/added to the input u . In a full state feedback control system, again k is introduced; if the system has multiple inputs/outputs, it can be a vector or matrix that multiplies with output y and then fed/added to the input u [24]. Thus, (11) can be modified to (12), where higher orders are divided into smaller single order equations.

$$\dot{x} = Ax + Bu(-Kx + r) = (A - BK)x + Br; y = Cx \quad (12)$$

Gains k of the closed-loop system are designed by equating characteristic equations of the closed-loop system, equating desired characteristic equation. Then, these equations are compared to get gain values. Typically, in state-space representation, a system can be represented as either phase variable form or canonical form [25]. Phase variable form is defined as

$$\begin{aligned} A &= \begin{bmatrix} 0 & 1 & 0 & \dots & 0 \\ \vdots & \vdots & \vdots & \vdots & \vdots \\ -a_0 & -a_1 & -a_2 & \dots & -a_{(n-1)} \end{bmatrix}; \\ B &= \begin{bmatrix} 0 \\ \vdots \\ 1 \end{bmatrix}; \\ C &= [c_1 \dots c_n]. \end{aligned} \quad (13)$$

The system modeling from the beginning is performed in phase variable form; thus, the controller design of the developed model is also done in phase variable form. It is done by introducing K (vector or matrix) in the closed-loop system of $A - BK$ as shown in the following equation:

$$A - BK = \begin{bmatrix} 0 & 1 & 0 & \dots & 0 \\ \vdots & \vdots & \vdots & \vdots & \vdots \\ -(a_0 + k_1) & -(a_1 + k_2) & -(a_2 + k_3) & \dots & -(a_{(n-1)} + k_n) \end{bmatrix}. \quad (14)$$

Thus, the closed-loop characteristic equation becomes

$$\det(sI - (A - BK)) = s^n + (a_{(n-1)} + k_n)s^{(n-1)} + \dots + (a_0 + k_1) = 0. \quad (15)$$

The desired characteristic equation is given in

$$s^n + d_{(n-1)}s^{(n-1)} + \dots + d_2s^2 + d_1s + d_0 = 0. \quad (16)$$

Since the gain matrix is desired from the characteristic equation, thus by subtracting (15) from (16), we get the desired gain values k .

$$k_{(i+1)} = d_i + a_i. \quad (17)$$

The controller for closed-loop systems cannot be directly designed as the system may have one or more than one uncontrollable state. Thus, to ensure that every state of the

system is controllable, a controllability matrix is designed and then evaluated by checking its rank and determinants. The controllability matrix is generated by putting the A and B matrices of the system into (17). This causes the highest order nonsingular square submatrix, which gives the system rank, and then the determinant of the matrix is evaluated as

$$C_c = [B \ AB \ A^2B \ \dots \ A^{n-1}B]. \quad (18)$$

For this system, poles are taken at $-2 \pm 1.96j$ to keep overshoot at less than 4%, while poles are paired at -1.5, -2, -2.5, -3, and -3.5. The pole placement controller design has K gain in the matrix form. The matrix is multiplied on the feedback terminal, i.e., from output to input.

3.3. Linear Quadratic Regulator Design. Optimal control theory is used to operate the dynamic system at lower costs. Linear Quadratic Controller (LQR) is a type of optimal

control that allows user custom cost/performance ratio control strategy design. LQR controller has better accuracy because, in contrast to pole placement where eigenvalues set location is specified in the designing process, LQR has performance weighting matrices that define eigenvalues set location guaranteeing system stability. So, LQR is an automated state feedback controller [26]. The cost function of the system is given as

$$J = \int_0^{\infty} (x^T Q z + u^T R u) dt. \quad (19)$$

Here, Q penalizes system performance, while R penalizes controller efforts. In this work, an iterative approach is used where the cost function is used to calculate the controller's gains. Q and R values are predefined, gains are calculated, and system response is noted for the designed controller. Since it is an iterative approach, it is repeated over 1000 times. Briefly, the steps of this approach are as follows:

- (1) Define the value of Q and change R over iteration
- (2) Design controller over this value and store system response
- (3) Change Q value by a step and change R over iteration
- (4) Design controller over this value and store system response
- (5) Repeat steps 1 to 4 over the defined iterative range of Q and R
- (6) Compare performance matrices of this system to shortlist the best performing controller

After comparing results of different iterations, the selected weight matrix Q and quantity weight matrix R are $100 \times I \times (12)$ and $0.1 \times I \times (12)$.

3.4. Stability Analysis. The Lyapunov stability analysis of the stable system is performed by using controlled A matrix obtained from $A - BK$ with Lyapunov equation with $Q = I_{12}$. The generic P matrix is defined in the following equation:

$$P = \begin{bmatrix} P_{11} & P_{12} & P_{13} & \cdots & P_{1n} \\ \vdots & \vdots & \vdots & \vdots & \vdots \\ P_{1n} & P_{2n} & P_{3n} & \cdots & P_{nm} \end{bmatrix}. \quad (20)$$

Unknown values of P are estimated using $A^T P + P A = -Q$. By solving the matrix P values, eigenvalues are calculated to be positive definite, thus proving that the system is stable.

4. Simulation Implementation and Results

The model-based design approach is used to develop the plant and controller models. The system is tested in two phases, SIL and PIL simulation.

4.1. Software in-the-Loop (SIL) Simulation. Initially, the system is designed for SIL simulation where plant and controller models are designed and simulated, and an interface is developed to monitor and control the system response. The front panel of LabVIEW is created where the 3D GUI of the quadcopter is designed, as shown in Figure 1; the object is shaped as a quadcopter in a plane environment. The position and orientation of the quadcopter with respect to the plane are set through inputs defined in the block window in the form of $x, y, z, \phi, \theta,$ and ψ

Latitude (X) is the x -axis, longitude (Y) is the y -axis, and attitude (Z) is the z -axis reference point for the designed model. In contrast, $\phi, \theta,$ and ψ reference points are set zero as system stability on angular axes is required. Figure 2 shows the block diagram of the implemented system. Here, the system in mathematical form is defined using modules with multiple pellets (e.g., CDSim pellet, programming pellet, etc.). PID controller is designed for position control along with altitude control.

Simulations are run for thirty seconds setting the reference altitude to one meter, reference angle ($\phi, \theta,$ and ψ) to zero, and environmental conditions are set as per Table 3.

Figure 3 shows the angular response of the plant model; it offers a very low angular change. The zoomed view shows the slight difference in $\phi,$ and θ angles to attain the required altitude of 1 meter within seconds (the altitude response is shown in Figure 4).

Although ψ response takes around 30 seconds to become zero completely, it is negligible since its value is relatively low. Pole placement and LQR controller are also capable of performing position control. Simulation for this scenario is run for thirty seconds. The reference positions of x, y and z are set to one meter, reference angles ($\phi, \theta,$ and ψ) are set to zero, and model conditions are set as per Table 1.

Figure 5 is the results comparison graph for two controllers where 5(a) shows the system linear response using LQR and pole placement controller. Figure 5(b) shows the angular response of the system using LQR and pole placement controller, where $\phi, \theta,$ and ψ changes can be observed minimizing as the required x and y positions are being approached. The angular response becomes zero as soon as the required position is reached.

Figure 6 shows the angular response of the quadcopter for ψ at 45° while the x and y are at 1 meter and altitude movement to 20 meters. The response of LQR is relatively stable since there is not much deviation with respect to the reference. The error between the reference and original position is obtained, and the mean error is calculated; the controller showed 94% accuracy. However, the accuracy is reduced if the position of the quadcopter is changed randomly and abruptly over small time steps.

4.2. Processor in-the-Loop (PIL) Simulation. After the system stability is verified in SIL simulation in the MBD approach, it is tested in a PIL simulator. The plant model is set in a LabVIEW simulator (without any controller) in PIL, and control techniques are deployed on the myRIO controller.

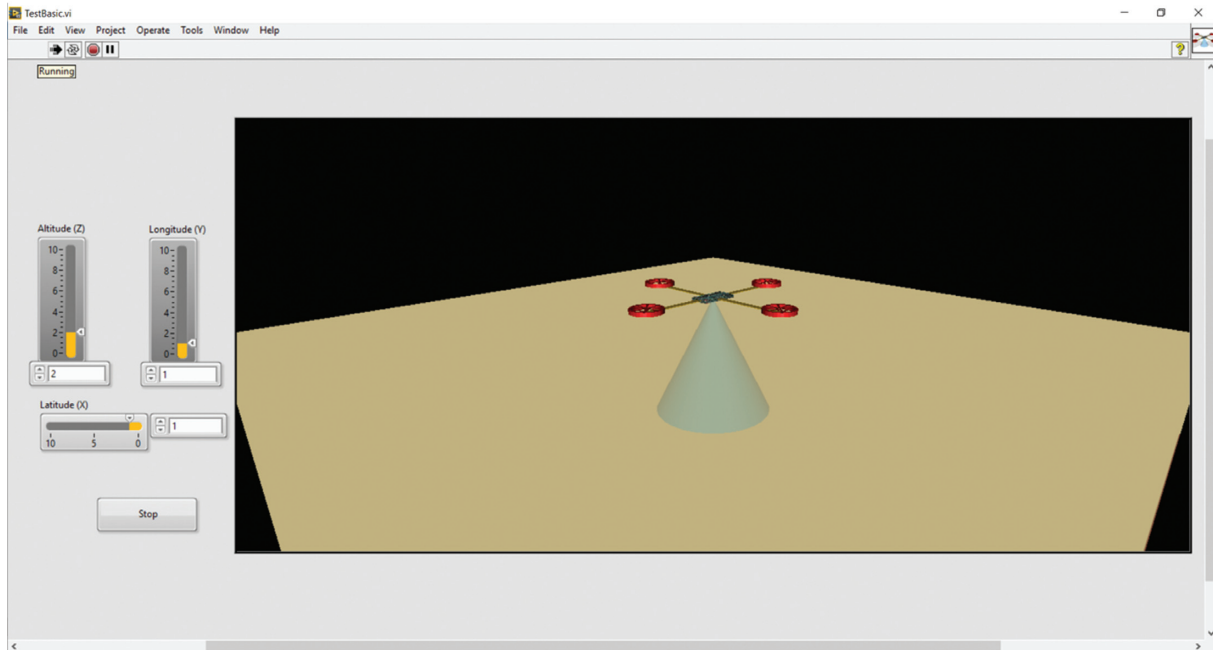


FIGURE 1: LabVIEW GUI of quadcopter flight simulation.

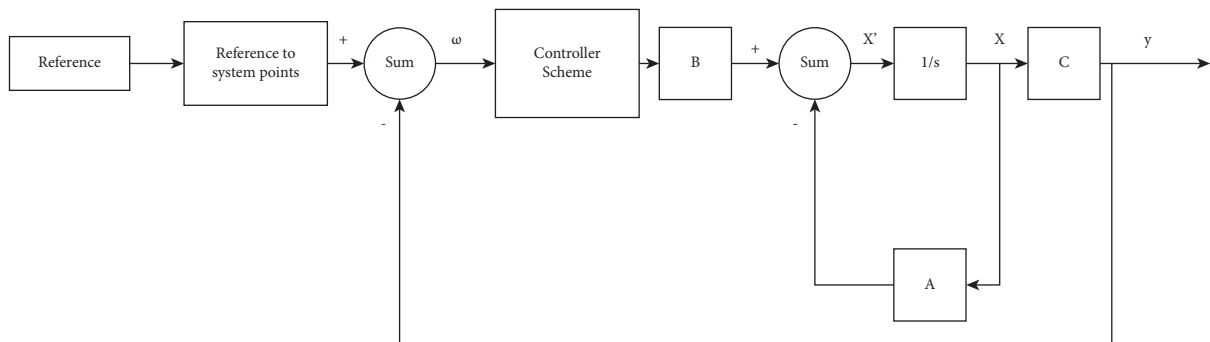


FIGURE 2: LabVIEW block diagram of SIL simulation.

TABLE 3: Model parameters.

Parameter	Value
Mass (m)	1.316 kg
Length of rotor from COG (l)	0.5 m
Lift coefficient (b)	$1.14e^{-7} \text{ N rad}^{-1} \text{ s}^{-1}$
Aerodynamic frictions	$0.45 \text{ N m}^{-1} \text{ s}^{-1}$
Body inertia	$3.57e^{-6} \text{ kgm}^2$
Gravity acceleration (g)	9.81 m s^{-2}
Drag coefficient (k)	$2.98e^{-6} \text{ Nm rad}^{-1} \text{ s}^{-1}$

myRIO is a real-time embedded evaluation board made by National Instruments and is used to develop applications that utilize a microcontroller. myRIO is programmed using LabVIEW, and for PIL simulation, it is used with the simulator (where the plant model is operational). For communication between controller and simulator, there is the network stream where a local network is defined and myRIO is connected using an IP address. The designed system modules from the Virtual Instrument Software

Architecture (VISA) palette enable communication in the plant model. Thus, the plant model structure is almost the same as that in Figure 2, but the controller structure has changed since it was deployed on myRIO. Figure 7 shows the block diagram of the controller designed and deployed on myRIO.

In PIL simulation, the system showed similar results as SIL results. Besides, the model is simulated in an infinite loop to monitor its continuous response for around 48 hours, and it ran without any errors, thus justifying the controller's stability. Table 4 shows the PID gains.

5. Hardware-in-the-Loop Testing

The second last step for system verification in the MBD system design approach is HIL testing. To perform HIL real-time simulation and testing, motors with sensors are deployed on the fixed frame to estimate their response under different conditions. Moreover, the controller is mounted on the prototype, while the plant model is still deployed on the simulator.

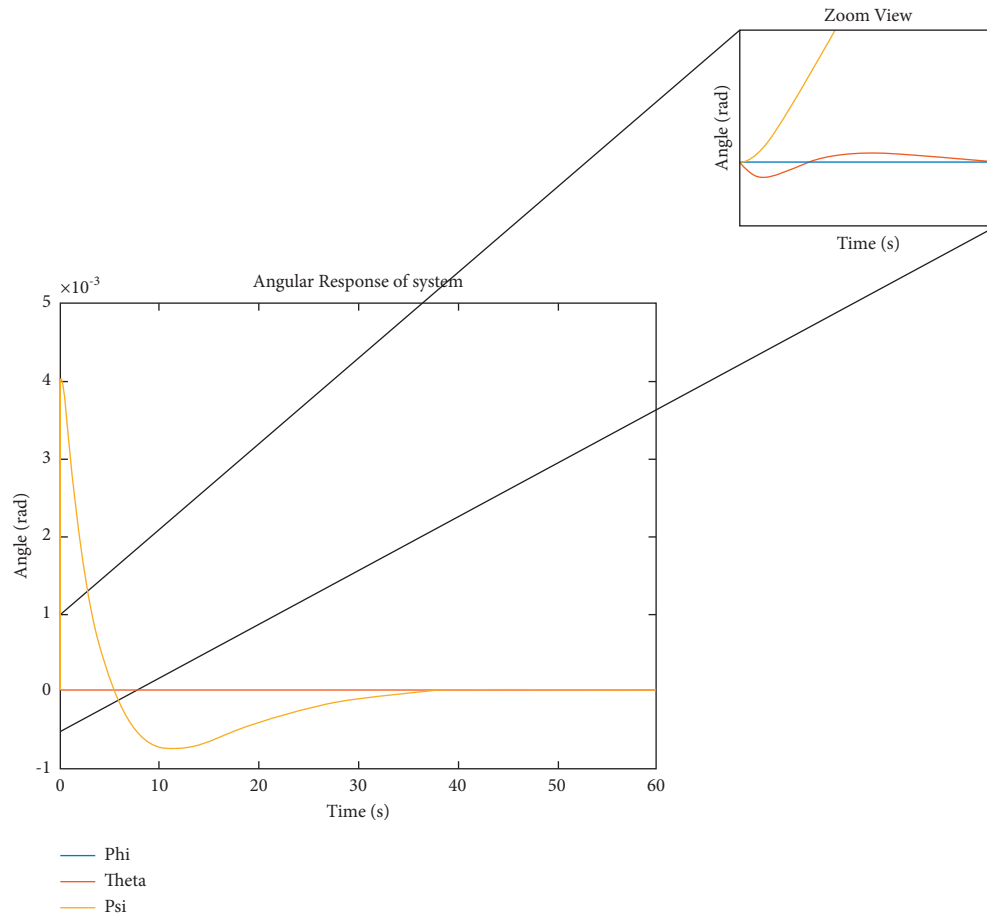


FIGURE 3: PID Angular Response of SIL simulation.

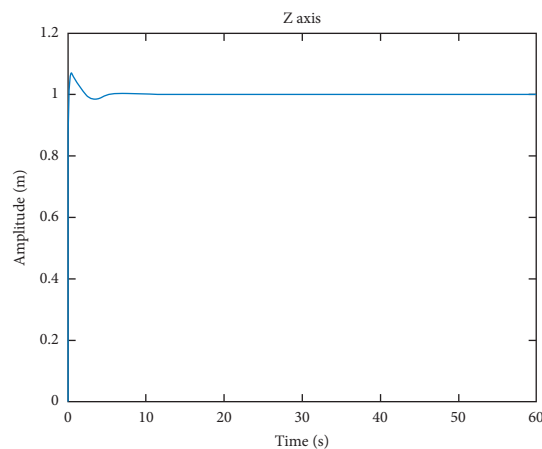
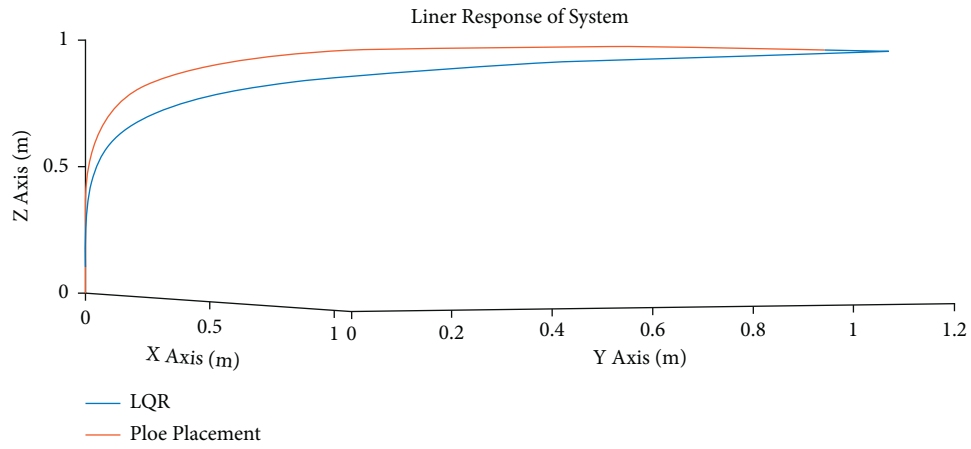


FIGURE 4: PID Altitude Response of SIL simulation.

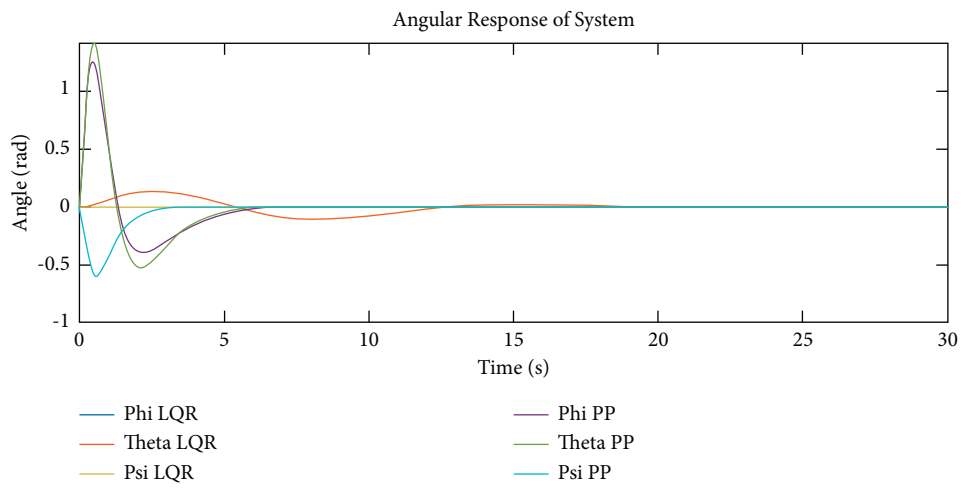
The basic frame is wood with a 1.5-meter height and 1-meter width (on both sides). The quadcopter frame is set in the middle through the ropes with maximum flexibility of approximately 20° between the string and the quadcopter frame. This ensures that the system's behavior is observable, while the propeller would not hit any part of the bindings. The limitation of this fixed/bounded prototype is that the system behavior for limited orientation angles (along with

pitch and yaw) and hovering state are measurable only. The quadcopter frame is set at 1-meter height (from the base of the frame) and centered in between. The quadcopter stability was tested by using myRIO and ATmega 328p.

The controller model developed in PIL testing is further improved by defining motors' output. A complementary filter is designed to enhance the signal-to-noise ratio (SNR) (noise in the plant model is generated using additive white

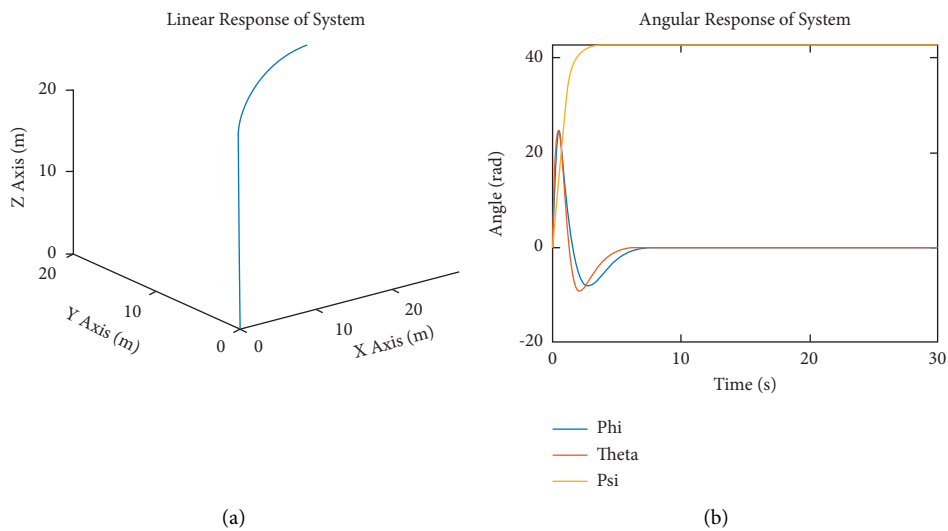


(a)



(b)

FIGURE 5: Pole Placement and LQR Controllers response comparison for system. (a) Liner Response of system. (b) Angular Response of system.



(a)

(b)

FIGURE 6: System response for psi at 45° and altitude 20 meters.

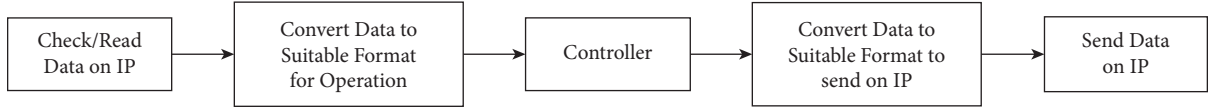


FIGURE 7: Block diagram for PIL simulation in simulator.

TABLE 4: Gains from PIL testing.

Axis	K_p	K_i	K_d
ϕ	0.55	0.4	0.1
θ	0.55	0.4	0.1
ψ	0.55	0.4	0.1
Z-axis/altitude	0.75	1.75	0.1

Gaussian noise). The complementary filters consist of two basic filters: a low pass filter (for filtering accelerometer data) and a high pass filter (for filtering gyroscope data). The signal is then passed to the controller gain, and the resultant values are serially sent to the plant model deployed in the LabVIEW simulator.

Pole placement gains and LQR controller showed better results, and the response observed from the motors with respect to variations in input was also satisfactory. The response of the PID controller to small changes was rather abrupt; after some manual adjustment of the derivative gain, the controller showed significant improvement. Table 5 shows the revised PID gains.

ATmega code to serially receive/send data from LabVIEW is developed (as shown in Figures 8 and 9).

Figure 10 shows the data obtained (without and with filter) from ATmega only as both controller strategies have shown identical responses.

6. Rapid Control Prototyping (RCP)

For the core of the quadcopter, i.e., the structure of the system, DJI 450 frame is selected to be used in the designed system. Propellers are responsible for propelling the quadcopter in the upward direction, and they consist of radiating blades with revolving hubs. The propellers selected for the frame are 1045. The correction factor from [27] is 1.45 (it is a unitless quantity).

The system's total weight is calculated by adding the values of different components used in the quadcopter (as given in Table 6). Here, the weight of motors, battery, and ESC is supposedly taken as an approximate value.

Force (upward exerted by the quadcopter) to weight is termed as thrust to weight ratio. It is calculated to estimate other requirements of the quadcopter. For the default chosen system, the weight from Table 6 is 1316 grams. Thus, its totally required thrust is the product of the desired thrust and the system's total weight. And for individual motors, the individual motor thrust is calculated by dividing the total thrust with total motors.

The motors' desired revolutions per minute (RPM) are computed using (24) [24] to calculate the motors and battery required for the system. The case of full throttle (i.e., motors running at the maximum possible speed) is considered to

ensure system durability. The quadcopter's already defined pitch, diameter, and desired thrust are used here. Battery voltage and capacity are taken to be 11.1 V and 5.2 A (ratings taken from the available batteries in the market). To estimate the motor RPM, the parameters of required thrust, propeller pitch, and diameter are used in the following equation:

$$\text{RPM} = \frac{2362.39}{P} \times \sqrt{\frac{(T \times D)/0.098102 \times \alpha^{1/3}}{(0.0254 \times D)^2 \times (D/(P * 3.29546))^{1.5}}}, \quad (21)$$

Here, T is the thrust generated by the quadcopter, D is the diameter of propellers, and P is the pitch (the distance the propeller would move forward in one rotation if it were moving through a soft solid).

Propellers are responsible for propelling the quadcopter in the upward direction, and they consist of radiating blades with a revolving hub. The propellers selected for the frame are 1045, so its dimensions are as follows: diameter is 10 inches, the pitch is 4.5 inches, and the correction factor from [27] is used to be 1.45 (unitless quantity).

Using (24) and putting the defined parameter values as required, the RPM value is 8281. In motors, the constant velocity is given by K_v and is measured by the number of RPMs that a motor turns when 1 V (one volt) is applied with no load attached to that motor [28].

Now, (21 and 22) are used to get the nominal battery voltage value of the required motor specs. Then, with respect to the estimated efficiency (in this scenario, according to the datasheet, it is taken as 0.8), the minimum required K_v of the motor is estimated to be 753, while the nominal K_v is 903.6.

$$K_{v_{\text{required}}} = \frac{\text{RPM}}{V_{\text{battery}}} = 753K_v, \quad (22)$$

$$K_{v_{\text{nominal}}} = K_{v_{\text{required}}} (1 + (1 - e)). \quad (23)$$

Here, $K_{v_{\text{required}}}$ is required K_v , $K_{v_{\text{nominal}}}$ is nominal K_v , V_{battery} is battery voltage, and e is efficiency.

The thrust force generation (electrical power for it) depends on the diameter and pitch of propellers and the estimated RPM of the motor. Thus, the electrical power consumption is estimated using Equation (23) to be 136 W. For nominal estimation, the efficiency is estimated to be 0.8,

TABLE 5: Gains from HIL testing.

Axis	K_p	K_i	K_d
ϕ	0.15	0.1	0.01
θ	0.15	0.1	0.01
ψ	0.15	0.1	0.01
Z-axis/altitude	0.75	1.5	0.1

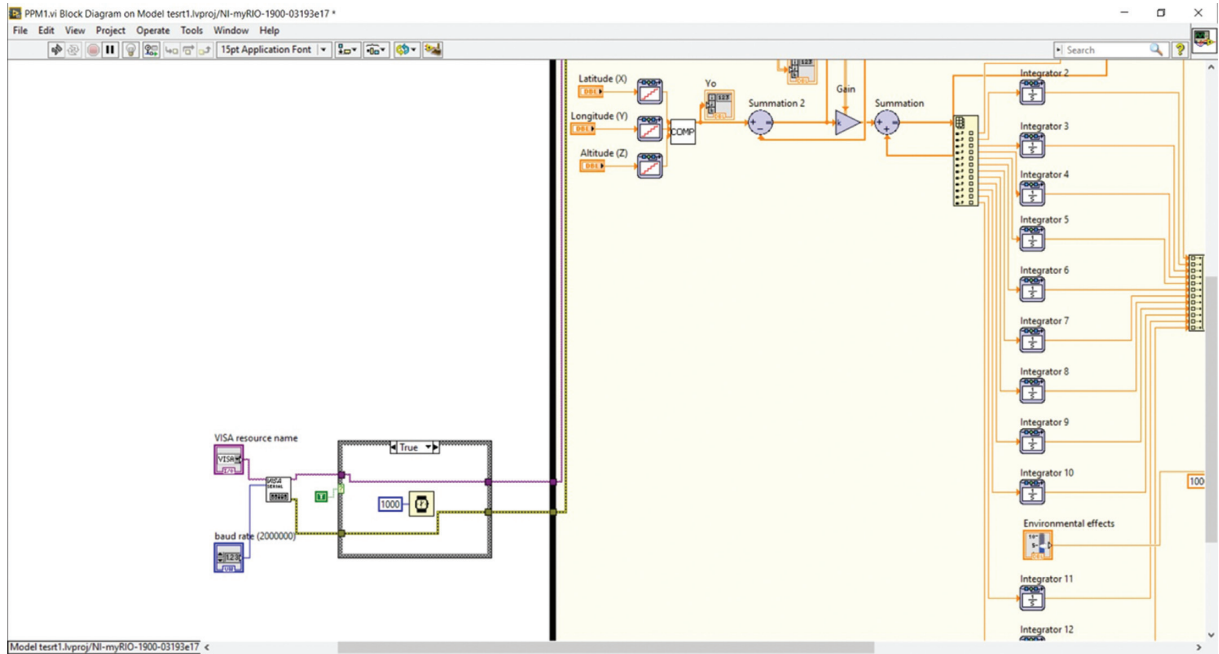


FIGURE 8: myRIO Serial Receiving Setup for ATmega Microcontroller.

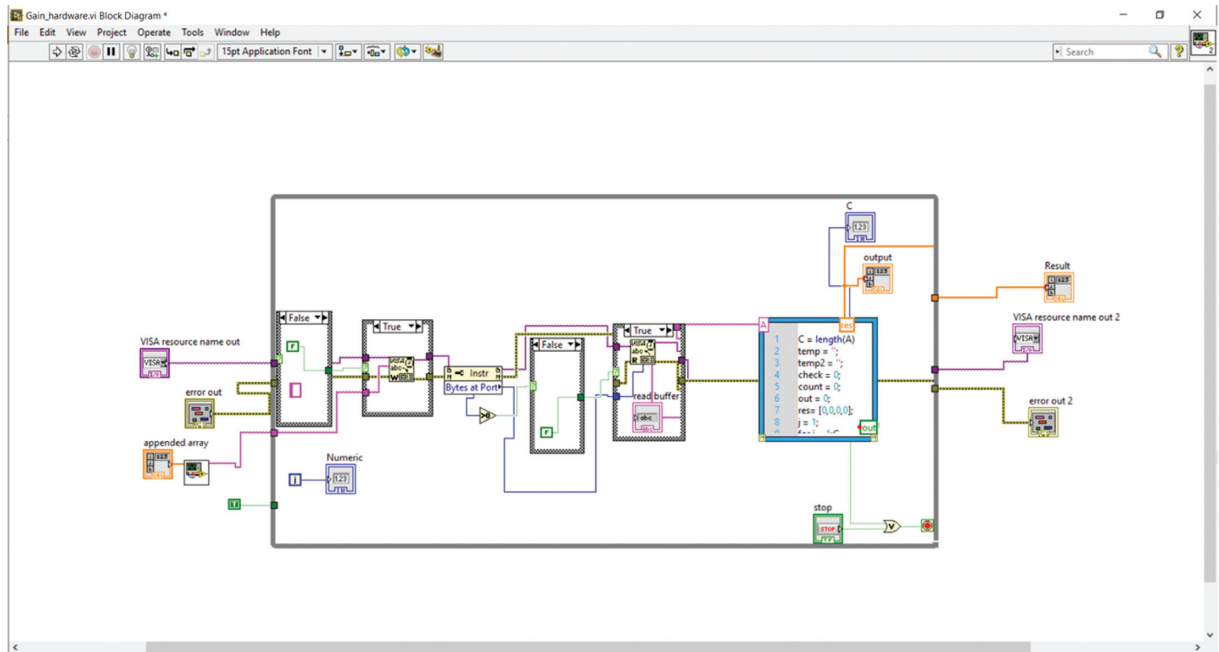


FIGURE 9: myRIO Serial Receiving and conversion from ASCII to Float Array.

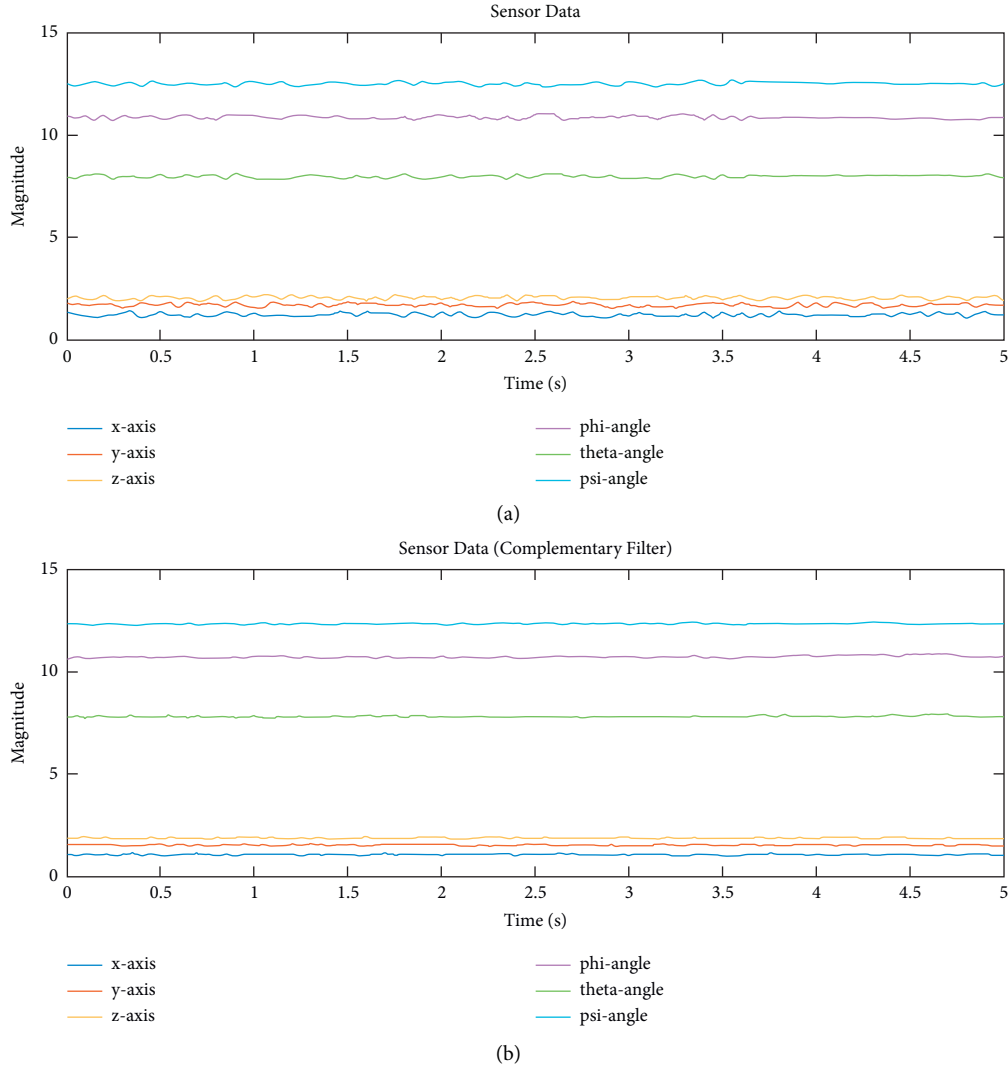


FIGURE 10: IMU Sensor Data on Inclined Surface with and without filter.

TABLE 6: System weight calculations.

Sr. no.	Parameter	Weight (grams)
1	Frame	282
2	Motor	75
3	ESC (α)	25
4	Battery	374
5	Miscellaneous (α)	260
Total		1316

which gives the desired power of 163.2 W. The required current for this system is estimated to be 18 A with an offset of 20%. Now, for the desired battery rating/discharge rate, (24) is used; it gives a rating of 14 C of discharge rate.

$$P_{\text{out}} = \frac{D^4 \times P \times \text{RPM}_{\text{required}}}{1.4 \times 10^{17}} \times 746. \quad (24)$$

Usually, a quadcopter starts to hover at 35–45% thrust of the total thrust generated by the motor. Updating the estimation in equations (20)–(28) shows that the new desired

power for the individual motor is approximately 4 A. System endurance depicts the amount of time a quadcopter can take flight and is calculated using equation (25). Estimated system endurance at full throttle is 4.16 minutes, while, in the hovering state, it is 15.6 minutes, thus giving an average flight time of around 9.88 minutes.

$$E = \frac{B_C \times e \times 60}{I_{\text{nominal}} \times 4}. \quad (25)$$

Here, e is endurance, B_C is battery capacity, and I_{nominal} is nominal current.

Considering the requirements and prototype availability in the local market, a 5200 mAh LiPo battery with 30C discharge rate, A2212 BLDC motor with specs given in Table 7, and ESCs of 30 A are used.

After calculating the required prototype specifications for the Inertial Measurement Unit (IMU), sensor GY-521 (Chinese variant of MPU-6050) is used. It has an accelerometer and gyroscope, is operable on 3.3–5V, and allows I2C communication. For GPS, Neo-M8N is selected; it offers an

TABLE 7: Summarized system.

Sr. no.	Parameter	Value	Value (weight)	Unit
1	Required RPM FT	8281	10985	RPM
2	Required kv FT	753	990	Kv
3	Required nom. kV FT	904	1188	Kv
4	<i>P_{out}</i> FT	136	318	W
5	<i>P_{in}</i> FT	163.2	380	RPM
6	Motor ampere	15	35	A
7	Required ESC	18	42	A
8	Battery rating	14	32.3	C
9	Endurance FT	4.16	1.78	Minutes
10	Required RPM H	5233	6947	RPM
11	<i>P_{out}</i> H	34.4	80.4	W
12	<i>P_{in}</i> H	41.28	96.4	W
13	Endurance H	15.6	9	Minutes
14	Flight time (average)	9.88	4.35	Minutes

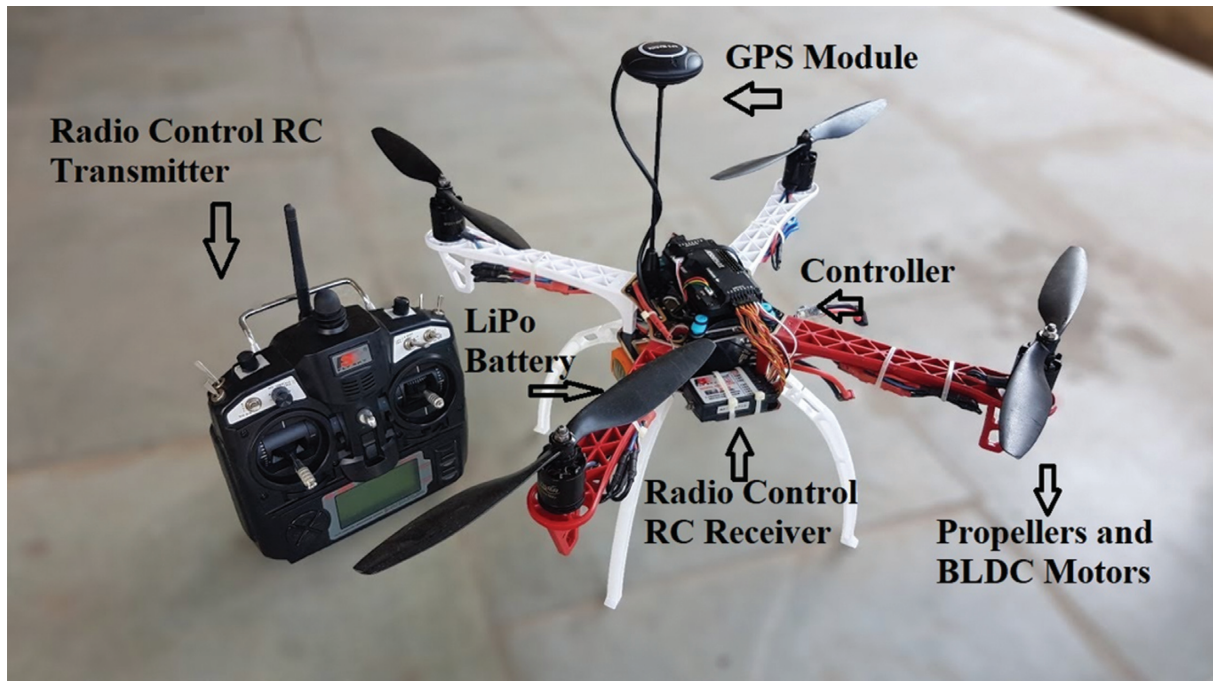


FIGURE 11: Assembled quadcopter prototype.

accuracy of 0.6–0.9 meters and supports a 10 Hz update rate; however, later, it was not deployed due to practical limitations. As for manual control of the quadcopter, Fly-Sky i6 is used with a TGY-iA6B receiver that supports six channels at 2.4 GHz and Pulse Position Modulation (PPM) data receiving. 2 Bluetooth (HC-05) devices are used in master-slave configuration to transmit data from the controller to the computer.

Figure 11 shows the assembled prototype with labeled hardware components. The assembled prototype is tested in two different conditions: initially in a room with constraints to minimize the possible damage, and then in an open environment for final testing. The quadcopter showed a stable response within the confined room, but results collection was quite tricky due to area limitations. Therefore, tests were conducted in the open area after some practice

and obtained relatively good results. Flight response in terms of attitude and position for around 70 seconds is shown in Figure 12.

The quadcopter took a stable takeoff and flew at low altitude; however, due to wind (the speed of the wind was around 10–14 km/h), the position of the quadcopter was not maintained. Still, due to robust orientation control, the quadcopter maintained its stability. Multiple flights are carried out to estimate battery drainage, and the average flight time, including takeoff and landing, was 9 minutes and 7 seconds, which is quite close to the estimated time.

Although there are several other prebuilt options available in the market (which are relatively way expensive), however, cost evaluation is done between the cheapest solutions available in the market to the proposed model. The calculations show that the proposed model is more than 25%

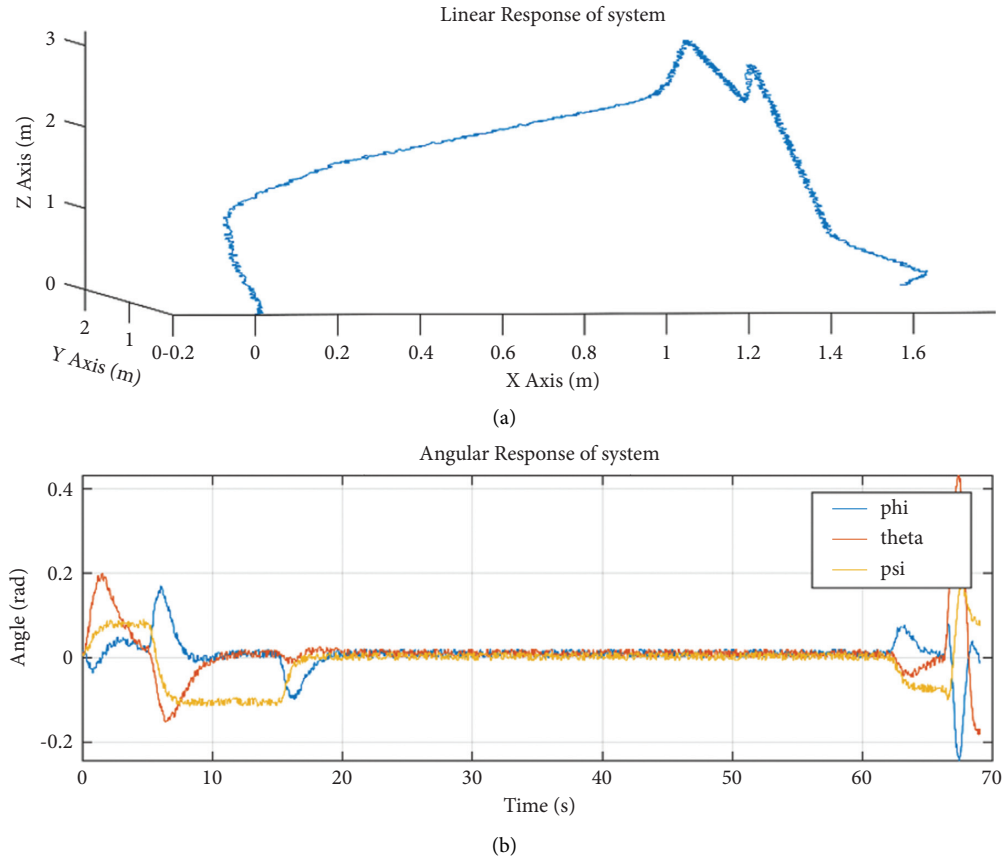


FIGURE 12: Prototype linear and angular response.

TABLE 8: Cost comparison.

Sr. no.	Component name	Price (PKR)	Prototype	Generic
1	DJI 450 frame	1700	Yes	Yes
2	Landing gear	1300	Yes	Yes
3	Fly-Sky Tx/Rx	10000	Yes	Yes
4	Pixhawk	10000	No	Yes
5	ATmega with PCB	800	Yes	No
6	GY-521	300	Yes	No
7	ESCs (4)	3200	Yes	Yes
8	Motors and propellers (4)	4400	Yes	Yes
9	Battery Li-Po	4500	Yes	Yes
Total			26200	35100

less expensive than the most affordable solution available in the market; details are given in the next section.

7. Computational Complexity and Cost Analysis

The computational cost analysis is done on the code by analyzing the function calls on different operations. The base initialization of parameters is considered constant c , thus making its complexity to $O(n)$; after that, receiving data from IMU and Rx (ground transceiver) also has the complexity of $O(n)$. However, the control and stabilization part has double nested loops, thus increasing the complexity to $O(n^2)$, making the overall operation complexity $O(n^2)$. As

for cost analysis, Table 8 gives a detailed cost analysis of the system, where the prototype costs PKR 26,200, and the generic model costs around PKR 35100. The professionally developed systems sold in the market cost from PKR 70,000 to PKR 200,000.

8. Conclusion

A cost-effective end-to-end quadcopter design, development, and validation framework is presented using model-based design, HIL testing, and a rapid control prototyping approach. Firstly, a mathematical model of the dynamic behavior of the quadcopter is developed, and PID, LQR, and

full state feedback controllers are designed and compared. Moreover, Lyapunov stability analysis, SIL, PIL, and HIL testing are performed to evaluate the stability of all the controllers. The LQR controller showed an accuracy of 94% with the limitation of a simple path. The accuracy decreased for abrupt path proving the validity of the designed model. Finally, the RCP approach has been used to implement a prototype and test the stability under different real-time scenarios. The developed POC prototype quadcopter took a stable flight and proved the idea of an affordable quadcopter design approach. It is concluded that the proposed framework and design approach can be employed with low-cost components and different design parameters for various quadcopter use cases and applications.

Future work includes a ground control station for the autonomous operation of the quadcopter to enable additional features like preflight planning, real-time flight observation, and data collection from onboard sensors during the flight.

Data Availability

No external data is used in this work.

Conflicts of Interest

The authors declare no conflicts of interest in preparing this paper.

Acknowledgments

This research was funded by Higher Education Commission Pakistan, grant number NRPU-5939.

References

- [1] S. T. Elliott and T. W. Carr, "Robust nonlinear control of BLDC motor in quadcopter applications," *American Journal of Undergraduate Research*, vol. 12, no. 2, 2016.
- [2] H. Menouar, I. Guvenc, K. Akkaya, A. S. Ulugac, A. Kadri, and A. Tuncer, "UAV-enabled intelligent transportation systems for the smart city: applications and challenges," *IEEE Communications Magazine*, vol. 55, no. 3, pp. 22–28, 2017.
- [3] A. Intwala and Y. Parikh, "A review on vertical take off and landing (vtol) vehicles," *International Journal of Innovative Research in Advanced Engineering (IJIRAE)*, vol. 2, no. 2, pp. 187–191, 2015.
- [4] V. Praveen and S. Pillai, "Modeling and simulation of quadcopter using PID controller," *International Journal of Control Theory and Applications*, vol. 9, no. 15, pp. 7151–7158, 2016.
- [5] A. Zenkin, I. Berman, K. Pachkouski, I. Pantiukhin, and V. Rzhvskiy, "Quadcopter simulation model for research of monitoring tasks," in *Proceedings of the 2020 Twenty Sixth Conference of Open Innovations Association (FRUCT)*, pp. 449–457, IEEE, Yaroslavl, Russia, April 2020.
- [6] H. Mo and G. Farid, "Nonlinear and adaptive intelligent control techniques for quadrotor UAV - a survey," *Asian Journal of Control*, vol. 21, no. 2, pp. 989–1008, 2019.
- [7] Y. Wang, A. Ramirez-Jaime, F. Xu, and V. Puig, "Nonlinear model predictive control with constraint satisfactions for a quadcopter," in *Journal of Physics: Conference Series* vol. 783, no. 1, IOP Publishing, Article ID 12025, 2017.
- [8] Z. Samadikhoshkho, S. Ghorbani, and F. Janabi-Sharifi, "Modeling and control of aerial continuum manipulation systems: a flying continuum robot paradigm," *IEEE Access*, vol. 8, Article ID 176883, 2020.
- [9] G. Feng, "A survey on analysis and design of model-based fuzzy control systems," *IEEE Transactions on Fuzzy Systems*, vol. 14, no. 5, pp. 676–697, 2006.
- [10] P. Wang, Z. Man, Z. Cao, J. Zheng, and Y. Zhao, "Dynamics modelling and linear control of quadcopter," in *Proceedings of the 2016 International Conference on Advanced Mechatronic Systems (ICAMEchS)*, pp. 498–503, IEEE, Melbourne, Australia, December 2016.
- [11] M. Alhaddad, M. Tyupkin, and L. Aeshina, "Modeling and attitude control OF a quadcopter using linear quadratic regulator," vol. 15, pp. 173–176, 2016.
- [12] M. Agha, K. Kanistras, M. J. Rutherford, and K. P. Valavanis, "Mathematical model derivation of an unmanned circulation control aerial vehicle UC2AV," *Control Theory and Technology*, vol. 18, no. 1, pp. 1–18, 2020.
- [13] F. Sharifi, M. Mirzaei, B. W. Gordon, and Y. Zhang, "Fault tolerant control of a quadrotor UAV using sliding mode control," in *Proceedings of the 2010 Conference on Control and Fault-Tolerant Systems (SysTol)*, pp. 239–244, IEEE, Nice, France, October 2010.
- [14] R. B. Anderson, J. A. Marshall, and A. L'Afflitto, "Constrained robust model reference adaptive control of a tilt-rotor quadcopter pulling an unmodeled cart," *IEEE Transactions on Aerospace and Electronic Systems*, vol. 57, no. 1, pp. 39–54, 2021.
- [15] S. Nekoo Rafee, J. Ángel Acosta, G. Heredia, and A. Ollero, "A benchmark mechatronics platform to assess the inspection around pipes with variable pitch quadrotor for industrial sites," *Mechatronics*, vol. 79, Article ID 102641, 2021.
- [16] R. Kumar, A. M. Deshpande, J. Z. Wells, and M. Kumar, "Flight Control of Sliding Arm Quadcopter with Dynamic Structural Parameters," in *Proceedings of the 2020 IEEE/R SJ International Conference on Intelligent Robots and Systems (IROS)*, pp. 1358–1363, Las Vegas, NV, USA, January 2020.
- [17] D. Gheorghiuță, I. Vintu, L. Mîrea, and C. . Brăescu, "Quadcopter control system," in *Proceedings of the 2015 Nineteenth International Conference on System Theory, Control and Computing (ICSTCC)*, pp. 421–426, IEEE, Cheile Gradistei, Romania, October 2015.
- [18] A. Irfan, M. Gufran Khan, and S. Ali Mohsin, "Quadcopter dynamic modeling and stability control design using hardware in loop," in *Proceedings of the Accepted to IEEE International Conference on Robotics, Automation, Artificial-Intelligence and Internet-Of-Things (RAAICON)*, Dhaka, Bangladesh, December 2021.
- [19] E. Paiva, J. Soto, J. Salinas, and W. Ipanaque, "Modeling, simulation and implementation of a modified PID controller for stabilizing a quadcopter," in *Proceedings of the 2016 IEEE International Conference on Automatica (ICA-ACCA)*, pp. 1–6, IEEE, Curico, Chile, October 2016.
- [20] D. Sikeridis, E. E. Tsiropoulou, M. Devetsikiotis, and S. Papavassiliou, "Wireless powered Public Safety IoT: a UAV-assisted adaptive-learning approach towards energy efficiency," *Journal of Network and Computer Applications*, vol. 123, pp. 69–79, 2018.
- [21] A. Nagaty, S. Saeedi, C. Thibault, M. Seto, and H. Li, "Control and navigation framework for quadrotor helicopters," *Journal of Intelligent & Robotic Systems*, vol. 70, no. 1, pp. 1–12, 2013.

- [22] T. Luukkonen, "Modelling and control of quadcopter." Independent research project in applied mathematics," *Espoo*, vol. 22, p. 22, 2011.
- [23] E. Vinodh Kumar and J. Jerome, "Robust LQR controller design for stabilizing and trajectory tracking of inverted pendulum," *Procedia Engineering*, vol. 64, pp. 169–178, 2013.
- [24] J.-S. Song and X.-H. Chang, "H ∞ controller design of networked control systems with a new quantization structure," *Applied Mathematics and Computation*, vol. 376, Article ID 125070, 2020.
- [25] M. Aoki, *State Space Modeling of Time Series*, Springer Science & Business Media, Berlin, Germany, 2013.
- [26] D. E. Rivera, M. Morari, and S. Skogestad, "Internal model control: PID controller design," *Industrial and Engineering Chemistry Process Design and Development*, vol. 25, no. 1, pp. 252–265, 1986.
- [27] Singfaye, "Aircraft Propeller Calculator," Singfaye.co.uk, 2020, <http://singfaye.co.uk/docs/e9d2ca-aircraft-propeller-calculator>.
- [28] RotorDrone, "Understanding Kv Ratings - RotorDrone," RotorDrone, 2020, <https://www.rotordronepro.com/understanding-kv-ratings/>.

Research Article

Event-Triggered Adaptive Dynamic Programming Consensus Tracking Control for Discrete-Time Multiagent Systems

Yuyang Zhao,¹ Xiaolin Dai,¹ Dawei Gong,¹ Xinzhi Lv,² and Yang Liu ¹

¹School of Mechanical and Electrical Engineering, University of Electronic Science and Technology of China, Chengdu 611731, China

²Science and Technology on Reactor System Design Technology Laboratory, Nuclear Power Institute of China, Chengdu 610213, China

Correspondence should be addressed to Yang Liu; ly2015@uestc.edu.cn

Received 17 December 2021; Revised 11 January 2022; Accepted 17 January 2022; Published 1 March 2022

Academic Editor: Chao Zeng

Copyright © 2022 Yuyang Zhao et al. This is an open access article distributed under the Creative Commons Attribution License, which permits unrestricted use, distribution, and reproduction in any medium, provided the original work is properly cited.

This paper proposes a novel adaptive dynamic programming (ADP) approach to address the optimal consensus control problem for discrete-time multiagent systems (MASs). Compared with the traditional optimal control algorithms for MASs, the proposed algorithm is designed on the basis of the event-triggered scheme which can save the communication and computation resources. First, the consensus tracking problem is transferred into the input-state stable (ISS) problem. Based on this, the event-triggered condition for each agent is designed and the event-triggered ADP is presented. Second, neural networks are introduced to simplify the application of the proposed algorithm. Third, the stability analysis of the MASs under the event-triggered conditions is provided and the estimate errors of the neural networks' weights are also proved to be ultimately uniformly bounded. Finally, the simulation results demonstrate the effectiveness of the event-triggered ADP consensus control method.

1. Introduction

Because of the wide applications in the control field [1–6], the consensus control of MASs gained more and more attentions. In recent years, quite a few methods have been reported to solve the consensus control problem of MASs, such as adaptive control [7, 8] and sliding mode control [9, 10]. It is worth mentioning that the previous methods focus on the stability of the MASs. However, the optimal characteristic is also worth considering in the consensus control problem. Optimal consensus control problem aims to find the optimal control policies which guarantee the stability of MASs and minimize the energy cost. As one of the core methods to achieve the optimal control policies, ADP approaches address the issue abovementioned by approximating the solutions of Hamilton–Jacobi–Bellman (HJB) equation [11–13].

Till now, ADP approaches have been applied in the optimal consensus control of MASs [14–20]. In [14], an optimal coordination control algorithm has been designed

to address the consensus problem of the multiagent differential games through fuzzy ADP. The optimal output heterogeneous MASs was considered in [15]. Based on this work, Gao et al. [16] considered the dynamic uncertainties factor in the cooperative output regulation problems. Zhang et al. [17, 18] considered the optimal consensus tracking control for discrete-time/continuous-time MASs. In order to address the optimal consensus problem for unknown MASs with input delay, the authors proposed a data-driven disturbed adaptive controller based on ADP technique in [19]. In [20], the problem of data-based optimal consensus control was studied for MASs with multiple time delays. All the above results are based on the assumption that the communication and computing resources are big enough to transmit system data and update the control policy in every time step. However, it is difficult to be satisfied in practice.

Event-triggered control (ETC) is a well-recognized technology to address the above issue [21–24]. Different from the time-triggered control, whether the systems sample the signals or not only depends on the event-triggered

condition. If it is satisfied at some time instants, then the data will be transmitted and the control policy will be updated. Therefore, compared with the control algorithms based on time-triggered scheme, the event-trigger control algorithms can efficiently save the computation resources [25]. In the past years, ETC is introduced to solve the optimal control problem under the limited computing resources [26–29]. In [26], an ETC method based on ADP is developed for continuous-time MASs. The authors considered the unknown internal states factor in the event-triggered optimal control for continuous-time MASs in [27]. The multiplayer zero-sum differential games are considered in [28] and an optimal consensus tracking control based on event-triggered is designed to solve this problem. In [29], an event-triggered optimal control algorithm is designed for unmatched uncertain nonlinear continuous-time systems. In [30], to save the limited network resources, an event-triggered mechanism was introduced to address the consensus problem of linear discrete-time MASs. The authors considered the event-triggered consensus problem of discrete-time multi-agent networks in [31]. It is worthy to say, all the results in [26–29] studied the event-triggered optimal control for continuous-time MASs, but there were few works [30, 31] which consider the discrete-time MASs.

Motivated by the above discussions, an event-triggered ADP control algorithm is designed to address the optimal consensus tracking problem for discrete-time MASs. The major contributions of this paper are emphasized as follows:

- (1) Comparing with the existing event-triggered ADP consensus control methods [27–29], we design the adaptive ET condition for every agent in the MASs. Then, the agent samples the data and communicates with the neighbors only when its event-triggered condition is satisfied. That means the agents in the MASs may not communicate with their neighbors or update their control policies at the same time instant, and then, the communicate resources are saved.
- (2) In this paper, we give the stability analysis for the MASs under the event-triggered condition. It shows all agents in the discrete-time MASs will achieve consensus under the ET condition. And, we also prove the weight estimate errors for the critic neural networks (NNs) and actor NNs are uniformly ultimately bounded during the learning process.

The rest of this paper is organized as follows. In Section 2, the discrete-time MASs are considered and the consensus problem is formed. The event-triggered conditions for each agent in the system are introduced and the stability analysis

is given in Section 3. Then, NN-based event-triggered ADP algorithm is introduced in Section 4, and the simulation results of this algorithm are given in Section 5. Finally, the conclusions are shown in Section 6.

2. Problem Formation

Consider the discrete-time MASs:

$$\mathbf{x}_i(k+1) = \mathbf{A}\mathbf{x}_i(k) + \mathbf{B}_i\mathbf{u}_i(k), \quad (1)$$

where $\mathbf{x}_i(k) \in R^{n \times 1}$ and $\mathbf{u}_i(k) \in R^{m_i \times 1}$ denote the state and the coordination control of agent $i, i = 1, 2, \dots, N$, respectively. $\mathbf{A} \in R^{n \times n}$ and $\mathbf{B}_i \in R^{n \times m_i}$ are the constant matrices.

The leader's dynamics function is defined as

$$\mathbf{x}_0(k+1) = \mathbf{A}\mathbf{x}_0(k), \quad (2)$$

where $\mathbf{x}_0(k) \in R^n$ denotes the state of the leader.

The local neighbor consensus tracking error ξ_i is defined as

$$\xi_i(k) = \sum_{j \in \mathcal{N}_i} \alpha_{ij}(\mathbf{x}_i(k) - \mathbf{x}_j(k)) + \beta_i(\mathbf{x}_i(k) - \mathbf{x}_0(k)). \quad (3)$$

where α_{ij} denotes the adjacency elements, $\alpha_{ij} > 0$ if agent i can communicate with agent j , otherwise, $\alpha_{ij} = 0$, and β_i denotes the pinning gain, $\beta_i > 0$, if agent i can communicate with the leader, otherwise, $\beta_i = 0$. We assume that there is at least one agent who can get the information from the leader.

Under the event-triggered scheme, the discrete-time MASs transmit the systems' data only when the event is triggered. Here, we define that the event is triggered at the discrete-time instants' sequence $k_{i,1}, k_{i,2}, \dots, k_{i,p-1}, k_{i,p}$, for $i = 1, 2, \dots, N$ and $p = 1, 2, \dots, \infty$. At the p th event-triggered instant of agent i , the consensus errors of agent i denote as $\tilde{\xi}_i(k_{i,p}) = \sum_{j \in \mathcal{N}_i} \alpha_{ij}(\mathbf{x}_i(k_{i,p}) - \mathbf{x}_j(k_{j,q})) + \beta_i(\mathbf{x}_i(k_{i,p}) - \mathbf{x}_0(k_{i,p}))$.

The event-triggered error is defined as

$$\delta(k) = \tilde{\xi}_i(k_{i,p}) - \xi_i(k), \quad (4)$$

which means the difference between the consensus tracking errors at the p th event-triggered instant and the current local neighbor consensus tracking errors.

Then, the consensus problem of the discrete-time MASs is to find the distributed feedback control law, $\mathbf{u}_i(k) = \chi(\tilde{\xi}_i(k_{i,p}))$, which becomes a continuous signal through a zero-order hold (ZOH) device when $k_{i,p} \leq k < k_{i,p+1}$.

Then, the local cost function is defined as

$$\begin{aligned} J_i(\xi_i(k), u_i(k), u_j(k)) &= \sum_{l=k}^{\infty} \rho^{l-k} U_i(\xi_i(l), u_i(l), u_j(l)) \\ &= U_i(\xi_i(k), u_i(k), u_j(k)) + \rho J_i(\xi_i(k+1), u_i(k+1), u_j(k+1)), \end{aligned} \quad (5)$$

where

(i) $U_i(\xi_i(k), \mathbf{u}_i(k), \mathbf{u}_j(k))$: the utility function, for agent i ,

$$U_i(\xi_i(k), \mathbf{u}_i(k), \mathbf{u}_j(k)) = \xi_i^T(k) \mathbf{Q}_{ii} \xi_i(k) + \mathbf{u}_i^T(k) \mathbf{R}_{ii} \mathbf{u}_i(k) + \sum_{j \in \mathcal{N}_i} \mathbf{u}_j^T(k) \mathbf{S}_{ij} \mathbf{u}_j(k). \quad (6)$$

(ii) $\mathbf{u}_j(k)$: the control of the neighbors of agent i .

(iii) \mathbf{Q}_{ii} , \mathbf{R}_{ii} , and \mathbf{S}_{ij} : positive symmetric weighting matrices.

(iv) p : the discount factor, $0 < p \leq 1$.

According to Bellman's principle, the optimal local cost function $J_i^*(\xi_i(k), \mathbf{u}_i(k), \mathbf{u}_j(k))$ can be defined as

$$J_i^*(\xi_i(k), \mathbf{u}_i(k), \mathbf{u}_j(k)) = \min_{\mathbf{u}_i(\xi_i(k_{i,p}))} \left\{ U_i(\xi_i(k), \mathbf{u}_i(k), \mathbf{u}_j(k)) + \rho J_i^*(\xi_i(k+1), \mathbf{u}_i(k+1), \mathbf{u}_j(k+1)) \right\}, \quad (7)$$

which is also called discrete-time HJB equations.

The optimal disturbed control law $\mathbf{u}_i^*(\xi_i(k_{i,p}))$ is defined as

$$\mathbf{u}_i^*(\xi_i(k_{i,p})) = \arg \min_{\mathbf{u}_i(\xi_i(k_{i,p}))} \left\{ U_i(\xi_i(k), \mathbf{u}_i(k), \mathbf{u}_j(k)) + \rho J_i^*(\xi_i(k+1), \mathbf{u}_i(k+1), \mathbf{u}_j(k+1)) \right\}. \quad (8)$$

3. Stability Analysis

Assumption 1 (see [32]). There exist positive constants L , L_1 , ϕ , and ψ , a C^1 function $V: \mathbb{R}^n \rightarrow \mathbb{R} \geq 0$, and class κ_∞ functions γ_1 and γ_2 , such that

$$\|\mathbf{A}\| \leq L, \|\mathbf{B}\| \leq L, \|\chi(\xi_i(k) + \delta(k))\| \leq L \|\widehat{\xi}_i(k_{i,p})\|, \quad (9)$$

$$\gamma_1(\|\mathbf{x}\|) \leq V(\mathbf{x}(k)) \leq \gamma_2(\|\mathbf{x}\|) \forall \mathbf{x} \in \mathbb{R}^n, \quad (10)$$

$$V(\mathbf{A}\mathbf{x}_i(k) + \mathbf{B}_i\chi(\xi_i(k) + \delta(k))) - V(\mathbf{x}_i(k)) \leq -\phi V(\mathbf{x}_i(k)) + \psi \|\delta(k)\|. \quad (11)$$

If (10) and (11) are satisfied, function V is called an ISS-Lyapunov function for the discrete-time MAS.

Let us consider a situation that $k \in [k_{i,p}, k_{i,p+1})$, which means that the ET condition is satisfied at the sampling instant $k_{i,p}$. In this situation, it is obvious that $\delta_{i,p}(k+1) = \widehat{\xi}_i(k_{i,p}) - \xi_i(k+1)$. Then, we have

$$\|\delta(k+1)\| \leq \|\widehat{\xi}_i(k_{i,p})\| + \|\xi_i(k+1)\|. \quad (12)$$

Substituting (1) and (2) into (3), we have

$$\begin{aligned} \xi_i(k+1) &= \sum_{j \in \mathcal{N}_i} \alpha_{ij} (\mathbf{A}(\mathbf{x}_i(k) - \mathbf{x}_j(k)) + \mathbf{B}_i \mathbf{u}_i(k) - \mathbf{B}_j \mathbf{u}_j(k)) + \beta_i (\mathbf{A}(\mathbf{x}_i(k) - \mathbf{x}_0(k)) + \mathbf{B}_i \mathbf{u}_i(k)) \\ &= \mathbf{A} \xi_i(k) + \sum_{j \in \mathcal{N}_i} \alpha_{ij} (\mathbf{B}_i \mathbf{u}_i(k) - \mathbf{B}_j \mathbf{u}_j(k)) + \beta_i \mathbf{B}_i \mathbf{u}_i(k). \end{aligned} \quad (13)$$

Then, we can have

$$\begin{aligned}
\|\xi_i(k+1)\| &\leq \|A\|\|\xi_i(k)\| + \sum_{j \in \mathcal{N}_i} \alpha_{ij} \left\| (\mathbf{B}_i \mathbf{u}_i(k) - \mathbf{B}_j \mathbf{u}_j(k)) \right\| + \beta_i \|\mathbf{B}_i \mathbf{u}_i(k)\| \\
&\leq \|A\|\|\xi_i(k)\| + \sum_{j \in \mathcal{N}_i} \alpha_{ij} \left\| (\mathbf{B}_i \mathbf{u}_i(k) - \mathbf{B}_j \mathbf{u}_j(k)) \right\| + \beta_i \|\mathbf{B}_i \mathbf{u}_i(k)\| \\
&\leq \|A\|\|\xi_i(k)\| + \sum_{j \in \mathcal{N}_i} \alpha_{ij} \left(\|\mathbf{B}_i \mathbf{u}_i(k)\| + \|\mathbf{B}_j \mathbf{u}_j(k)\| \right) + \beta_i \|\mathbf{B}_i \mathbf{u}_i(k)\|.
\end{aligned} \tag{14}$$

Substituting (9) into (14), we have

$$\begin{aligned}
\|\xi_i(k+1)\| &\leq \|A\|\|\xi_i(k)\| + \sum_{j \in \mathcal{N}_i} \alpha_{ij} \left(\|\mathbf{B}_i \mathbf{u}_i(k)\| + \|\mathbf{B}_j \mathbf{u}_j(k)\| \right) + \beta_i L \|\mathbf{u}_i(k)\| \\
&\leq L \|\xi_i(k)\| + L \sum_{j \in \mathcal{N}_i} \alpha_{ij} \left(\|\mathbf{u}_j(k)\| + \|\mathbf{u}_i(k)\| \right) + \beta_i L \|\mathbf{u}_i(k)\| \\
&\leq L \|\xi_i(k)\| + L \sum_{j \in \mathcal{N}_i} \alpha_{ij} \left(\|\mathbf{u}_j(k)\| + L \|\tilde{\xi}_i(k_{i,p})\| \right) + \beta_i L^2 \|\tilde{\xi}_i(k_{i,p})\|.
\end{aligned} \tag{15}$$

Therefore,

$$\begin{aligned}
\|\delta(k)\| &\leq \|\tilde{\xi}_i(k_{i,p})\| + \|\xi_i(k-1)\| \leq \|\tilde{\xi}_i(k_{i,p})\| + L \|\xi_i(k-1)\| \\
&\quad + L \sum_{j \in \mathcal{N}_i} \alpha_{ij} \left(\|\mathbf{u}_j(k)\| + L \|\tilde{\xi}_i(k_{i,p})\| \right) + \beta_i L^2 \|\tilde{\xi}_i(k_{i,p})\| \\
&= \|\tilde{\xi}_i(k_{i,p})\| + \beta_i L^2 \|\tilde{\xi}_i(k_{i,p})\| + L \sum_{j \in \mathcal{N}_i} \alpha_{ij} \left(\|\mathbf{u}_j(k)\| + L \|\tilde{\xi}_i(k_{i,p})\| \right) \\
&\quad + L \|\xi_i(k-1)\| \leq (1 + \beta_i L^2) \|\tilde{\xi}_i(k_{i,p})\| + L \sum_{j \in \mathcal{N}_i} \alpha_{ij} \left(\|\mathbf{u}_j(k)\| + L \|\tilde{\xi}_i(k_{i,p})\| \right) \\
&\quad + L \left(L \|\xi_i(k-2)\| + L \sum_{j \in \mathcal{N}_i} \alpha_{ij} \left(\|\mathbf{u}_j(k)\| + L \|\tilde{\xi}_i(k_{i,p})\| \right) + \beta_i L^2 \|\tilde{\xi}_i(k_{i,p})\| \right) \\
&\dots \leq (1 + \beta_i L^2 + \beta_i L^3 + \dots + \beta_i L^{k-k_{i,p}+1}) \|\tilde{\xi}_i(k_{i,p})\| \\
&\quad + (1 + L + \dots + L^{k-k_{i,p}-1}) L \sum_{j \in \mathcal{N}_i} \alpha_{ij} \left(\|\mathbf{u}_j(k)\| + L \|\tilde{\xi}_i(k_{i,p})\| \right) + L^{k-k_{i,p}} \|\tilde{\xi}_i(k_{i,p})\|.
\end{aligned} \tag{16}$$

Then, we can rewrite the ET condition as

$$\begin{aligned}
\|\delta_{i,p}(k)\| &\leq \delta_{iT} = (1 + L^{k-k_{i,p}}) \|\tilde{\xi}_i(k_{i,p})\| + \beta_i \frac{L^2(1 - L^{k-k_{i,p}})}{1 - L} \|\tilde{\xi}_i(k_{i,p})\| \\
&\quad + L \frac{1 - L^{k-k_{i,p}}}{1 - L} \sum_{j \in \mathcal{N}_i} \alpha_{ij} \left(\|\mathbf{u}_j(k)\| + L \|\tilde{\xi}_i(k_{i,p})\| \right),
\end{aligned} \tag{17}$$

for every $k \in [k_{i,p}, k_{i,p+1})$.

To better illustrate the control process, a flowchart has been displayed in Figure 1. The transmitted data and control policies are updated at $k_{i,p}$ instant, and the event-triggered error is reset to zero. Once the event-triggered condition is satisfied, the current instant becomes the next triggering instant $k_{i,p+1}$, and the system data are transmitted.

Otherwise, keep the transmitted data and control policies unchanged.

Then, we will prove the discrete-time MAS is stable under our event-triggered conditions.

Theorem 1. *If a discrete-time MASs which is under assumption 1 and satisfies the function,*

$$V(\mathbf{x}(k)) \leq V(\mathbf{x}(k_{i,p+1})) = -\varphi\phi V(\mathbf{x}(k_{i,p})) + \psi V(\mathbf{x}(k_{i,p})), \quad (18)$$

for every $k \in [k_{i,p}, k_{i,p+1})$, where $\varphi \in (0, 1)$, then the system is asymptotically stable.

$$V(\mathbf{A}\mathbf{x}_i(k) + \mathbf{B}_i\chi(\xi_i(k) + \delta(k))) \leq (1 - \phi)V(\mathbf{x}_i(k)) + \psi\|\delta(k)\|. \quad (19)$$

Proof. According to (9) and (11), we obtain

Then, applying (18) into (19), we have

$$\begin{aligned} V(\mathbf{A}\mathbf{x}_i(k) + \mathbf{B}_i\chi(\xi_i(k) + \delta(k))) &\leq (1 - \phi)V(\mathbf{x}_i(k)) + \psi\delta(k) \\ &\leq (1 - \phi)V(\mathbf{x}_i(k)) + \psi \left(\left(1 + L^{k-k_{i,p}} + \beta_i \frac{L^2(1-L^{k-k_{i,p}})}{1-L} \right) \|\tilde{\xi}_i(k_{i,p})\| \right. \\ &\quad \left. + L \frac{1-L^{k-k_{i,p}}}{1-L} \sum_{j \in \mathcal{N}_i} \alpha_{ij} (\|\mathbf{u}_j(k)\| + L \|\tilde{\xi}_i(k_{i,p})\|) \right). \end{aligned} \quad (20)$$

Solving (20), we can obtain

$$\begin{aligned} V(\mathbf{A}\mathbf{x}_i(k) + \mathbf{B}_i\chi(\xi_i(k) + \delta(k))) &\leq (1 - \phi)^{k-k_{i,p}} V(\mathbf{x}_i(k_{i,p})) \\ &\quad + \psi \frac{1 - (1 - \phi)^{k-k_{i,p}}}{\phi} \left(\left(1 + L^{k-k_{i,p}} + \beta_i \frac{L^2(1-L^{k-k_{i,p}})}{1-L} \right) \|\tilde{\xi}_i(k_{i,p})\| \right. \\ &\quad \left. + L \frac{1-L^{k-k_{i,p}}}{1-L} \sum_{j \in \mathcal{N}_i} \alpha_{ij} (\|\mathbf{u}_j(k)\| + L \|\tilde{\xi}_i(k_{i,p})\|) \right). \end{aligned} \quad (21)$$

We define a function as

$$F(\mathbf{x}(k)) = -\varphi\phi V(\mathbf{x}(k_{i,p})) + \psi V(\mathbf{x}(k_{i,p})), \quad \forall k \in [k_{i,p}, k_{i,p+1}). \quad (22)$$

According to (18), we have

$$V(\mathbf{x}(k)) \leq F(\mathbf{x}(k)), \quad (23)$$

for every $k \in [k_{i,p}, k_{i,p+1})$.

From (22), we obtain

$$\Delta F = F(\mathbf{x}(k+1)) - F(\mathbf{x}(k)) = -\varphi\phi V(\mathbf{x}(k_{i,p})). \quad (24)$$

Applying (9) into (24), we have

$$\Delta F \leq -\varphi\phi\gamma_1 \|\mathbf{x}(k_{i,p})\| \forall k \in [k_{i,p}, k_{i,p+1}). \quad (25)$$

Since (23) and (25) hold, the stability of the discrete-time MAS is proved. \square

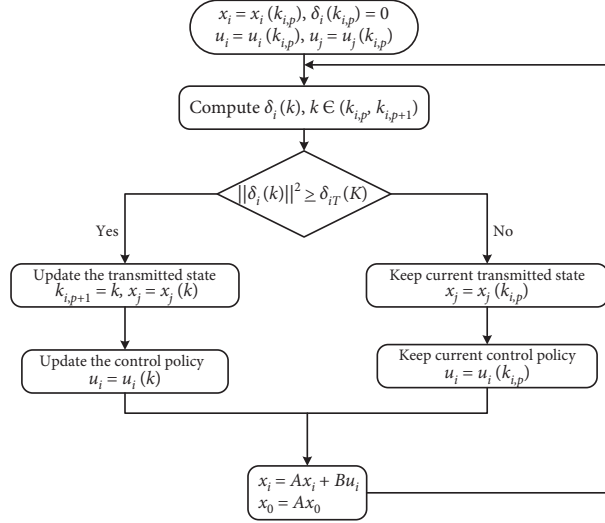


FIGURE 1: The flowchart of the event-triggered consensus control algorithm.

Remark 1. We give the event-triggered condition for each agent in the discrete-time MASs. Moreover, the stability of the systems is also proved in this paper.

4. Event-Triggered Controller Design

In this section, considering the good fitting characteristics of the neural networks (NN) [33, 34], the actor-critic neural network structure is introduced to approximate the local cost function $J_i(\xi_i(k), u_i(k), u_j(k))$ and the distributed feedback control law $u_i(x)$. The actor-critic NNs are defined as

$$\widehat{\mathcal{F}}(\omega, z, w) = \omega^T \Psi(w^T z) = \omega^T \Psi(Z), \quad (26)$$

where z denotes the input data, $\Psi(\cdot)$ denotes the activation functions, and w and ω denote the weight matrices of the NNs.

4.1. Formulation of the Critic Networks. The critic NN approximates the local cost function $J_i(\xi_i(k), u_i(k), u_j(k))$ in this paper as follows:

$$\widehat{V}_i(k) = \widehat{\omega}_{ci}^T \Psi_{ci}(\widehat{w}_{ci}^T z_{ci}(k)), \quad (27)$$

where $z_{ci}(k)$ denotes the input vector of the critic NN which is constituted by $\xi_i(k)$, $u_i(k)$, and $u_{\mathcal{N}(i)}(k)$, $\Psi_{ci}(\cdot)$ denotes the activation function of the critic NN, and \widehat{w}_{ci} and $\widehat{\omega}_{ci}$ are the weight matrices for the critic NN.

We define the difference between the current cost value and the estimate value as the error function of the critic NN as follows:

$$\varepsilon_{ci}(k) = -U_i(\xi_i(k), u_i(k), u_j(k) + \rho \widehat{\omega}_{ci}^T \Psi_{ci}(\widehat{w}_{ci}^T z_{ci}(k+1))) + \widehat{\omega}_{ci}^T \Psi_{ci}(\widehat{w}_{ci}^T z_{ci}(k)). \quad (28)$$

Then, the loss function for the critic NN is given as

$$E_{ci} = \frac{1}{2} \varepsilon_{ci}^T(k) \varepsilon_{ci}(k). \quad (29)$$

Our objective is to minimize the loss function during the critic NN training.

The weights for the critic NN are updated according to the gradient-based rule, which is given as follows:

$$\begin{aligned} \widehat{\omega}_{ci}(k+1) &= \widehat{\omega}_{ci}(k) - \mathcal{K}_{ci} \frac{\partial E_{ci}(k)}{\partial \varepsilon_{ci}(k)} \frac{\partial \varepsilon_{ci}(k)}{\partial \widehat{\omega}_{ci}(k)} \\ &= \widehat{\omega}_{ci}(k) - \mathcal{K}_{ci} \varepsilon_{ci}^T(k) - \rho \Psi_{ci}(\widehat{w}_{ci}^T z_{ci}(k+1)) \\ &\quad + \Psi_{ci}(\widehat{w}_{ci}^T z_{ci}(k)), \end{aligned} \quad (30)$$

where \mathcal{K}_{ci} denotes the learning rate.

4.2. Formulation of the Actor Networks. The actor NN approximates the disturbed control law $u_i(k)$, which can be formulated as

$$\widehat{u}_i(k) = \widehat{\omega}_{ai}^T \Psi_{ai}(\widehat{w}_{ai}^T z_{ai}(k)), \quad (31)$$

where $z_{ai}(k)$ is the input vector of the actor NN, $\Psi_{ai}(\cdot)$ is the activation function for the actor NN, and $\widehat{\omega}_{ai}$ and \widehat{w}_{ai} are the weight matrices for the actor NN.

We define the difference between the current local cost value $\widehat{V}_i(k)$ and the target cost value $P_i(k)$ as the error function, which is given as

$$\varepsilon_{ai} = \widehat{V}_i(k) - P_i(k). \quad (32)$$

In this paper, the target cost value is defined as 0. Then, the loss function for the actor NN is given as

$$E_{ai} = \frac{1}{2} \varepsilon_{ai}^T(k) \varepsilon_{ai}(k). \quad (33)$$

Our objective is to minimize the loss function during the actor NN training.

The weights for the actor NN is updated according to the gradient-based rule, which is given as follows:

$$\begin{aligned} \widehat{w}_{ai}(k+1) &= \widehat{w}_{ai}(k) - \mathcal{H}_{ai} \frac{\partial E_{ai}(k)}{\partial \varepsilon_{ai}(k)} \frac{\partial \varepsilon_{ai}(k)}{\partial \widehat{V}_i(k)} \frac{\partial \widehat{V}_i(k)}{\partial \widehat{u}_i(k)} \frac{\partial \widehat{u}_i(k)}{\partial \widehat{w}_{ai}(k)} \\ &= \widehat{w}_{ai}(k) - \mathcal{H}_{ai} \varepsilon_{ai}^T(k) \widehat{w}_{ci} \Omega(k) C_i \Psi_{ai}(\widehat{w}_{ai}^T z_{ai}(k)), \end{aligned} \quad (34)$$

where $\Omega(k) = \partial \Psi_{ci}(\widehat{w}_{ci}^T z_{ci}) / \partial z_{ci}$, $C_i = \partial z_{ci} / \partial u_i$, and \mathcal{H}_{ai} is the learning rate for the actor NN.

The procedure of the NN-based event-triggered optimal consensus control algorithm for discrete-time MASs is shown in Algorithm 1.

Theorem 2. Consider a discrete-time MAS. The weights of critic NN and actor NN are updated following (30) and (34), respectively, under condition (17). The state x_i , the critic NN

weight estimation error, $\widetilde{w}_{ci} = w_{ci} - w_{ci}^*$, and the action weight estimation error, $\widetilde{w}_{ai} = w_{ai} - w_{ai}^*$, in the close loop system are UUB.

Proof

Case 1: the ET condition is satisfied at iteration index k . The Lyapunov function for agent i can be defined as follows:

$$\mathcal{L}_i(k) = \mathcal{L}_{i,1}(k) + \mathcal{L}_{i,2}(k) + \mathcal{L}_{i,3}(k), \quad (35)$$

where $L_{i,1}(k) = \mathbf{x}_i^T(k) \mathbf{x}_i(k)$, $L_{i,2}(k) = (1/\mathcal{H}_{ci}) \text{tr}\{\widetilde{w}_{ci}^T(k) \widetilde{w}_{ci}(k)\}$, and $L_{i,3}(k) = 1/\mathcal{H}_{ai} \cdot \text{tr}\{\widetilde{w}_{ai}^T(k) \widetilde{w}_{ai}(k)\}$. The difference between $\mathcal{L}_{i,1}(k+1)$ and $\mathcal{L}_{i,1}(k)$ can be given as

$$\begin{aligned} \Delta \mathcal{L}_{i,1} &= \mathbf{x}_i^T(k+1) \mathbf{x}_i(k+1) - \mathbf{x}_i^T(k) \mathbf{x}_i(k), \\ &= \|\mathbf{x}_i(k+1)\|^2 - \|\mathbf{x}_i(k)\|^2, \\ &= -\|\mathbf{x}_i(k)\|^2 + \|\mathbf{A}_i \mathbf{x}_i(k) + \mathbf{B}_i w_{ai}^* \Psi(w_{ai} \xi_i)\|^2. \end{aligned} \quad (36)$$

The difference between $\mathcal{L}_{i,2}(k+1)$ and $\mathcal{L}_{i,2}(k)$ can be given as

$$\begin{aligned} \Delta \mathcal{L}_{i,2} &= (1/\mathcal{H}_{ci}) \text{tr}\{\widetilde{w}_{ci}^T(k+1) \widetilde{w}_{ci}(k+1)\} - (1/\mathcal{H}_{ci}) \text{tr}\{\widetilde{w}_{ci}^T(k) \widetilde{w}_{ci}(k)\} \\ &= (1/\mathcal{H}_{ci}) \text{tr}\{\widetilde{w}_{ci}^T(k+1) \widetilde{w}_{ci}(k+1) - \widetilde{w}_{ci}^T(k) \widetilde{w}_{ci}(k)\}. \end{aligned} \quad (37)$$

According to the update function for the weight matrix of critic NN (30), we have

$$\begin{aligned} \widetilde{w}_{ci}(k+1) &= \widetilde{w}_{ci}(k) - \mathcal{H}_{ci} \varepsilon_{ci}^T(k) (-\rho \Psi_{ci}(\widehat{w}_{ci}^T z_{ci}(k+1)) + \Psi_{ci}(\widehat{w}_{ci}^T z_{ci}(k))) \\ &= \widetilde{w}_{ci}(k) - \mathcal{H}_{ci} (-\rho \Psi_{ci}(\widehat{w}_{ci}^T z_{ci}(k+1)) + \Psi_{ci}(\widehat{w}_{ci}^T z_{ci}(k))) \\ &\quad \times (-U_i(k) + \rho \widehat{w}_{ci}^T \Psi_{ci}(\widehat{w}_{ci}^T z_{ci}(k+1)) + \widehat{w}_{ci}^T \Psi_{ci}(\widehat{w}_{ci}^T z_{ci}(k))) \\ &= \widetilde{w}_{ci}(k) - \mathcal{H}_{ci} \eta(k) (-U_i(k) + \widehat{w}_{ci}^T(\eta(k))) \\ &= (I - \mathcal{H}_{ci} \eta(k) \eta^T(k)) \widetilde{w}_{ci}(k) + \mathcal{H}_{ci} U_i(k) \eta(k), \end{aligned} \quad (38)$$

where $\eta(k) = -\rho \Psi_{ci}(\widehat{w}_{ci}^T z_{ci}(k+1)) + \Psi_{ci}(\widehat{w}_{ci}^T z_{ci}(k))$.

Substituting (38) into 37 we have

$$\begin{aligned} \Delta \mathcal{L}_{i,2} &= (1/\mathcal{H}_{ci}) \text{tr} \left\{ \begin{aligned} &((I - \mathcal{H}_{ci} \eta(k) \eta^T(k)) \widetilde{w}_{ci}(k) + \mathcal{H}_{ci} U_i(k) \eta(k))^T \\ &\times ((I - \mathcal{H}_{ci} \eta(k) \eta^T(k)) \widetilde{w}_{ci}(k) + \mathcal{H}_{ci} U_i(k) \eta(k)) - \widetilde{w}_{ci}^T(k) \widetilde{w}_{ci}(k) \end{aligned} \right\} \\ &\leq (1/\mathcal{H}_{ci}) \left(\|\mathcal{H}_{ci} \eta(k) \eta^T(k)\|_F^2 \|\widetilde{w}_{ci}(k)\|^2 + \|\mathcal{H}_{ci} U_i(k) \eta(k)\|^2 \right) \\ &= \|\eta(k) \eta^T(k)\|_F^2 \|\widetilde{w}_{ci}(k)\|^2 + U_i(k) \|\eta(k)\|^2 \\ &= \|\eta(k)\|^4 \|\widetilde{w}_{ci}(k)\|^2 + U_i(k) \|\eta(k)\|^2. \end{aligned} \quad (39)$$

The difference between $\mathcal{L}_{i,3}(k+1)$ and $\mathcal{L}_{i,3}(k)$ can be given as

$$\begin{aligned}\Delta\mathcal{L}_{i,3} &= (1/\mathcal{K}_{ai}^2)tr\{\tilde{\omega}_{ai}^T(k+1)\tilde{\omega}_{ai}(k+1)\} - (1/\mathcal{K}_{ai})tr\{\tilde{\omega}_{ai}^T(k)\tilde{\omega}_{ai}(k)\}, \\ &= (1/\mathcal{K}_{ai}^2)tr\{\tilde{\omega}_{ai}^T(k+1)\tilde{\omega}_{ai}(k+1) - \tilde{\omega}_{ai}^T(k)\tilde{\omega}_{ai}(k)\}.\end{aligned}\quad (40)$$

According to the update function for the weight matrix of critic NN (34), we have

$$\begin{aligned}\tilde{\omega}_{ai}(k+1) &= \tilde{\omega}_{ai}(k) - \mathcal{K}_{ai}\varepsilon_{ai}^T(k)\hat{\omega}_{ci}\Omega(k)C_i\Psi_{ai}(\hat{w}_{ai}^T z_{ai}(k)) \\ &= \tilde{\omega}_{ai}(k) - \mathcal{K}_{ai}\hat{V}_i(k)\hat{\omega}_{ci}\Omega(k)C_i\Psi_{ai}(\hat{w}_{ai}^T z_{ai}(k)).\end{aligned}\quad (41)$$

Substituting (41) into (40), we have

$$\begin{aligned}\Delta\mathcal{L}_{i,3} &= \frac{1}{\mathcal{K}_{ai}}tr\left\{\begin{aligned} &(\tilde{\omega}_{ai}(k) - \mathcal{K}_{ai}\hat{V}_i(k)\hat{\omega}_{ci}\Omega(k)C_i\Psi_{ai}(\hat{w}_{ai}^T z_{ai}(k)))^T \\ &\times(\tilde{\omega}_{ai}(k) - \mathcal{K}_{ai}\hat{V}_i(k)\hat{\omega}_{ci}\Omega(k)C_i\Psi_{ai}(\hat{w}_{ai}^T z_{ai}(k))) \\ &- \tilde{\omega}_{ai}^T(k)\tilde{\omega}_{ai}(k) \end{aligned}\right\} \\ &= \frac{1}{\mathcal{K}_{ai}}tr\left\{\begin{aligned} &-\tilde{\omega}_{ai}^T(k)\mathcal{K}_{ai}\hat{V}_i(k)\hat{\omega}_{ci}\Omega(k)C_i\Psi_{ai}(\hat{w}_{ai}^T z_{ai}(k)) \\ &-\mathcal{K}_{ai}\hat{V}_i(k)\Psi_{ai}^T(\hat{w}_{ai}^T z_{ai}(k))C_i^T\Omega^T(k)\hat{\omega}_{ci}^T\tilde{\omega}_{ai}(k) \\ &+\mathcal{K}_{ai}^2\hat{V}_i^2(k)\Psi_{ai}^T(\hat{w}_{ai}^T z_{ai}(k))C_i^T\Omega^T(k)\hat{\omega}_{ci}^T\hat{\omega}_{ci}\Omega(k)C_i\Psi_{ai}(\hat{w}_{ai}^T z_{ai}(k)) \end{aligned}\right\} \\ &= tr\left\{\begin{aligned} &-2\hat{V}_i(k)\Psi_{ai}^T(\hat{w}_{ai}^T z_{ai}(k))C_i^T\Omega^T(k)\hat{\omega}_{ci}^T\tilde{\omega}_{ai}(k) \\ &+\mathcal{K}_{ai}\hat{V}_i^2(k)\Psi_{ai}^T(\hat{w}_{ai}^T z_{ai}(k))C_i^T\Omega^T(k)\hat{\omega}_{ci}^T\hat{\omega}_{ci}\Omega(k)C_i\Psi_{ai}(\hat{w}_{ai}^T z_{ai}(k)) \end{aligned}\right\} \\ &= -2\hat{V}_i(k)tr\{\tilde{\omega}_{ai}^T(k)\hat{\omega}_{ci}\Omega(k)C_i\Psi_{ai}(\hat{w}_{ai}^T z_{ai}(k))\} + \mathcal{K}_{ai}\hat{V}_i^2(k)\|\hat{\omega}_{ci}\Omega(k)C_i\Psi_{ai}(\hat{w}_{ai}^T z_{ai}(k))\|_F^2.\end{aligned}\quad (42)$$

Combining (36), (39), and (42), the difference between $\Delta\mathcal{L}(k)$ and $\Delta\mathcal{L}(k+1)$ is given as

$$\begin{aligned}\Delta\mathcal{L} &\leq -\|\mathbf{x}_i(k)\|^2 - 2\hat{V}_i(k)tr\{\tilde{\omega}_{ai}^T(k)\hat{\omega}_{ci}\Omega(k)C_i\Psi_{ai}(\hat{w}_{ai}^T z_{ai}(k))\} \\ &\quad + \|\mathbf{A}_i\mathbf{x}_i(k) + \mathbf{B}_i\omega_{ai}^*\Psi(w_{ai}\xi_i)\|^2 + \|\eta(k)\|^4 + U_i(k)\|\eta(k)\|^2 \\ &\quad + \mathcal{K}_{ai}\hat{V}_i^2(k)\|\hat{\omega}_{ci}\Omega(k)C_i\Psi_{ai}(\hat{w}_{ai}^T z_{ai}(k))\|_F^2 \\ &\leq -\|\mathbf{x}_i(k)\|^2 - 2\hat{V}_i(k)tr\{\tilde{\omega}_{ai}^T(k)\hat{\omega}_{ci}\Omega(k)C_i\Psi_{ai}(\hat{w}_{ai}^T z_{ai}(k))\} + D_{mi},\end{aligned}\quad (43)$$

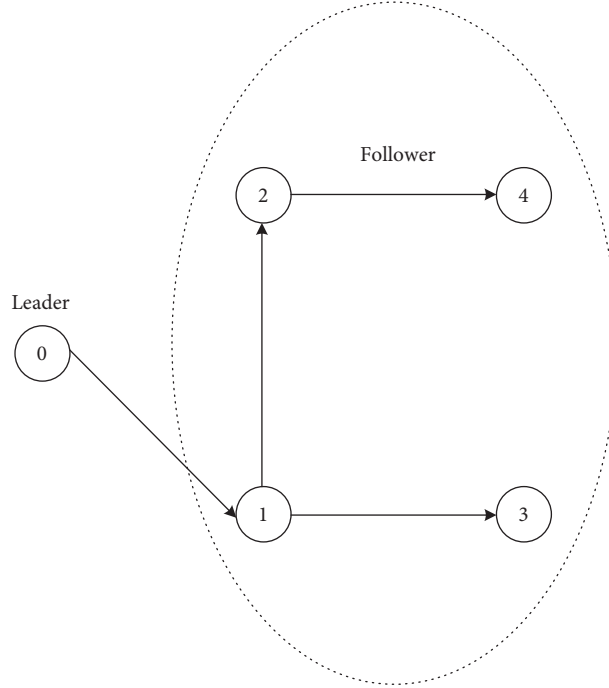


FIGURE 2: The network topology for the discrete-time MAS.

where $D_{mi} = \sup(\|A_i x_i(k) + B_i \omega_{ai}^* \Psi(w_{ai} \xi_i)\|^2 + \|\eta(k)\|^4 + U_i(k) \|\eta(k)\|^2 + \mathcal{K}_{ai} \widehat{V}_i^2(k) \|\widehat{\omega}_{ci} \Omega((k) C_i \Psi_{ai}(\widehat{\omega}_{ai}^T z_{ai}(k)))\|_F^2)$.

If one of the conditions $\|x(k)\| \geq \sqrt{D_{mi}}$ or $\widehat{V}_i(k) \text{tr}\{\widehat{\omega}_{ai}^T(k) \widehat{\omega}_{ci} \Omega(k) C_i \Psi_{ai}(\widehat{\omega}_{ai}^T z_{ai}(k))\} \geq D_{mi}$ holds, the difference is $\Delta \mathcal{L} < 0$. This means the states of the system and the error of the weight matrices for critic NN and actor NN are UUB.

Case 2: if the ET condition is not satisfied at iteration instant k , consider the Lyapunov function (35) in case 1. The difference between $\mathcal{L}_{i,1}(k+1)$ and $\mathcal{L}_{i,1}(k)$ can be given as

$$\begin{aligned} \Delta \mathcal{L}_{i,1} &= \mathbf{x}_i^T(k+1) \mathbf{x}_i(k+1) - \mathbf{x}_i^T(k) \mathbf{x}_i(k) \\ &= \|\mathbf{x}_i(k+1)\|^2 - \|\mathbf{x}_i(k)\|^2 \\ &\leq -\|\mathbf{x}_i(k)\|^2 + \|\mathbf{L} \mathbf{x}(k) + \mathbf{L}^2 \|\xi(k)\|. \end{aligned} \quad (44)$$

The weight matrices for the critic NN and actor NN are not updated when the ET condition is not satisfied, so the differences are $\Delta \mathcal{L}_{i,2} = 0$ and $\Delta \mathcal{L}_{i,3} = 0$.

Combining $\Delta \mathcal{L}_{i,1}$, $\Delta \mathcal{L}_{i,2}$, and $\Delta \mathcal{L}_{i,3}$, the difference between $\Delta \mathcal{L}(k)$ and $\Delta \mathcal{L}(k+1)$ is given as

$$\begin{aligned} \Delta \mathcal{L} &= \Delta \mathcal{L}_{i,1} + \Delta \mathcal{L}_{i,2} + \Delta \mathcal{L}_{i,3} \\ &\leq -\|\mathbf{x}_i(k)\|^2 + \|\mathbf{L} \mathbf{x}(k) + \mathbf{L}^2 \|\xi(k)\|. \end{aligned} \quad (45)$$

If the condition $\|\mathbf{x}_i(k)\| \geq \sqrt{\|\mathbf{L} \mathbf{x}(k) + \mathbf{L}^2 \|\xi(k)\|}$ holds, the difference is $\Delta \mathcal{L} < 0$. This means when the ET condition is not satisfied at the time index k , the states of the system and the error of the weights matrices for the critic NN and actor NN are UUB. \square

5. Simulation Analysis

To test the effectiveness of the proposed algorithm, we apply the proposed algorithm in a numerical example. Consider a discrete-time leader-follower MAS consisting of 4 agents with a network topology, as shown in Figure 2. In the topology, agent 0 denotes the leader and the followers are labeled as agent 1 to agent 4. The adjacency elements α_{21} , α_{31} , and α_{42} are set to 1. The other adjacency elements are set to 0. In this numerical example, only agent 1 can communicate with the leader, which means $\beta_1 = 1$ and $\beta_2 = \beta_3 = \beta_4 = 0$. The weight matrices of the utility function are selected as $Q_{11} = Q_{11} = Q_{11} = Q_{11} = I_{2 \times 2}$, $R_{11} = R_{22} = R_{33} = R_{44} = 1$, and $S_{12} = S_{13} = S_{14} = S_{23} = S_{24} = S_{32} = S_{34} = S_{41} = S_{43} = 0$.

The dynamics matrix for the leader are set to $\mathbf{A} = \begin{bmatrix} 0.9950 & 0.0798 \\ -0.0798 & 0.9950 \end{bmatrix}$. The dynamics matrices for the followers are set to $\mathbf{A} = \begin{bmatrix} 0.9950 & 0.0798 \\ -0.0798 & 0.9950 \end{bmatrix}$,

$$\mathbf{B}_1 = \begin{bmatrix} 0.2047 \\ 0.0898 \end{bmatrix}, \quad \mathbf{B}_2 = \begin{bmatrix} 0.2147 \\ 0.2895 \end{bmatrix}, \quad \mathbf{B}_3 = \begin{bmatrix} 0.2097 \\ 0.1897 \end{bmatrix}, \quad \text{and} \\ \mathbf{B}_4 = \begin{bmatrix} 0.2000 \\ 0.1000 \end{bmatrix}.$$

The parameters for the critic NN and the actor NN are set to $\rho = 0.9$, and $\mathcal{K}_{c1} = \mathcal{K}_{c2} = \mathcal{K}_{c3} = 0.01$, $K_{c4} = 0.001$, and $\mathcal{K}_{a1} = \mathcal{K}_{a2} = \mathcal{K}_{a3} = \mathcal{K}_{a4} = 0.01$. $\Psi_{c1}(k_{1,p}) = [\xi_{11}(k_{1,p}), \xi_{12}(k_{1,p}), \widehat{u}_1(k_{1,p})]$, $\Psi_{c2}(k_{2,p}) = [\xi_{21}(k_{2,p}), \xi_{22}(k_{2,p}), \widehat{u}_2^2(k_{2,p}), \widehat{u}_2^2(k_{2,p})]$, $\Psi_{c3}(k_{3,p}) = [\xi_{31}(k_{3,p}), \xi_{32}(k_{3,p}), \widehat{u}_3^2(k_{3,p}), \widehat{u}_3^2(k_{3,p})]$, and $\Psi_{c4}(k_{4,p}) = [\xi_{41}(k_{4,p}), \xi_{42}(k_{4,p}), \widehat{u}_4(k_{4,p}), \widehat{u}_4(k_{4,p})]$ are the activation functions of the critic NNs. The activation functions of the actor NNs are set to $\Psi_{ai}(k_{i,p}) = [\xi_i(k_{i,p})]$. $\mathbf{x}_0(0) = [0.6311, 0.0899]^T$, $\mathbf{x}_1(0)$

Initialization:
 Give the computation precision τ and the initial state $x_i(0)$ for agent i ;
 Give the initial state $\mathbf{x}_0(0)$ for the leader;
 Select the learning rate \mathcal{H}_{ai} and \mathcal{H}_{ci} ;
 Give the positive matrices \mathbf{Q}_{ii} , \mathbf{R}_{ii} , and \mathbf{S}_{ij} ;
 Initialize the event-triggered error condition $\delta_{iT}(0) = 0$;
 Select the positive constant L ;

Iteration:
 Let the iteration index $k = 0$;
repeat:
 Calculate the tracking error $\hat{\xi}_i(k)$ and the event-triggered error $\delta_i(k)$;
IF $\|\delta_i(k)\| \geq \delta_{iT}(k)$:
 Event-triggered error $\|\delta_i(k)\| = 0$;
 Event-triggered index $k_{i,p} = k$;
 Compute the control law $\hat{u}_i(k)$;
 Compute the local cost function $\hat{V}_i(k)$;
 Compute the next state $\hat{x}_i(k+1)$ of agent i and the next state $\hat{x}_0(k+1)$ of the leader agent;
 Calculate the next tracking error $\hat{\xi}_i(k)$;
 Compute the control law $\hat{u}_i(k+1)$;
 Compute the local cost function $\hat{V}_i(k+1)$;
 Update the weights matrix of the critic NN;
 Update the weights matrix of the actor NN;
ELSE:
 The control law $\hat{u}_i(k) = \hat{u}_i(k-1)$;
 Compute the control law $\hat{u}_i(k)$;
 Compute the next state $\mathbf{x}_i(k+1)$ of agent i and the next state $\mathbf{x}_0(k+1)$ of the leader agent according to the model NN;
 $k = k + 1$;
Until $|\hat{\omega}_{ci}(k+1) - \hat{\omega}_{ci}(k)| \leq \tau$;
End

ALGORITHM 1: NN-based event-triggered optimal consensus control algorithm for discrete-time MASs.

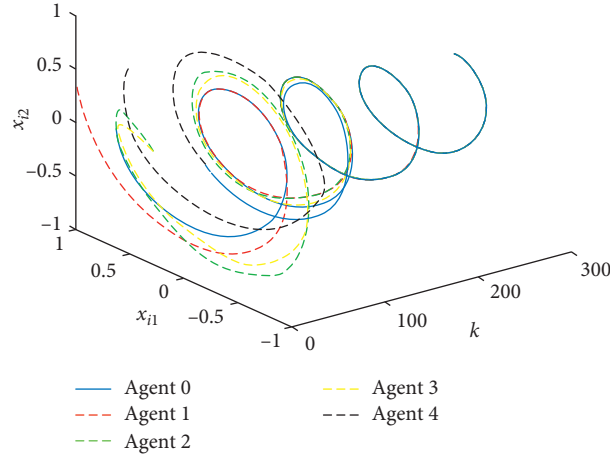


FIGURE 3: The tracking path for the system under the ET condition.

$= [0.9954, 0.3321]^T$, $\mathbf{x}_2(0) = [0.2973, 0.0620]^T$, $\mathbf{x}_3(0) = [0.2982, 0.0464]^T$, and $\mathbf{x}_4(0) = [0.5054, 0.7614]^T$ are chosen as the initial states for the leader and the follower agents in the system. We set $L = 0.1$.

The tracking path for every agent in the discrete-time MAS is shown in Figure 3. From Figure 3, we can observe that all the agents in the system can reach the same state as the leader, and then, they achieve synchronization. The

driving errors for the agents in the system are shown in Figure 4. All the agents' driving error all are not updated at every instant k , that is to say, all the agents are driven when the ET condition is satisfied. Figure 5 shows the comparisons of event-triggered errors and thresholds for every agent in the system. In Figure 5, we can observe that the event-triggered errors are always smaller than the thresholds during the tracking process, and we only sample the data

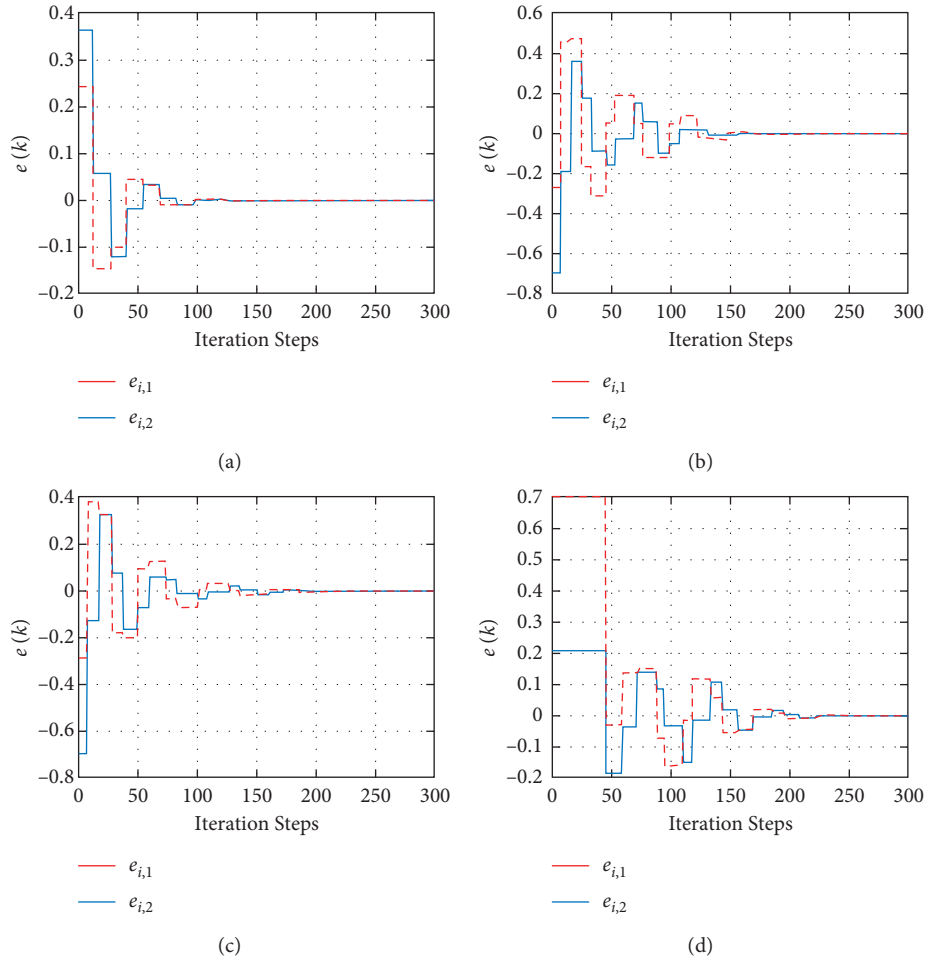


FIGURE 4: The driving error for every agent in the system under the ET condition. (a) Driving error for agent1. (b) Driving error for agent2. (c) Driving error for agent3. (d) Driving error for agent4.

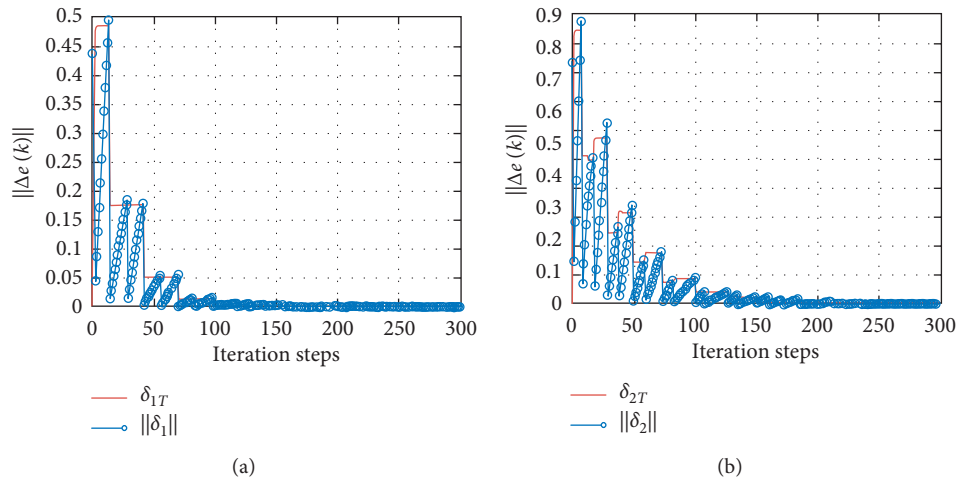


FIGURE 5: Continued.

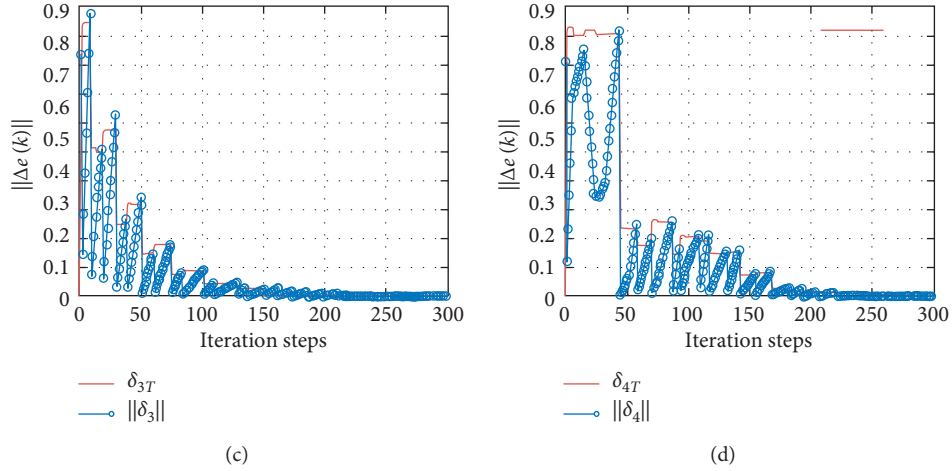


FIGURE 5: Comparisons of event-triggered errors and thresholds for every agent in the system. (a) Comparisons of event-triggered errors and thresholds for agent1. (b) Comparisons of event-triggered errors and thresholds for agent2. (c) Comparisons of event-triggered errors and thresholds for agent3. (d) Comparisons of event-triggered errors and thresholds for agent4.

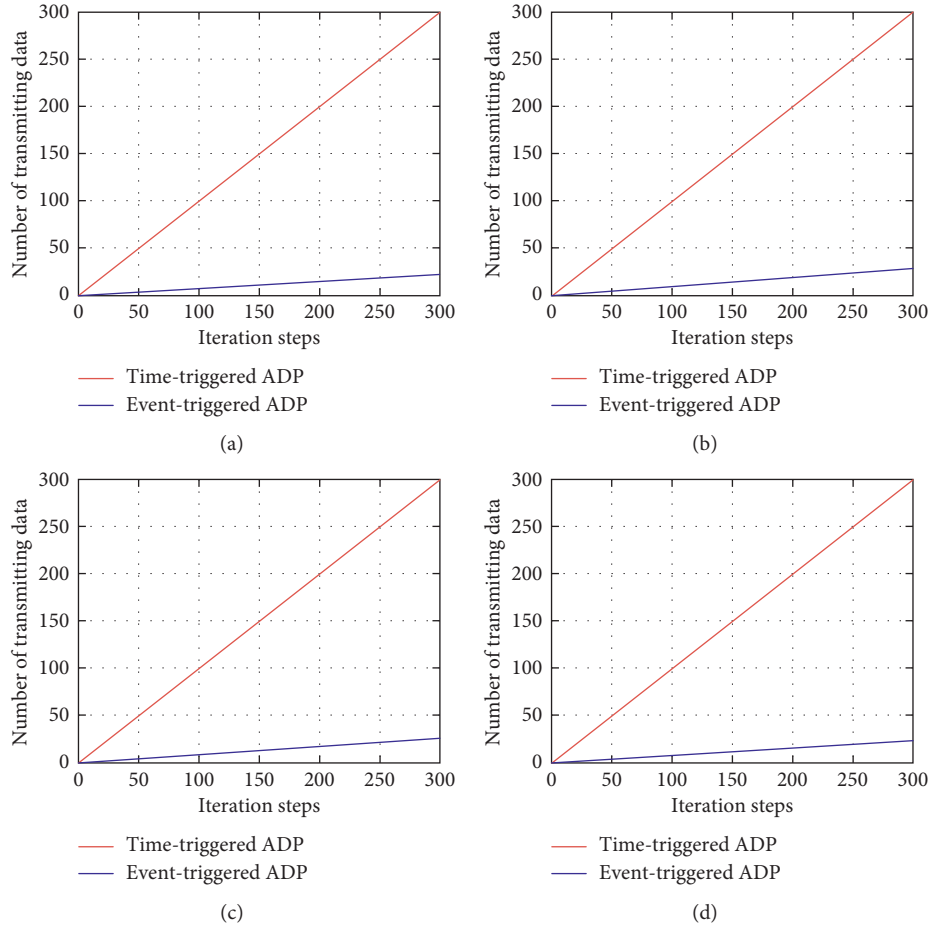


FIGURE 6: Comparisons of required number of transmitting data under the time-triggered and event-triggered ADP for every agent in the system. (a) The required number of transmitting data under the time-triggered ADP and event-triggered ADP for agent1. (b) The required number of transmitting data under the time-triggered ADP and event-triggered ADP for agent2. (c) The required number of transmitting data under the time-triggered ADP and event-triggered ADP for agent1. (d) The required number of transmitting data under the time-triggered ADP and event-triggered ADP for agent1.

when the event-triggered errors are bigger or equal to the thresholds, so we sample the less data and save computing resources using our algorithm. Figure 6 shows the comparisons of the required number of transmitting data under the time-triggered and event-triggered ADP algorithm for every agent in the system. We can observe the required number of the event-triggered algorithm is much less than the required number of the time-triggered algorithm.

6. Conclusion

An event-triggered optimal consensus tracking control algorithm based on the ADP structure is proposed in this paper. To save the communication and computation resources, we introduce the event-triggered scheme to the optimal consensus tracking control algorithm. The neural networks technology is introduced to simplify the application of the proposed algorithm. It is proved the discrete-time MASs are stable with the proposed algorithm and the estimate errors of the weights for NNs are UUB. The simulation results illustrate the efficiency of the proposed method.

Data Availability

All data included in this study are available from the corresponding author upon request.

Conflicts of Interest

The authors declare that they have no conflicts of interest.

Acknowledgments

This work was supported by the National Natural Science Foundation of China (61803285 and 62001332) and National Defense Pre-Research Foundation of China (H04W201018).

References

- [1] Z. Lin, L. Wang, Z. Han, and M. Fu, "Distributed formation control of multi-agent systems using complex laplacian," *IEEE Transactions on Automatic Control*, vol. 59, no. 7, pp. 1765–1777, 2014.
- [2] Y.-B. Bae, Y.-H. Lim, and H.-S. Ahn, "Distributed robust adaptive gradient controller in distance-based formation control with exogenous disturbance," *IEEE Transactions on Automatic Control*, vol. 66, no. 6, pp. 2868–2874, 2021.
- [3] J. Zhan and X. Li, "Flocking of multi-agent systems via model predictive control based on position-only measurements," *IEEE Transactions on Industrial Informatics*, vol. 9, no. 1, pp. 377–385, 2013.
- [4] C. Yang, G. Peng, L. Cheng, J. Na, and Z. Li, "Force sensorless admittance control for teleoperation of uncertain robot manipulator using neural networks," *IEEE Transactions on Systems, Man, and Cybernetics: Systems*, vol. 51, no. 5, pp. 3282–3292, 2021.
- [5] C. Yang, J. Luo, C. Liu, M. Li, and S.-L. Dai, "Haptics electromyography perception and learning enhanced intelligence for teleoperated robot," *IEEE Transactions on Automation Science and Engineering*, vol. 16, no. 4, pp. 1512–1521, 2019.
- [6] C. Yang, C. Chen, N. Wang, Z. Ju, J. Fu, and M. Wang, "Biologically inspired motion modeling and neural control for robot learning from demonstrations," *IEEE Transactions on Cognitive and Developmental Systems*, vol. 11, no. 2, pp. 281–291, 2019.
- [7] Z. Zuo, J. Zhang, and Y. Wang, "Adaptive fault-tolerant tracking control for linear and lipschitz nonlinear multi-agent systems," *IEEE Transactions on Industrial Electronics*, vol. 62, no. 6, pp. 3923–3931, 2015.
- [8] H. Rezaee and F. Abdollahi, "Adaptive leaderless consensus control of strict-feedback nonlinear multiagent systems with unknown control directions," *IEEE Transactions on Systems, Man, and Cybernetics: Systems*, vol. 51, no. 10, pp. 6435–6444, 2021.
- [9] D. Yao, H. Li, R. Lu, and Y. Shi, "Distributed sliding-mode tracking control of second-order nonlinear multiagent systems: an event-triggered approach," *IEEE Transactions on Cybernetics*, vol. 50, no. 9, pp. 3892–3902, 2020.
- [10] J. Zhang, M. Lyu, T. Shen, L. Liu, and Y. Bo, "Sliding mode control for a class of nonlinear multi-agent system with time delay and uncertainties," *IEEE Transactions on Industrial Electronics*, vol. 65, no. 1, pp. 865–875, 2018.
- [11] D. Liu, H. Li, and D. Wang, "Online synchronous approximate optimal learning algorithm for multi-player non-zero-sum games with unknown dynamics," *IEEE Transactions on Systems, Man, and Cybernetics: Systems*, vol. 44, no. 8, pp. 1015–1027, 2014.
- [12] D. Liu and Q. Wei, "Policy iteration adaptive dynamic programming algorithm for discrete-time nonlinear systems," *IEEE Transactions on Neural Networks and Learning Systems*, vol. 25, no. 3, pp. 621–634, 2014.
- [13] B. Mu, K. Zhang, and Y. Shi, "Discrete-time nonlinear HJB solution using approximate dynamic programming," *IEEE Transactions on Systems, Man, and Cybernetics, Part B (Cybernetics)*, vol. 38, no. 4, 2008.
- [14] H. Zhang, J. Zhang, G.-H. Yang, and Y. Luo, "Leader-based optimal coordination control for the consensus problem of multiagent differential games via fuzzy adaptive dynamic programming," *IEEE Transactions on Fuzzy Systems*, vol. 23, no. 1, pp. 152–163, 2015.
- [15] H. Zhang, H. Liang, Z. Wang, and T. Feng, "Optimal output regulation for heterogeneous multiagent systems via adaptive dynamic programming," *IEEE Transactions on Neural Networks and Learning Systems*, vol. 28, no. 1, pp. 18–29, 2017.
- [16] W. Gao, Y. Jiang, and M. Davari, "Data-driven cooperative output regulation of multi-agent systems via robust adaptive dynamic programming," *IEEE Transactions on Circuits and Systems II: Express Briefs*, vol. 66, no. 3, pp. 447–451, 2019.
- [17] H. Zhang, H. Jiang, Y. Luo, and G. Xiao, "Data-driven optimal consensus control for discrete-time multi-agent systems with unknown dynamics using reinforcement learning method," *IEEE Transactions on Industrial Electronics*, vol. 64, no. 5, pp. 4091–4100, 2017.
- [18] J. Zhang, H. Zhang, and T. Feng, "Distributed optimal consensus control for nonlinear multiagent system with unknown dynamic," *IEEE Transactions on Neural Networks and Learning Systems*, vol. 29, no. 8, pp. 3339–3348, 2018.
- [19] H. Zhang, D. Yue, C. Dou, W. Zhao, and X. Xie, "Data-driven distributed optimal consensus control for unknown multi-agent systems with input-delay," *IEEE Transactions on Cybernetics*, vol. 49, no. 6, pp. 2095–2105, 2019.
- [20] H. Zhang, Y. Liu, G. Xiao, and H. Jiang, "Data-based adaptive dynamic programming for a class of discrete-time systems

- with multiple delays,” *IEEE Transactions on Systems, Man, and Cybernetics: Systems*, vol. 50, no. 2, pp. 432–441, 2020.
- [21] R. Song and L. Liu, “Event-triggered constrained robust control for partly-unknown nonlinear systems via ADP,” *Neurocomputing*, vol. 404, no. 3, pp. 294–303, 2020.
- [22] S. Xue, B. Luo, D. Liu, and Y. Li, “Adaptive dynamic programming based event-triggered control for unknown continuous-time nonlinear systems with input constraints,” *Neurocomputing*, vol. 396, no. 5, pp. 191–200, 2020.
- [23] B. Zhao and D. Liu, “Event-triggered decentralized tracking control of modular reconfigurable robots through adaptive dynamic programming,” *IEEE Transactions on Industrial Electronics*, vol. 67, no. 4, pp. 3054–3064, 2020.
- [24] L. Cui, X. Xie, X. Wang, Y. Luo, and J. Liu, “Event-triggered single-network ADP method for constrained optimal tracking control of continuous-time non-linear systems,” *Applied Mathematics and Computation*, vol. 352, pp. 220–234, 2019.
- [25] B. Luo, Y. Yang, D. Liu, and H.-N. Wu, “Event-triggered optimal control with performance guarantees using adaptive dynamic programming,” *IEEE Transactions on Neural Networks and Learning Systems*, vol. 31, no. 1, pp. 76–88, 2020.
- [26] W. Zhao and H. Zhang, “Distributed optimal coordination control for nonlinear multi-agent systems using event-triggered adaptive dynamic programming method,” *ISA Transactions*, vol. 91, pp. 184–195, 2019.
- [27] X. Zhong and H. He, “An event-triggered ADP control approach for continuous-time system with unknown internal states,” *IEEE Transactions on Cybernetics*, vol. 47, no. 3, pp. 683–694, 2017.
- [28] J. Sun and T. Long, “Event-triggered distributed zero-sum differential game for nonlinear multi-agent systems using adaptive dynamic programming,” *ISA Transactions*, vol. 110, pp. 39–52, 2021.
- [29] S. Xue, B. Luo, and D. Liu, “Event-triggered adaptive dynamic programming for unmatched uncertain nonlinear continuous-time systems,” *IEEE Transactions on Neural Networks and Learning Systems*, vol. 32, no. 7, pp. 2939–2951, 2021.
- [30] M. Chen, H. Yan, M. Wang, and Z. Li, “Dynamic event-triggered consensus for discrete-time multi-agent systems,” in *Proceedings of the IECON 2021 - 47th Annual Conference of the IEEE Industrial Electronics Society*, Toronto, ON, Canada, October 2021.
- [31] D. Zhao, T. Dong, and W. Hu, “Event-triggered consensus of discrete time second-order multi-agent network,” *International Journal of Control, Automation and Systems*, vol. 16, no. 1, pp. 87–96, 2009.
- [32] A. Eqtami, D. V. Dimarogonas, and K. J. Kyriakopoulos, “Event-triggered control for discrete-time systems,” in *Proceedings of the 2010 American Control Conference*, pp. 4719–4724, Baltimore, MD, USA, July 2010.
- [33] C. Yang, C. Chen, W. He, R. Cui, and Z. Li, “Robot learning system based on adaptive neural control and dynamic movement primitives,” *IEEE Transactions on Neural Networks and Learning Systems*, vol. 30, no. 3, pp. 777–787, 2019.
- [34] H. Huang, T. Zhang, C. Yang, and C. L. P. Chen, “Motor learning and generalization using broad learning adaptive neural control,” *IEEE Transactions on Industrial Electronics*, vol. 67, no. 10, pp. 8608–8617, 2020.

Research Article

Vibration Suppression of a Coupled Aircraft Wing with Finite-Time Convergence

Yiming Liu , Zhifeng Tan , Xiaofen Yang , and Xiaowei Wang 

School of Mechanical and Electric Engineering, Guangzhou University, Guangzhou 510006, China

Correspondence should be addressed to Xiaowei Wang; meewxw_ee@gzhu.edu.cn

Received 6 August 2021; Accepted 9 September 2021; Published 16 February 2022

Academic Editor: Zhenyu Lu

Copyright © 2022 Yiming Liu et al. This is an open access article distributed under the Creative Commons Attribution License, which permits unrestricted use, distribution, and reproduction in any medium, provided the original work is properly cited.

A nonlinear coupled wing model subject to unknown external disturbances is proposed in this paper. Since the model is modeled by partial differential equations, the traditional control design scheme based on the ordinary differential equation model is not applicable, and the control law design becomes very complex. In this paper, a new antidisturbance boundary control scheme based on a finite time convergent disturbance observer is proposed. The control laws are designed based on the new disturbance observers to make the external disturbance errors converge to zero in a finite time and ensure the uniformly bounded stability of the controlled system. Finally, the effectiveness of the controllers and the finite-time convergence of disturbance errors are verified by the simulation and comparison.

1. Introduction

Due to the characteristics of maneuverability, flexibility, and wide vision, aircrafts are widely used in various fields. Aircrafts include the fixed-wing, rotary-wing, and flapping-wing aircraft. Among them, the flapping-wing aircraft has unique advantages, including higher flight maneuverability and low flight costs. In addition, although the size is small and the flight resistance is large, the flight efficiency of the flapping-wing aircraft will not be reduced [1]. Therefore, more and more researchers are engaged in the research of flapping-wing aircraft [2–6]. Researchers combined the structural design with bionics to develop and research the flapping-wing aircraft. Some researchers used rigid materials to make the wings, which ignored the influence of fluid dynamic changes caused by the deformation of insect wings so that the fuselage may not be flexible enough and prone to failure during execution [7]. Because flexible materials have the advantages of improving the running speed of the mechanical system and further reducing the weight of the structure, they are widely used in the mechanical structure manufacturing in recent years [8, 9]. Therefore, we can use flexible materials to make flapping-wing aircraft wings [10]. Although the flexible wing can improve the flexibility of

flapping-wing aircraft, the vibration and deformation of wings will affect the control effect and flight performance. Consequently, the problem of wing vibration needs to be solved urgently, which inspired our research. In this paper, we regard a single wing as a coupled distributed parameter system and use the combination of partial differential equation and ordinary differential equation (PDE-ODE) to describe the wing dynamic model. Due to the complexity of distributed parameter system control design, more and more attention has been paid in recent years [11–21].

For the problem of vibration suppression of distributed parameter systems, several researchers have proposed various control methods including the modal reduction method [22] and boundary control [23–29]. The modal reduction method can effectively reduce the order of the infinite-dimensional system and treat the system as a finite dimension, but this method can easily cause spillover effects. The boundary control strategy can effectively solve this problem and improve the robustness of the system. In recent years, the research on vibration suppression of flexible structural systems based on the boundary control has made great progress. For example, in [30], with the method of barrier Lyapunov function, the controller could suppress the vibration of the system and cope with the input and output

constraints at the same time. In [31], a boundary controller was constructed to suppress the vibration excursion of the hose using the backstepping control method, and a smooth hyperbolic tangent function was introduced to cope with the input amplitude and rate constraints. In [32], a boundary control was designed for the flexible string system with vibration and input backlash. In [33], with the help of a new disturbance observer, the external disturbance was effectively suppressed, and the purpose of vibration reduction was achieved. A robust adaptive controller was proposed to deal with parameter uncertainties and stabilize the system in [34]. In [35], the authors put forward an adaptive NN control strategy for flexible string systems with input constraints and actuator failures. Two iterative learning boundary control schemes were designed for a flexible microair vehicle under spatiotemporal variation disturbances to suppress structural vibration and make it track the target trajectory in [36]. As for the boundary control of the flexible aircraft wing system, many scholars have researched in recent years [37–39]. However, these studies did not consider that the system was affected by both distributed disturbances and boundary disturbances, and their existence may bring great side effects to the system. Therefore, disturbance suppression has become a key problem in the wing control design.

In the past few years, one of the most commonly used antidisturbance methods is the disturbance observer technique. This method can be used for nonlinear systems with uncertainties and efficiently improve the robustness of the system [40–42]. The boundary disturbance observer-based control problem of a vibrating single-link flexible manipulator system with external disturbances was studied in [43]. In [44], considering the influence of extraneous disturbance acting on the wing, a new observer was proposed for controller design. A new disturbance observer was proposed to deal with the distributed disturbance and boundary disturbance of a flexible-link manipulator in [45]. However, it is noted that although the disturbance observer proposed in the above research could effectively track the change of unknown disturbance, it must be assumed that the disturbance changes slowly, and it could not ensure that the disturbance error converged in a finite time. For systems affected by the external disturbance with unknown varying frequency, it is very important to ensure that the disturbance error converges in a finite time [46]. So far, there has been no research on the finite-time convergence control of the coupled aircraft wing system, which motivates this research.

In this article, the stability of nonlinear flexible coupled wing systems under external disturbances is studied. We briefly describe the contributions of this work: (i) Considering the unknown boundary disturbances of the flexible wing, the model is updated on this basis. (ii) The proposed observer can guarantee that the disturbance errors can converge to zero in a finite time. (iii) The vibration problem of the wing structure is well solved, and there is no spillover effect in the system control.

The rest of this paper is organized as follows: the dynamics of the coupled aircraft wing system are presented in Section 2. Section 3 presents the new finite-time control

scheme and a detailed analysis of the stability of the closed-loop system. Simulation and analysis are carried out in Section 4. Finally, the conclusion is given in Section 5.

2. Problem Statement

2.1. System Model. A vibrating flexible flapping-wing aircraft subject to unknown disturbances is depicted in Figure 1. In this paper, \mathcal{R} represents a collection of real numbers, x_c is the length between the shear center and the mass center of the wing cross section, and x_{ac} is the distance from the aerodynamic center to the shear center of the wing. ρ is the mass per unit of the wing, I_p describes the polar moment of inertia, EI_b denotes the bending rigidity, GJ represents torsion rigidity, $g_h(z, t)$ denotes the distributed disturbance, ξ represents the Kelvin–Voigt damping coefficient, and $\tau_1(t)$ and $\tau_2(t)$ represent the control inputs. Besides, $g_1(t)$ and $g_2(t)$ are the unknown disturbances at the wing tip $z = s$. For simplicity, some symbols are replaced with $(\dot{\cdot}) = \partial(\cdot)/\partial t$, $(\cdot)' = \partial(\cdot)/\partial z$, $(\ddot{\cdot}) = \partial^2(\cdot)/\partial z^2 \partial t$, $(\cdot)'' = \partial^2(\cdot)/\partial z^2$, and $(\ddot{\cdot}) = \partial^2(\cdot)/\partial t^2$.

The kinetic energy $E_k(t)$ of the flexible wing in this study is given directly as follows:

$$E_k(t) = \frac{1}{2}\rho \int_0^s [\dot{q}(z, t)]^2 dz + \frac{1}{2}I_p \int_0^s [\dot{\theta}(z, t)]^2 dz. \quad (1)$$

$E_p(t)$ denotes the potential energy of the flexible wing:

$$E_p(t) = \frac{1}{2}EI_b \int_0^s [q''(z, t)]^2 dz + \frac{1}{2}GJ \int_0^s [\theta'(z, t)]^2 dz. \quad (2)$$

The virtual work of damping on the wing is expressed by

$$\begin{aligned} \delta H_d(t) = & -\xi EI_b \int_0^s \dot{q}''(z, t) \delta q''(z, t) dz \\ & - \xi GJ \int_0^s \dot{\theta}'(z, t) \delta \theta'(z, t) dz. \end{aligned} \quad (3)$$

The virtual work of the coupling of bending and torsion stiffness is presented as follows:

$$\begin{aligned} \delta H_c(t) = & \rho x_c c \int_0^s \ddot{q}(z, t) \delta \theta(z, t) dz \\ & + \rho x_c c \int_0^s \ddot{\theta}(z, t) \delta q(z, t) dz. \end{aligned} \quad (4)$$

The virtual work of unknown disturbance is given as

$$\begin{aligned} \delta H_f(t) = & \int_0^s [g_h(z, t) \delta q(z, t) - x_{ac} g_h(z, t) \delta \theta(z, t)] dz \\ & + g_1(t) \delta q(s, t) + g_2(t) \delta \theta(s, t). \end{aligned} \quad (5)$$

The virtual work $\delta H_\tau(t)$ performed by the control inputs can be obtained as follows:

$$\delta H_\tau(t) = \tau_1(t) \delta q(s, t) + \tau_2(t) \delta \theta(s, t). \quad (6)$$

Then, we add all the virtual works of the system:

$$\delta H(t) = \delta [H_c(t) + H_d(t) + H_f(t) + H_\tau(t)]. \quad (7)$$

Hamilton's principle is formulated as follows [47, 48]:

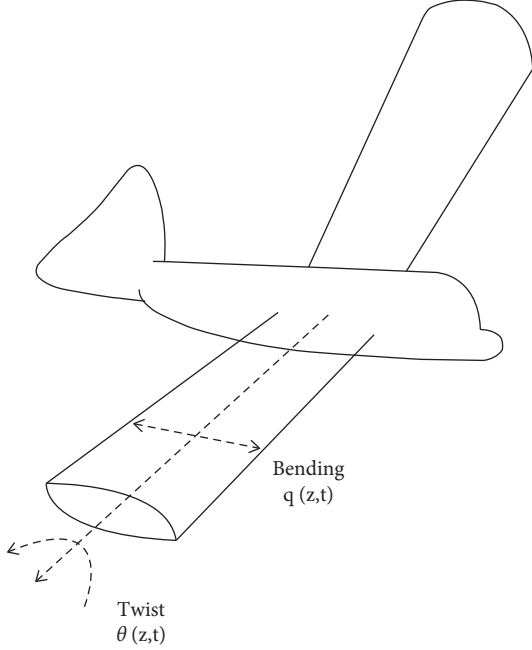


FIGURE 1: Flapping-wing robotic aircraft.

$$\int_{t_1}^{t_2} \delta [E_k(t) - E_p(t) + H(t)] dt = 0. \quad (8)$$

According to (8), we can obtain the flexible wing dynamics as follows:

$$\begin{aligned} I_p \ddot{\theta}(z, t) - GJ\theta''(z, t) - \rho x_e c \ddot{q}(z, t) \\ - \xi GJ\dot{\theta}''(z, t) = -x_{ac} g_h(z, t), \\ \rho \ddot{q}(z, t) + EI_b q''''(z, t) \\ - \rho x_e c \ddot{\theta}(z, t) + \xi EI_b \dot{q}''''(z, t) = g_h(z, t). \end{aligned} \quad (9)$$

Moreover, we can get the boundary conditions of the system:

$$\begin{aligned} q(0, t) = q'(0, t) = q''(s, t) = \theta(0, t) = 0, \\ EI_b q''''(s, t) + \xi EI_b \dot{q}''''(s, t) = -\tau_1(t) - g_1(t), \\ GJ\theta'(s, t) + \xi GJ\dot{\theta}'(s, t) = \tau_2(t) + g_2(t). \end{aligned} \quad (10)$$

2.2. Preliminaries. The lemmas and assumption are proposed here to facilitate the later controller design and stability analysis.

Assumption 1. For $g_1(t)$, $g_2(t)$, and $g_h(z, t)$, we suppose that there exist $\zeta_1 > 0$, $\zeta_2 > 0$, and $g_{h\max} > 0$ such that $|g_1(t)| \leq \zeta_1$, $|g_2(t)| \leq \zeta_2$, and $|g_h(z, t)| \leq g_{h\max}$, $(z, t) \in t[0, s]n \times q[0, +\infty)$. This assumption is reasonable because the energy of external disturbances is limited.

Lemma 1 (see [49]). *If there exist $\bar{\omega}_1(s, t)$, $\bar{\omega}_2(s, t) \in \mathcal{R}$, $p > 0$ with $(s, t) \in t[0, f]n \times q[0, +\infty)$, we can obtain*

$$\bar{\omega}_1 \bar{\omega}_2 \leq \frac{1}{p} \bar{\omega}_1^2 + p \bar{\omega}_2^2. \quad (11)$$

Lemma 2 (see [49]). *If $\bar{\omega}(s, t) \in \mathcal{R}$ satisfies the condition $\bar{\omega}(0, t) = 0$, then*

$$\bar{\omega}^2 \leq f \int_0^f \bar{\omega}^2 ds, \quad (12)$$

where $(s, t) \in t[0, f]n \times q[0, +\infty)$.

Lemma 3. *The following inequality for the positive definite function $Q(t)$ is used to derive our main results as follows:*

$$\dot{Q}(t) \leq -\phi_1 Q(t) - \phi_2 Q^{\phi_3}(t). \quad (13)$$

Then, the function $Q(t)$ will have an equilibrium point. It can converge to the point in a finite time as follows:

$$t_f \leq \frac{1}{\phi_1(1-\phi_3)} \ln \frac{\phi_1 Q^{1-\phi_3}(0) + \phi_2}{\phi_2}, \quad (14)$$

with $\phi_1 > 0$, $\phi_2 > 0$, and $0 < \phi_3 < 1$ being undetermined constants.

3. Control Design

The emphasis of the research is how to construct boundary controllers to suppress the vibration of a coupled wing system. For the sake of the control goal, a new control scheme based on finite-time disturbance observer is adopted, which can ensure the stability of the closed-loop system. The control block diagram of the system is shown in Figure 2.

First, the boundary control laws are proposed as follows:

$$\begin{aligned} \tau_1(t) &= -k_1 [aq(s, t) + b\dot{q}(s, t)] - \hat{g}_1(t), \\ \tau_2(t) &= -k_2 [a\theta(s, t) + b\dot{\theta}(s, t)] - \hat{g}_2(t), \end{aligned} \quad (15)$$

where $k_1, k_2 > 0$.

Step 1. The auxiliary functions are defined as follows:

$$\sigma_1(t) = -\xi EI_b q''''(s, t) - \nu_1(t), \quad (16)$$

$$\begin{aligned} \dot{\nu}_1(t) &= \kappa_1 \sigma_1(t) + \kappa_2 \text{sign}(\sigma_1(t)) + \kappa_3 \sigma_1^{2a_1 - a_2/a_2}(t) \\ &\quad + \tau_1(t) + EI_b q''''(s, t), \end{aligned} \quad (17)$$

$$\sigma_2(t) = \xi GJ\theta'(s, t) - \nu_2(t), \quad (18)$$

$$\begin{aligned} \dot{\nu}_2(t) &= \kappa_4 \sigma_2(t) + \kappa_5 \text{sign}(\sigma_2(t)) + \kappa_6 \sigma_2^{2b_1 - b_2/b_2}(t) \\ &\quad + \tau_2(t) - GJ\theta'(s, t). \end{aligned} \quad (19)$$

To arrive at the control objectives that deal with the unknown disturbances $g_1(t)$ and $g_2(t)$, we define the estimation form of disturbance terms as follows:

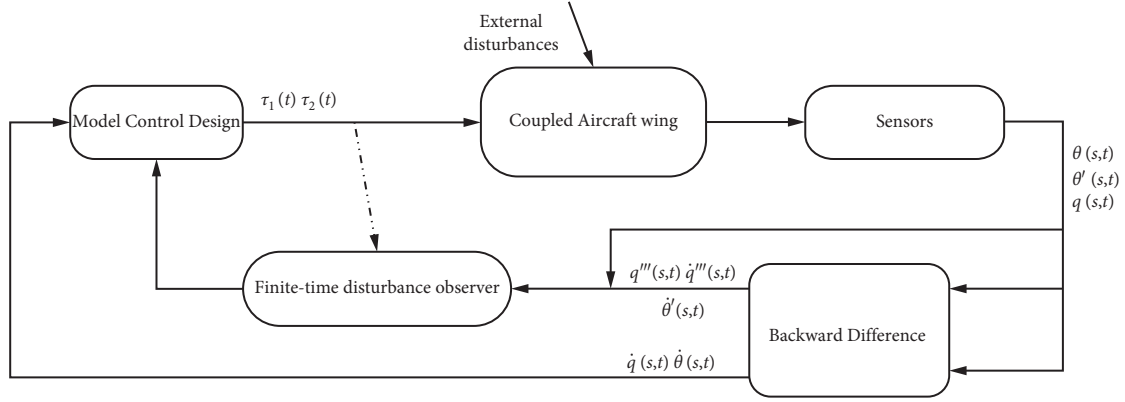


FIGURE 2: Finite-time control for the coupled aircraft wing.

$$\hat{g}_1(t) = \kappa_1 \sigma_1(t) + \kappa_2 \text{sign}(\sigma_1(t)) + \kappa_3 \sigma_1^{2a_1 - a_2/a_2}(t), \quad (20)$$

$$\hat{g}_2(t) = \kappa_4 \sigma_2(t) + \kappa_5 \text{sign}(\sigma_2(t)) + \kappa_6 \sigma_2^{2b_1 - b_2/b_2}(t), \quad (21)$$

where $\kappa_1, \kappa_2, \kappa_3, \kappa_4, \kappa_5$, and κ_6 are all positive numbers. Moreover, a_1, a_2, b_1 , and b_2 are all odd numbers that satisfied $a_1 < a_2 < 2a_1$ and $b_1 < b_2 < 2b_1$.

Step 2. We choose Lyapunov candidate function as

$$W(t) = W_a(t) + W_o(t), \quad (22)$$

where

$$\begin{aligned} W_a(t) &= \frac{b}{2}\rho \int_0^s [\dot{q}(z,t)]^2 dz + \frac{b}{2}EI_b \int_0^s [q''(z,t)]^2 dz + \frac{b}{2}I_p \int_0^s [\dot{\theta}(z,t)]^2 dz + \frac{b}{2}GJ \int_0^s [\theta'(z,t)]^2 dz, \\ W_o(t) &= a\rho \int_0^s \dot{q}(z,t)q(z,t)dz + aI_p \int_0^s \dot{\theta}(z,t)\theta(z,t)dz \\ &\quad - a\rho x_c \int_0^s [\dot{q}(z,t)\theta(z,t) + q(z,t)\dot{\theta}(z,t)]dz - bx_c \int_0^s \dot{q}(z,t)\dot{\theta}(z,t)dz, \end{aligned} \quad (23)$$

where $a > 0$ and $b > 0$.

Remark 1. In this paper, we use the Lyapunov direct method to design the controller given in the specific form of Lyapunov function, where $W_a(t)$ is derived from the system kinetic energy $E_k(t)$ and potential energy $E_p(t)$, which is called the energy term. $W_o(t)$ is derived from the coupling of various state quantities of the system and becomes a crossing term. $Q_1(t)$ and $Q_2(t)$ will be given later in this article, which represent the auxiliary items of the system to deal with disturbance errors. By adjusting the control laws (15)–(21) and Lyapunov candidate function, we ensure that the derivative of Lyapunov function $W(t)$ has an upper bound and let $Q_1(t)$ and $Q_2(t)$ satisfy Lemma 3 so as to prove the uniform boundedness of state variables and the finite-time convergence of disturbance errors.

Remark 2. The control signals $q(s,t), \dot{q}(s,t), \theta(s,t), \dot{\theta}(s,t), q'''(s,t), \theta'(s,t), \dot{q}'''(s,t)$, and $\dot{\theta}'(s,t)$ in the control equations (15)–(21) can be obtained during execution, where $q(s,t)$ and $\theta(s,t)$ are obtained by the laser displacement sensors, and $\theta'(s,t)$ is obtained by the inclinometer. The

remaining variables $\dot{q}(s,t), \dot{\theta}(s,t), q'''(s,t), \dot{q}'''(s,t)$, and $\dot{\theta}'(s,t)$ are further obtained by the backward difference algorithms.

Theorem 1. The Lyapunov function (22) has upper and lower bounds:

$$0 \leq \lambda_2 \kappa(t) \leq W(t) \leq \lambda_1 \kappa(t), \quad (24)$$

where λ_1 and λ_2 are positive numbers.

Proof. A new function is defined as follows:

$$\kappa(t) = \int_0^s \left\{ [\dot{q}(z,t)]^2 + [q''(z,t)]^2 + [\dot{\theta}(z,t)]^2 + [\theta'(z,t)]^2 \right\} dz. \quad (25)$$

Hence, we obtain

$$y_2 \kappa(t) \leq W_a(t) \leq y_1 \kappa(t), \quad (26)$$

where y_1 and y_2 are two positive numbers, $y_1 = (b/2)\max\{EI_b, I_p, GJ, \rho\}$, and $y_2 = (b/2)\min\{\rho, EI_b, I_p, GJ\}$. For $W_o(t)$, we can obtain

$$\begin{aligned}
|W_o(t)| \leq & a\rho \left\{ \int_0^s [\dot{q}(z,t)]^2 dz + s^4 \int_0^s [q''(z,t)]^2 dz \right\} + aI_p \left\{ \int_0^s [\dot{\theta}(z,t)]^2 dz + s^2 \int_0^s [\theta'(z,t)]^2 dz \right\} \\
& + a\rho x_e c \left\{ \int_0^s [\dot{q}(z,t)]^2 dz + \int_0^s [\dot{\theta}(z,t)]^2 dz \right\} + a\rho x_e c \left\{ s^4 \int_0^s [q''(z,t)]^2 dz + s^2 \int_0^s [\theta'(z,t)]^2 dz \right\} \\
& + b\rho x_e c \left\{ \int_0^s [\dot{q}(z,t)]^2 dz + \int_0^s [\dot{\theta}(z,t)]^2 dz \right\} + (aI_p + a\rho x_e c + b\rho x_e c) \int_0^s [\dot{\theta}(z,t)]^2 dz + (aI_p + a\rho x_e c) s^2 \\
& \cdot \int_0^s [\theta'(z,t)]^2 dz \leq y_3 \kappa(t),
\end{aligned} \tag{27}$$

where $y_3 = \max\{a\rho + a\rho x_e c + b\rho x_e c, (a\rho + a\rho x_e c)s^4, aI_p + a\rho x_e c + b\rho x_e c, (aI_p + a\rho x_e c)s^2\}$ and b satisfies $b > 2y_3/\min\{\rho, I_p, EI_b, GJ\}$.

Now, we can prove equation (24) as follows:

$$O \leq \lambda_2 \kappa(t) \leq W(t) \leq \lambda_1 \kappa(t), \tag{28}$$

where $\lambda_2 = y_2 - y_3$ and $\lambda_1 = y_1 + y_3$. \square

Step 3. The derivative of $W_a(t)$ gives

$$\begin{aligned}
\dot{W}_a(t) \leq & -b\dot{q}(s,t)[EI_b q'''(s,t) + \xi EI_b \dot{q}'''(s,t)] + b\dot{\theta}(s,t)[GJ\theta'(s,t) + \xi GJ\dot{\theta}'(s,t)] \\
& + b\rho x_e c \int_0^s [\dot{q}(z,t)\ddot{\theta}(z,t) + \ddot{q}(z,t)\dot{\theta}(z,t)] dz - \left(\frac{b\xi GJ}{2s^2} - \eta_2 b x_a c\right) \int_0^s [\dot{\theta}(z,t)]^2 dz - \left(\frac{b\xi EI_b}{2s^4} - \eta_1 b\right) \int_0^s [\dot{q}(z,t)]^2 dz \\
& + \left(\frac{b}{\eta_1} + \frac{b x_a c}{\eta_2}\right) s g_{h\max}^2 - \frac{b\xi EI_b}{2} \int_0^s [q''(z,t)]^2 dz - \frac{b\xi GJ}{2} \int_0^s [\theta''(z,t)]^2 dz.
\end{aligned} \tag{29}$$

Similarly, differentiating $W_o(t)$ leads to

$$\begin{aligned}
\dot{W}_o(t) = & a\rho \int_0^s \ddot{q}(z,t)q(z,t) dz \\
& + aI_p \int_0^s \ddot{\theta}(z,t)\theta(z,t) dz \\
& - a\rho x_e c \int_0^s \ddot{q}(z,t)\theta(z,t) dz \\
& - a\rho x_e c \int_0^s q(z,t)\ddot{\theta}(z,t) dz \\
& + a\rho \int_0^s [\dot{q}(z,t)]^2 dz + aI_p \int_0^s [\dot{\theta}(z,t)]^2 dz \\
& - b\rho x_e c \int_0^s \ddot{q}(z,t)\dot{\theta}(z,t) dz \\
& - b\rho x_e c \int_0^s \dot{q}(z,t)\ddot{\theta}(z,t) dz \\
& - 2a\rho x_e c \int_0^s [\dot{q}(z,t)\dot{\theta}(z,t)] dz.
\end{aligned} \tag{30}$$

Considering (10) and controllers (15)–(21), we obtain

$$\begin{aligned}
\dot{W}(t) \leq & -\left(k_2 - \frac{1}{\eta_9}\right)[a\theta(s,t) + b\dot{\theta}(s,t)]^2 + \bar{g}_2^2(t)\eta_9 \\
& -\left(k_1 - \frac{1}{\eta_8}\right)[aq(s,t) + b\dot{q}(s,t)]^2 + \bar{g}_1^2(t)\eta_8 \\
& -\left(aEI_b - \frac{a\xi EI_b}{\eta_3} - \eta_6 a s^4\right) \int_0^s [q''(z,t)] dz \\
& -\left(aGJ - \frac{a\xi GJ}{\eta_4} - \eta_7 s^2 x_a c\right) \int_0^s [\theta'(z,t)]^2 dz \\
& -\left(\frac{b\xi EI_b}{2s^4} - \eta_1 b - a\rho - 2a\rho x_e c \eta_5\right) \int_0^s [\dot{q}(z,t)]^2 dz \\
& -\left(\frac{b\xi GJ}{2s^2} - \eta_2 b x_a c - aI_p - \frac{2a\rho x_e c}{\eta_5}\right) \int_0^s [\dot{\theta}(z,t)]^2 dz \\
& -\left(\frac{b\xi EI_b}{2} - a\xi EI_b \eta_3\right) \int_0^s [q''(z,t)]^2 dz \\
& -\left(\frac{b\xi GJ}{2} - a\xi GJ \eta_4\right) \int_0^s [\theta'(z,t)]^2 dz \\
& + \left(\frac{b}{\eta_1} + \frac{b x_a c}{\eta_2} + \frac{a}{\eta_6} + \frac{a x_a c}{\eta_7}\right) s g_{h\max}^2 \\
\leq & -\lambda_3 \kappa(t) + \varepsilon,
\end{aligned} \tag{31}$$

where $\eta_i > 0, i = 1 \dots 9$. In addition, because $\widehat{g}_1(t)$ and $\widehat{g}_2(t)$ are estimates of $g_1(t)$ and $g_2(t)$, under the action of disturbance observers, the errors between them are also bounded. Thus, there exist positive numbers ζ_3 and ζ_4 , satisfying $|\widehat{g}_1(t)| \leq \zeta_3$ and $|\widehat{g}_2(t)| \leq \zeta_4$.

Let $\mu_1 = k_2 - (1/\eta_9) > 0$ and $\mu_2 = k_1 - (1/\eta_8) > 0$. The selection of intermediate parameters is provided as follows:

$$\mu_3 = \frac{b\xi EI_b}{2s^4} - \eta_1 b - a\rho - 2a\rho x_e c \eta_5 > 0,$$

$$\mu_4 = \frac{b\xi GJ}{2s^2} - \eta_2 b x_a c - aI_p - \frac{2a\rho x_e c}{\eta_5} > 0,$$

$$\mu_5 = aEI_b - \frac{a\xi EI_b}{\eta_3} - \eta_6 a s^4 > 0,$$

$$\mu_6 = aGJ - \frac{a\xi GJ}{\eta_4} - \eta_7 a s_2 x_a c > 0,$$

$$\lambda_3 = \min\{\mu_3, \mu_4, \mu_5, \mu_6\} > 0,$$

$$\varepsilon = \left(\frac{b}{\eta_1} + \frac{b x_a c}{\eta_2} + \frac{a}{\eta_6} + \frac{a x_a c}{\eta_7} \right) s g_{h \max}^2 + \eta_9 \zeta_4^2 + \eta_8 \zeta_3^2 < +\infty. \quad (32)$$

Therefore, we can obtain

$$\dot{W}(t) \leq -\lambda W(t) + \varepsilon, \quad (33)$$

where $\lambda = \lambda_3/\lambda_1$.

Theorem 2. *Through the dynamical system and the proposed control laws, the controlled system's states $q(z, t)$ and $\theta(z, t)$ are uniformly ultimately bounded.*

Proof. Invoking (33) and multiplying $e^{\lambda t}$ yields

$$\dot{W}(t)e^{\lambda t} \leq -\lambda W(t)e^{\lambda t} + \varepsilon e^{\lambda t}. \quad (34)$$

Integrating (34), we have

$$W(t) \leq \left[W(0) - \frac{\varepsilon}{\lambda} \right] e^{-\lambda t} + \frac{\varepsilon}{\lambda} \leq W(0)e^{-\lambda t} + \frac{\varepsilon}{\lambda}. \quad (35)$$

Furthermore, invoking (24) and Lemma 2, we have

$$\begin{aligned} \frac{1}{s^3} [q(z, t)]^2 &\leq \frac{1}{s^2} \int_0^s [q'(z, t)]^2 dz \\ &\leq \int_0^s [q''(z, t)]^2 dz \leq \kappa(t) \leq \frac{1}{\lambda} W(t). \end{aligned} \quad (36)$$

Finally, this results in

$$\begin{aligned} |q(z, t)| &\leq \sqrt{\frac{s^3}{\lambda_2} \left(W(0)e^{-\lambda t} + \frac{\varepsilon}{\lambda} \right)}, \forall (z, t) \in [0, s] \times [0, +\infty), \\ |\theta(z, t)| &\leq \sqrt{\frac{s}{\lambda_2} \left(W(0)e^{-\lambda t} + \frac{\varepsilon}{\lambda} \right)}, \forall (z, t) \in [0, s] \times [0, +\infty). \end{aligned} \quad (37)$$

□

Theorem 3. *Provided that $\kappa_2 \geq \zeta_1$ holds, the disturbance error $\widehat{g}_1(t)$ ensures convergence to zero before $t \geq t_{f1}$, where*

$$t_{f1} \leq \frac{a_2}{2\kappa_1(a_2 - a_1)} \ln \left\{ \frac{\kappa_1 Q_1^{a_2 - a_1/a_2}(0) + 2^{(a_1/a_2) - 1} \kappa_3}{2^{a_1/a_2 - 1} \kappa_3} \right\}, \quad (38)$$

with $Q_1(0)$ denoting an initial value of $Q_1(t)$, and $Q_1(t) = \sigma_1^2(t)/2$

Theorem 4. *Provided that $\kappa_5 \geq \zeta_2$ holds, the disturbance error $\widehat{g}_2(t)$ converges to zero before $t \geq t_{f2}$, where*

$$t_{f2} \leq \frac{b_2}{2\kappa_4(b_2 - b_1)} \ln \left\{ \frac{\kappa_4 Q_2^{b_2 - b_1/b_2}(0) + 2^{(b_1/b_2) - 1} \kappa_6}{2^{b_1/b_2 - 1} \kappa_6} \right\}, \quad (39)$$

with $Q_2(0)$ denoting an initial value of $Q_2(t)$, and $Q_2(t) = \sigma_2^2(t)/2$.

Proof. Differentiating $Q_1(t)$ and invoking (16) and (17), we have

$$\begin{aligned} \dot{Q}_1(t) &= \sigma_1(t) \dot{\sigma}_1(t) \\ &= \sigma_1(t) [\xi EI_b \dot{q}'''(s, t) - \dot{\nu}_1(t)] \\ &= \sigma_1(t) [\xi EI_b \dot{q}'''(s, t) - \kappa_1 \phi_1(t) - \kappa_2 \text{sign}(\phi_1(t)) - \kappa_3 \sigma_1^{2a_1 - a_2/a_2}(t) - \tau_1(t) - EI_b q(s, t)] \\ &= -\kappa_1 \sigma_1^2(t) - \kappa_2 |\sigma_1(t)| - \kappa_3 \sigma_1(t)^{2a_1 - a_2/a_2}(t) + \sigma_1(t) + g_1(t) \\ &\leq -\kappa_1 \sigma_1^2(t) - (\kappa_2 - \zeta_1) |\sigma_1(t)| - \kappa_3 \phi_1(t) \sigma_1^{2a_1 - a_2/a_2}(t) \\ &\leq -\kappa_1 \sigma_1^2(t) - \kappa_3 \sigma_1(t) \sigma_1^{2a_1 - a_2/a_2}(t). \end{aligned} \quad (40)$$

Therefore, $Q_1(t)$ will converge to an equilibrium point in a finite time t_{f1} . We define $p = a_1/a_2$, and then we multiply (40) by $Q_1^p(t)/(1-p)$ to derive the following:

$$dQ_1 \leq \frac{\{-2\kappa_1(1-p)Q_1^{1-p}(t) - 2^p \kappa_3(1-p)\} Q_1^p(t)}{((1-p)dt)}. \quad (41)$$

Letting $\iota(t) = Q_1^{1-p}(t)$, with the analysis made in (41), we derive

$$\dot{\iota}(t) \leq -2\kappa_1(1-p)\iota(t) - 2^p\kappa_3(1-p). \quad (42)$$

Multiplying (42) by $e^{2\kappa_1(1-p)t}$ results in

$$\begin{aligned} \dot{\iota}(t)e^{2\kappa_1(1-p)t} &\leq -2\kappa_1(1-p)e^{2\kappa_1(1-p)t}\iota(t) \\ &\quad - 2^p\kappa_3(1-p)e^{2\kappa_1(1-p)t}. \end{aligned} \quad (43)$$

Then, we obtain

$$\frac{d(\iota(t)e^{2\kappa_1(1-p)t})}{dt} \leq -2^p\kappa_3(1-p)e^{2\kappa_1(1-p)t}. \quad (44)$$

We apply the integral of (44) as follows:

$$\iota(t) \leq -\frac{2^{(p-1)}\kappa_3}{\kappa_1} + \left\{ \iota(0) + \frac{2^{(p-1)}\kappa_3}{\kappa_1} \right\} e^{-2\kappa_1(1-p)t}. \quad (45)$$

Equation (45) can be rewritten as

$$Q_1^{1-p}(t) \leq -\frac{2^{(p-1)}\kappa_3}{\kappa_1} + \left\{ Q_1^{1-p}(0) + \frac{2^{(p-1)}\kappa_3}{\kappa_1} \right\} e^{-2\kappa_1(1-p)t}. \quad (46)$$

Invoking $Q_1(t)$ and (40) yields

$$Q_1(t) \geq 0, \dot{Q}_1(t) \leq 0. \quad (47)$$

According to (46) and (47), we have

$$\left\{ Q_1^{1-p}(0) + \frac{2^{(p-1)}\kappa_3}{\kappa_1} \right\} e^{-2\kappa_1(1-p)t_{f1}} - \frac{2^{(p-1)}\kappa_3}{\kappa_1} \geq 0. \quad (48)$$

When $t = t_{f1}$ and $Q_1(t_{f1}) = 0$, then we have $Q_1(t) \equiv 0$. We can further obtain

$$e^{2\kappa_1(1-p)t_{f1}} \leq \frac{\kappa_1 Q_1^{1-p}(0) + 2^{(p-1)}\kappa_3}{2^{(p-1)}\kappa_3}. \quad (49)$$

Taking the logarithm for it as follows:

$$\begin{aligned} t_{f1} &\leq \frac{1}{2\kappa_1(1-p)} \ln \left\{ \frac{\kappa_1 Q_1^{1-p}(0) + 2^{(p-1)}\kappa_3}{2^{(p-1)}\kappa_3} \right\} \\ &= \frac{a_2}{2\kappa_1(a_2 - a_1)} \ln \left\{ \frac{\kappa_1 Q_1^{a_2 - a_1/a_2}(0) + 2^{a_1/a_2} - 1\kappa_3}{2^{a_1/a_2 - 1}\kappa_3} \right\}. \end{aligned} \quad (50)$$

In a word, considering $\kappa_2 \geq \zeta_1$, when $t \geq t_{f1}$, we derive

$$Q_1(t) \equiv 0. \quad (51)$$

Invoking (51) and $Q_1(t)$, we obtain the following when $t \geq t_{f1}$,

$$\sigma_1(t) \equiv 0. \quad (52)$$

Moreover, when $t \geq t_{f1}$, we arrive at

$$\dot{\sigma}_1(t) \equiv 0. \quad (53)$$

The disturbance estimation error is expressed as follows:

$$\tilde{g}_1(t) = g_1(t) - \hat{g}_1(t). \quad (54)$$

The combination of (10), (20), and (54) gives

$$\begin{aligned} \tilde{g}_1(t) &= -\tau_1(t) - \xi EI_b \dot{q}'''(s, t) - EI_b \dot{q}'''(s, t) - \hat{g}_1(t) \\ &= -\xi EI_b \dot{q}'''(s, t) + \left\{ -\tau_1(t) - (EI_b \dot{q}'''(s, t) + \kappa_1 \sigma_1(t) \right. \\ &\quad \left. + \kappa_2 \text{sign}(\sigma_1(t) + \kappa_3 \sigma_1^{2a_1 - a_2/a_2})) \right\} \\ &= \dot{\sigma}_1(t). \end{aligned} \quad (55)$$

Invoking (53) and (55), we can conclude that if $\kappa_2 \geq \zeta_1$ holds, $\tilde{g}_1(t)$ converges to zero for $\forall t \geq t_{f1}$. Similarly, we can prove that if $\kappa_5 \geq \zeta_2$ holds, $\tilde{g}_2(t)$ converges to zero for $\forall t \geq t_{f2}$. \square

4. Simulation

In this section, the finite difference method is used to approximate the dynamics of the system with system parameters as $s = 2.0m$, $x_c c = 0.35m$, $EI_b = 0.2Nm^2$, $GJ = 0.5Nm^2$, $\rho = 10kg/m$, $x_a c = 0.05N$, $I_p = 1.5kgm$, and $\xi = 0.6$. The initial condition of the system is set as $q(z, 0) = z/s$, and $\theta(z, 0) = (\pi z/2s)$. Besides, we have $\dot{q}(z, 0) = 0$ and $\dot{\theta}(z, 0) = 0$. The inevitable external disturbances are defined as follows:

$$\begin{aligned} g_h(z, t) &= (1 + 3 \cos(3\pi t) + \sin(\pi t))z/30 \\ g_1(t) &= 0.02 + 0.06 \sin(0.05t) \\ g_2(t) &= 0.04 + 0.02 \sin(0.1t). \end{aligned} \quad (56)$$

Figures 3 and 4 show the displacement of the coupled wing without control, that is, $\tau_1(t) = 0$ and $\tau_2(t) = 0$. Figures 5 and 6 depict the three-dimensional representation of flexible wings with boundary control. The control parameters are chosen as $k_1 = 2$, $k_2 = 1$, $\kappa_1 = 0.8$, $\kappa_2 = 1$, $\kappa_3 = 4$, $\kappa_4 = 0.8$, $\kappa_5 = 1$, $\kappa_6 = 4$, $a_1 = b_1 = 7$, and $a_2 = b_2 = 13$. Figures 7 and 8 represent the response generated by the control inputs $\tau_1(t)$ and $\tau_2(t)$. As shown in Figures 9 and 10, we can conclude that the control design can ensure that the flexible wing system has good performance by comparing with the freely vibrating situation. At last, we provide two pictures Figures 11 and 12 about the disturbance estimation errors. It can be concluded from the figures that the disturbance estimation errors can converge to zero in a finite time.

The simulation results Figures 3–12 show that the designed controller can effectively suppress the vibration of flexible wing, and the bending and torsion deformation of a flexible wing $q(z, t)$ and $\theta(z, t)$ under the presented control are guaranteed to be stable. The last two figures show the finite-time convergence of the disturbance estimation errors $\tilde{g}_1(t)$ and $\tilde{g}_2(t)$. In order to further highlight the advantages of the proposed control strategy, a boundary control strategy based on the nonlinear disturbance observers (DOBC) is expressed as follows:

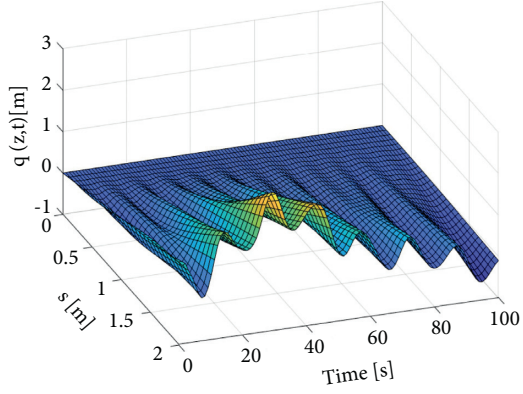


FIGURE 3: Bending displacement of the wing without control.

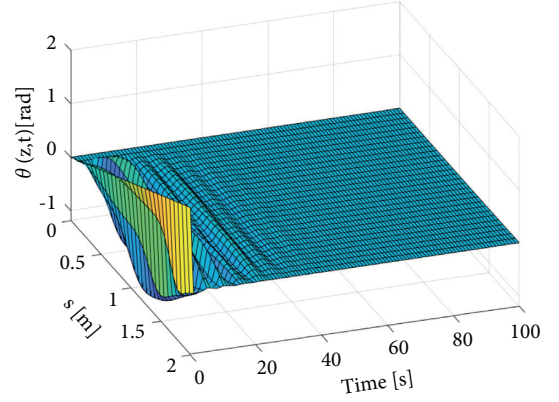


FIGURE 6: Twist displacement of the wing with the proposed control.

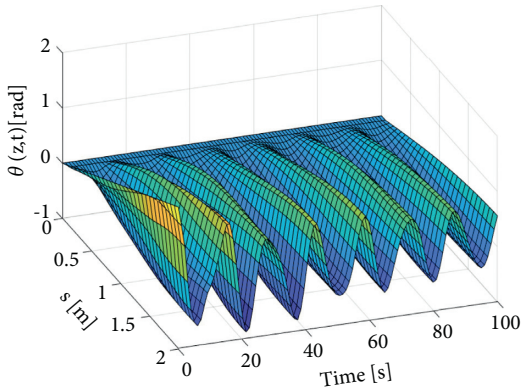


FIGURE 4: Twist displacement of the wing under without control.

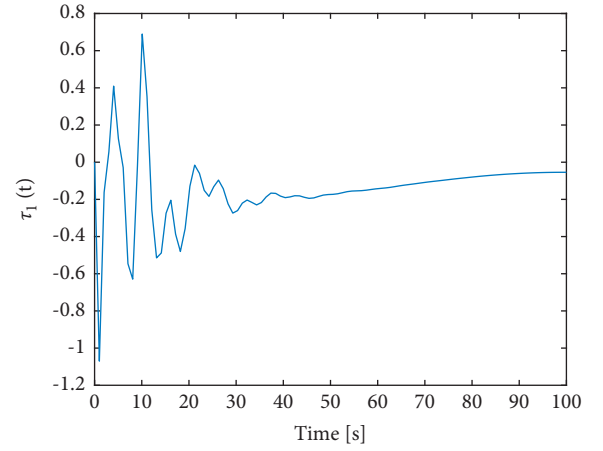
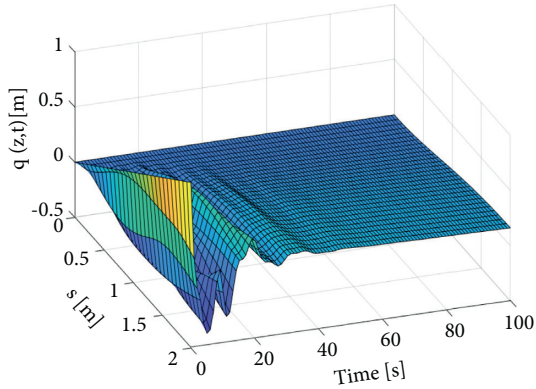
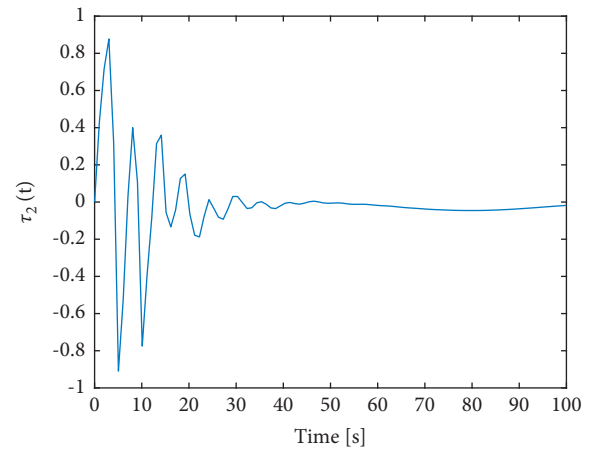
FIGURE 7: Designed control command $\tau_1(t)$ with the proposed control.

FIGURE 5: Bending displacement of the wing with the proposed control.

FIGURE 8: Designed control command $\tau_2(t)$ with the proposed control.

$$\begin{aligned}
 \tau_1(t) &= -k_1 [aq(s,t) + bq(s,t)] - \hat{g}_1(t), \\
 \tau_2(t) &= -k_2 [a\theta(s,t) + b\dot{\theta}(s,t)] - \hat{g}_2(t), \\
 \hat{g}_1(t) &= -\xi EI q'''(s,t) + \sigma_1(t), \\
 \dot{\sigma}_1(t) &= -\tau_1(t) - EI_b q'''(s,t) - \hat{g}_1(t), \\
 \hat{g}_2(t) &= \xi GJ \theta'(s,t) + \sigma_2(t), \\
 \dot{\sigma}_2(t) &= -\tau_2(t) + GJ \theta'(s,t) - \hat{g}_2(t),
 \end{aligned} \tag{57}$$

where parameter selections are consistent with the above design. Figures 13–20 show the control effect of the system using the DOBC strategy. It can be seen that the control

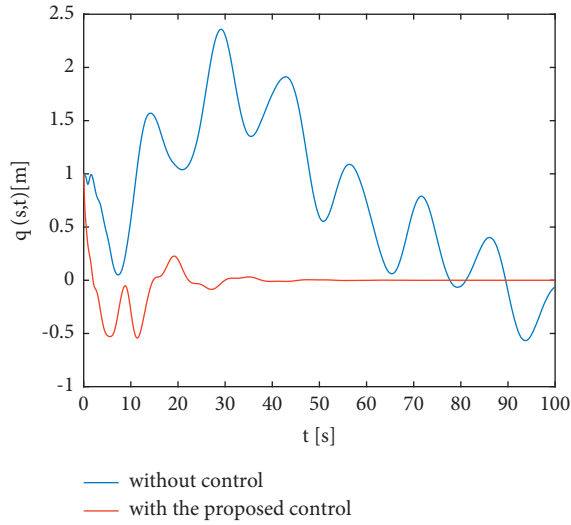


FIGURE 9: Boundary bending displacement of the wing with the proposed control.

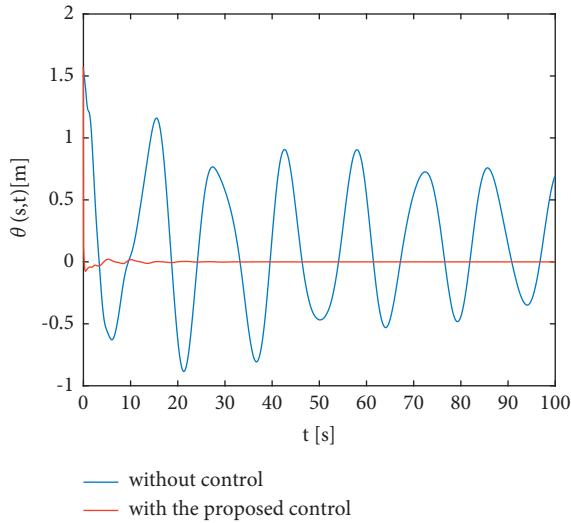


FIGURE 10: Boundary twist displacement of the wing with the proposed control.

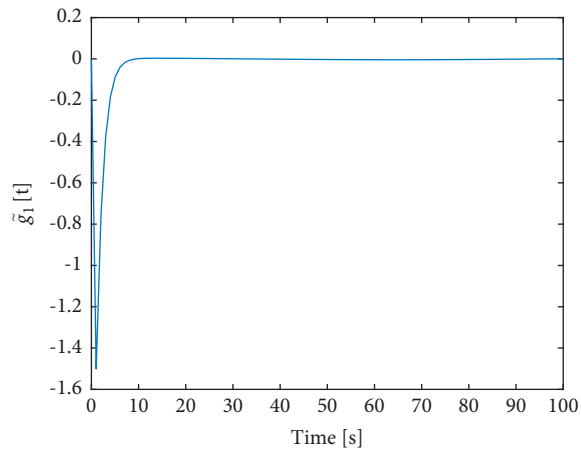


FIGURE 11: Disturbance estimation error $\tilde{g}_1(t)$ with the proposed control.

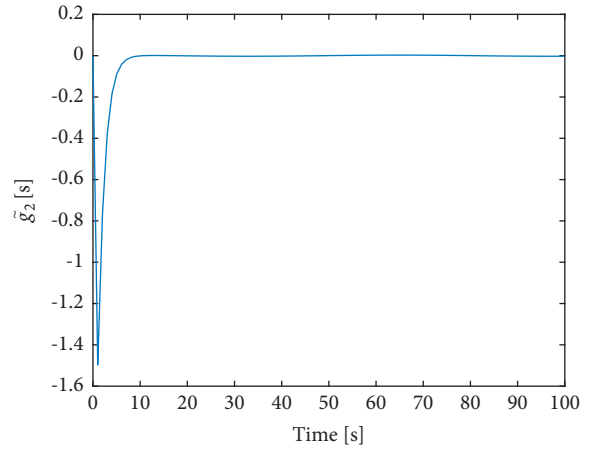


FIGURE 12: Disturbance estimation error $\tilde{g}_2(t)$ with the proposed control.

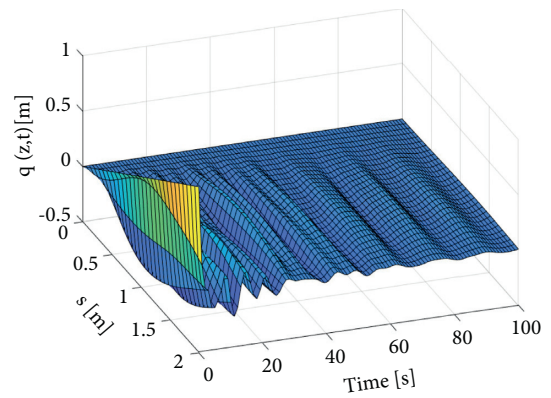


FIGURE 13: Bending displacement of the wing with DOBC.

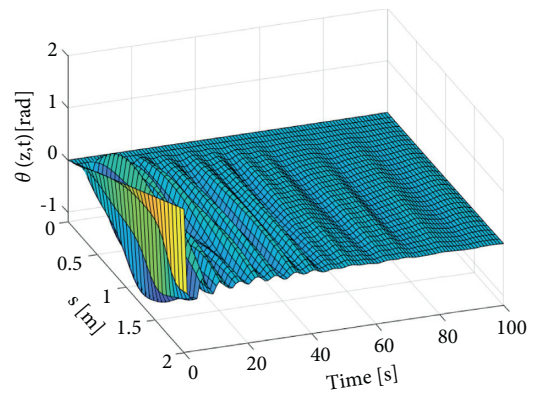


FIGURE 14: Twist displacement of the wing with DOBC.

effect is worse than that of the control strategy proposed in this paper. As can be seen from the figures, the inputs $\tau_1(t)$ and $\tau_2(t)$ and displacements $q(z,t)$, $\theta(z,t)$, $q(s,t)$, and $\theta(s,t)$ cannot converge to zero quickly. Although the disturbance observers can track the change of external disturbances to a certain extent, they will still produce a certain disturbance errors. To sum up, we can get that the control

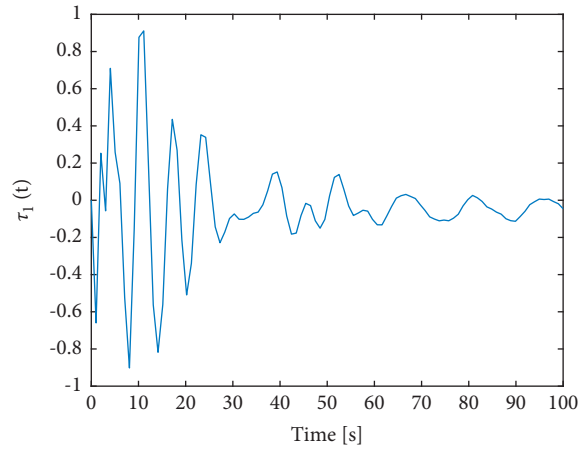
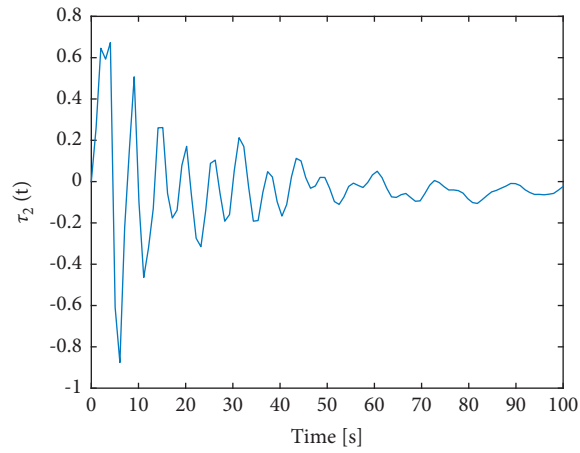
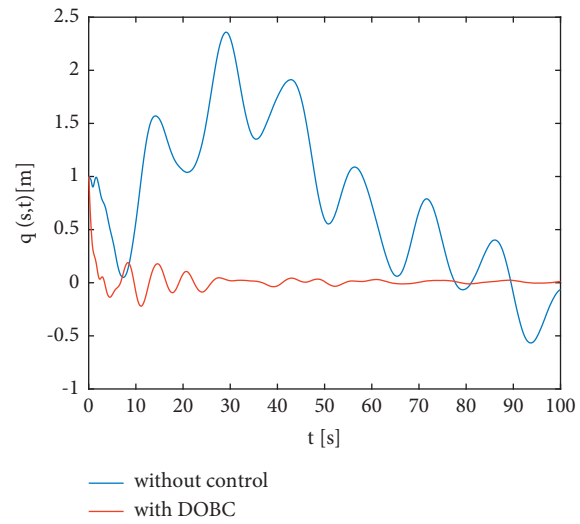
FIGURE 15: Designed control command $\tau_1(t)$ with DOBC.FIGURE 16: Designed control command $\tau_2(t)$ with DOBC.

FIGURE 17: Boundary bending displacement of the wing with DOBC.

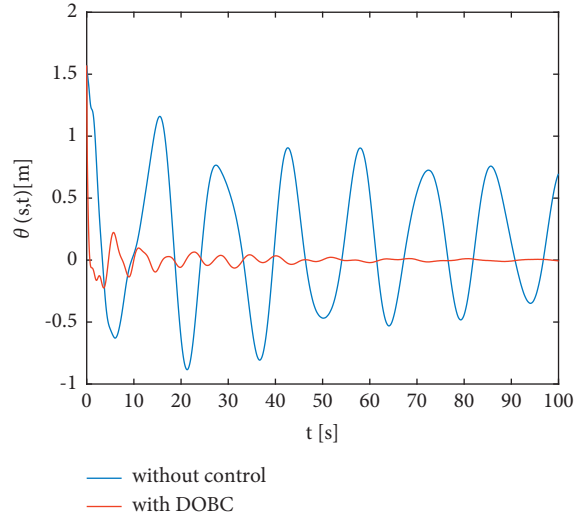


FIGURE 18: Boundary twist displacement of the wing with DOBC.

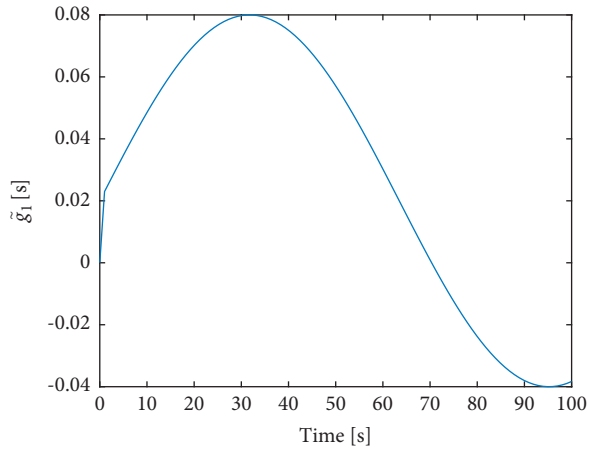


FIGURE 19: Disturbance estimation error $\tilde{g}_1(t)$ with DOBC.

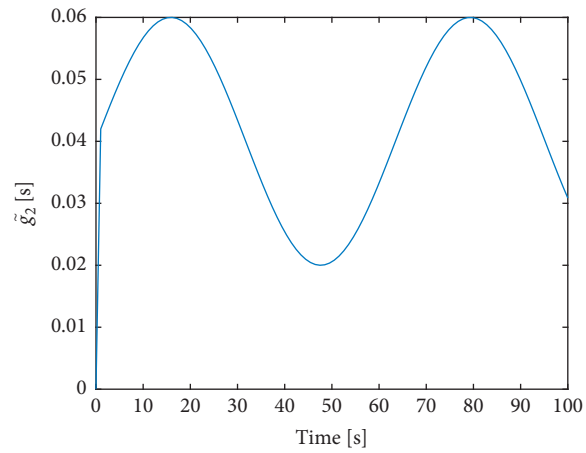


FIGURE 20: Disturbance estimation error $\tilde{g}_2(t)$ with DOBC.

effect of the derived finite-time convergence antidisturbance control strategy is better than that of the DOBC strategy.

5. Conclusion

In this paper, based on Lyapunov's direct method and the new coupled wing model, we addressed the control problem for the flexible wing subject to external disturbances with a new finite-time convergence antidisturbance control strategy. Under the action of the controllers, the external disturbance errors converged to zero in a finite time. Hence, we concluded that the proposed control scheme could stabilize the flexible wing system with a better performance. Finally, we analyzed the stability of the closed-loop system and the effectiveness of the boundary controller through strict theoretical proof and simulation results. Future research directions may include the adaptive control [50–53], intelligent techniques [54–57], and the uncertainty and disturbance estimator-based control [58–60].

Data Availability

The data used to support the results of this study are available from the first author (1707700028@e.gzhu.edu.cn).

Conflicts of Interest

The authors declare that they have no conflicts of interest.

Acknowledgments

This work was supported in part by the Innovative School Project of Education Department of Guangdong (202011078022).

References

- [1] K. Y. Ma, P. Chirattananon, S. B. Fuller, and R. J. Wood, "Controlled flight of a biologically inspired, insect-scale robot," *Science*, vol. 340, no. 6132, pp. 603–607, 2013.
- [2] M. Hamamoto, Y. Ohta, K. Hara, and T. Hisada, "A fundamental study of wing actuation for a 6-in-wingspan flapping microaerial vehicle," *IEEE Transactions on Robotics*, vol. 26, no. 2, pp. 244–255, 2010.
- [3] G. K. Lau, Y. W. Chin, J. T. W. Goh, and R. J. Wood, "Dipteran-insect-inspired thoracic mechanism with nonlinear stiffness to save inertial power of flapping-wing flight," *IEEE Transactions on Robotics*, vol. 30, no. 5, pp. 1187–1197, 2014.
- [4] A. A. Paranjape, S. J. Chung, and J. Kim, "Novel dihedral-based control of flapping-wing aircraft with application to perching," *IEEE Transactions on Robotics*, vol. 29, no. 5, pp. 1071–1084, 2013.
- [5] W. He, Z. Yan, C. Sun, and Y. Chen, "Adaptive neural network control of a flapping wing micro aerial vehicle with disturbance observer," *IEEE Transactions on Cybernetics*, vol. 47, no. 10, pp. 3452–3465, 2017.
- [6] W. He, X. Mu, L. Zhang, and Y. Zou, "Modeling and trajectory tracking control for flapping-wing micro aerial vehicles," *IEEE/CAA Journal of Automatica Sinica*, vol. 8, no. 1, pp. 148–156, 2020.
- [7] M. H. Dickinson, F. O. Lehmann, and S. P. Sane, "Wing rotation and the aerodynamic basis of insect flight," *Science*, vol. 284, no. 5422, pp. 1954–1960, 1999.
- [8] X. Xing and J. Liu, "Vibration and position control of overhead crane with three-dimensional variable length cable subject to input amplitude and rate constraints," *IEEE Transactions on Systems, Man, and Cybernetics: Systems*, vol. 51, 2019.
- [9] S. Zhang, Y. Wu, X. He, and Z. Liu, "Cooperative fault-tolerant control for a mobile dual flexible manipulator with output constraints," *IEEE Transactions on Automation Science and Engineering*, 2021.
- [10] S. Gao and J. Liu, "Adaptive neural network vibration control of a flexible aircraft wing system with input signal quantization," *Aerospace Science and Technology*, vol. 96, Article ID 105593, 2020.
- [11] H. N. Wu and J. W. Wang, "Static output feedback control via PDE boundary and ODE measurements in linear cascaded ODE-beam systems," *Automatica*, vol. 50, no. 11, pp. 2787–2798, 2014.
- [12] Y. Ren, M. Chen, and J. Liu, "Unilateral boundary control for a suspension cable system of a helicopter with horizontal motion," *IET Control Theory & Applications*, vol. 13, no. 4, pp. 467–476, 2018.
- [13] Z. Zhao, Z. Liu, W. He, K. S. Hong, and H. X. Li, "Boundary adaptive fault-tolerant control for a flexible Timoshenko arm with backlash-like hysteresis," *Automatica*, vol. 130, Article ID 109690, 2021.
- [14] U. H. Shah and K. S. Hong, "Active vibration control of a flexible rod moving in water: application to nuclear refueling machines," *Automatica*, vol. 93, pp. 231–243, 2018.
- [15] C. Sun, W. He, and J. Hong, "Neural network control of a flexible robotic manipulator using the lumped spring-mass model," *IEEE Transactions on Systems, Man, and Cybernetics: Systems*, vol. 47, no. 8, pp. 1863–1874, 2016.
- [16] D. Zhao, B. Jiang, H. Yang, and G. Tao, "A sliding mode fault compensation scheme for a coupled rigid-flexible system in PDE-ODE form," *Journal of the Franklin Institute*, vol. 357, no. 14, pp. 9174–9194, 2020.
- [17] Z. Zhao, X. He, Z. Ren, and G. Wen, "Boundary adaptive robust control of a flexible riser system with input nonlinearities," *IEEE Transactions on Systems, Man, and Cybernetics: Systems*, vol. 49, no. 10, pp. 1971–1980, 2018.
- [18] M. Chen, Y. Ren, and J. Liu, "Antidisturbance control for a suspension cable system of helicopter subject to input nonlinearities," *IEEE Transactions on Systems, Man, and Cybernetics: Systems*, vol. 48, no. 12, pp. 2292–2304, 2017.
- [19] L. Su, J. M. Wang, and M. Krstic, "Boundary feedback stabilization of a class of coupled hyperbolic equations with nonlocal terms," *IEEE Transactions on Automatic Control*, vol. 63, no. 8, pp. 2633–2640, 2017.
- [20] B. D. A. Novel and J. M. Coron, "Exponential stabilization of an overhead crane with flexible cable via a back-stepping approach," *Automatica*, vol. 36, no. 4, pp. 587–593, 2000.
- [21] W. He, T. Meng, X. He, and S. S. Ge, "Unified iterative learning control for flexible structures with input constraints," *Automatica*, vol. 96, 2018.
- [22] G. Zhu, S. S. Ge, and T. H. Lee, "Simulation studies of tip tracking control of a single-link flexible robot based on a lumped model," *Robotica*, vol. 17, no. 1, pp. 71–78, 1999.
- [23] Z. Zhao and Z. Liu, "Finite-time convergence disturbance rejection control for a flexible Timoshenko manipulator," *IEEE/CAA Journal of Automatica Sinica*, vol. 8, no. 1, pp. 157–168, 2020.

- [24] Y. Ma, X. He, M. Chen, and W. He, "Predictor-based control for a flexible satellite subject to output time delay," *IEEE Transactions on Control Systems Technology*, 2021.
- [25] X. He, Y. Song, Z. Han, S. Zhang, P. Jing, and S. Qi, "Adaptive inverse backlash boundary vibration control design for an Euler-Bernoulli beam system," *Journal of the Franklin Institute*, vol. 357, no. 6, pp. 3434–3450, 2020.
- [26] Z. Zhao and C. K. Ahn, "Boundary output constrained control for a flexible beam system with prescribed performance," *IEEE Transactions on Systems, Man, and Cybernetics: Systems*, vol. 51, 2019.
- [27] Y. Liu, X. Chen, Y. Mei, and Y. Wu, "Observer-based boundary control for an asymmetric output-constrained flexible robotic manipulator," *Science China Information Sciences*, vol. 65, no. 3, pp. 1–3, 2020.
- [28] G. Ma, Z. Tan, Y. Liu, Z. Zhao, and T. Zou, "Adaptive robust barrier-based control of a 3D flexible riser system subject to boundary displacement constraints," *International Journal of Robust and Nonlinear Control*, 2021.
- [29] Z. Liu, J. Shi, X. Zhao, Z. Zhao, and H. X. Li, "Adaptive fuzzy event-triggered control of aerial refueling hose system with actuator failures," *IEEE Transactions on Fuzzy Systems*, 2021.
- [30] X. He, Z. Zhao, and Y. Song, "Active control for flexible mechanical systems with mixed deadzone-saturation input nonlinearities and output constraint," *Journal of the Franklin Institute*, vol. 356, no. 9, pp. 4749–4772, 2019.
- [31] Z. Liu, X. He, Z. Zhao, C. K. Ahn, and H. X. Li, "Vibration control for spatial aerial refueling hoses with bounded actuators," *IEEE Transactions on Industrial Electronics*, vol. 68, 2020.
- [32] S. Zhang, W. He, and D. Huang, "Active vibration control for a flexible string system with input backlash," *IET Control Theory & Applications*, vol. 10, no. 7, pp. 800–805, 2016.
- [33] Z. Zhao, C. K. Ahn, and H. X. Li, "Boundary antidisturbance control of a spatially nonlinear flexible string system," *IEEE Transactions on Industrial Electronics*, vol. 67, no. 6, pp. 4846–4856, 2019.
- [34] Z. Zhao, C. K. Ahn, and H. X. Li, "Dead zone compensation and adaptive vibration control of uncertain spatial flexible riser systems," *IEEE*, vol. 25, no. 3, pp. 1398–1408, 2020.
- [35] Z. Zhao, Y. Ren, C. Mu, T. Zou, and K. S. Hong, "Adaptive neural-network-based fault-tolerant control for a flexible string with composite disturbance observer and input constraints," *IEEE Transactions on Cybernetics*, 2021.
- [36] W. He, T. Meng, X. He, and C. Sun, "Iterative learning control for a flapping wing micro aerial vehicle under distributed disturbances," *IEEE Transactions on Cybernetics*, vol. 49, no. 4, pp. 1524–1535, 2018.
- [37] A. A. Paranjape, J. Guan, S. J. Chung, and M. Krstic, "PDE boundary control for flexible articulated wings on a robotic aircraft," *IEEE Transactions on Robotics*, vol. 29, no. 3, pp. 625–640, 2013.
- [38] W. He and S. Zhang, "Control design for nonlinear flexible wings of a robotic aircraft," *IEEE Transactions on Control Systems Technology*, vol. 25, no. 1, pp. 351–357, 2016.
- [39] W. He, T. Wang, X. He, L. J. Yang, and O. Kaynak, "Dynamical modeling and boundary vibration control of a rigid-flexible wing system," *IEEE*, vol. 25, no. 6, pp. 2711–2721, 2020.
- [40] B. Xu, D. Wang, Y. Zhang, and Z. Shi, "DOB-based neural control of flexible hypersonic flight vehicle considering wind effects," *IEEE Transactions on Industrial Electronics*, vol. 64, no. 11, pp. 8676–8685, 2017.
- [41] M. Chen and J. Yu, "Disturbance observer-based adaptive sliding mode control for near-space vehicles," *Nonlinear Dynamics*, vol. 82, no. 4, pp. 1671–1682, 2015.
- [42] S. Shao, M. Chen, J. Hou, and Q. Zhao, "Event-triggered-based discrete-time neural control for a quadrotor UAV using disturbance observer," *IEEE*, vol. 26, no. 2, pp. 689–699, 2021.
- [43] Z. Zhao, X. He, and C. K. Ahn, "Boundary disturbance observer-based control of a vibrating single-link flexible manipulator," *IEEE Transactions on Systems, Man, and Cybernetics: Systems*, vol. 51, 2019.
- [44] Y. Zhang, J. Liu, and W. He, "Disturbance observer design and vibration control for a flexible aircraft wing," *Transactions of the Institute of Measurement and Control*, vol. 40, no. 13, pp. 3760–3773, 2018.
- [45] H. Yang, J. Liu, and W. He, "Distributed disturbance-observer-based vibration control for a flexible-link manipulator with output constraints," *Science China Technological Sciences*, vol. 61, no. 10, pp. 1528–1536, 2018.
- [46] M. V. Basin, F. G. Avellaneda, and Y. B. Shtessel, "Stock management problem: adaptive fixed-time convergent continuous controller design," *IEEE Transactions on Systems, Man, and Cybernetics: Systems*, vol. 50, no. 12, pp. 4974–4983, 2019.
- [47] S. S. Ge, W. He, B. V. E. How, and Y. S. Choo, "Boundary control of a coupled nonlinear flexible marine riser," *IEEE Transactions on Control Systems Technology*, vol. 18, no. 5, pp. 1080–1091, 2009.
- [48] W. He, X. Mu, Y. Chen, X. He, and Y. Yu, "Modeling and vibration control of the flapping-wing robotic aircraft with output constraint," *Journal of Sound and Vibration*, vol. 423, pp. 472–483, 2018.
- [49] C. D. Rahn, *Mechatronic Control of Distributed Noise and Vibration*, Springer-Verlag, New York, NY, USA, 2001.
- [50] C. Yang, Y. Jiang, J. Na, Z. Li, L. Cheng, and C. Y. Su, "Finite-time convergence adaptive fuzzy control for dual-arm robot with unknown kinematics and dynamics," *IEEE Transactions on Fuzzy Systems*, vol. 27, no. 3, pp. 574–588, 2018.
- [51] Z. Zhao, Y. Liu, T. Zou, and K. S. Hong, "Robust adaptive control of a riser-vessel system in three-dimensional space," *IEEE Transactions on Systems, Man, and Cybernetics: Systems*, 2021.
- [52] C. Yang, C. Chen, W. He, R. Cui, and Z. Li, "Robot learning system based on adaptive neural control and dynamic movement primitives," *IEEE Transactions on Neural Networks and Learning Systems*, vol. 30, no. 3, pp. 777–787, 2018.
- [53] N. Wang, C. Chen, and C. Yang, "A robot learning framework based on adaptive admittance control and generalizable motion modeling with neural network controller," *Neurocomputing*, vol. 390, pp. 260–267, 2020.
- [54] C. Yang, D. Huang, W. He, and L. Cheng, "Neural control of robot manipulators with trajectory tracking constraints and input saturation," *IEEE Transactions on Neural Networks and Learning Systems*, vol. 32, 2020.
- [55] C. Yang, G. Peng, L. Cheng, J. Na, and Z. Li, "Force sensorless admittance control for teleoperation of uncertain robot manipulator using neural networks," *IEEE Transactions on Systems, Man, and Cybernetics: Systems*, vol. 51, 2019.
- [56] Y. Liu, X. Chen, Y. Wu, H. Cai, and H. Yokoi, "Adaptive neural network control of a flexible spacecraft subject to input nonlinearity and asymmetric output constraint," *IEEE Transactions on Neural Networks and Learning Systems*, 2021.
- [57] C. Liu, G. Wen, Z. Zhao, and R. Sedaghati, "Neural-network-based sliding-mode control of an uncertain robot using

- dynamic model approximated switching gain,” *IEEE Transactions on Cybernetics*, vol. 51, no. 5, pp. 2339–2346, 2020.
- [58] J. Dai and B. Ren, “UDE-based robust boundary control for an unstable parabolic PDE with unknown input disturbance,” *Automatica*, vol. 93, pp. 363–368, 2018.
- [59] Y. Dong and B. Ren, “UDE-based variable impedance control of uncertain robot systems,” *IEEE Transactions on Systems, Man, and Cybernetics: Systems*, vol. 49, no. 12, pp. 2487–2498, 2017.
- [60] Q. C. Zhong, Y. Wang, and B. Ren, “UDE-based robust droop control of inverters in parallel operation,” *IEEE Transactions on Industrial Electronics*, vol. 64, no. 9, pp. 7552–7562, 2017.

Research Article

Higher-Order Iterative Learning Control with Optimal Control Gains Based on Evolutionary Algorithm for Nonlinear System

Yun-Shan Wei ¹, Xiaofen Yang,² Wenli Shang ¹ and Ying-Yu Chen¹

¹School of Electronics and Communication Engineering, Guangzhou University, Guangzhou 510006, China

²School of Mechanical and Electric Engineering, Guangzhou University, Guangzhou 510006, China

Correspondence should be addressed to Wenli Shang; shangwl@gzhu.edu.cn

Received 12 October 2021; Accepted 20 December 2021; Published 30 December 2021

Academic Editor: Zhenyu Lu

Copyright © 2021 Yun-Shan Wei et al. This is an open access article distributed under the Creative Commons Attribution License, which permits unrestricted use, distribution, and reproduction in any medium, provided the original work is properly cited.

For the nonlinear discrete-time system, higher-order iterative learning control (HOILC) with optimal control gains based on evolutionary algorithm (EA) is developed in this paper. Since the updating actions are constituted by the tracking information from several previous iterations, the suitably designed HOILC schemes with appropriate control gains usually achieve fast convergence speed. To optimize the control gains in HOILC approach, EA is introduced. The encoding strategy, population initialization, and fitness function in EA are designed according to the HOILC characteristics. With the global optimization of EA, the optimal control gains of HOILC are selected adaptively so that the number of convergence iteration is reduced in ILC process. It is shown in simulation that the sum absolute error, total square error, and maximum absolute error of tracking in the proposed HOILC based on EA are convergent faster than those in conventional HOILC.

1. Introduction

In real applications such as robot manipulator systems [1–5] and flexible systems [6–8], there are many unmanned autonomous systems in complex environments. The exact mathematical model is hard to construct. For these systems, iterative learning control (ILC) is proposed. It is an effective intelligent control approach applied in dynamical systems that perform repetitive tasks to track a specific trajectory in a certain time interval. By using the control input and tracking information of previous iterations, the control input signal can be gradually updated from iteration to iteration such that the tracking performance can be improved. Less previous knowledge about the controlled systems makes ILC popular in theoretical fields [9–14] as well as applicable fields [15–19].

First-order ILC, which generates the control input from tracking information at last iteration, is widely applied to dynamical systems for perfect tracking in a finite time interval [20–26]. However, only the tracking information of last iteration is utilized to update the current control input in first-order ILC, and thus it is difficult to obtain a satisfactory

convergence speed. To achieve faster convergence speed, higher-order ILC (HOILC) adopting the tracking information of many previous iterations to generate the current control input signal was proposed [27–31]. Since the updating actions are constituted by the tracking information from several previous iterations, the tracking performance of suitably designed HOILC is better than that of first-order ILC. Specifically, the appropriate control gains can accelerate the convergence process of HOILC. Thus, how to select optimal control gains is a significant issue in HOILC designs.

Motivated by the above observation, in this paper, the evolutionary algorithm (EA) originating from biological evolutionism is adopted to choose the optimal control gains in HOILC scheme adaptively. EA is a heuristic optimizing algorithm which simulates the reproduction, selection, crossover, and mutation in biological evolution process. It has been widely introduced to deal with various optimal issues [32–34]. In this paper, the encoding strategy, population initialization, and fitness function of EA are designed according to the HOILC characteristics such that the generations in EA are reduced. Then, the designed EA is involved in HOILC to optimize the control gains. After that,

the optimal control gains and the control inputs are generated simultaneously. Comparing with traditional HOILC, the number of convergence iteration is reduced in the proposed EA scheme based HOILC (EA-HOILC). The EA with global optimization is introduced to optimize the control gains of HOILC in this paper.

The rest of paper is organized as follows. The problem formulation is given in Section 2. The HOILC with its convergence analysis is provided in Section 3. Section 4 presents the designed EA-HOILC scheme with optimal control gains. In Section 5, an example is provided to illustrate the effectiveness of the proposed EA-HOILC. Section 6 concludes this paper.

2. Problem Formulation

Consider the following nonlinear discrete-time system which performs repetitive operation:

$$\begin{cases} x_j(i+1) = f(x_j(i), i) + B(i)u_j(i), \\ y_j(i) = C(i)x_j(i), \end{cases} \quad (1)$$

where $j \in \{0, 1, 2, \dots\}$ and $i \in \{0, 1, \dots, M\}$ represent the iteration index and the time point, respectively. $x_j(i) \in R^w$, $u_j(i) \in R$, and $y_j(i) \in R$ denote the state, control input, and output of system (1), respectively. $B(i) \in R^w$, $C(i) \in R^{1 \times w}$, and $f(\cdot, \cdot) \in R^w$. $y_d(i) = C(i)x_d(i)$ for $i \in \{0, 1, \dots, M\}$ is the reference output, where $x_d(i)$ is the corresponding reference state. $e_j(i) = y_d(i) - y_j(i)$ is the ILC tracking error at j th iteration for $i \in \{0, 1, \dots, M\}$. The following assumptions are required for the technical analysis. $\|\cdot\|$ represents the required norm in this paper.

Assumption 1. For all j , the initial state satisfies

$$x_j(0) = x_d(0). \quad (2)$$

As the identical initial condition considered in Assumption 1 cannot be satisfied, the techniques proposed in [29–31] can be introduced to deal with the vibration of initial state.

Assumption 2. The nonlinear function $f(\cdot, \cdot)$ in system (1) is assumed to be differentiable to i and to be globally Lipschitz in the first variable, that is, $\forall \tilde{x}, \hat{x} \in R^w$,

$$\|f(\tilde{x}, i) - f(\hat{x}, i)\| \leq c_f \|\tilde{x} - \hat{x}\|, \quad (3)$$

where $c_f > 0$ is the Lipschitz constant.

Assumption 3. The number $C(i+1)B(i) \neq 0$.

Remark 1. It is noted that Assumption 3 implies that the relative degree of system (1) is one. For the nonlinear discrete-time systems with higher relative degree, the ILC law can be modified according to the order of system relative degree as discussed in [31].

Suppose that the reference output $y_d(i)$ is realizable, there exists a unique control input $u_d(i) \in R$ such that

$$\begin{cases} x_d(i+1) = f(x_d(i), i) + B(i)u_d(i), \\ y_d(i) = C(i)x_d(i). \end{cases} \quad (4)$$

The objective of this paper is to develop an EA-HOILC method, which generates the control input from the tracking information of several previous iterations. The control gains are optimized by EA to reduce the number of convergence iteration. For HOILC convergence analysis, the following lemma is adopted.

Lemma 1 (see [31]). Let $\{g_j\}$ be a real sequence defined as

$$g_j \leq \omega_1 g_{j-1} + \omega_2 g_{j-2} + \dots + \omega_N g_{j-N} + d_j, \quad (5)$$

for $j \geq N+1$, where d_j is a specific real sequence. If $\omega_1, \omega_2, \dots, \omega_N$ are nonnegative numbers satisfying

$$\omega = \sum_{v=1}^N \omega_v < 1, \quad (6)$$

then $\lim_{j \rightarrow +\infty} d_j = 0$ implies that $\lim_{j \rightarrow +\infty} g_j = 0$.

3. HOILC Design and Convergence Analysis

In this section, for nonlinear discrete-time system (1) under Assumptions 1–3, the following HOILC law is designed for $i \in \{0, 1, \dots, M\}$ and $j \geq N-1$:

$$u_{j+1}(i) = \sum_{v=1}^N W_v u_{j-v+1}(i) + \sum_{v=1}^N L_v e_{j-v+1}(i+1), \quad (7)$$

where $N \geq 1$ is the order of HOILC law (7), and $W_v \in R$ and $L_v \in R$ ($|L_v| \leq s_L$) for $v = 1, 2, \dots, N$ are the control gains.

Remark 2. In the existing HOILC schemes [30, 31], the initial control inputs $u_0(i), u_1(i), \dots, u_{N-1}(i)$ are normally set as zero vectors. In this paper, since the control inputs can be obtained by EA along with the optimal control gains, we can set the initial control inputs $u_0(i), u_1(i), \dots, u_{N-1}(i)$ same as the generated control inputs. It means that the initial control inputs are optimized by EA, which can also accelerate the convergence speed.

Theorem 1. For nonlinear discrete-time system (1) under Assumptions 1–3, the HOILC law (7) is applied. If the control gains W_v and L_v ($|L_v| \leq s_L$) for $v = 1, 2, \dots, N$ are selected to make

$$\sum_{v=1}^N W_v = 1, \quad (8)$$

$$|W_v - L_v C(i+1)B(i)| \leq \gamma_v, \quad (9)$$

$$\sum_{v=1}^N \gamma_v < 1, \quad (10)$$

then $\lim_{j \rightarrow +\infty} e_j(i) = 0$ for $i \in \{0, 1, \dots, M+1\}$.

Proof. Let $\delta u_j(i) = u_d(i) - u_j(i)$ and $\delta x_j(i) = x_d(i) - x_j(i)$. Subtracting both sides of (7) with $u_d(i)$ and considering (1), (4), and (8), we obtain

$$\begin{aligned}
\delta u_{j+1}(i) &= \sum_{v=1}^N W_v \delta u_{j-v+1}(i) - \sum_{v=1}^N L_v e_{j-v+1}(i+1), \\
&= \sum_{v=1}^N W_v \delta u_{j-v+1}(i) - \sum_{v=1}^N L_v C(i+1) \delta x_{j-v+1}(i+1), \\
&= \sum_{v=1}^N W_v \delta u_{j-v+1}(i) - \sum_{v=1}^N L_v C(i+1) [f(x_d(i), i) - f(x_{j-v+1}(i), i) + B(i) \delta u_{j-v+1}(i)], \\
&= \sum_{v=1}^N [W_v - L_v C(i+1) B(i)] \delta u_{j-v+1}(i) - \sum_{v=1}^N L_v C(i+1) [f(x_d(i), i) - f(x_{j-v+1}(i), i)].
\end{aligned} \tag{11}$$

Then, noting convergence condition (9) and Assumption 2, we can further deduce that

$$\begin{aligned}
|\delta u_{j+1}(i)| &\leq \sum_{v=1}^N \gamma_v |\delta u_{j-v+1}(i)| \\
&\quad + \sum_{v=1}^N s_L s_C c_f \|\delta x_{j-v+1}(i)\|,
\end{aligned} \tag{12}$$

where $\|C(i)\| \leq s_C$ and $|L_v| \leq s_L$ for $v = 1, 2, \dots, N$.

On the other hand, it follows from (1) and (4) that

$$\begin{aligned}
\delta x_j(i) &= f(x_d(i-1), i-1) \\
&\quad - f(x_j(i-1), i-1) + B(i-1) \delta u_j(i-1).
\end{aligned} \tag{13}$$

Taking norm on both sides of (13) and considering Assumptions 1-2, it yields

$$\begin{aligned}
\|\delta x_j(i)\| &\leq c_f \|\delta x_j(i-1)\| + s_B |\delta u_j(i-1)| \\
&\leq c_f^2 \|\delta x_j(i-2)\| + c_f s_B |\delta u_j(i-2)| + s_B |\delta u_j(i-1)| \\
&\leq \dots \\
&\leq c_f^i \|\delta x_j(0)\| + \sum_{k=0}^{i-1} c_f^{i-k-1} s_B |\delta u_j(k)| \\
&= \sum_{k=0}^{i-1} c_f^{i-k-1} s_B |\delta u_j(k)|,
\end{aligned} \tag{14}$$

where $\|B(i)\| \leq s_B$. Substituting (14) into (12),

$$\begin{aligned}
|\delta u_{j+1}(i)| &\leq \sum_{v=1}^N \gamma_v |\delta u_{j-v+1}(i)| \\
&\quad + \sum_{v=1}^N \sum_{k=0}^{i-1} s_L s_C s_B c_f^{i-k} |\delta u_{j-v+1}(k)|.
\end{aligned} \tag{15}$$

As $i = 0$, considering (2) of Assumption 1, it is derived from (12) that

$$|\delta u_{j+1}(0)| \leq \sum_{v=1}^N \gamma_v |\delta u_{j-v+1}(0)|. \tag{16}$$

Applying Lemma 1 to (16) with convergence condition (10), we have

$$\lim_{j \rightarrow +\infty} |\delta u_j(0)| = 0. \tag{17}$$

As $i = 1$, from (16), there is

$$\begin{aligned}
|\delta u_{j+1}(1)| &\leq \sum_{v=1}^N \gamma_v |\delta u_{j-v+1}(1)| \\
&\quad + \sum_{v=1}^N s_L s_C s_B c_f |\delta u_{j-v+1}(0)|.
\end{aligned} \tag{18}$$

Applying Lemma 1 to (18) with convergence condition (10) and considering (17), we obtain

$$\lim_{j \rightarrow +\infty} |\delta u_j(1)| = 0. \tag{19}$$

Assume that for $i = 1, 2, \dots, n-1$, there is

$$\lim_{j \rightarrow +\infty} |\delta u_j(i)| = 0. \tag{20}$$

As $i = n$, it follows from (15) that

$$|\delta u_{j+1}(n)| \leq \sum_{v=1}^N \gamma_v |\delta u_{j-v+1}(n)| + \sum_{v=1}^N \sum_{k=0}^{n-1} s_L s_C s_B c_f^{n-k} |\delta u_{j-v+1}(k)|. \tag{21}$$

Applying Lemma 1 to (21) with convergence condition (10) and considering (17) and (20), we can derive

$$\lim_{j \rightarrow +\infty} |\delta u_j(n)| = 0. \tag{22}$$

Finally, based on the mathematical induction, the following result can be deduced:

$$\lim_{j \rightarrow +\infty} |\delta u_j(i)| = 0, i \in \{0, 1, \dots, M\}. \tag{23}$$

Noting (2) in Assumption 1, then it can be obtained from (15) and (24) that

$$\lim_{j \rightarrow +\infty} \|\delta x_j(i)\| = 0, i \in \{0, 1, \dots, M+1\}. \quad (24)$$

Furthermore, for $i \in \{0, 1, \dots, M+1\}$, it follows from (1) and (4) that

$$\lim_{j \rightarrow +\infty} |e_j(i)| \leq \lim_{j \rightarrow +\infty} s_C \|\delta x_j(i)\| = 0. \quad (25)$$

Then, we have $\lim_{j \rightarrow +\infty} e_j(i) = 0$ for $i \in \{0, 1, \dots, M+1\}$. The proof is completed. \square

4. EA-HOILC Scheme with Optimal Control Gains

Theorem 1 provides the asymptotic convergence of the proposed HOILC. It is well known that the control gains can affect the convergence performance significantly. In this section, the control gains of the HOILC developed in Section 3 are optimized by EA to reduce the number of convergence iteration.

EA is an intelligent optimization algorithm which simulates the process of biological evolution to gain the optimal solution. The main idea of EA-HOILC is presented as follows.

4.1. Encoding Strategy. In this paper, the control gains of HOILC are real numbers, so it is appropriate to choose the real encoding strategy. The control gains to be optimized in HOILC law (7) are W_ν and L_ν ($\nu = 1, 2, \dots, N$). Since the convergence condition (8) holds, it is easily obtained that $W_N = 1 - \sum_{\nu=1}^{N-1} W_\nu$. As a result, we can assume the variable vector in EA to be $\lambda \in R^{1 \times (2N-1)}$, and the encoding strategy is represented as

$$\lambda = [W_1 \ W_2 \ \dots \ W_{N-1} \ L_1 \ L_2 \ \dots \ L_N]. \quad (26)$$

4.2. Population Initialization and Individual Evaluation. Based on the convergence conditions (8)–(10), the value range of control gains W_ν and L_ν for $\nu = 1, 2, \dots, N$ could be determined. Thus, the initial population can be produced according to the convergent conditions. Let P be the population size, without loss of generality, assume that P is even. The variable vector of h th individual in the population is represented as $\lambda_h = [W_{1,h} \ W_{2,h} \ \dots \ W_{N-1,h} \ L_{1,h} \ L_{2,h} \ \dots \ L_{N,h}] \in R^{1 \times (2N-1)}$ which are initialized to $\lambda_h^{\text{ini}} \in R^{1 \times (2N-1)}$ for $h = 1, 2, \dots, P$. On the other hand, for variable λ_h , let the system output for h th individual at i th time point be $Y_h(i, \lambda_h)$. To evaluate the individual superiority, the following fitness function $\text{fit}_h(\lambda_h) \in R$ of h th individual is established:

$$\text{fit}_h(\lambda_h) = \overline{M} - E_h(\lambda_h), \quad (27)$$

where \overline{M} is a constant large enough and $E_h(\lambda_h)$ is the sum of absolute value of tracking error represented as

$$E_h(\lambda_h) = \sum_{i=0}^M |y_d(i) - Y_h(i, \lambda_h)|. \quad (28)$$

From the fitness function (27) and the initial variable λ_h^{ini} , the initial fitness value of h th individual $\text{fit}_h^{\text{ini}}$ is obtained. Then, we have the following initial fitness vector $\text{fit}^{\text{ini}} \in R^P$ of population:

$$\text{fit}^{\text{ini}} = [\text{fit}_1^{\text{ini}} \ \text{fit}_2^{\text{ini}} \ \dots \ \text{fit}_P^{\text{ini}}]^T. \quad (29)$$

Hence, the initial population $\text{pop}^{\text{ini}} \in R^{P \times 2N}$ is constructed as

$$\text{pop}^{\text{ini}} = [\lambda^{\text{ini}} \ \text{fit}^{\text{ini}}], \quad (30)$$

where the initial variable of population is

$$\lambda^{\text{ini}} = [\lambda_1^{\text{ini}} \ \lambda_2^{\text{ini}} \ \dots \ \lambda_P^{\text{ini}}]^T. \quad (31)$$

From (31), the α th ($1 \leq \alpha \leq 2N-1$) variable of the β th ($1 \leq \beta \leq P$) individual is represented as the β th row of α th column. The last column of pop^{ini} shown in (30) is the fitness value of the corresponding initial variable in population.

4.3. Selection Strategy. The individuals are selected into next generation by roulette strategy and elitism strategy. The individual with bigger fitness value is selected at higher probability by the roulette strategy. However, one shortcoming of the roulette strategy is that the best individual in old population might be missed. So, we adopt elitism strategy to ensure that the best individual of last generation can be retained. Due to these two strategies, the number of convergence generation of EA can be reduced.

4.4. Crossover Operator. The crossover probability $0 < p_c < 1$ depends whether an individual needs to cross. For h' th individual, where $h' = 1, 3, 5, \dots, P-1$, a random number is produced between 0 and 1, which is represented as $r_{h'}$. If $r_{h'} > p_c$, the crossover operation occurs. Otherwise, the crossover operation does not occur. Due to the real encoding strategy, arithmetical crossover operator is adopted. Assume the variable vectors of h' th and $h'+1$ th parent individuals to be $\text{par}_{\lambda_{h'}}$ and $\text{par}_{\lambda_{h'+1}}$, respectively, which are selected to cross. After crossover, they generate two new individuals, of which the variable vectors are represented as $\text{chi}_{\lambda_{h'}}$ and $\text{chi}_{\lambda_{h'+1}}$. For $h' = 1, 3, 5, \dots, P-1$, the crossover operation is expressed as

$$\begin{cases} \text{chi}_{\lambda_{h'}} = \eta_{h'} \cdot \text{par}_{\lambda_{h'}} + (1 - \eta_{h'}) \cdot \text{par}_{\lambda_{h'+1}}, \\ \text{chi}_{\lambda_{h'+1}} = (1 - \eta_{h'}) \cdot \text{par}_{\lambda_{h'}} + \eta_{h'} \cdot \text{par}_{\lambda_{h'+1}}, \end{cases} \quad (32)$$

where $\eta_{h'} \in (0, 1)$ is the crossover weighting for the h' th and $h'+1$ th parent individuals.

4.5. Mutation Operator. In this paper, we adopt the stochastic mutation strategy. Let $0 < p_m < 1$ be the mutation probability. For h th individual, a number is produced randomly between 0 and 1 represented as r_h , $h = 1, 2, \dots, P$. If $r_h > p_m$, the mutation operation occurs. Otherwise, the

mutation operation does not occur. Let $\text{par}_h \lambda_h$ be the variable vector of h th individual which is selected to mutate. After mutation, a new variable vector $\text{chi}_h \lambda_h$ is produced. The mutation operator is defined as

$$\text{chi}_h \lambda_h = \text{par}_h \lambda_h + m_h, h = 1, 2, \dots, P, \quad (33)$$

where $m_h \in R^{1 \times (2N-1)}$ is the mutation weighting for h th individual.

4.6. Terminative Conditions. The terminative conditions can be determined by the fitness value or by the tracking error. In simulation, the number of generation in EA is set to be 100. Finally, we can obtain the optimal control gains W_v^{best} ($v = 1, 2, \dots, N-1$) and L_v^{best} ($v = 1, 2, \dots, N$) from the best individual produced by EA. According to the convergence condition (8), the last control gain W_N^{best} is derived by $W_N^{\text{best}} = 1 - \sum_{v=1}^{N-1} W_v^{\text{best}}$.

4.7. Overview of the Proposed EA-HOILC. The flowchart of the proposed EA-HOILC is depicted in Figure 1. First of all, according to the control gains characteristics and convergence conditions (9) and (10), the initial variable λ_h^{ini} ($h = 1, 2, \dots, P$) is obtained. Then, we apply the traditional HOILC at $i \in \{0, 1, \dots, M\}$ with initial control gains in each λ_h^{ini} , where convergence condition (8) is considered. By using the tracking error $E_h(\lambda_h^{\text{ini}})$ with λ_h^{ini} as shown in (29) produced by HOILC, the corresponding fitness $\text{fit}_h^{\text{ini}}$ ($h = 1, 2, \dots, P$) is derived from (27). Combining λ_h^{ini} and $\text{fit}_h^{\text{ini}}$ for $h = 1, 2, \dots, P$, the initial population pop^{ini} as shown in (31) with (30) and (32) is produced. Secondly, selection, crossover, and mutation are performed by the selection strategy, crossover operator, and mutation operator, respectively. After that, a new input $u_p(i)$, $i \in \{0, 1, \dots, M\}$, is obtained along with the optimal control gains. Set the initial control inputs of the EA-HOILC $u_0(i) = u_1(i) = \dots = u_{N-1}(i) = u_p(i)$, $i = 0, 1, \dots, M$. Then, the HOILC with optimal control gains process begins.

5. Simulation

To verify the effectiveness of the proposed EA-HOILC, a two-link robotic fish is employed. The system dynamic of the two-link robotic fish is described as follows [22]:

$$M_f \dot{V}_j(t) = -\xi V_j^2(t) + F_j(t), \quad (34)$$

where $M_f = 0.4$ kg is the mass of robotic fish, $\xi = 165.7056$ kg/m is the water resistance coefficient, $V_j(t)$ denotes the velocity, and $F_j(t)$ is the forward thrust produced by the tail motion. Let the velocity $V_j(i \cdot T_s)$ and the forward thrust

$F_j(i \cdot T_s)$ be the system state $x_j(i)$ and the control input $u_j(i)$, respectively, where $T_s = 0.1$ is the sampling time. We can discretize system (34) by using $\dot{V}_j(i \cdot T_s) \approx (V_j((i+1) \cdot T_s) - V_j(i \cdot T_s))/T_s$. Thus, the discrete-time system is

$$\begin{cases} x_j(i+1) = x_j(i) + A_f x_j^2(i) + B_f u_j(i), \\ y_j(i) = x_j(i), \end{cases} \quad (35)$$

where $A_f = -\xi \cdot T_s / M_f$ and $B_f = T_s / M_f$.

The reference output trajectory is represented as

$$y_d(i) = 0.016[1 + \sin(2\pi i/M - \pi/2)], i \in \{0, 1, \dots, M+1\}, \quad (36)$$

with $M = 99$. For the proposed HOILC algorithm, set the order $N = 2$. The control gains W_1 , L_1 , and L_2 are selected by EA. Another control gain $W_2 = 1 - W_1$ is obtained from convergence condition (8). The crossover probability $p_c = 0.7$, and the mutation probability $p_m = 0.3$. To evaluate the tracking performance, three tracking indexes on sum absolute error SE_k , total square error TE_k , and maximum absolute error ME_k are defined as follows:

$$\begin{aligned} SE_k &= \sum_{i=0}^{100} |e_j(i)|, \\ TE_k &= \sum_{i=0}^{100} [e_j(i)]^2, \\ ME_k &= \sup_{i \in \{0, 1, \dots, 100\}} |e_j(i)|. \end{aligned} \quad (37)$$

In the simulation, the EA-HOILC is run 10 times, and the optimized control gains are shown in Table 1.

Figure 2 exhibits the system output performance at iterations $j = 15$, $j = 22$, and $j = 39$ by using EA-HOILC with the average values of optimal control gains in 10 times. To compare the convergence speed between EA-HOILC and conventional HOILC with different parameters, the control gains in HOILC proposed in [30] with 2-order are, respectively, chosen as following two cases. Case 1: $W_1 = 0.7$, $W_2 = 0.3$, $L_1 = 0.3$, and $L_2 = 0.2$ and Case 2: $W_1 = 0.6$, $W_2 = 0.4$, $L_1 = 0.2$, and $L_2 = 0.1$. The corresponding sum absolute error SE_k , total square error TE_k , and maximum absolute error ME_k of tracking are shown in Figure 3. From Figure 3, one can observe that the case with larger control gains in W_1 , L_1 , and L_2 can achieve faster convergent speed in conventional HOILC. Moreover, it is clearly revealed that the proposed EA-HOILC can make the convergence iterations less than the conventional HOILC with the same order.

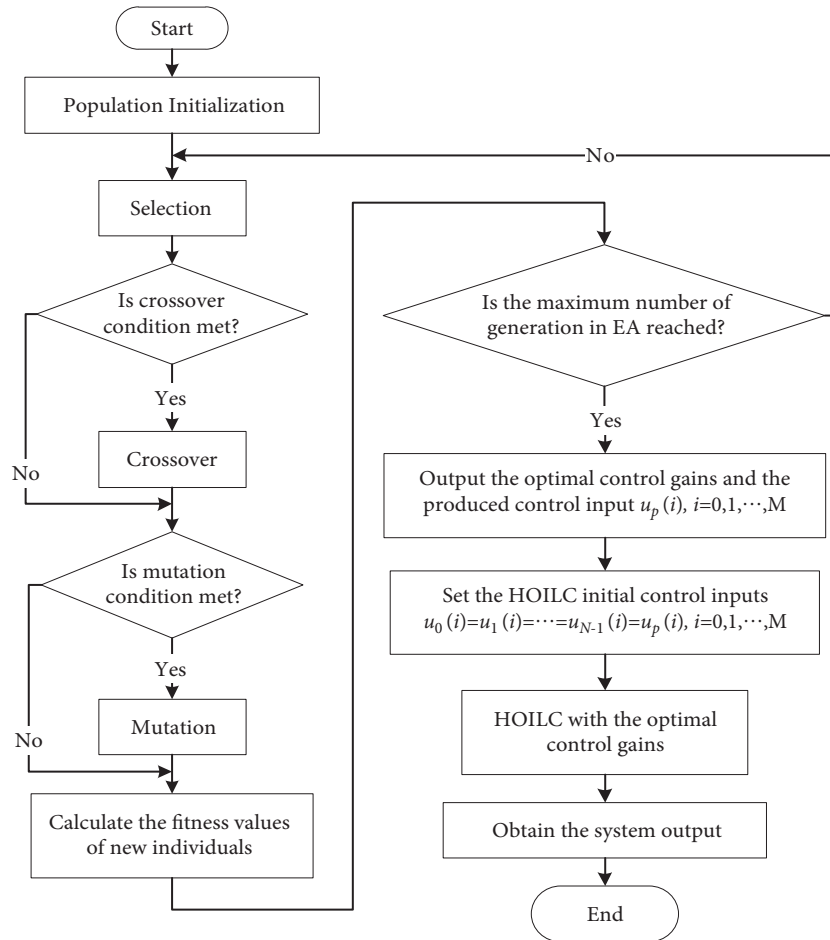


FIGURE 1: The flowchart of the proposed EA-HOILC.

TABLE 1: Optimized control gains of EA-HOILC in different times.

Times	W_1	W_2	L_1	L_2
1	0.7474	0.2526	0.4932	0.4570
2	0.7827	0.2173	0.4724	0.4569
3	0.7313	0.2687	0.4924	0.4068
4	0.7972	0.2028	0.4067	0.4856
5	0.7161	0.2839	0.4209	0.4177
6	0.7243	0.2757	0.4456	0.4744
7	0.7465	0.2535	0.4424	0.4678
8	0.7502	0.2498	0.4209	0.4682
9	0.7543	0.2457	0.4954	0.4156
10	0.7474	0.2526	0.4932	0.4570
Average	0.7827	0.2173	0.4724	0.4569

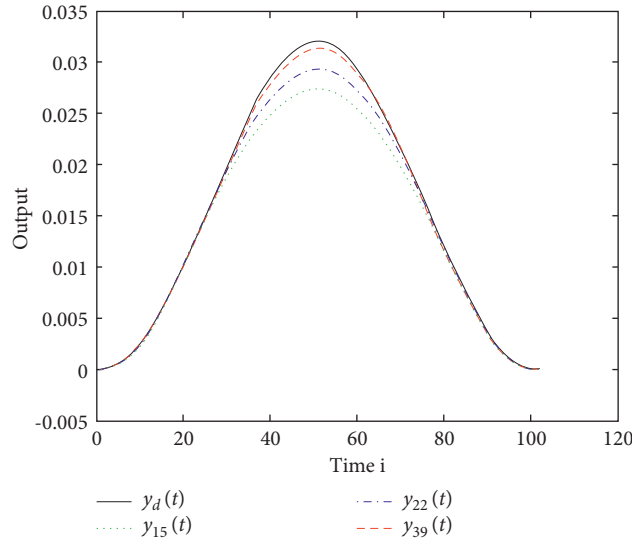


FIGURE 2: Output performance of EA-HOILC with the average values of optimized control gains at iterations $j = 15$, $j = 22$, and $j = 39$.

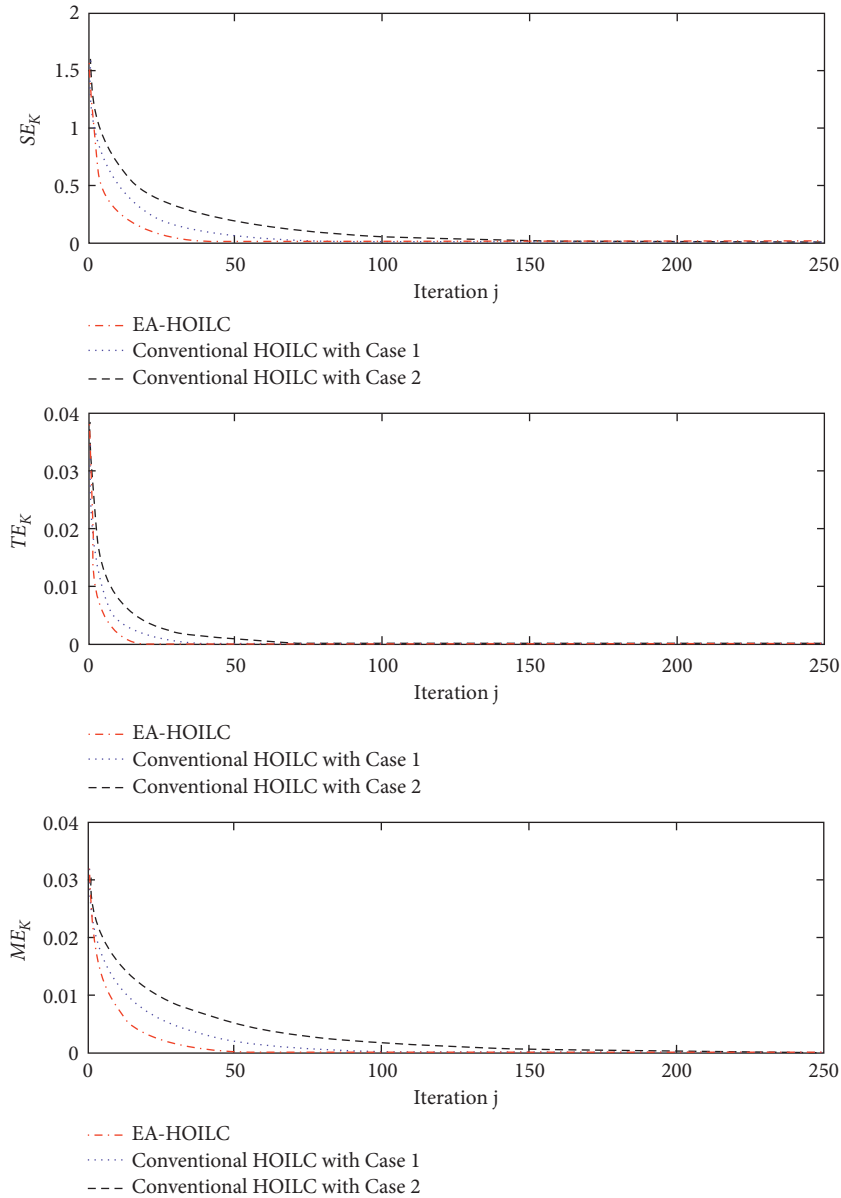


FIGURE 3: The tracking indexes (a) SE_k , (b) TE_k , and (c) ME_k at different iterations by using EA-HOILC and conventional HOILC with two cases.

6. Conclusions

In this paper, an HOILC law utilizing the tracking information of several previous iterations is proposed for the nonlinear discrete-time system. The convergence is rigorously analyzed based on the mathematical induction. In order to improve the convergence performance of the developed HOILC, the EA with global optimization is introduced to optimize the control gains. With the optimal control gains, the proposed EA-HOILC can achieve faster convergence speed. In simulation, it is shown that the sum absolute error, total square error, and maximum absolute error of tracking in EA-HOILC are convergent faster than those in the conventional HOILC with same order. However, it is worth noting that because EA is adopted to select the control gains, the offline computing time of EA-HOILC is longer. It is very suitable for the cases in which fewer iterations are required only. For instance, to destroy a target with bombs, the proposed method can reduce the number of bombs at the cost of computing time. Future research will extend the EA-HOILC developed in this paper to the dynamical systems with uncertainties in real application [35–37].

Data Availability

The data used to support the findings of this study are included within the article.

Conflicts of Interest

The authors declare that there are no conflicts of interest.

Acknowledgments

This research was funded in part by National Natural Science Foundation of China with grant nos. 61903096 and 62173101, Science and Technology Program of Guangzhou with grant no. 201904010475, and Zhijiang Laboratory's Open Project with grant no. 2021KF0AB06.

References

- [1] G. Peng, C. L. P. Chen, and C. Yang, "Neural networks enhanced optimal admittance control of robot-environment interaction using reinforcement learning," *IEEE Transactions on Neural Networks and Learning Systems*, pp. 1–11, 2021.
- [2] D. Huang, H. Zhan, and C. Yang, "Impedance model-based optimal regulation on force and position of bimanual robots to hold an object," *Complexity*, vol. 2020, Article ID 3561807, 13 pages, 2020.
- [3] H. Huang, C. Yang, and C. L. P. Chen, "Optimal robot-environment interaction under broad fuzzy neural adaptive control," *IEEE Transactions on Cybernetics*, vol. 51, no. 7, pp. 3824–3835, 2021.
- [4] D. Huang, C. Yang, Y. Pan, and L. Cheng, "Composite learning enhanced neural control for robot manipulator with output error constraints," *IEEE Transactions on Industrial Informatics*, vol. 17, no. 1, pp. 209–218, 2020.
- [5] C. Yang, D. Huang, W. He, and L. Cheng, "Neural control of robot manipulators with trajectory tracking constraints and input saturation," *IEEE Transactions on Neural Networks and Learning Systems*, vol. 32, no. 9, pp. 4231–4242, 2021.
- [6] Z. Zhao, Z. Liu, W. He, K. S. Hong, and H. X. Li, "Boundary adaptive fault-tolerant control for a flexible Timoshenko arm with backlash-like hysteresis," *Automatica*, vol. 13, Article ID 109690, 2021.
- [7] Z. Zhao, C. K. Ahn, and H.-X. Li, "Boundary antidisturbance control of a spatially nonlinear flexible string system," *IEEE Transactions on Industrial Electronics*, vol. 67, no. 6, pp. 4846–4856, 2020.
- [8] Z. Zhao, X. He, and C. K. Ahn, "Boundary disturbance observer-based control of a vibrating single-link flexible manipulator," *IEEE Transactions on Systems, Man, and Cybernetics: Systems*, vol. 51, no. 4, pp. 2382–2390, 2021.
- [9] W. He, T. Meng, S. Zhang, J.-K. Liu, G. Li, and C. Sun, "Dual-loop adaptive iterative learning control for a Timoshenko beam with output constraint and input backlash," *IEEE Transactions on Systems, Man, and Cybernetics: Systems*, vol. 49, no. 5, pp. 1027–1038, 2019.
- [10] K. Wan and X.-D. Li, "Robust iterative learning control of 2-D linear discrete FMMII systems subject to iteration-dependent uncertainties," *IEEE Transactions on Systems, Man, and Cybernetics: Systems*, vol. 51, no. 10, pp. 5949–5961, 2021.
- [11] D. Meng and J. Zhang, "Convergence analysis of robust iterative learning control against nonrepetitive uncertainties: system equivalence transformation," *IEEE Transactions on Neural Networks and Learning Systems*, vol. 32, no. 9, pp. 3867–3879, 2021.
- [12] J. Liu, X. Ruan, and Y. Zheng, "Iterative learning control for discrete-time systems with full learnability," *IEEE Transactions on Neural Networks and Learning Systems*, pp. 1–15, 2020.
- [13] J. Chen, C. Hua, and X. Guan, "Iterative learning model-free control for networked systems with dual-direction data dropouts and actuator faults," *IEEE Transactions on Neural Networks and Learning Systems*, vol. 32, no. 11, pp. 5232–5240, 2021.
- [14] Q. Yu, Z. Hou, X. Bu, and Q. Yu, "RBFNN-based data-driven predictive iterative learning control for nonaffine nonlinear systems," *IEEE Transactions on Neural Networks and Learning Systems*, vol. 31, no. 4, pp. 1170–1182, 2020.
- [15] X. Bu, J. Liang, Z. Hou, and R. Chi, "Data-driven terminal iterative learning consensus for nonlinear multiagent systems with output saturation," *IEEE Transactions on Neural Networks and Learning Systems*, vol. 32, no. 5, pp. 1963–1973, 2021.
- [16] X. Jin, "Fault-tolerant iterative learning control for mobile robots non-repetitive trajectory tracking with output constraints," *Automatica*, vol. 94, pp. 63–71, 2018.
- [17] T. Meng, W. He, and X. He, "Tracking control of a flexible string system based on iterative learning control," *IEEE Transactions on Control Systems Technology*, vol. 29, no. 1, pp. 436–443, 2021.
- [18] W. He, T. Meng, X. He, and C. Sun, "Iterative learning control for a flapping wing micro aerial vehicle under distributed disturbances," *IEEE Transactions on Cybernetics*, vol. 49, no. 4, pp. 1524–1535, 2019.
- [19] X. Bu, Q. Yu, Z. Hou, and W. Qian, "Model free adaptive iterative learning consensus tracking control for a class of nonlinear multiagent systems," *IEEE Transactions on Systems, Man, and Cybernetics: Systems*, vol. 49, no. 4, pp. 677–686, 2019.
- [20] X. Li, D. Shen, and B. Ding, "Iterative learning control for output tracking of nonlinear systems with unavailable state

- information,” *IEEE Transactions on Neural Networks and Learning Systems*, pp. 1–8, 2021.
- [21] L. Wang, J. Yu, R. Zhang, P. Li, and F. Gao, “Iterative learning control for multiphase batch processes with asynchronous switching,” *IEEE Transactions on Systems, Man, and Cybernetics: Systems*, vol. 51, no. 4, pp. 2536–2549, 2021.
- [22] X. Li, Q. Ren, and J. Xu, “Precise speed tracking control of a robotic fish via iterative learning control,” *IEEE Transactions on Industrial Electronics*, vol. 63, no. 4, pp. 2221–2228, 2016.
- [23] D. Meng and K. L. Moore, “Contraction mapping-based robust convergence of iterative learning control with uncertain, locally Lipschitz nonlinearity,” *IEEE Transactions on Systems, Man, and Cybernetics: Systems*, vol. 50, no. 2, pp. 442–454, 2020.
- [24] X. Wang and J. Wang, “Iterative learning control for one-sided Lipschitz nonlinear singular conformable differential equations,” *International Journal of Robust and Nonlinear Control*, vol. 30, no. 17, pp. 7791–7805, 2020.
- [25] R. Chi, Y. Lv, and Z. Hou, “Compensation-based data-driven ILC with input and output package dropouts,” *International Journal of Robust and Nonlinear Control*, vol. 30, no. 3, pp. 950–965, 2020.
- [26] J. Zhang and D. Meng, “Convergence analysis of saturated iterative learning control systems with locally Lipschitz nonlinearities,” *IEEE Transactions on Neural Networks and Learning Systems*, vol. 31, no. 10, pp. 4025–4035, 2020.
- [27] J. Shi, J. Xu, J. Sun, and Y. Yang, “Iterative learning control for time-varying systems subject to variable pass lengths: application to robot manipulators,” *IEEE Transactions on Industrial Electronics*, vol. 67, no. 10, pp. 8629–8637, 2020.
- [28] Q. Ai, D. Ke, J. Zuo et al., “High-order model-free adaptive iterative learning control of pneumatic artificial muscle with enhanced convergence,” *IEEE Transactions on Industrial Electronics*, vol. 67, no. 11, pp. 9548–9559, 2020.
- [29] D. Meng and J. Zhang, “Robust tracking of nonrepetitive learning control systems with iteration-dependent references,” *IEEE Transactions on Systems, Man, and Cybernetics: Systems*, vol. 51, no. 2, pp. 842–852, 2021.
- [30] Y. S. Wei and X. D. Li, “Robust higher-order ILC for nonlinear discrete-time systems with varying trail lengths and random initial state shifts,” *IET Control Theory & Applications*, vol. 11, no. 15, pp. 2240–2247, 2017.
- [31] M. Sun and D. Wang, “Analysis of nonlinear discrete-time systems with higher-order iterative learning control,” *Dynamics and Control*, vol. 11, pp. 81–96, 2001.
- [32] Z. Song, H. Wang, C. He, and Y. Jin, “A Kriging-assisted two-archive evolutionary algorithm for expensive many-objective optimization,” *IEEE Transactions on Evolutionary Computation*, vol. 25, no. 6, pp. 1013–1027, 2021.
- [33] Y. Tian, X. Zhang, C. Wang, and Y. Jin, “An evolutionary algorithm for large-scale sparse multiobjective optimization problems,” *IEEE Transactions on Evolutionary Computation*, vol. 24, no. 2, pp. 380–393, 2020.
- [34] L. Chen, H.-L. Liu, K. C. Tan, and K. Li, “Transfer learning based parallel evolutionary algorithm framework for bi-level optimization,” *IEEE Transactions on Evolutionary Computation*, p. 1, 2021.
- [35] Z. Zhao and Z. Liu, “Finite-time convergence disturbance rejection control for a flexible Timoshenko manipulator,” *IEEE/CAA Journal of Automatica Sinica*, vol. 8, no. 1, pp. 157–168, 2021.
- [36] K. Wan and X. D. Li, “Robust iterative learning control of 2-D linear discrete FMMII systems subject to iteration-dependent uncertainties,” *IEEE Trans. Syst., Man, Cybern., Syst.* vol. 51, no. 3, pp. 1462–1472, 2021.
- [37] Z. Zhao, C. K. Ahn, and H.-X. Li, “Dead zone compensation and adaptive vibration control of uncertain spatial flexible riser systems,” *IEEE*, vol. 25, no. 3, pp. 1398–1408, 2020.

Research Article

Multiscale Efficient Channel Attention for Fusion Lane Line Segmentation

Kang Liu  and Xin Gao 

School of Mechanical Electronic & Information Engineering, China University of Mining & Technology, Beijing, Beijing 100 083, China

Correspondence should be addressed to Xin Gao; bqt2000405024@student.cumtb.edu.cn

Received 10 August 2021; Revised 1 November 2021; Accepted 23 November 2021; Published 7 December 2021

Academic Editor: Chao Zeng

Copyright © 2021 Kang Liu and Xin Gao. This is an open access article distributed under the Creative Commons Attribution License, which permits unrestricted use, distribution, and reproduction in any medium, provided the original work is properly cited.

The use of multimodal sensors for lane line segmentation has become a growing trend. To achieve robust multimodal fusion, we introduced a new multimodal fusion method and proved its effectiveness in an improved fusion network. Specifically, a multiscale fusion module is proposed to extract effective features from data of different modalities, and a channel attention module is used to adaptively calculate the contribution of the fused feature channels. We verified the effect of multimodal fusion on the KITTI benchmark dataset and A2D2 dataset and proved the effectiveness of the proposed method on the enhanced KITTI dataset. Our method achieves robust lane line segmentation, which is 4.53% higher than the direct fusion on the precision index, and obtains the highest F2 score of 79.72%. We believe that our method introduces an optimization idea of modal data structure level for multimodal fusion.

1. Introduction

Reliable and robust lane line segmentation is one of the basic requirements of autonomous driving. After all, in order to ensure that unmanned vehicles drive on the correct and reasonable roads, the vehicle must be able to detect the lane line the first time. The driving assistance system provides a decision-making basis for the autonomous driving control module through the results of lane line detection [1]. In this article, we focus on lane line segmentation based on multiple sensor fusion.

Existing algorithms rely heavily on the camera, which provides a rich visual description of the environment [2, 3]. The camera image has the original high-resolution and efficient array storage structure. It can provide long-distance dense information under good light and sunny weather conditions, and it is efficient in storage and calculation. However, when perceiving the surrounding environment, the performance of the camera is easily affected by the light intensity and sharp changes in light [4, 5]. Unlike cameras, LiDAR retains an accurate three-dimensional point cloud of

the surrounding environment and directly provides accurate distance measurement. Although the depth information is very accurate, the LiDAR usually has a measurement range of only 10 to 100 meters and can only provide sparse and irregular point cloud data. The empty voxels caused by the sparse point cloud bring the accuracy requirements of lane line detection. Here comes the challenge.

At present, most of the sensing sensors of vehicles on the road work independently, which means that they hardly exchange information with each other. Instead, their respective sensing modules process the data of a single sensor and then deliver the sensing results to the decision-making module. This method increases the number of perception modules and imposes a great burden on the calculation efficiency of onboard computing resources and decision-making modules [6, 7]. The fusion of information from multiple sensors is a growing trend and the key to efficient autonomous driving. Multimodal fusion can take advantage of the complementarity of different sensor information and use feature-level fusion to promote semantic segmentation, thereby improving the accuracy and efficiency of lane line

segmentation and ensuring the correctness and timeliness of decision-making.

Some recent work has explored the use of camera images and LiDAR point clouds for lane line segmentation tasks in autonomous driving. Due to the perspective transformation in imaging, the camera image cannot describe the accurate distance information, and the method of directly using the two-dimensional camera image for lane line segmentation is unreliable [8]. Although the depth information of the LiDAR point cloud is already available, so far, the main success of the fusion method is to use the advantages of multimodal data to supplement the camera image with the precise depth information of the LiDAR. Previous studies put multimodal fusion in a two-dimensional space, usually using a direct stacking method to fuse the depth information of point cloud data with the camera image with a fixed weight. Another idea is to fuse multimodality [9, 10]; they put it in the three-dimensional space, make full use of the accurate representation of the distance information of the point cloud data, and fuse the data in the three-dimensional space. However, the camera image and the LiDAR point cloud are data of different modalities and have great differences[11]. The direct stacking fusion method ignores the characteristics of multimodal data and will inhibit the respective advantages of multimodal data, and may even appear the effective fusion information is misjudged as the negative effect of noise. While placing multimodal fusion in a high-dimensional space, algorithms based on 3D detection often require large computing resources, which are difficult to meet the needs of lightweight and real time in autonomous driving[12]. For this reason, we propose a novel multimodal fusion lane line segmentation method based on multiscale convolution and channel attention mechanisms. We believe that multimodal fusion should focus on the fusion feature space, and use reasonable methods and weights to guide multimodal fusion.

In order to make full use of multisource data for reasonable control and use, we need to explore a question: what method should be used to promote semantic segmentation to obtain better lane line segmentation results. To this end, we first analyzed the benchmark dataset for lane line segmentation. In the KITTI dataset, the area occupied by lane lines in the image is only 1.5% to 2%, and the problem of class imbalance is quite serious. In this article, we hope that when the deep learning network is extracting features, it can more effectively focus on the characteristics of lane lines, thereby improving the quality of the segmentation results. For this reason, we use multiscale convolution for feature fusion in multimodal fusion and introduce the channel attention mechanism to modify the fusion weight. The results are shown in Figure 1, and we believe that the task of lane line segmentation should find a way to maximize the effect of multimodal data under the premise of ensuring the quality of the data.

This article is organized as follows: in Section 2, we separately analyzed the current lane line segmentation algorithms based on camera images and point clouds and introduced the current status of the fusion method; in Section 3, we carried out the proposed method and network

structure in detail; Section 4 discussed the processing of the dataset, as well as the experimental results and performance evaluation obtained after applying the proposed method; in Section 5, an ablation experiment was used to measure the contribution of each module in the proposed method; and in Section 6, the proposed methods are summarized and future directions are provided.

In conclusion, the main contributions of the article are as follows: (1) an idea of using multiscale convolution for multimodal fusion lane line segmentation is proposed; (2) ECANet[13] is used for the weight correction of the fusion feature channel, which effectively improves the accuracy of the lane line segmentation model; and (3) the proposed multiscale efficient channel attention(MS-ECA) can be widely used in the field of multimodal fusion and has good mobility.

2. Related Work

2.1. Lane Line Segmentation. The traditional lane line segmentation uses the canny operator to detect the sharp change in brightness[14], which is defined as an edge under a given threshold, and then uses the Hough transform to find the lane line. In recent years, the emergence of machine learning has promoted the development of artificial intelligence, and the wide application of deep learning has made feature-level lane line segmentation algorithms gradually mature [15, 16]. Wenjie Song et al. [17] designed an adaptive traffic lane model in the Hough space. The model has a maximum likelihood angle and a dynamic rod detection area (ROI) of interest. This model can also be improved through geographic information systems or electronic maps to obtain more accurate results. To get more accurate results. Xingang Pan et al.[18] proposed spatial CNN(SCNN), which extended the traditional layer-by-layer convolution to the slice-by-slice convolution in the feature map, thereby enabling message passing between pixels between rows and columns in a layer. Bei He et al. [19] designed a DVCNN network that optimizes both the front view and the top view. The front view image is used to eliminate false detections, the top view image is used to remove nonclub-shaped structures, such as ground arrows and text, and a large number of complex constraints are used. Conditions improve the quality of lane line detection. However, due to the photosensitivity of the camera, lane line detection based on pure vision still has great challenges in terms of performance and robustness.

Some recent work has explored the use of multimodal fusion for detection and segmentation tasks in autonomous driving [17, 20, 21]. Andreas Eitel introduced a multistage training method that effectively encodes the depth information of CNN[22], so that learning does not require large depth datasets, through the data enhancement scheme of robust learning of the depth image, it is corroded with the real noise mode [23]. Hyunggi Cho et al. [20] redesigned the sensor configuration and installed multiple LiDAR pairs and vision sensors. Based on the combination of measurement models of multiple sensors, they proposed a new moving target detection and tracking system. Reference [24] explored all aspects of pedestrian detection by fusing LiDAR

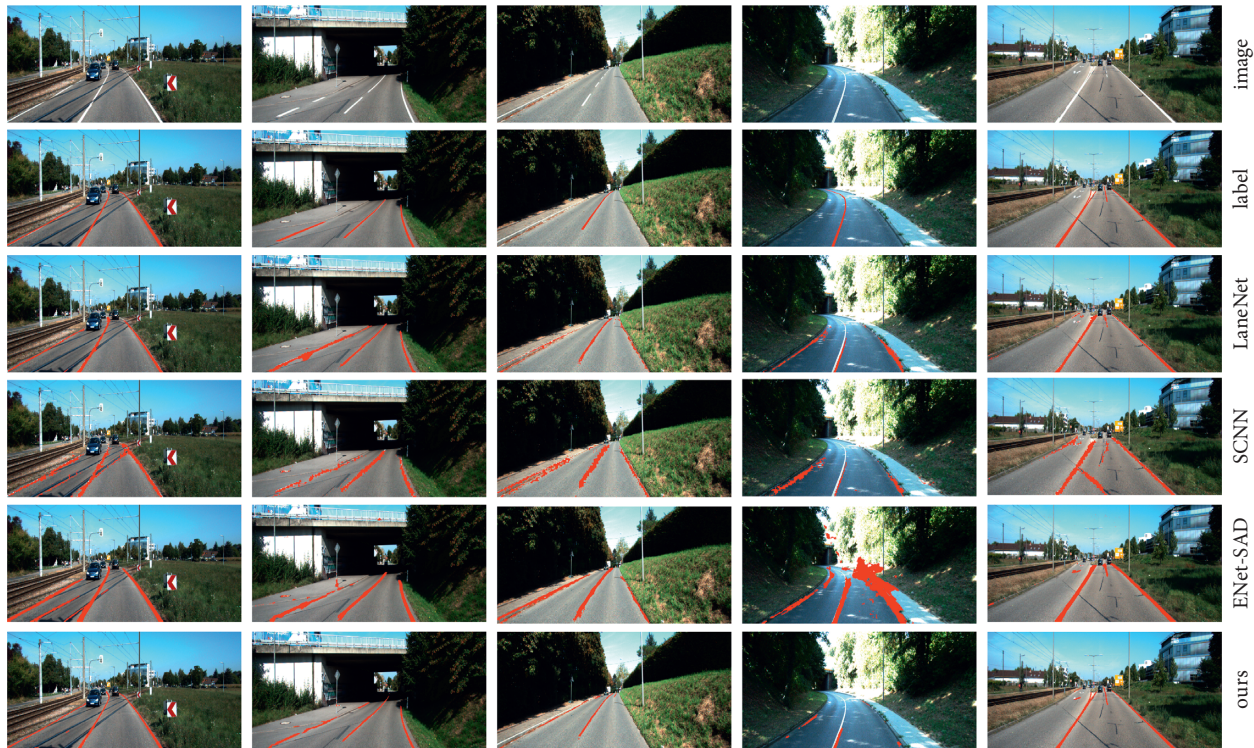


FIGURE 1: Test results on KITTI-aug dataset. The rows from top to bottom are input images, ground truth, output from LaneNet, SCNN, ENet-SAD, and ours.

and color images in the context of convolutional neural networks. This work samples the point cloud into a dense depth map, then extracts three features representing different aspects of the 3D scene, and use LiDAR as an additional image channel for training. However, current fusion algorithms pay more attention to data quality and network structure, and the characteristics of multimodal data and the representation of fusion data have not been paid attention to. The difference is that our proposed method naturally selects the fusion weight and the fusion channel adaptively in the fusion and effectively shows the advantages of multimodal data.

2.2. Attention Mechanism. The attention mechanism has recently been widely used to learn the weight distribution [25], and the neural network is used to focus on different parts of the input data or feature maps, so that the attention module is designed to weight the input data or feature maps. Jianlong Fu et al. [26] used a classification network and a network to generate attention proposal on each target scale of concern, defined a rank loss to train the attention proposal, and forced the final scale to obtain a classification result that was better than the previous one, so that the attention proposal extracts the target part that is more conducive to fine classification [27]. In the classification network, an attention module composed of two branches is added [28]: one is a traditional convolution operation, and the other is two downsampling plus two upsampling operations; the purpose is to obtain the larger receptive field serves as an attention map. High-level information is more

important in classification problems; they use an attention map to improve the receptive field of low-level features and highlight features that are more beneficial to classification. Liang-Chieh Chen et al. [29] constructed multiple scales by scaling the scale of the input picture. The traditional method is to use average pooling or max pooling to fuse features of different scales, and they constructed an attention model composed of two convolutional layers to automatically learn the weights of different scales for fusion. We have empirically found that due to the small proportion of lane lines in the image, the overall attention of the spatial attention mechanism may interfere with segmentation. Therefore, our work pays more attention to the effect of the channel attention mechanism on multimodal fusion.

3. Methods

In this part, we introduce the basic structure of our network and introduce the proposed multiscale convolution fusion module, and related experiments are completed based on this part of the network.

3.1. Baseline for Multimodal Fusion. Lane line segmentation is a typical pixel-level segmentation task. We established a baseline fusion model based on Unet [30]. As shown in Figure 2, its input is two modal data, which is the same as most current fusion methods. Multimodal data are concatenated together after a convolution. The baseline model is trained end-to-end by an encoder and a decoder, and the size of the convolution kernel of all convolution blocks is $3 * 3$.

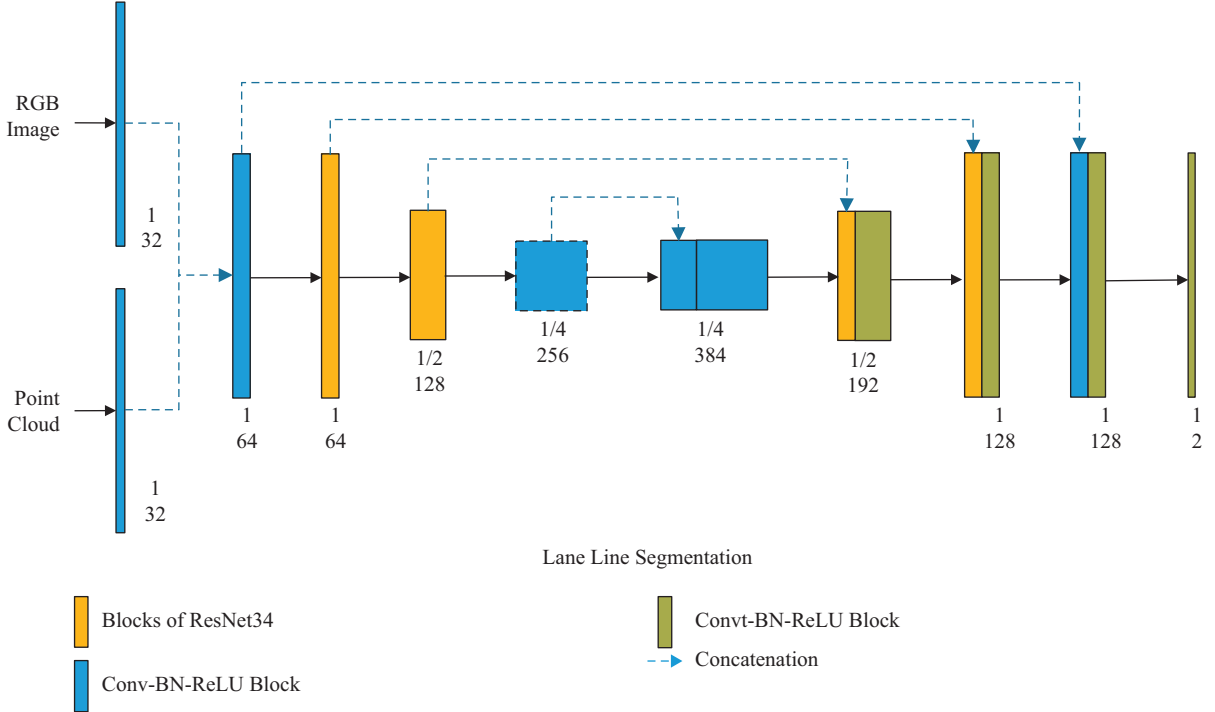


FIGURE 2: Our fusion modal baseline: it takes an RGB image and a point cloud as input and outputs a $512 * 256$ binary map.

Based on Unet’s skip connection, we link the output of each block in the encoder to a block of the corresponding size in the decoder and use different levels of feature map semantic information through concatenating.

3.2. Multiscale Convolution Fusion. Generally, for a given task model, the size of the convolution kernel is determined, and the convolution kernel of uniform size can be easily calculated. However, studies have shown that for a given input, if the network can adaptively adjust the size of the receptive field according to the multiple scales of the input information, extract the features under the multiscale receptive field, and finally, use the “selection” mechanism to fuse multiscale features, the performance of the model can be effectively improved. For the camera image and LiDAR point cloud data, although they are not the same input data, they are aligned to describe the same scene. We creatively use multiscale convolution to extract features for these two modalities. Obtain multimodal features under different sizes of receptive fields, and finally fuse them to obtain multiscale multimodal fusion features.

Based on SKNet’s[31] dynamic selection strategy, we also choose $3 * 3$ and $5 * 5$ size convolution kernels as multiscale convolution kernels. Generally speaking, a camera image will have millions of pixels. In contrast, the performance of LiDAR for the same scene is often only tens of thousands of effective points. Even after point cloud completion processing, it still looks sparse compared to the camera image. Therefore, as shown in Figure 3, we use the $5 * 5$ size convolution kernel for the point cloud branch and use the $3 * 3$ convolution kernel for the camera image branch, which will be more conducive to the extraction of

the original effective information. In order to further improve the efficiency, the conventional convolution of the $5 * 5$ convolution kernel is replaced with a $3 * 3$ convolution kernel and an expanded convolution with an expansion size of 2.

We naturally use the Fuse and Select operations in SKNet to calculate fusion multiscale features. We embed global information by simply using global average pooling to generate channel-level statistics. Specifically, the c -th element of s is calculated by reducing the spatial dimension $H * W$:

$$s_c = \mathcal{F}_{gp}(U_c) = \frac{1}{H * W} \sum_{i=1}^H \sum_{j=1}^W U_c(i, j), \quad (1)$$

and then, a simple fully connected layer is used to realize the guidance of accurate and adaptive selection, and reduce the dimension to improve the efficiency:

$$z = \mathcal{F}_{fc}(s) = \delta(\mathcal{B}(Ws)), \quad (2)$$

where δ is the ReLU function and \mathcal{B} is the batch normalization, and $W \in \mathbb{R}^{d \times c}$. Finally, we adaptively choose different spatial scales to obtain cross-channel attention weight. Specifically, the softmax operator is applied to the channel-wise digits; in (3), z is the compact feature descriptor, and a , b denote the soft attention vectors:

$$a_c = \frac{e^{A_c z}}{e^{A_c z} + e^{B_c z}}, b_c = \frac{e^{B_c z}}{e^{A_c z} + e^{B_c z}}. \quad (3)$$

In this process, convolution kernels of different sizes provide multiscale receptive fields for the two modes of data, and large convolution kernels can extract the features of

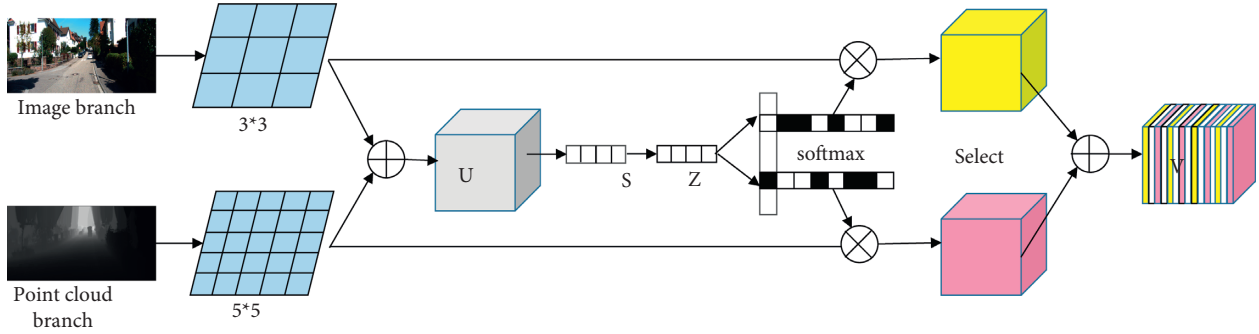


FIGURE 3: Structure of multimodal multiscale fusion. We use a $3 * 3$ convolution kernel for the image branch and a $5 * 5$ convolution kernel for the point cloud branch.

sparse point cloud data more effectively, which is very helpful for multiscale fusion. In addition, in the process of using channel-level statistical information to embed global information, the nonlinear learning in the network is increased, which alleviates the negative impact of rough conversion of multimodal data to the same feature space to a certain extent, and improves the learning ability of the network. After weighting the features of multimodal branches with the weights of channel level, the expression of lane line features of each modal branch can be increased better, so that lane line features can be extracted more effectively after fusion.

3.3. Local Interaction of Fusion Feature Channels. In the task of lane line segmentation, the proportion of the lane line area in the image is very small, and it is a serious challenge to efficiently extract the lane line features from a large amount of background or noise. In this kind of unbalanced data, in order to allow the network structure to adaptively pay attention to the lane line features, we use an efficient attention mechanism. It can be seen from the figure that in the process of extracting features from the network, due to the difference of filters, the focus of feature extraction from different feature channels is different. In this process, some feature channels can extract rich features. Information and some feature channels contain a lot of noise information. In a neural network, these feature channels will be stacked in sequence to act on the segmentation task. Naturally, how to enhance this part of the efficient feature channel becomes a problem.

At the same time, considering that the lane line segmentation task is a prerequisite for unmanned driving decision planning and has high real-time requirements, we use the lightweight channel attention mechanism model ECANet for the fusion features after multimodal fusion. Note that we only discuss the effect of lightweight attention mechanism on multiscale and multimodal fusion. Through the channel attention mechanism, we calculate the importance of each feature channel of the fusion feature in the network and let the network adaptively learn the contribution of each feature channel to the lane line segmentation task, and the feature channels that make a positive

contribution to the segmentation will be adaptively enhanced; otherwise, they will be suppressed.

As shown in Figure 4, in the idea of ECANet, the importance of each feature channel will be represented by modeling, and the neighboring channels are correlated, and the weight of each feature channel will be calculated by its neighboring neighbor channels, so that it can avoid dimensional loss while capturing local cross-channel interactive information. We integrate ECANet into the task of multimodal fusion lane line segmentation and obtain a model with lower model complexity and smaller network parameters. The network structure of ECANet is shown in Figure 5.

Without dimensionality reduction, ECANet calculates the nearby k channels of each feature channel centered on itself and uses the correlation between adjacent channels to interact with local information. In this channel weight calculation, the lane feature channels that perform well in the effective features of the line will receive greater attention, which will lead to positive positive contributions to the feature channels nearby. When the channel dimension C is given, the value of k can be determined adaptively according to the following formula:

$$C = \phi(k) = 2^{(\gamma * k - b)}. \quad (4)$$

$$k = \psi(C) = \left\lfloor \frac{\log_2(C)}{\gamma} + \frac{b}{\gamma} \right\rfloor_{\text{odd}}, \quad (5)$$

where $\lfloor T \rfloor_{\text{odd}}$ indicates the nearest odd number of t . Same as ECANet, we set γ and b to 2 and 1. In the experiment, the calculation result of k is an odd number not exceeding 9.

We embed the channel attention module after the fusion module to perform channel-level weight correction on the fusion features after multimodal fusion. The fusion features obtained through fusion between the image branch and the point cloud branch are used as the input of the channel attention module, and the output of the channel attention module is used as the input of the next layer of the network structure in the original baseline. The network structure is shown in Figure 5, and the whole of the multimodal fusion module and the channel attention module is called MS-ECA (Table 1).

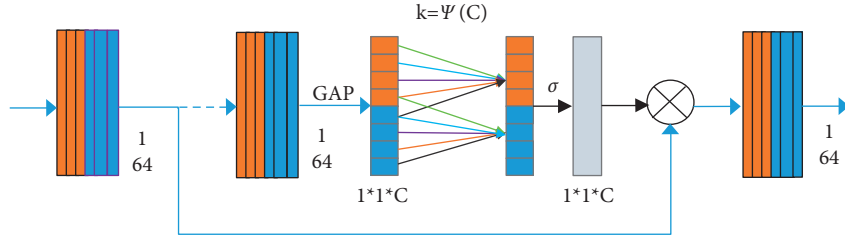


FIGURE 4: The structure of efficient channel attention. The input channel here is 64.

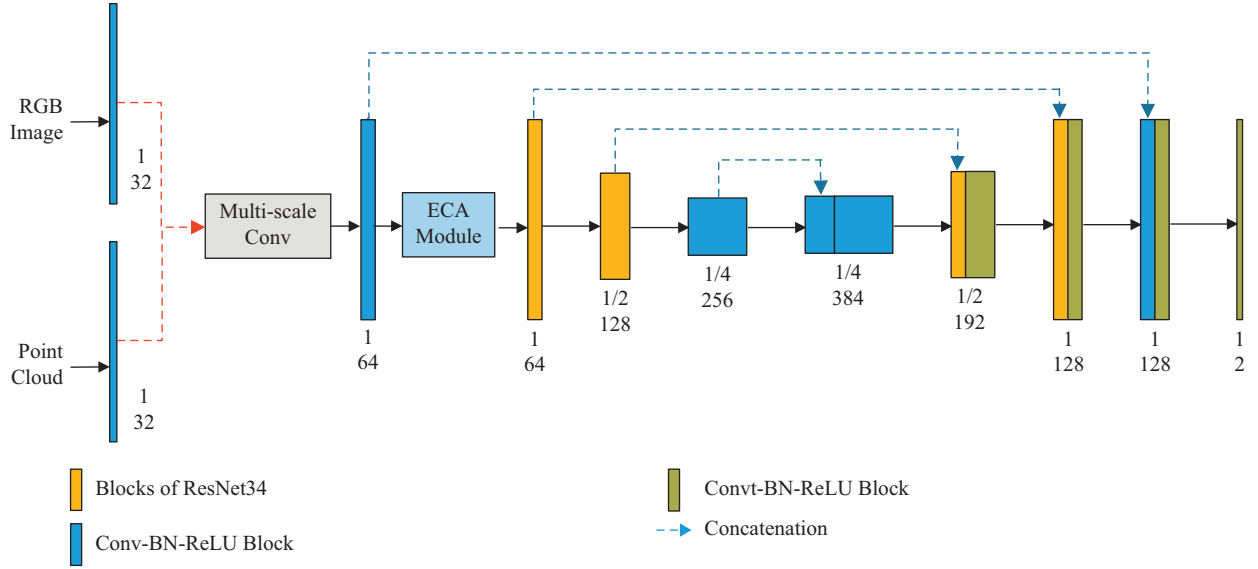


FIGURE 5: The structure of our method (multiscale efficient channel attention) embedded in the baseline.

TABLE 1: Information of the lane line segmentation datasets.

Name	Frame	Train	Validation	Test	Resolution
KITTI	383	228	40	115	1242 × 375
KITTI-aug	3331	2736	480	115	1242 × 375
A2D2	470	282	47	141	1920 × 1208

4. Experiment

4.1. Dataset Preparation. The current multimodal lane line segmentation dataset is relatively lacking. To verify the proposed method, we conducted extensive experiments on the benchmark datasets KITTI-Road[32] and A2D2[33]. As shown in Figure 6, the KITTI-Road and A2D2 datasets include synchronized camera images and LiDAR point clouds with calibration parameters and ground truth values. We filter out complex cross-lines or forward lines in the dataset and use the remaining data to validate our proposed method and model.

In the processing of the dataset, we also filtered out confusing lane lines, such as markings on the sidewalk and signs outside the lane lines to better meet the task requirements of lane line segmentation. Compared with the TuSimple dataset, in order to extract the lane line features more accurately, we only use the visible lane line pixels on the image and ignore the part of the lane line behind

obstacles or other invisible lane lines to ensure that the network learns completely the characteristics of the lane line. Finally, the dataset annotations are redone as pixel-level lane line labels. In training, we use the same feature extraction module to extract features of the camera image and the point cloud. As for the network input, the initial size of the original camera image and the corresponding point cloud is 1242 * 375, in order to reduce the calculation overhead, in the data preprocessing, we reshape them to the size of (256, 512) in the same way and then input them into the network.

The KITTI and A2D2 datasets have limited samples. In order to conduct experiments better, we need to carry out reasonable data enhancement. In the acquisition of the A2D2 dataset, only one 8-line and two 16-line LiDARs are used to collect point cloud data. The point cloud is very sparse and contains little information. In contrast, KITTI uses a 64-line LiDAR to complete the point cloud collection, and the resulting point cloud has a richer description of the entire space. Therefore, we use the KITTI dataset as the main verification dataset. In addition, we performed strategies such as cropping, brightness conversion, and adding noise to the KITTI data and obtained a dataset 12 times the original KITTI data, which is represented by KITTI-AUG. All experiments use 60% of the data as the training set, 30% for the test model, and the remaining data for verification in training. The dataset information we use is shown in Table 1.



FIGURE 6: Examples of KITTI(top row) and A2D2(bottom row). The columns from left to right are camera image, lane line label, and point cloud.

4.2. Training Procedure. In order to ensure fairness, all experiments are implemented on a standard training platform, with only differences in the methods in the neural network. Our hardware platform has the following: 8 GB of RAM, a three-core E5 series CPU, and an NVIDIA TiTan XP GPU with 12G memory, and the operating system is Ubuntu 16.04. All the codes are based on the PyTorch framework. We have implemented end-to-end network training. In order to speed up the convergence, we use the Adam optimization algorithm, and the parameters in Adam are default values. In order to prevent the difficulty of finding the optimal solution during training, we also use a learning rate LR with periodic decay:

$$\text{nllloss} = - \sum_{n=1}^N y_n \log \text{prob}(x_n), \quad (6)$$

and we use the Adam optimization algorithm [34] to train the network end-to-end, using a periodic decay learning rate LR:

$$lr_0 = 0.0001lr = 2^{\lfloor \text{epoch}/50 \rfloor} \times 0.8^{\lfloor \text{epoch}/1 \rfloor} \times lr_0, \quad (7)$$

where $lr_0 = 0.0001lr_0$ is the initial learning rate. The training rounds and batch sizes of all experiments are set to 200 and 4, respectively. In the training process, we use the strategy of using the validation set to verify the current model while training. Specifically, we will use the current model parameters to perform a performance evaluation on the validation set every 5 epochs of training. If the current model parameters have achieved performance upgrade, the corresponding weight file and related verification results will be automatically saved.

In semantic segmentation tasks, recall and accuracy are both important indicators to measure model performance. For lane line segmentation, the recall rate reflects the proportion of lane line pixels correctly predicted by the model in all positive samples, and the accuracy rate reflects the proportion of real lane line pixels in the result of the model prediction. The formula is as follows:

$$\text{precision} = \frac{tp}{tp + fp}, \quad (8)$$

$$\text{recall} = \frac{tp}{tp + fn}. \quad (9)$$

In addition, in order to make a clearer comparison, we also used F-measure(including F1 and F2) and calculated the accuracy of the overall prediction as “acc.” Finally, in order to verify the real-time performance of the proposed method, we calculated the FPS of the lane line segmentation in the test for some experimental models.

4.3. Experimental Results. The experiment in Table 2 compares the performance of single-mode and multimodal fusion for lane line segmentation in the two datasets of KITTI and A2D2. It can be seen that in the task of lane line segmentation, using only camera data has a slight advantage over using only LiDAR data, and multimodal fusion has obvious advantages over single-modal data. Lane line segmentation is a pixel classification problem. Camera data with good pixel continuity are more suitable for lane line segmentation. The data structure of the LiDAR point cloud is discrete points, and the accurate description of the edge of the lane line is not as good as the camera image. This is also an important factor for us to project the point cloud data to the camera plane for multimodal fusion. From the comparison of the experimental results of KITTI and A2D2, it can be seen that the lane line detection effect of the KITTI data is better, and the detection results reflect the data quality and the difficulty of the scene. We can see that KITTI data is more universal, therefore, in subsequent experiments, we will mainly use KITTI dataset and the data-enhanced KITTI-aug. In the experiment, we will mainly use the KITTI dataset and the data-enhanced KITTI-aug.

We have conducted extensive experiments on the KITTI dataset and KITTI-aug. As shown in Table 3, we have conducted experimental comparisons between the single-modal, multimodal direct fusion and the proposed method.

TABLE 2: Comparison of single-modal and multimodal fusion in KITTI and A2D2. “REC” denotes “Recall” and “PRE” denotes “Precision,” and we use the same abbreviation in the following sections.

Dataset	Mode	REC	PRE	F1	F2	Acc
KITTI	LiDAR	85.43	25.82	37.84	54.41	95.19
	Camera	82.30	45.53	55.59	67.06	97.84
	Fusion	93.34	45.89	57.89	71.22	98.16
A2D2	LiDAR	84.44	22.60	35.51	48.54	94.45
	Camera	87.47	24.36	36.27	54.65	95.22
	Fusion	87.06	32.09	45.06	61.57	98.87

TABLE 3: Comparison of different methods in KITTI and KITTI-aug. F-MS-ECA denotes fusion with our method(multiscale efficient channel attention).

Dataset	Mode	REC	PRE	F1	F2	Acc
KITTI	LiDAR	85.43	25.82	37.84	54.41	95.19
	Camera	82.30	45.53	55.59	67.06	97.84
	Fusion	93.34	45.89	57.89	71.22	98.16
	F-MS-ECA	93.66	48.16	62.81	77.68	98.50
KITTI-aug	LiDAR	85.19	29.40	42.57	60.83	96.22
	Camera	82.44	47.65	57.31	71.19	97.95
	Fusion	92.24	48.57	62.89	77.12	98.44
	F-MS-ECA	92.23	51.38	65.25	78.57	98.65

After data enhancement, the overall test effect of the direct fusion of single modal and multimodality has been significantly improved. Among them, the F2 score of direct fusion of multimodality on KITTI-aug is 5.9% higher than that on KITTI, which shows that the used data enhancement can improve the robustness of the model. After using the proposed MS-ECA fusion method, the overall performance of the model has been further improved, and the F2 scores on KITTI and KITTI-aug have been improved by 6.46% and 1.45%, respectively. It can be seen that the precision index of the main factor of performance improvement has been significantly improved, which shows that the proposed multimodal fusion method MS-ECA can effectively reduce the false detection rate of the model to the lane line. The proposed fusion method is of great benefit to the detection of actual lane lines.

We compared our model with the current advanced models SCNN [18], LaneNet [3], and ENet-SAD [35]. All models are trained from scratch, except SCNN, and LaneNet load pretrained VGG-16 [36] weights to accelerate learning. To be fair, we train SCNN and LaneNet for 60 000 iterations (equivalent to 175 epochs). They stopped optimization after 3000 iterations. For ENet-SAD, we added the SAD strategy at the 40 000 iterations. Our model was trained for 200 epochs, and they almost converged after about 150 epochs. The experimental results are shown in Table 4. It can be seen that our model has the characteristics of lightweight and is in the same order of magnitude as the lightest ENet-SAD. Compared with the current state-of-the-art model, our model has obvious overall performance advantages and at the same time has a very high FPS, reaching 59.5 frames per second.

TABLE 4: Performance of different SOTA algorithms on KITTI-aug testing set.

Algorithm	Size (M)	REC	PRE	F2	Acc	FPS
LaneNet	285.7	80.97	32.81	60.97	96.87	69.1
SCNN	270.3	88.61	30.37	63.06	97.07	14.4
ENet-SAD	11.0	91.21	33.96	66.90	97.44	22.5
Ours	25.0	92.23	51.38	78.57	98.65	59.5

4.4. Ablation Study. In order to verify the contribution of each structure in the proposed method to the performance of the model, we conducted extensive ablation experiments under different backbones, and the loss curve of using ResNet34 is shown in Figure 7. As shown in Table 5, we conducted experiments on the performance of the multiscale fusion module and ECA module in the proposed method, named, F-MS and F-ECA, respectively, and the visualization results are shown in Figure 8. It can be seen that the impact of multiscale module and the ECA module on the method is mainly to improve the precision index. The multiscale module has a slight advantage in the gain of precision. When ResNet50 is used as the backbone, the gain of multiscale to precision reached 3.27%. It can be seen from the FPS that the frame rate of all models is maintained above 50, and the amount of calculation required to multiscale fusion module is greater, which leads to a more significant increase in the reasoning time of the model. Our method guarantees a high frame rate, while the overall performance of the model is excellent. It can be seen that as the network deepens, the accuracy of all models is gradually improving. When ResNet50 is used as the backbone, our method improves the precision index by 4.53% compared to the direct fusion. It is worth noting that the actual vehicle-mounted autonomous driving platform needs to carry multiple deep learning models. The deeper the network parameters, the greater the number of network parameters. Although when ResNet50 is used as the backbone, our model still has at least 50 FPS on the current test platform. In order to ensure sufficient accuracy and lightness, we still recommend using ResNet18 or ResNet34 as the backbone for actual use.

In order to verify the role of point cloud data in the lane line segmentation task, we split the information in the point cloud and fused the depth, height, and tensity with the camera image for experiments. Note that this experiment used ResNet34’s pretraining parameters, and the results are shown in Table 6. It can be seen that the three types of information contribute differently to the fusion. Among them, precision is increased by 0.72 when using height information, and recall is slightly reduced when using tensity and depth information, but precision has been greatly improved with 1.42 and 1.37, respectively. This shows that the tensity and depth information in the fusion is more important than the height. It is worth noting that the tensity has a better effect in the task of lane line segmentation; however, in other fusion tasks, we suggest to pay more attention to the depth information in the point cloud, which can make up for the lack of depth information for two-dimensional images.

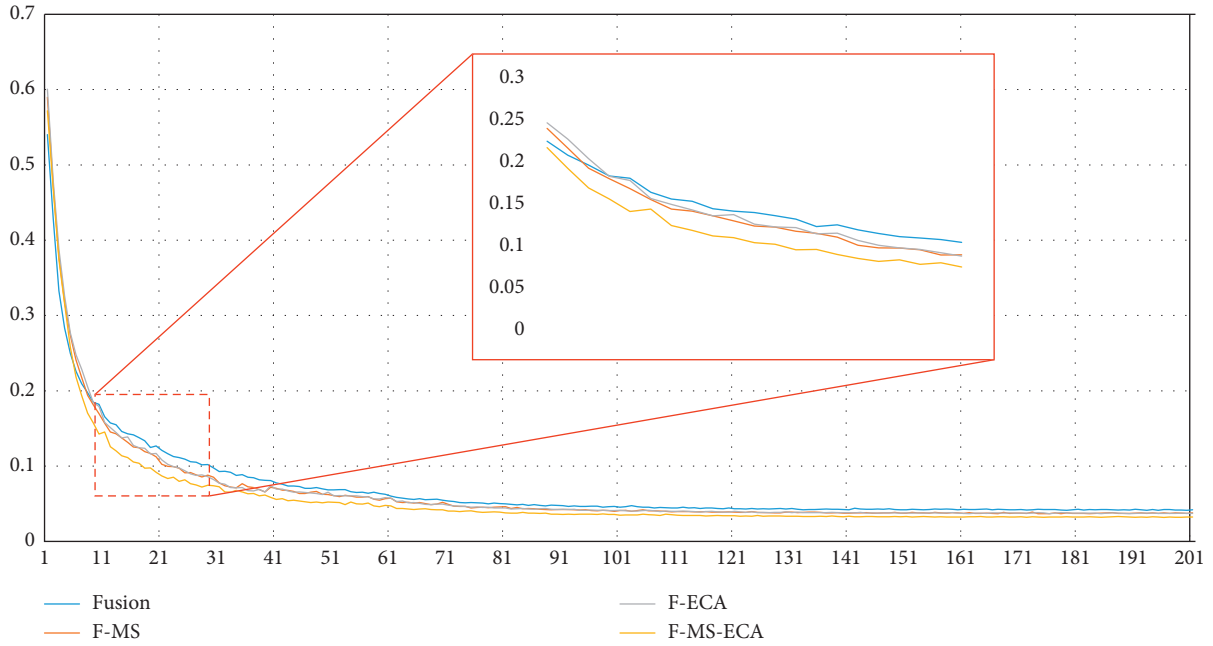


FIGURE 7: Loss curve during training; all training uses the pretraining parameters of ResNet34.

TABLE 5: The performance of using different pretrained parameters in fusion. F-MS denotes fusion only with multiscale strategy, and F-ECA denotes that fusion only with ECA.

Backbone	Method	REC	PRE	F2	Acc	FPS
ResNet18	Fusion	92.24	48.57	77.12	98.44	79.0
	F-MS	92.17	50.52	77.97	98.41	66.5
	F-ECA	92.13	50.66	78.03	98.57	78.3
	F-MS-ECA	93.08	51.21	78.34	98.62	60.2
ResNet34	Fusion	92.75	49.37	78.23	98.54	75.3
	F-MS	92.08	50.77	78.47	98.61	65.2
	F-ECA	92.12	50.36	78.46	98.61	73.9
	F-MS-ECA	92.23	51.38	78.57	98.65	59.5
ResNet50	Fusion	93.09	49.84	78.53	98.58	65.9
	F-MS	92.35	53.11	79.15	98.73	57.1
	F-ECA	92.27	52.97	78.83	98.69	62.8
	F-MS-ECA	93.17	54.37	79.72	98.81	53.6

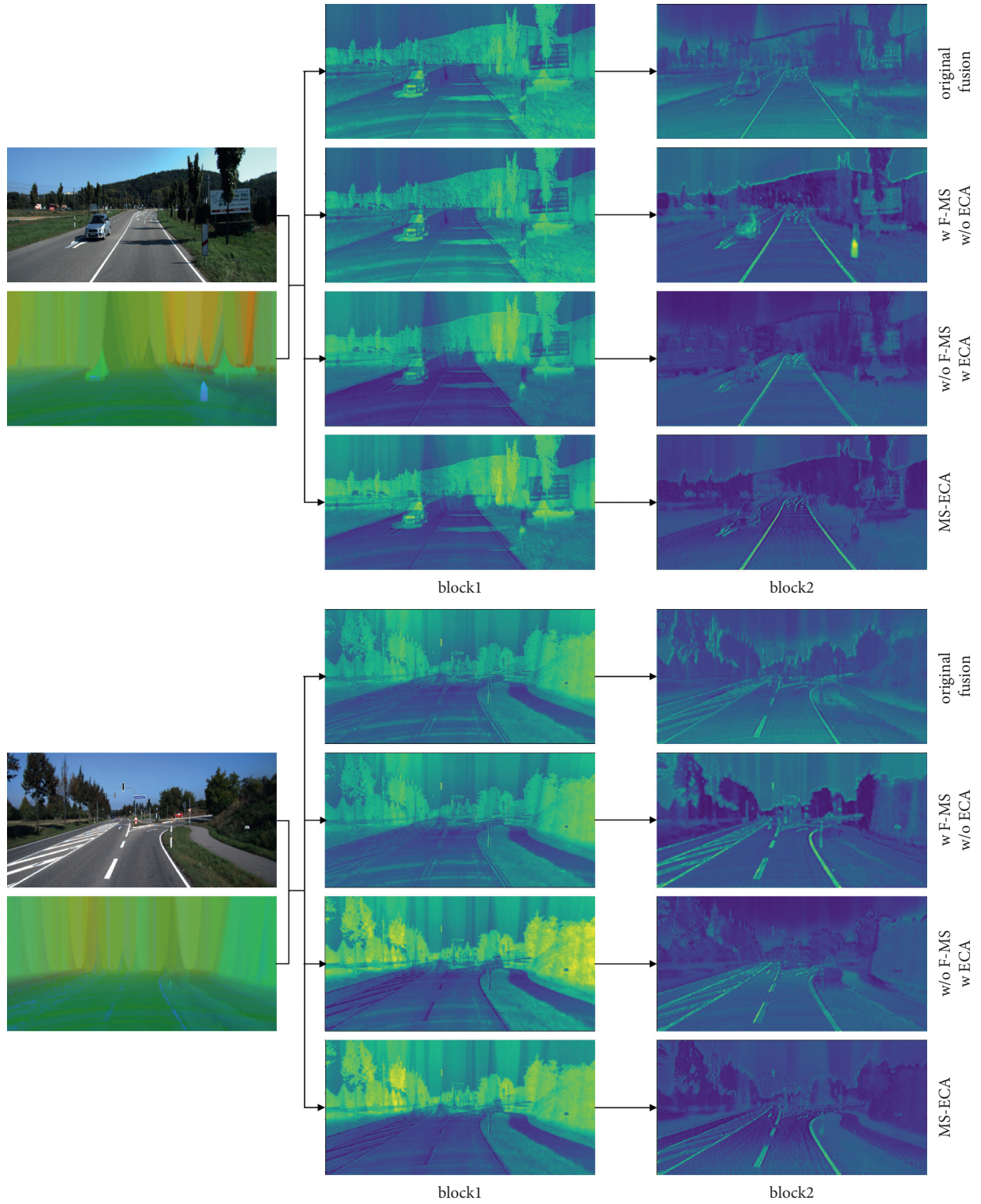


FIGURE 8: Visualization results of the fusion with and without MS/ECA in the feature channels of two different convolution blocks in the fusion.

TABLE 6: Performance comparison when only partial point cloud information is used. For example, F-depth means that only the depth information in the point cloud is used.

Method	REC	PRE	F2	Acc
Fusion	92.75	49.37	78.23	98.54
F-height	92.68	50.09	78.39	98.55
F-tensity	92.31	50.79	78.54	98.61
F-depth	92.44	50.74	78.43	98.60
F-all	92.23	51.38	78.57	98.65

5. Conclusion

This article proposes to optimize the multimodal fusion by using the multiscale fusion and ECA module for the task of lane line segmentation. By extracting features of different scales from camera images and LiDAR point clouds, and using the channel attention mechanism to calculate the weights of fusion features, we have achieved excellent results in a multimodal fusion network. In the test on the KITTI-aug dataset, we obtained the best performance model when using ResNet50 as the backbone, with the highest F2 score of 79.72%. At the same time, our method can maintain excellent test speed in actual tests. The structural difference between the modalities is one of the main problems that make the current multimodal fusion difficult. In the future, we will explore the fusion of different modalities in high-dimensional space and analyze the differences and differences between the modalities from the structure of the data and achieve more robust fusion.

Data Availability

All the data generated or analyzed during this study are included within this article.

Conflicts of Interest

The authors declare that there are no conflicts of interest regarding the publication of this article.

Acknowledgments

This research was funded by the Natural Science Foundation of Shanxi Province under Grant No. 201901D111467.

References

- [1] N. Garnett, R. Cohen, T. Pe'er, R. Lahav, and D. Levi, "3d-lanenet: end-to-end 3d multiple lane detection," in *Proceedings of the IEEE/CVF International Conference on Computer Vision*, pp. 2921–2930, Seoul, Korea (South), November 2019.
- [2] J. Zhang, Yi Xu, B. Ni, and Z. Duan, "Geometric constrained joint lane segmentation and lane boundary detection," in *Proceedings of the european conference on computer vision (ECCV)*, pp. 486–502, Munich, Germany, October 2018.
- [3] Ze Wang, W. Ren, and Q. Qiu, "Lanenet: real-time lane detection networks for autonomous driving," <https://arxiv.org/abs/1807.01726>.
- [4] X. Xu, G. Li, G. Xie, J. Ren, and X. Xie, "Weakly supervised deep semantic segmentation using cnn and elm with semantic candidate regions," *Complexity*, vol. 2019, 2019.
- [5] An Feng-Ping and J.-e Liu, "Medical image segmentation algorithm based on optimized convolutional neural network-adaptive dropout depth calculation," *Complexity*, vol. 2020, 2020.
- [6] R. Yin, Y. Cheng, H. Wu, Y. Song, B. Yu, and R. Niu, "Fusionlane: multi-sensor fusion for lane marking semantic segmentation using deep neural networks," *IEEE Transactions on Intelligent Transportation Systems*, pp. 1–11, 2020.
- [7] L. Tong, Z. Chen, Yi Yang, Z. Wu, and H. Li, "Lane detection in low-light conditions using an efficient data enhancement: light conditions style transfer," in *Proceedings of the 2020 IEEE Intelligent Vehicles Symposium (IV)*, pp. 1394–1399, IEEE, Las Vegas, NV, USA, November 2020.
- [8] E. Arnold, O. Y. Al-Jarrah, M. Dianati, S. Fallah, D. Oxtoby, and A. Mouzakitis, "A survey on 3d object detection methods for autonomous driving applications," *IEEE Transactions on Intelligent Transportation Systems*, vol. 20, no. 10, pp. 3782–3795, 2019.
- [9] Y. Cui, R. Chen, W. Chu et al., "Deep learning for image and point cloud fusion in autonomous driving: a review," *IEEE Transactions on Intelligent Transportation Systems*, pp. 1–18, 2021.
- [10] K. Zhu, R. Guo, W. Hu, Z. Li, and Y. Li, "Legal judgment prediction based on multiclass information fusion," *Complexity*, vol. 2020, 2020.
- [11] S. Gu, Y. Zhang, J. Tang, J. Yang, and H. Kong, "Road detection through crf based lidar-camera fusion," in *Proceedings of the 2019 International Conference on Robotics and Automation (ICRA)*, pp. 3832–3838, IEEE, Montreal, QC, Canada, May 2019.
- [12] L. Caltagirone, M. Bellone, L. Svensson, and M. Wahde, "LiDAR-camera fusion for road detection using fully convolutional neural networks," *Robotics and Autonomous Systems*, vol. 111, pp. 125–131, 2019.
- [13] Q. Wang, B. Wu, P. Zhu, P. Li, W. Zuo, and Q. Hu, "Eca-net: efficient channel attention for deep convolutional neural networks," in *Proceedings of the 2020 IEEE/CVF Conference on Computer Vision and Pattern Recognition (CVPR)*, Seattle, WA, USA, June 2020.
- [14] P. M. Daigavane and P. R. Bajaj, "Road lane detection with improved canny edges using ant colony optimization," in *Proceedings of the 2010 3rd International Conference on Emerging Trends in Engineering and Technology*, pp. 76–80, IEEE, Goa, India, November 2010.
- [15] W. Van Gansbeke, B. De Brabandere, D. Neven, M. Proesmans, and L. Van Gool, "End-to-end lane detection through differentiable least-squares fitting," in *Proceedings of the IEEE/CVF International Conference on Computer Vision Workshops*, Seoul, Korea (South), October 2019.
- [16] Y. Ko, Y. Lee, S. Azam, F. Munir, M. Jeon, and W. Pedrycz, "Key points estimation and point instance segmentation approach for lane detection," *IEEE Transactions on Intelligent Transportation Systems*, pp. 1–10, 2021.
- [17] W. Song, Y. Yang, M. Fu, Y. Li, and M. Wang, "Lane detection and classification for forward collision warning system based on stereo vision," *IEEE Sensors Journal*, vol. 18, no. 12, pp. 5151–5163, 2018.
- [18] X. Pan, J. Shi, P. Luo, X. Wang, and X. Tang, "Spatial as deep: spatial cnn for traffic scene understanding," in *Proceedings of the Thirty-Second AAAI Conference on Artificial Intelligence*, Louisiana, USA, February 2018.

- [19] B. He, Ai Rui, Y. Yang, and X. Lang, "Accurate and robust lane detection based on dual-view convolutional neural network," in *Proceedings of the 2016 IEEE Intelligent Vehicles Symposium (IV)*, pp. 1041–1046, IEEE, Gothenburg, Sweden, June 2016.
- [20] H. Cho, Y.-W. Seo, B. V. K. Vijaya Kumar, and R. Raj Rajkumar, "A multi-sensor fusion system for moving object detection and tracking in urban driving environments," in *Proceedings of the 2014 IEEE International Conference on Robotics and Automation (ICRA)*, pp. 1836–1843, IEEE, Hong Kong, China, June 2014.
- [21] Ma Han, Y. Ma, J. Jiao et al., "Multiple lane detection algorithm based on optimised dense disparity map estimation," in *Proceedings of the 2018 IEEE International Conference on Imaging Systems and Techniques (IST)*, pp. 1–5, IEEE, Krakow, Poland, October 2018.
- [22] A. Eitel, J. Tobias Springenberg, L. Spinello, M. Riedmiller, and W. Burgard, "Multimodal deep learning for robust rgb-d object recognition," in *Proceedings of the 2015 IEEE/RSJ International Conference on Intelligent Robots and Systems (IROS)*, pp. 681–687, IEEE, Hamburg, Germany, October 2015.
- [23] H. Wang, F. Zhou, W. Zhou, and L. Chen, "Human pose recognition based on depth image multifeature fusion," *Complexity*, vol. 2018, 2018.
- [24] Joel Schlosser, C. K. Chow, and Z. Kira, "Fusing lidar and images for pedestrian detection using convolutional neural networks," in *Proceedings of the 2016 IEEE International Conference on Robotics and Automation (ICRA)*, pp. 2198–2205, IEEE, Stockholm, Sweden, May 2016.
- [25] A. Vaswani, N. Shazeer, N. Parmar et al., "Attention is all you need," in *Advances in Neural Information Processing Systems*, pp. 5998–6008, MIT Press, Cambridge, MA, 2017.
- [26] J. Fu, H. Zheng, and T. Mei, "Look closer to see better: recurrent attention convolutional neural network for fine-grained image recognition," in *Proceedings of the IEEE conference on computer vision and pattern recognition*, pp. 4438–4446, Honolulu, HI, USA, May 2017.
- [27] X. Cheng, H. Wang, J. Zhou, H. Chang, X. Zhao, and Y. Jia, "Dtfa-net: dynamic and texture features fusion attention network for face antispoofing," *Complexity*, vol. 2020, 2020.
- [28] F. Wang, M. Jiang, C. Qian et al., "Residual attention network for image classification," in *Proceedings of the IEEE conference on computer vision and pattern recognition*, pp. 3156–3164, Honolulu, HI, USA, July 2017.
- [29] L.-C. Chen, Yi Yang, J. Wang, W. Xu, and A. L. Yuille, "Attention to scale: scale-aware semantic image segmentation," in *Proceedings of the IEEE conference on computer vision and pattern recognition*, pp. 3640–3649, Las Vegas, NV, USA, June 2016.
- [30] O. Ronneberger, P. Fischer, and T. Brox, "U-net: convolutional networks for biomedical image segmentation," in *Proceedings of the International Conference on Medical image computing and computer-assisted intervention*, pp. 234–241, Springer, Munich, Germany, May 2015.
- [31] Li Xiang, W. Wang, X. Hu, and J. Yang, "Selective kernel networks," in *Proceedings of the IEEE/CVF Conference on Computer Vision and Pattern Recognition*, pp. 510–519, Long Beach, CA, USA, June 2019.
- [32] A. Geiger, P. Lenz, and R. Urtasun, "Are we ready for autonomous driving? the kitti vision benchmark suite," in *Proceedings of the 2012 IEEE conference on computer vision and pattern recognition*, pp. 3354–3361, IEEE, Providence, RI, USA, June 2012.
- [33] J. Geyer, Y. Kassahun, M. Mahmudi et al., "A2d2: audi autonomous driving dataset," 2020, <https://arxiv.org/abs/2004.06320>.
- [34] D. P. Kingma and Ba Jimmy, "Adam: a method for stochastic optimization," 2014, <https://arxiv.org/abs/1412.6980>.
- [35] Y. Hou, M. Zheng, C. Liu, and C. C. Loy, "Learning light-weight lane detection cnns by self attention distillation," in *Proceedings of the IEEE/CVF international conference on computer vision*, pp. 1013–1021, Seoul, Korea (South), November 2019.
- [36] K. Simonyan and A. Zisserman, "Very deep convolutional networks for large-scale image recognition," 2014, <https://arxiv.org/abs/1409.1556>.

Research Article

Cell on Wheels-Unmanned Aerial Vehicle System for Providing Wireless Coverage in Emergency Situations

Hazim Shakhatreh ¹, **Khaled Hayajneh** ¹, **Khaled Bani-Hani** ¹, **Ahmad Sawalmeh** ^{2,3}
and **Muhammad Anan** ⁴

¹Department of Telecommunications Engineering, Hijjawi Faculty for Engineering Technology, Yarmouk University, Irbid, Jordan

²Computer Science Department, Northern Border University, Arar, Saudi Arabia

³Remote Sensing Unit, Northern Border University, Arar 91431, Saudi Arabia

⁴Software Engineering Department, Alfaisal University, Riyadh 11533, Saudi Arabia

Correspondence should be addressed to Hazim Shakhatreh; hazim.s@yu.edu.jo

Received 5 October 2021; Revised 1 November 2021; Accepted 6 November 2021; Published 22 November 2021

Academic Editor: Chao Liu

Copyright © 2021 Hazim Shakhatreh et al. This is an open access article distributed under the Creative Commons Attribution License, which permits unrestricted use, distribution, and reproduction in any medium, provided the original work is properly cited.

Due to natural disasters, unmanned aerial vehicles (UAVs) can be deployed as aerial wireless base stations when conventional cellular networks are out of service. They can also supplement the mobile ground station to provide wireless devices with improved coverage and faster data rates. Cells on wheels (CoWs) can also be utilized to provide enhanced wireless coverage for short-term demands. In this paper, a single CoW cooperates with a single UAV in order to provide maximum wireless coverage to ground users. The optimization problem is formulated to find the following: (1) the optimal 2D placement of the CoW, (2) the optimal 3D placement of the UAV, (3) the optimal bandwidth allocation, (4) the percentage of the available bandwidth that must be provided to the CoW and UAV, and (5) the priority of wireless coverage; which maximizes the number of covered users. We utilize the exhaustive search (ES) and particle swarm optimization (PSO) algorithms to solve the optimization problem. The effectiveness of the proposed algorithms is validated using simulation results.

1. Introduction

UAV networks have been developed as a possible technology of quickly providing wireless coverage to a geographic area, where a flying UAV can be quickly deployed to operate as a cell site [1, 2]. The advantage of deploying UAVs as flying base stations over traditional terrestrial base stations is their ability to change altitude, avoid obstacles, and increase the possibility of establishing line of sight (LoS) communication connections with wireless devices [3, 4]. UAVs are especially useful in situations when the conventional cellular network is either unavailable or requires assistance to offer the necessary capacity and coverage [5, 6]. Verizon, for example, has developed an airborne long-term evolution (LTE) service to provide 4G-LTE connectivity during disaster recovery exercises and emergency management [7]. The authors in [8] study the emergency UAV deployment to

minimize the UAV deployment delay until covering the entire geographical area by considering the UAVs' different flying speeds and altitudes during the deployment. In [9], the authors establish a unified framework for a UAV-assisted emergency network. The scheduling and trajectory of drones are jointly optimized to provide wireless connectivity to wireless devices with surviving ground mobile stations. The authors in [10] propose a deployment tool for a drone-aided emergency network to provide wireless device coverage in a large-scale disaster scenario. LTE femtocell base stations are mounted on drones and deployed to their assigned placement. Such a network's deployment tool takes into account the characteristics of the UAVs (such as battery life and flight time), user requirements, and a 3D representation of the environment. In [11], the authors propose energy-efficient planning of drones for emergencies. Their problem formulation considers both outdoor and indoor users, where

the objective is to find the placements of multiple drones that provide wireless coverage based on the locations and distribution of users. In addition, supplementing the surviving communication infrastructure and keeping first responders connected to their command centers, a portable cell or CoW can be utilized [12]. One can establish a temporary network to enable important public safety communication throughout the disaster area by efficiently deploying these mobile cells. These portable cells, which are simple to deploy, configure, and adapt, are an ideal solution for any disaster response effort. The authors in [12] present a decentralized relocation algorithm that enables CoWs to change their locations in response to the potential mobility of ground users. In [13], the authors describe and propose a portable mobile wireless network infrastructure that is ideally suited for emergency response and disaster recovery operations. The authors in [14] study the challenges of emergency communication networks for disaster response. These challenges include popularity, usability, capacity, operability, reliability, and adaptability. In [15], the authors demonstrate that drone assistance in CoW-UAV wireless networks can provide significant advantages to mmWave backhaul under certain system parameters. The authors in [16] proposed an efficient 3D placement of a single UAV for assisting terrestrial wireless networks. In their proposed model, a single UAV is utilized to assist the GBS and provide wireless coverage for arbitrarily distributed ground terminals, considering the impact of the obstacle blockage for the A2G path loss model. The authors in [17] propose a framework that combines UAV support with wireless-powered communication techniques to further improve energy efficiency in distributed nonorthogonal multiple access public safety networks. In [18], the authors propose a distributed user-centric risk-aware resource management framework in a UAV-assisted public safety network supported by both a static UAV and a mobile UAV. The authors in [19] introduce a resource orchestration framework in a UAV-assisted wireless-powered communication network within a public safety system, based on the principles of contract theory and reinforcement learning.

In this paper, a single CoW and a single UAV are utilized to maximize the wireless communication coverage in emergency situations. The objective of the proposed optimization problem is to find the optimal 2D placement of the CoW, the optimal 3D placement of the UAV, optimal bandwidth allocation to the UAV and CoW, and the priority of wireless coverage that maximizes the number of covered wireless devices. To the best of our knowledge, this is the first work that proposes using a CoW-UAV system to maximize the wireless coverage in emergency situations. The main contributions of this paper are summarized as follows:

- (1) Realistic path loss models for a CoW-UAV system are presented, and the trade-off introduced by these models is described
- (2) The optimization problem for a CoW-UAV system is formulated with the objective of maximizing the wireless coverage

- (3) Exhaustive search (ES) and particle swarm optimization (PSO) algorithms are utilized to solve the optimization problem

The remainder of this paper is organized as follows. In Section 2, the system model is described. Then, in Section 3, the optimization problem is formulated, where the goal is to maximize the number of covered wireless devices. Next, the proposed algorithms are presented to solve the optimization problem in Section 4. The numerical results are presented in Section 5. Finally, Section 6 concludes the paper.

2. System Model

Consider an urban area denoted as $\mathbb{E} \in (AxA)$ served by a CoW assisted by a UAV that acts as an aerial base station, as shown in Figure 1. Both the CoW and UAV have fixed transmission power. Let $(x_c, y_c, 6m)$ denote the 2D placement of the CoW, and let (x_u, y_u, z_u) denote the 3D placement of the UAV, as shown in Figure 1. The movement of the UAV is restricted to specific heights according to the law restrictions, while the roads on the given area restrict the movement of the CoW. It is assumed that all users are located inside the urban environment, and use $(x_i, y_i, 0)$ to denote the placement of user $i \in I$. The CoW or the UAV serves the user's wireless device i if the quality of service (QoS), measured by the signal-to-noise ratio (SNR), is above a predefined threshold. Such a threshold depends on the type of service (e.g., voice, data, and video) required by the user.

The CoW and the UAV are equipped with transceiver antennas, and a downlink scenario is envisioned, in which the frequency division multiple access (FDMA) technology is used to transfer data and provide coverage for wireless devices. As a result, each wireless device has its own dedicated communication channel, and there is no interference or channel overlap between CoW and UAV channels. The bandwidths of the CoW and the UAV are B_1 and B_2 , respectively. The CoW and the UAV are supported by backhaul links that connect them to Internet's core. The highest benefit from CoW and UAV deployment may be obtained by finding the optimal placements for them. Assuming that all wireless devices have the same QoS, the highest benefit can be realized by connecting the CoW and the UAV to as many wireless devices as possible. The CoW and the UAV placements affect both the number of served wireless devices and the quality of the channel between each wireless device and the base station (CoW or UAV). The critical question in this context that we need to answer is which base station starts the wireless coverage first, CoW or UAV? In the downlink scenario, we consider two types of channels: CoW to wireless device channel and UAV to wireless device channel.

2.1. CoW to Wireless Device Channel. In this paper, we utilize the independent Rayleigh fading model to represent the time-varying channel between the CoW and a wireless device i in an urban environment [20, 21]. Time variation occurs when the status of obstacles between the transmitter and the receiver is uncertain due to the movement of the obstacles. Changes in the amplitudes, delays, and quantity of

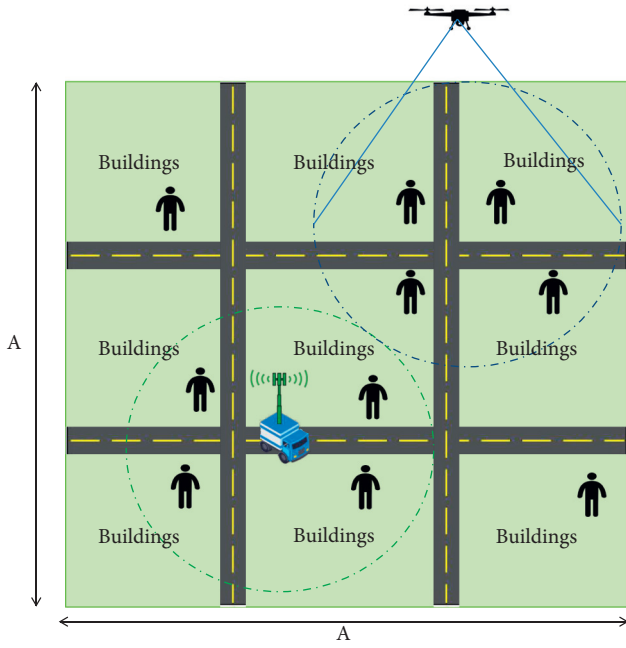


FIGURE 1: The proposed system model. The area ($A \times A$) is covered by a CoW assisted by a UAV.

multipath components related to each signal can thus be detected. Over a much longer time scale, these changes result in a constructive and destructive addition of multipath components. The received power of wireless device i served by the CoW is formulated as follows:

$$P_{r_{i,1}} [\text{dBm}] = P_{\text{CoW}} (\text{dBm}) + 20 \log(g_i) - 10n \log(d_{(i,1)}), \quad (1)$$

where P_{CoW} is the transmitted power by CoW in dBm, g_i is the Rayleigh fading power for the wireless device i in dB, and $d_{(i,1)}$ is the distance between the CoW and the wireless device i which is given by

$$d_{(i,1)} = \sqrt{(x_i - x_c)^2 + (y_i - y_c)^2}. \quad (2)$$

2.2. UAV to Wireless Device Channel. For the downlink communication between the UAV and wireless devices, we use the air-to-ground channel model, which is one of the most commonly used radio propagation models [22]. In general, it is dependent on the line of sight (LoS) and non-line of sight (NLoS) links, as well as their respective chance of occurrence. This channel model takes into account two types of propagation: LoS propagation and NLoS propagation. Based on the environment and the placement of the UAV, the following formula is used to calculate the probability of getting a LoS signal:

$$P_{\text{LoS}} = \frac{1}{1 + \alpha \exp[-\beta(\theta - \alpha)]}, \quad (3)$$

where α and β are constants, and their values are affected by the environment, $\theta = \arctan(h_u/r_{(u,i)})$ is the elevation angle

from the UAV to wireless device i , h_u is the UAV altitude, and $r_{(u,i)}$ is the horizontal distance between the projection of the UAV placement on the ground and the placement of wireless device i . The trade-off in this model was described by the authors of [23]. The path loss between the UAV and the wireless device decreases as the altitude decreases, while the probability of line of sight links also decreases. On the other hand, line of sight links occur with a high probability at high altitudes, while path loss increases. Taking into account the LoS and NLoS link, the total average path loss in this model can be found as follows:

$$PL(h_u, r_{u,i}) (\text{dB}) = 10n \log\left(\frac{4\pi f_c d_{i,2}}{c}\right) + P_{\text{LoS}} \xi_{\text{LoS}} + P_{\text{NLoS}} \xi_{\text{NLoS}}, \quad (4)$$

where the first term represents the free-space path loss, f_c is the carrier frequency, c is the speed of light, n is the path loss exponent, $d_{(i,2)}$ is the distance between the UAV and wireless device i , and ξ_{LoS} and ξ_{NLoS} are the average additional losses for LoS and NLoS links in dB, respectively. These losses are environment-dependent.

The received power of wireless device i served by the UAV is given by

$$r_{(i,2)} (\text{dBm}) = P_u (\text{dBm}) - PL(h_u, r_{u,i}) (\text{dB}), \quad (5)$$

where P_u is the transmitted power by UAV in dBm and $PL(h_u, r_{(u,i)})$ is the total average path loss in dB.

3. Problem Formulations

The received SNR ($\text{SNR}_{(i,q)}$) of wireless device $i \in I$ from the CoW ($q = 1$) or the UAV ($q = 2$) is given by

$$\text{SNR}_{(i,q)} = \frac{Pr_{(i,q)}}{N_i}, \quad i \in I, q \in \{1, 2\}, \quad (6)$$

where $Pr_{(i,q)}$ is the received power at a wireless device $i \in I$ from the q -th base station and N_i is the channel noise power, which is given by $N_i = N_o b_{(i,q)}$, in which N_o is the power spectral density of noise channel and $b_{(i,q)}$ is the bandwidth allocated for a wireless device $i \in I$ from base station $q \in \{1, 2\}$.

The main goal of this paper is to find the optimal placements for the CoW and the UAV that maximize the number of served wireless devices, as illustrated in Figure 1. To formulate the optimization problem, we define the binary variable $V_{(i,q)}$, $i \in I$ and $q \in 1, 2$ which ensures whether a wireless device $i \in I$ is served by base station $q \in \{1, 2\}$ or not. The binary variable $V_{(i,q)}$ takes value 1 if $\text{SNR}_{(i,q)} \geq \text{SNR}_{\text{th}}$, and it takes value 0 otherwise, where SNR_{th} is the threshold SNR.

Then, if wireless device $i \in I$ is served, $\text{SNR}_{(i,q)} \geq \text{SNR}_{\text{th}}$ must be satisfied. This constraint can be further formulated as follows:

$$\text{SNR}_{(i,q)} \geq \text{SNR}_{\text{th}} - A(1 - V_{(i,q)}), \quad (7)$$

where A is significantly constant, greater than the maximum value of SNR_{th} . The bandwidth allocated to each base station

(either CoW or UAV) cannot exceed its available bandwidth. Therefore,

$$\sum_{i=1}^{|I|} b_{(i,q)} V_{(i,q)} \leq B_q, \quad \forall q \in \{1, 2\}, \quad (8)$$

where $b_{(i,q)}$ is the bandwidth allocated to a wireless device $i \in I$ from base station $q \in 1, 2$. Here, each base station's bandwidth is not fixed; therefore, it must be optimized. Many factors influence the optimal bandwidth, including available bandwidth, QoS requirement, wireless device demands, environment, and scenario.

The bandwidth allocated for each BS should be obtained in this research work in order to serve as many wireless devices from the total number of devices in the urban area as possible. Hence, we define the variable γ , $\gamma \in [0, 1]$, which indicates how much bandwidth should be allocated to CoW. The bandwidth allotted to CoW is calculated as follows: $B_1 = \gamma B$, while the bandwidth allotted to UAV is specified as follows: $B_2 = (1 - \gamma)B$. The optimization problem aims to find the following: (1) the optimal 2D placement of the CoW, (2) the optimal 3D placement of the UAV, (3) optimal bandwidth allocation, and (4) the priority of wireless coverage, which maximize the number of covered users. The optimization problem is given by

$$\begin{aligned} & \text{maximize} && \sum_{i=1}^{|I|} \sum_{q=1}^2 V_{(i,q)}, \\ & ((x_c, y_c), (x_u, y_u, z_u), \gamma, V_{(i,q)}) \end{aligned} \quad (9a)$$

$$\text{Subject to } \text{SNR}_{i,q} \geq \text{SNR}_{\text{th}} - A(1 - V_{(i,q)}), \quad \forall i \in I, q \in \{1, 2\}, \quad (9b)$$

$$\sum_{i=1}^{|I|} b_{(i,q)} V_{(i,q)} \leq B_q, \quad \forall q \in \{1, 2\}, \quad (9c)$$

$$\sum_{q=1}^2 V_{(i,q)} \leq 1, \quad \forall i \in I, \quad (9d)$$

$$B_1 = \gamma B, \quad (9e)$$

$$B_2 = (1 - \gamma)B, \quad (9f)$$

$$0 \leq \gamma \leq 1, \quad (9g)$$

$$(x_c, y_c) \in R_c^2, \quad (9h)$$

$$(x_c, y_c, z_u) \in R_u^3, \quad (9i)$$

The first constraint set ensures that the QoS of each wireless device should be greater or equal to SNR_{th} to be served from either the CoW or the UAV. The second constraint set guarantees that the sum of wireless devices bandwidths does not exceed the base station bandwidth. The third constraint set ensures that a wireless device should be connected to one base station at most or none of them. The constraint sets 9e–9g represent the bandwidth that

should be allocated to each base station. The constraint sets 9h–9i represent the allowable values for 2D and 3D placements of the CoW and the UAV, respectively.

4. Methodology

This section presents methods of finding the solution of CoW and UAV positions and the percentage of the allocated bandwidth for each one. This work employs exhaustive search and PSO algorithms to find the maximum number of served users in the proposed area.

4.1. Exhaustive Search (ES). The exhaustive search is considered as optimal solution. It can find the best 2D position of CoW, 3D position of UAV, and the available bandwidth at each one of them. Considering the priority, the BS (i.e., CoW or UAV) that has the priority is assumed to be BS_1 , and the other one is BS_2 . Firstly, the BS_1 will be deployed in allowable positions and serve a set of users (U) from I . Secondly, the BS_2 will be deployed to serve as much users as possible from set $(|I| - |U|)$. Determining the placements of BS_1 , BS_2 will be synchronized at each search point. The ES algorithm will require a lot of calculations, and possibly even impossible in practice. The PSO algorithm is employed to overcome the high computational overhead issue in ES.

4.2. PSO. The PSO algorithm is being used in the study to provide a solution [24, 25]. The PSO is considered a sub-optimal solution, where the efficient solution of the 2D position of CoW, 3D position of UAV, and the available bandwidth at each one of them can be found. The PSO algorithm generates a set of (nP) random solutions as its starting point, where each solution delivers the BS (i.e., CoW or UAV) position. It seeks to promote candidate solutions iteratively based on each candidate's best experience ($P_{\text{best}}(i)$) and candidate's best global experience (G_{best}). The particle's locations and velocities are evaluated depending on the best location ($P_{\text{best}}(i)$) and the best global location (G_{best}), where both are enhanced at each iteration. The velocity term is modified using the approach below:

$$\begin{aligned} P_{\text{velocity}}(i) &= wP_{\text{velocity}}(i) + a_1 * \text{rand}(V\text{size}) \\ & * (P_{\text{best}}(i) - P(i)) + a_2 * \text{rand}(V\text{size}). \end{aligned} \quad (10)$$

$$* (G_{\text{best}}(i) - P(i)),$$

The factor w is the inertia weight, which is used to adjust the convergence speed, a_1 and a_2 are factors that represent the particle's stride size toward its local and global best solutions, and $(\text{rand}(V\text{size}))$ is random positive numbers. Each particle's location is enhanced as follows:

$$P(i) = P(i) + P_{\text{velocity}}(i), \quad (11)$$

In the same manner, in ES, the PSO finds the solution in two loops. Initially, the BS that has the priority is illustrated as BS_1 , and it is deployed to serve a set of users (U) from I . The other BS is illustrated as BS_2 , and it is deployed next to

```

(i) Input: the lower and upper bounds of decision variable (Varmin, Varmax), construction coefficients ( $\kappa, \phi_1, \phi_2$ ), maximum
    number of iterations (MIt), population size ( $nP$ ), total number of users ( $I$ ), and served users by BS1 ( $U$ )
(ii) Initialization:  $\phi = \phi_1 + \phi_2, X = 2\kappa / (|2 - \phi - (\phi^2 - 4\phi)|^{0.5}), w = X, a_1 = X\phi_1, a_2 = X\phi_2, G_{\text{Best.Cost}} = -\text{inf}$ ;
(iii) BS1 Loop:
(iv) for  $k \leftarrow 1$  to  $|I|$ 
(v) for  $j \leftarrow 1$  to  $nP$ 
(vi)  $P(j) = \text{unifrnd}(\text{Varmin}, \text{Varmax}, \text{Varsize})$ 
(vii)  $P_{\text{Velocity}}(j) = \text{zeros}(\text{Varsize})$ 
(viii)  $P_{\text{Cost}}(j) = \text{Objectivefunction}(P(j))$ 
(ix)  $P_{\text{Best}}(j) = P(j)$ 
(x)  $P_{\text{Best.Cost}}(j) = P_{\text{Cost}}(j)$ 
(xi) if  $P_{\text{Best.Cost}}(j) > G_{\text{Best.Cost}}$ 
(xii)  $G_{\text{Best}} = P_{\text{Best}}(j)$ 
(xiii) end if
(xiv) end
(xv) PSO Loop:
(xvi) for  $It \leftarrow 1$  to MIt
(xvii) for  $j \leftarrow 1$  to  $nP$ 
     $P_{\text{Velocity}}(j) = w * P_{\text{Velocity}}(j) + a_1 * \text{rand}(\text{Varsize}) * (P_{\text{Best}}(j) - P(j)) + a_2 * \text{rand}(\text{Varsize}) * (G_{\text{Best}} - P(j))$ 
     $P(j) = P(j) + P_{\text{Velocity}}(j)$ 
     $P_{\text{Cost}}(j) = \text{Objectivefunction}(P(j))$ 
    if  $P_{\text{Cost}}(j) > P_{\text{Best.Cost}}(j)$ 
     $P_{\text{Best}}(j) = P(j)$ 
     $P_{\text{Best.Cost}}(j) = P_{\text{Cost}}(j)$ 
    if  $P_{\text{Best.Cost}}(j) > G_{\text{Best.Cost}}$ 
     $G_{\text{Best}} = P_{\text{Best}}(j)$ 
    end if
    end if
    end
    end
    end
    BS2 Loop:
    for  $kk \leftarrow 1$  to  $|I| - |U|$ 
    for  $j \leftarrow 1$  to  $nP$ 
     $P(j) = \text{unifrnd}(\text{Varmin}, \text{Varmax}, \text{Varsize})$ 
     $P_{\text{Velocity}}(j) = \text{zeros}(\text{Varsize})$ 
     $P_{\text{Cost}}(j) = \text{Objectivefunction}(P(j))$ 
     $P_{\text{Best}}(j) = P(j)$ 
     $P_{\text{Best.Cost}}(j) = P_{\text{Cost}}(j)$ 
    if  $P_{\text{Best.Cost}}(j) > G_{\text{Best.Cost}}$ 
     $G_{\text{Best}} = P_{\text{Best}}(j)$ 
    end if
    end
    PSO Loop:
    for  $It \leftarrow 1$  to MIt
    for  $j \leftarrow 1$  to  $nP$ 
     $P_{\text{Velocity}}(j) = w * P_{\text{Velocity}}(j) + a_1 * \text{rand}(\text{Varsize}) * (P_{\text{Best}}(j) - P(j)) + a_2 * \text{rand}(\text{Varsize}) * (G_{\text{Best}} - P(j))$ 
     $P(j) = P(j) + P_{\text{Velocity}}(j)$ 
     $P_{\text{Cost}}(j) = \text{Objectivefunction}(P(j))$ 
    if  $P_{\text{Cost}}(j) > P_{\text{Best.Cost}}(j)$ 
     $P_{\text{Best}}(j) = P(j)$ 
     $P_{\text{Best.Cost}}(j) = P_{\text{Cost}}(j)$ 
    if  $P_{\text{Best.Cost}}(j) > G_{\text{Best.Cost}}$ 
     $G_{\text{Best}} = P_{\text{Best}}(j)$ 
    end if
    end if
    end
    end
    end
    end

```

ALGORITHM 1: PSO algorithm that finds the efficient UAVBS placement.

serve as much users as possible from the set ($|I| - |U|$). The pseudocode for PSO algorithm is described in Algorithm 1:

4.3. Computational Complexity. This section shows the complexity of using either PSO or ES algorithms. It is well known that the ES algorithm finds the optimal solution to the problem. However, its computational complexity is high. Practically, the ES complexity is $O(X \times Y \times Z \times |U_u|) + O(X \times Y \times |U_c|)$, where (X, Y, Z) is the 3D possible locations of the UAV in the proposed area, $|U_u|$ is the number of served users by UAV, (X, Y) is the 2D possible locations of the CoW in the proposed area, and $|U_c| = |I| - |U_u|$ is the number of unserved users by UAV.

In order to reduce the computational complexity, a suboptimal solution is obtained using heuristic algorithms such as the PSO algorithm. Thus, the PSO complexity is $O(nP \times \text{MI} \times |U_u|) + O(nP \times \text{MI} \times |U_c|)$, where nP is a population of random solutions, MI is the number of iterations, $|U_u|$ is the number of users served by UAV, and $|U_c| = |I| - |U_u|$ is the number of unserved users by UAV.

5. Performance Evaluations

Simulation results describing the performance of PSO and exhaustive search algorithms in terms of the served number of users are presented in this section. Simulation results are obtained using MATLAB R2020a. We assume an urban area of (1000m \times 1000m), which consists of roads as shown in Figure 1. Furthermore, a total of 200 users are supposed to be uniformly distributed over the given area. We use the evaluation parameters as shown in Table 1. In addition, the parameters of the PSO algorithm are listed in Table 2.

Figure 2 shows the number of served users versus the percentage of allocated bandwidth for CoW (γ) using the aforementioned algorithms. The figure is obtained when the priority is given to the CoW at the beginning. As shown in the figure, there is a clear trend of decreasing the number of served users of the UAV as its percentage of bandwidth decreases (equivalently, γ increases). Similarly, there is an apparent increase in the number of served users of the CoW as its percentage of bandwidth, γ , increases. As a result, there is an optimal percentage of bandwidth, γ , where the number of served users is maximized. In this case, the optimal percentage of bandwidth given to the CoW is $\gamma=0.7$, whereas the remaining percentage of bandwidth $(1-\gamma)=0.3$ should be provided to the UAV. In addition, the figure shows that the served number of users of CoW using the PSO algorithm almost coincides with that result once using the exhaustive search algorithm. The reason behind this is the flexibility of CoW to choose its location once it is given priority before the UAV. However, there is a small gap in the served number of users of UAV (as well as the total number of users).

Figure 3 depicts the number of served users in terms of the percentage of bandwidth provided to the CoW, γ , when the UAV has the priority at the beginning. The figure shows a clear trend of increasing (decreasing) the number of served users of the CoW (UAV) as the percentage of the bandwidth

TABLE 1: Values of the evaluation parameters.

Parameter	f_c	B	h_{CoW}	$(h_{\text{min}}, h_{\text{max}})$	n
Value	2 GHz	40 MHz	6 m	(100 m, 300 m)	(2, 4)
Parameter	P_{CoW}	P_u	$P_{i,q}$	SNR_{th}	
Value	40 dBm	20 dBm	200 kHz	20 dB	

TABLE 2: Values of the PSO algorithm's parameters.

Parameter	nP	MI	(Varmin, Varmax)	Varsize	(w, a_1, a_2)
Value	20	100	(0, 1000)	3	(1, 2.05, 2.05)

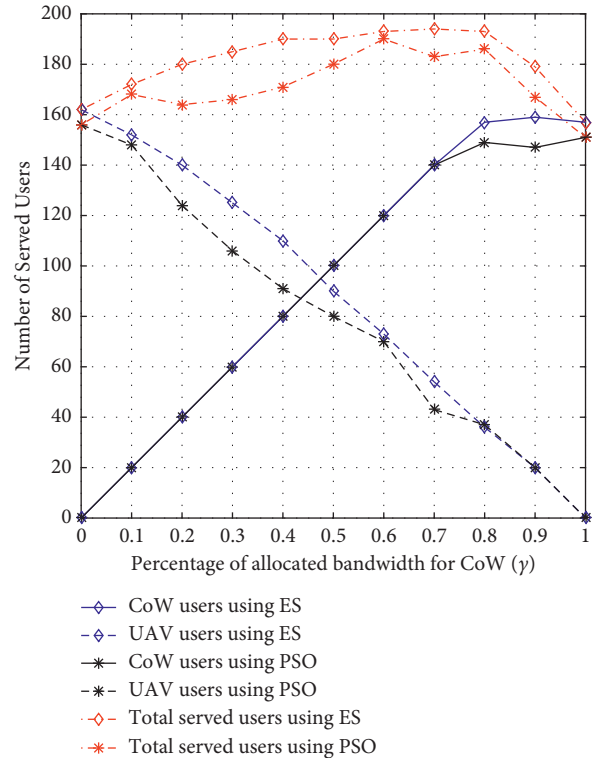


FIGURE 2: Number of served users using PSO and ES algorithms when the priority is given to the CoW at the beginning.

given to the CoW, γ , increases. As shown in the figure, the served users of the UAV using the PSO algorithm, or exhaustive search algorithm, are the same. That is because the UAV has the priority of choosing its location before the CoW does. In addition, the figure shows that the results of the PSO algorithm can achieve the results of the exhaustive search algorithm with no more than a 5% deviation. However, the complexity of the PSO algorithm is much lower than the complexity of the exhaustive search algorithm.

To show which BS should be given priority at the beginning, Figure 4 shows the probability of priority provided to the UAV and CoW depending on the percentage of bandwidth provided to the CoW (γ). The figure shows that the UAV must prioritize choosing its location before the CoW when its percentage of bandwidth $(1-\gamma)$ is higher than 0.35 (or when γ is less than 0.65). In contrast, the CoW must be prioritized at the beginning when its percentage of bandwidth

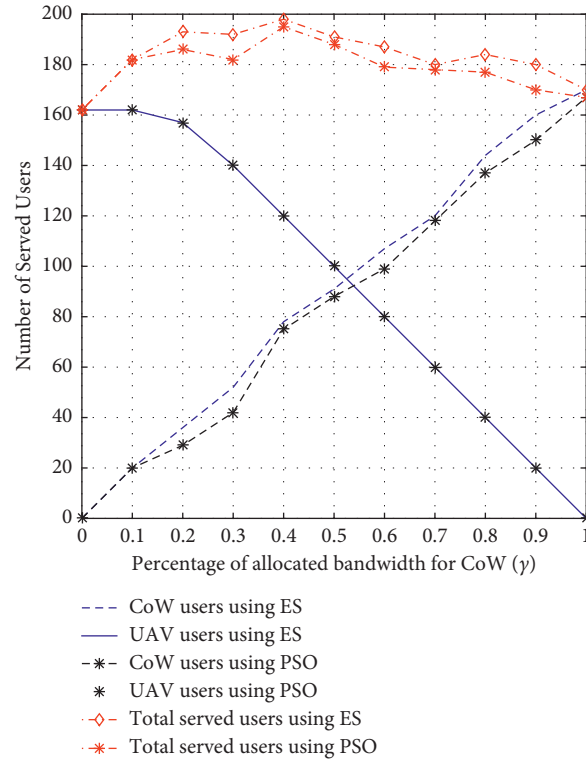


FIGURE 3: Number of served users using PSO and ES algorithms when the priority is given to the UAV at the beginning.

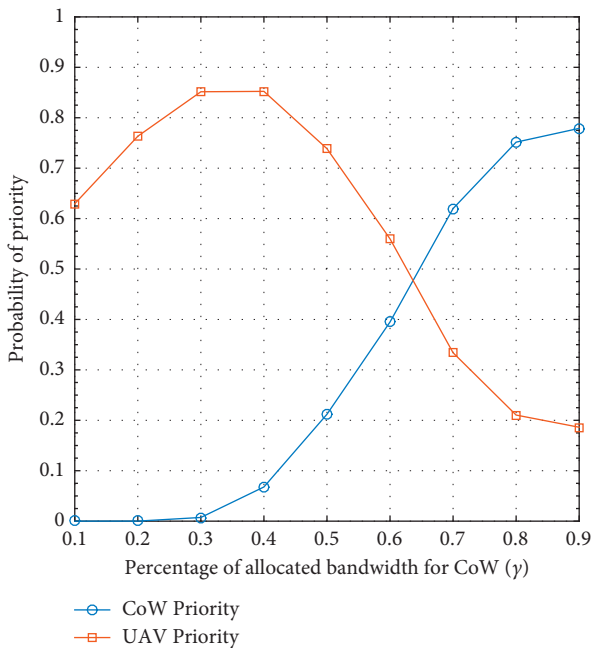


FIGURE 4: Probability of priority versus the percentage of bandwidth given to the CoW (γ).

(γ) is more than 0.65. Among the plausible explanations for these results is the fact that the UAV has more flexibility of movement than CoW. The CoW can move only on the roads, as shown in Figure 1. However, the UAV can freely move between all of the 3D possible locations in the given area. It is essential to realize that the priority does not matter in the

extreme cases, where CoW is only working (i.e., $\gamma = 1$) or only UAV is only working (i.e., $\gamma = 0$).

Now, to show the optimization results of our proposed algorithm, Figure 5 shows the optimized locations of the UAV (blue square) at (1000, 600, 290) and CoW (green circle) at (225, 610) using the ES algorithm. Note that the height of the CoW is fixed at 6 m. In this setting, priority is given to the UAV at the beginning with the percentage of bandwidth $(1-\gamma) = 0.6$. Thus, the UAV serves 120 users (blue dots), and then CoW serves 78 users (green dots). As a result, 99% of the users will be served.

Moreover, Figure 6 shows the optimized locations of the CoW (green circle) and UAV (blue square) using the ES algorithm once the priority is given to the CoW at the beginning. In this case, the best CoW location is (610, 343) with the percentage of the bandwidth of $\gamma = 0.7$ and then the best UAV location of the UAV is (400, 750, 290) with the percentage of bandwidth $(1-\gamma) = 0.3$. Accordingly, the CoW serves 140 users, and then the UAV serves 54 users. Therefore, 97% of users are served under this setting.

To show the computational complexity of both ES and PSO algorithms, Table 3 shows the running time of each algorithm under different values of the bandwidth percentage provided to the CoW (γ). As it can be seen from the table, the PSO algorithm improves the required time significantly. In addition, note that these results of the ES algorithm are obtained at 50m step size. If the step size is decreased to locate the UAV and CoW precisely, the running time will be extremely increased. For example, if the step size is 25m and $\gamma = 0.6$, the running time will be 963.5 seconds.

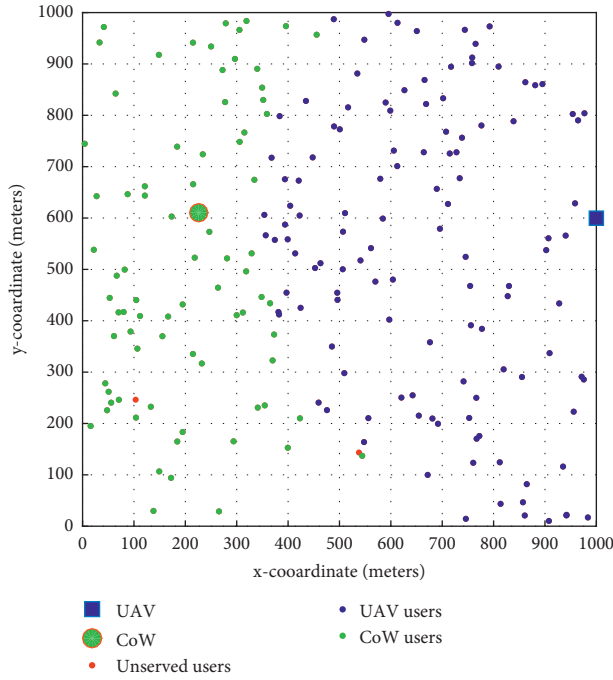


FIGURE 5: Deployment of the CoW and UAV using ES algorithm when the priority is given to the UAV at the beginning.

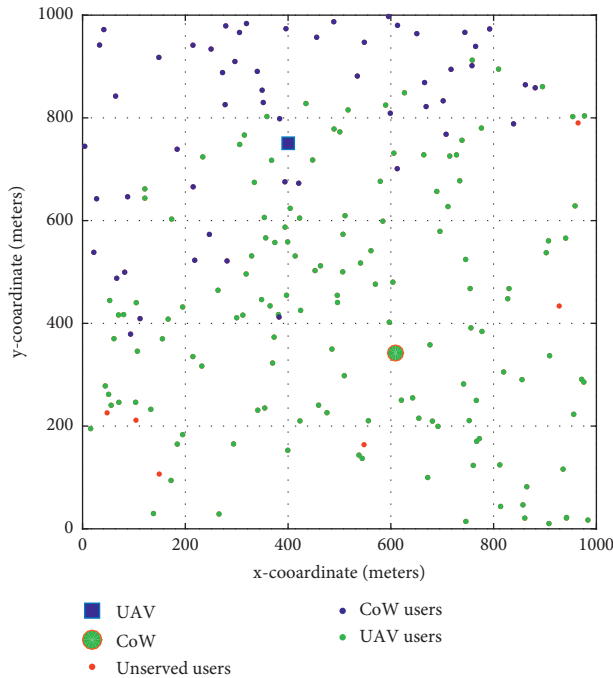


FIGURE 6: Deployment of the CoW and UAV using ES algorithm when the priority is given to the CoW at the beginning.

Finally, to show the robustness of our proposed algorithm, we study its performance over three different users' distributions. The first distribution (D_1) is, what we have used, overall evaluations. The second distribution (D_2) is a random distribution. The third distribution (D_3) is a uniform distribution, where the users are distributed uniformly

TABLE 3: Running time (in seconds) of the PSO and ES algorithms.

γ	0	0.4	0.6	1
PSO	20.37	20.56	20.78	21.01
ES	128.16	128.91	131.16	153.78

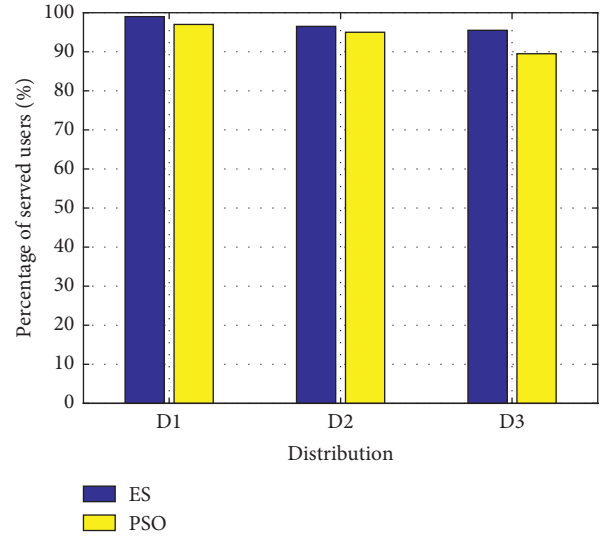


FIGURE 7: Robustness of the proposed algorithm.

over the given area. Figure 7 shows the performance over all the three aforementioned distributions. It can be seen that a very low change in the served users percentage would have occurred. In addition, in the impractical scenario where the distribution is uniform (i.e., D_3), the dropping in the served users percentage would be at minimum, around 5%.

6. Conclusion

This paper proposes a cooperative scheme between a CoW and a UAV intending to maximize the wireless coverage in emergencies. First, we found which one of the CoW and UAV must be located at the beginning. Then, the best 2D location for the CoW and the 3D location for the UAV are optimized. In addition, the percentage of the available bandwidth that must be provided for each base station (CoW and UAV) is calculated. Finally, we found that the priority depends on the percentage of the bandwidth given to each base station. For CoW-UAV system, the simulation results show that the UAV must prioritize choosing its location before the CoW when its percentage of bandwidth (γ) is less than 0.65. In contrast, the CoW must be prioritized at the beginning when its percentage of bandwidth (γ) is more than 0.65. In addition, the simulation results show that the PSO algorithm can achieve the results of the exhaustive search algorithm with no more than a 5% deviation. However, the complexity of the PSO algorithm is much lower than the complexity of the exhaustive search algorithm.

Data Availability

Data are available from the corresponding author upon request.

Conflicts of Interest

The authors declare that they have no conflicts of interest.

Acknowledgments

This research work was supported by the Office of Research and Innovation at Alfaisal University, Saudi Arabia.

References

- [1] X. Zhang and L. Duan, "Fast deployment of uav networks for optimal wireless coverage," *IEEE Transactions on Mobile Computing*, vol. 18, no. 3, pp. 588–601, 2018.
- [2] H. Shakhathreh, A. Alenezi, A. Sawalmeh, M. Almutiry, and W. Malkawi, "Efficient placement of an aerial relay drone for throughput maximization," *Wireless Communications and Mobile Computing*, vol. 2021, 2021.
- [3] M. Mozaffari, W. Saad, M. Bennis, Y.-H. Nam, and M. Debbah, "A tutorial on uavs for wireless networks: Applications, challenges, and open problems," *IEEE Communications Surveys & Tutorials*, vol. 21, no. 3, pp. 2334–2360, 2019.
- [4] A. Sawalmeh, N. Othman, and H. Shakhathreh, "Efficient deployment of multi-uavs in massively crowded events," *Sensors*, vol. 18, no. 11, Article ID 3640, 2018.
- [5] N. Namvar, A. Homaifar, A. Karimoddini, and B. Maham, "Heterogeneous uav cells: An effective resource allocation scheme for maximum coverage performance," *IEEE Access*, vol. 7, pp. 164708–164719, 2019.
- [6] A. H. Sawalmeh, N. S. Othman, H. Shakhathreh, and A. Khreishah, "Wireless coverage for mobile users in dynamic environments using uav," *IEEE Access*, vol. 7, pp. 126376–126390, 2019.
- [7] W. D. Ivancic, R. J. Kerczewski, R. W. Murawski, K. Matheou, and A. N. Downey, "Flying drones beyond visual line of sight using 4g lte: Issues and concerns," in *Proceedings of the 2019 Integrated Communications, Navigation and Surveillance Conference (ICNS)*, pp. 1–13, Herndon, VA, USA, April 2019.
- [8] X. Zhang and L. Duan, "Optimization of emergency uav deployment for providing wireless coverage," in *Proceedings of the GLOBECOM 2017-2017 IEEE Global Communications Conference*, pp. 1–6, Singapore, December 2017.
- [9] N. Zhao, W. Lu, M. Sheng et al., "Uav-assisted emergency networks in disasters," *IEEE Wireless Communications*, vol. 26, no. 1, pp. 45–51, 2019.
- [10] M. Deruyck, J. Wyckmans, W. Joseph, and L. Martens, "Designing uav-aided emergency networks for large-scale disaster scenarios," *EURASIP Journal on Wireless Communications and Networking*, vol. 2018, no. 1, pp. 1–12, 2018.
- [11] G. Liu, H. Shakhathreh, A. Khreishah, X. Guo, and N. Ansari, "Efficient deployment of uavs for maximum wireless coverage using genetic algorithm," in *Proceedings of the 2018 IEEE 39th Sarnoff Symposium*, pp. 1–6, Newark, NJ, USA, September 2018.
- [12] L. Rabieekenari, K. Sayrafian, and J. S. Baras, "Autonomous relocation strategies for cells on wheels in environments with prohibited areas," in *Proceedings of the 2017 IEEE International Conference on Communications (ICC)*, pp. 1–6, Paris, France, May 2017.
- [13] D. Abusch-Magder, P. Bosch, T. E. Klein, P. A. Polakos, L. G. Samuel, and H. Viswanathan, "911-now: A network on wheels for emergency response and disaster recovery operations," *Bell Labs Technical Journal*, vol. 11, no. 4, pp. 113–133, 2007.
- [14] J.-S. Huang and Y.-N. Lien, "Challenges of emergency communication network for disaster response," in *Proceedings of the 2012 IEEE International Conference on Communication Systems (ICCS)*, pp. 528–532, Singapore, November 2012.
- [15] M. Gapeyenko, V. Petrov, D. Moltchanov, S. Andreev, N. Himayat, and Y. Koucheryavy, "Flexible and reliable uav-assisted backhaul operation in 5g mmwave cellular networks," *IEEE Journal on Selected Areas in Communications*, vol. 36, no. 11, pp. 2486–2496, 2018.
- [16] K. F. Hayajneh, K. Bani-Hani, H. Shakhathreh, M. Anan, and A. Sawalmeh, "3d deployment of unmanned aerial vehicle-base station assisting ground-base station," *Wireless Communications and Mobile Computing*, vol. 2021, p. 2021.
- [17] D. Sikeridis, E. E. Tsiropoulou, M. Devetsikiotis, and S. Papavassiliou, "Wireless powered public safety iot: A uav-assisted adaptive-learning approach towards energy efficiency," *Journal of Network and Computer Applications*, vol. 123, pp. 69–79, 2018.
- [18] P. Vamvakas, E. E. Tsiropoulou, and S. Papavassiliou, "Risk-aware resource management in public safety networks," *Sensors*, vol. 19, no. 18, Article ID 3853, 2019.
- [19] N. Patrizi, G. Fragkos, E. E. Tsiropoulou, and S. Papavassiliou, "Contract-theoretic resource control in wireless powered communication public safety systems," in *Proceedings of the GLOBECOM 2020-2020 IEEE Global Communications Conference*, pp. 1–6, Taipei, Taiwan, December 2020.
- [20] T. S. Rappaport, *Wireless communications: principles and practice*, Vol. 2, Prentice hall PTR, , New Jersey, NY, USA, 1996.
- [21] A. Goldsmith, *Wireless communications*, Cambridge university press, Cambridge, England, 2005.
- [22] A. Al-Hourani, S. Kandeepan, and S. Lardner, "Optimal lap altitude for maximum coverage," *IEEE Wireless Communications Letters*, vol. 3, no. 6, pp. 569–572, 2014.
- [23] M. Mozaffari, W. Saad, M. Bennis, and M. Debbah, "Drone small cells in the clouds: Design, deployment and performance analysis," in *Proceedings of the 2015 IEEE global communications conference (GLOBECOM)*, pp. 1–6, San Diego, CA, USA, December 2015.
- [24] R. Eberhart and J. Kennedy, "A new optimizer using particle swarm theory," in *Proceedings of the MHS'95. Proceedings of the Sixth International Symposium on Micro Machine and Human Science*, pp. 39–43, Nagoya, Japan, October 1995.
- [25] Y. Shi and R. Eberhart, "A modified particle swarm optimizer," in *Proceedings of the 1998 IEEE international conference on evolutionary computation proceedings. IEEE world congress on computational intelligence (Cat. No. 98TH8360)*, pp. 69–73, Anchorage, AK, USA, May 1998.

Research Article

Grasp Detection under Occlusions Using SIFT Features

Zhaojun Ye,^{1,2} Yi Guo ^{1,2}, Chengguang Wang,³ Haohui Huang,^{1,2} and Genke Yang ^{1,2,3}

¹Department of Automation, Shanghai Jiao Tong University, Shanghai 200240, China

²Ningbo Artificial Intelligence Institute of Shanghai Jiao Tong University, Ningbo, Zhejiang 315000, China

³Ningbo Industrial Internet Institute, Ningbo, Zhejiang 315000, China

Correspondence should be addressed to Yi Guo; guo.yi@sjtu.edu.cn and Genke Yang; gkyang@sjtu.edu.cn

Received 30 August 2021; Accepted 22 October 2021; Published 13 November 2021

Academic Editor: Zhenyu Lu

Copyright © 2021 Zhaojun Ye et al. This is an open access article distributed under the Creative Commons Attribution License, which permits unrestricted use, distribution, and reproduction in any medium, provided the original work is properly cited.

Distinguishing target object under occlusions has become the forefront of research to cope with grasping study in general. In this paper, a novel framework which is able to be utilized for a parallel robotic gripper is proposed. There are two key steps for the proposed method in the process of grasping occluded object: generating template information and grasp detection using the matching algorithm. A neural network, trained by the RGB-D data from the Cornell Grasp Dataset, predicts multiple grasp rectangles on template images. A proposed matching algorithm is utilized to eliminate the influence caused by occluded parts on scene images and generates multiple grasp rectangles for objects under occlusions using the grasp information of matched template images. In order to improve the quality of matching result, the proposed matching algorithm improves the SIFT algorithm and combines it with the improved RANSAC algorithm. In this way, this paper obtains suitable grasp rectangles on scene images and offers a new thought about grasping detection under occlusions. The validation results show the effectiveness and efficiency of this approach.

1. Introduction

Robotic grasping has been a hot-spot topic and drawn increasing attention from researchers. With the growing demand of intelligent robot, robotic grasping technique has been extensively adopted in our daily life, such as workshop assembly, service robotic grasping, and agricultural robotic grasping [1–5]. However, compared with human beings, robots still have great limitations in grasping, such as grasping in occlusion case. Meanwhile, manipulating objects in occlusion occasion is an inevitable application for robots, like grasping under household [5] and industrial [6] scenes. Consequently, improving the ability of grasping objects in the case of occlusion and overlap is a difficult but necessary work for robotic manipulation.

Many works focus on predicting grasp rectangles on single-object scene [1, 7–9]. Nevertheless, robots usually face the scenes of grasping target from multiple objects. This type of problem is also called “bin picking.” Some works [10–13] offer solutions to such problem, and they settle multiple objects grasp detection to a certain extent. However, they

pay no attention on overlapped situations and may predict grasp rectangles in the overlapping areas. It can cause collision between objects and the robotic manipulator. Other works [14, 15] consider the occlusions of objects and work out such problem in their own way but cause high cost of dataset acquisition.

The proposal method in this paper divides such question into two main stages and predicts suitable grasp configurations (grasp configuration will be shown in Section 3) using an RGB input image. Inspired by [1], the first stage predicts multiple grasp rectangles on template images using the neural network ResNet-50. Each template image is taken in advance and contains only one object. Template images and the corresponding grasp rectangles are integrated into the template information; the second stage utilizes the proposed matching algorithm to connect the scene information with the template information and decreases the influence caused by occluded parts on scene images. Then, several grasp rectangles are predicted using the template information and connection between the template information and the scene information. A matrix M is used to

represent scaling, translation, and rotation information of a same object between two images. The proposal matching algorithm consists of the scale-invariant feature transform (SIFT) algorithm and random sample consensus (RANSAC) algorithm and connects two images based on SIFT features. In order to obtain a better connection, this paper improved the SIFT algorithm and RANSAC algorithm, respectively, and received a more accurate transformation matrix M between the template image and the scene image. The proposed grasp detection algorithm predicts multiple grasp rectangles with corresponding quality scores for objects under occlusions.

The main contributions of this paper are as follows:

- (1) A novel grasp detection algorithm is proposed to predict grasp configurations for objects under occlusions. This algorithm, which is composed of a grasp rectangle predicting neural network and our key-point matching algorithm, predicts multiple grasp configurations on template images and generates several grasp configurations for objects on scene images using the connection between scene information and template information, rather than using an end-to-end network.
- (2) The paper proposes a new way to predict grasp rectangles under occlusions by matching template images with scene images using our matching algorithm. The matching algorithm combines the SIFT algorithm and RANSAC algorithm and improves the two algorithms in order to receive a better matching result.

The rest of the paper is organised as follows. Related work about grasp detection is presented in Section 2. Problem formulation and a brief introduction to the SIFT algorithm are provided in Section 3. The detail of the proposed algorithm is discussed in Section 4. Section 5 provides the description of our experiment setup and validation results, respectively. The conclusion part can be found in Section 6.

2. Related Work

2.1. Grasp Detection Using Neural Network. In previous works like [16–18], model-based methods have played a primary position in solving the grasp detection problem. Such method uses the complete 3D model of the target object to define the grasp operation. However, robots face different environments, and obtaining the accurate 3D model in advance seems to be impossible [19]. On the contrary, it is more convenient to capture RGB images than reconstructed 3D models. Meanwhile, the learning-based method offers a strong generalization ability over object classification, target detection, and regression [10, 20]. Many works about object grasp detection have been done using the learning-based method. Early research studies focus on solving grasp detection problem in single-object scenes. These works pay no attention on multiobject, occluded cases and instruct the robot to grasp objects only under ideal circumstances [19]. Lenz et al. [21] connected two single

neural networks in series in order to detect grasp positions in an RGB-D image. Similarly, Guo et al. [22] considered grasp detection using multiple sensors and proposed a hybrid deep architecture fusing the visual and the tactile information for grasp detection. The author collected a THU grasp dataset with visual, tactile, and grasp configuration information for network training. Reference [1] proposed a deep learning architecture to predict graspable locations using an RGB-D image for robotic manipulation. Different from some previous works, the paper considered to define the angle learning problem as classification with null hypothesis competition rather than regression and detected multiple grasp candidates for each object in a single shot with the input of RGB-D image.

The above works are all single-object scenes with objects in Cornell Grasp Dataset. However, grasping in multiobject scenes is inevitable in reality. Guo et al. [23] proposed a convolutional neural network to detect the target object and its optimal grasp configuration simultaneously on a fruit dataset. However, this model can just predict the grasp rectangle information of the most exposed object, without considering about partially visible objects. Vohra et al. [24] proposed a real-time grasp pose detection strategy for novel objects in our daily life. The proposed technique predicts the contour of the object in the point cloud and detects the grasp configurations along with the object skeleton in the image plane. Reference [25] explained a robotic grasp detection algorithm named ROI-GD to detect objects and their possible grasp configurations at the same time based on region of interest (ROI). The experiment results showed that this algorithm solved grasp detection problem of the object in the case of contact to some extent but did not offer the results of occluded cases.

Employed the neural network in [1], this paper trains a model using the Cornell Grasp Dataset and succeeds to obtain multiple grasp rectangles on the template image containing only one object. Then, these template images and relevant grasp configurations are used to generate grasp configurations for the target objects under occlusions during experiments. In order to build the connection between scene images and template images, this paper adopts a matching algorithm based on SIFT features to realize image matching task.

2.2. SIFT-Based Matching Algorithm. SIFT is a feature point extraction and matching algorithm proposed by Lowe in 1999 and perfectly improved in 2004 [26–28]. SIFT is proposed to extract distinctive invariant features from images in order to perform reliable match between different views of an object or a scene [27]. SIFT features are invariant to rotation and scale and can match robustly across affine distortion, change in 3D viewpoint, disturbance of noise, illumination variation, and even partial occlusion [29]. However, the original SIFT algorithm matches the key points by comparing the distance of the closest neighbor and the second-closest neighbor, and that method makes the detecting quality of the SIFT algorithm sensitive to the threshold. Duo to the requirements of different works,

researchers improved the performance of the SIFT algorithm in many ways. Dellinger et al. [30] proposed a new algorithm named SAR-SIFT based on the SIFT algorithm to reduce the influence caused by speckle noise on synthetic aperture radar (SAR). In [31], Alhwarin et al. improved the original SIFT algorithm for the purpose of providing a more reliable object recognition. Before matching the features, they divided the features of both test and template images into several subcollections according to the different octaves. Compared with the original SIFT algorithm, the processing time of the improved SIFT algorithm reduced 40% for matching the stereo images. Reference [32] utilized the improved RANSAC algorithm to realize a better SIFT feature point matching result and received an obvious promotion. The paper eliminated the mismatches using the improved RANSAC algorithm and obtained a more accuracy connection between images, also improved efficiency of processing. Other works like [33, 34] also proposed algorithms based on the SIFT algorithm to realize better results.

3. Preliminaries

3.1. Problem Formulation. Given an RGB scene image containing several arbitrarily placed objects, the objective of this paper is to identify the suitable grasp configurations for the target object even the target object is occluded by other objects. Inspired by [21], a grasp configuration of the target object can be represented using a six-dimensional vector:

$$g = (x, y, w, h, \theta, s), \quad (1)$$

where the grasp configuration g describes the grasp location, orientation information, and approximate opening distance of a parallel plate gripper. As shown in Figure 1(a), point G is the gripper's location and also the center of grasp rectangle, (x, y) is the coordinate of point G , angle θ is the orientation information, it represents the angle of rotation of the gripper in a certain direction, w and h represent the width and opening size of parallel plate gripper, respectively, and s represents the grasp quality score of the grasp configuration and is used to be the criterion of selecting the best grasp configuration. For each object, there may have several possible grasp configurations, and a set of proper grasp configurations $S(g)$ is obtained; each element of $S(g)$ represents a proper grasp configuration information for the target object in the scene:

$$S(g) = \{g_1, g_2, \dots, g_n\}, \quad (2)$$

where n represents the number of grasp configurations we predict for the target object. We choose the best one for robotic manipulation depending on the quality scores of these grasp configurations.

Note that, this paper only predicts such grasp configurations for template images; each template image contains only one object we want to grasp and then generating grasp

configurations for scene images using our matching algorithm.

3.2. Introduction of SIFT Algorithm. SIFT features are invariant to rotation and scale and can match robustly across affine distortion, change in 3D viewpoint, disturbance of noise, illumination variation, and even partial occlusion [29]. The original SIFT algorithm includes four main parts. The detail of the SIFT algorithm can be obtained from [27].

3.3. Scale Space Extrema Detection. The SIFT algorithm selects the extreme points of scale space as candidate feature points. The scale space of an image $I(x, y)$ is defined as follows:

$$L(x, y, \delta) = G(x, y, \delta) * I(x, y), \quad (3)$$

where $L(x, y, \delta)$ defines the convolution of original image $I(x, y)$ and a Gaussian function. $*$ presents two-dimensional convolution, and δ is the standard deviation of normal Gaussian distribution.

The SIFT algorithm uses scale space difference-of-Gaussian (DoG) function to generate a large number of extremas. The DoG image $D(x, y, \delta)$ is defined as follows:

$$D(x, y, \delta) = L(x, y, k\delta) - L(x, y, \delta), \quad (4)$$

where k is a constant over all scales; thus, it does not influence extrema location [27].

3.4. Key-Point Localization. This step is aimed to filter the key points in order to only retain the stable key points. The Taylor expansion of DoG function is constructed in scale space:

$$D(X) = D + \frac{\partial D^T}{\partial X} X + \frac{1}{2} X^T \frac{\partial^2 D}{\partial X^2} X, \quad (5)$$

$$X = (x, y, \delta)^T,$$

and then the stable key point is obtained by solving the formula as follows:

$$\hat{X} = -\frac{\partial^2 D^{-1}}{\partial^2 X} \frac{\partial D}{\partial X}, \quad (6)$$

$$D(\hat{X}) = D + \frac{1}{2} \frac{\partial D}{\partial X} \hat{X}.$$

3.5. Orientation Assignment. In this step, every key point is assigned an orientation to make the descriptor invariant to rotation. Every direction contains gradient magnitude $m(x, y)$ and gradient direction $\theta(x, y)$ as follows:

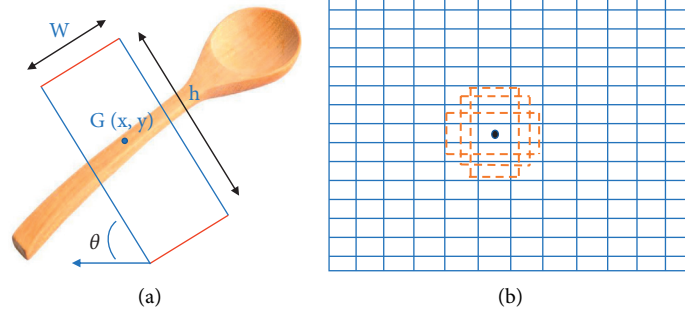


FIGURE 1: (a) Grasp configuration for parallel robotic gripper. Each grasp configuration contains the position information, orientation information, and grasp quality score. (b) Each anchor is corresponded to 9 possible grasp boxes with 3 scales and 3 aspect ratios (here only shows 3 of the possible grasp boxes of a same scale).

$$m(x, y) = \left[(L(x, y + 1) - L(x, y - 1))^2 + (L(x + 1, y) - L(x - 1, y))^2 \right]^{1/2},$$

$$\theta(x, y) = \arctan \frac{L(x, y + 1) - L(x, y - 1)}{L(x + 1, y) - L(x - 1, y)}. \quad (7)$$

3.6. Key Point Descriptor. The last step divides the image region around the critical point to blocks; for each block, the gradient histogram of it is calculated, and then a 128-dimensional key point descriptor is generated.

In order to decrease the disturbance caused by occluded parts of scene images, this paper improves the original SIFT algorithm and receives fewer mismatches. Several matched SIFT features are extracted by the improved SIFT algorithm and fed into the remaining matching algorithm to build a more robust connection between the scene image and the corresponding template image.

4. Approach

The proposed algorithm can be divided into two stages (Figure 2): template generation and image matching. Firstly, before predicting grasp configurations during experiments with robotic gripper, several template images are taken in advance. Each template image contains only one object and performed grasp detection using neural network proposed in [1]. Then, a matching algorithm matches the target object in a scene image with template images and generates several grasp configurations for the target object under occlusions using the connection between the scene image and the template images.

The next three subsections describe the whole system in detail. It includes the architecture of the network and generates template information using the network, a description of obtaining connection between template images and scene images using the proposed matching algorithm, and a strategy of generating grasp configurations on scene images using the information of template images and connection.

4.1. Template Generation Using Neural Network. Currently, convolutional neural networks (CNNs) receive great performances on classification, detection, and

regression problems. We use modified ResNet-50 with 50 layers to solve grasp detection problem. ResNet overcomes the challenge of learning mapping function by its residual learning concept. Every residual block is designed to be an incorporation which is a skip connection with the standard CNN. Meanwhile, ResNet can avoid time-consuming sliding-window approach shown in [8, 22] by utilizing the capacity of neural networks to execute bounding box regression and predict candidate regions on the whole image directly. The structure of our network is shown in Figure 3; we adopt the architecture proposed in [1] and train a model on Cornell Grasp Dataset.

The network takes RG-D images as input. The RG-D image is composed of the RGB image and corresponding depth image. Thus, the original dataset contains RGB images and depth images. Then, the data preprocessing part combines RGB images with the corresponding depth images to obtain RG-D images and crops them. After that, every cropped RG-D image is sent to intermediate convolutional layers (1–40 layer of ResNet-50). The intermediate convolutional layer extracts a common feature map with the size of $14 \times 14 \times 1024$. The feature map with r anchors is then sent to section Grasp Proposal Network. The Grasp Proposal Network slides a mini-network of 3×3 over the feature map and generates 9 possible grasp boxes with 3 aspect ratios and 3 scales for each anchors (Figure 1(b)). Thus, there are $r \times 9$ possible grasp boxes for each feature map. The Grasp Proposal Network outputs a $1 \times 1 \times 512$ feature map and then sends it into two sibling fully connected layers. Afterwards, the outputs of two layers represent the probability of grasp proposal and bounding box for each of r anchors on the feature map. The feature of each proposal bounding boxes is extracted by the ROI layer and sent to the remaining layers of the ResNet-50. Let t_i be the i -th grasp configuration with the form of (x, y, w, h) and p_i be the probability of the corresponding grasp proposal. In is an index set of all proposals; we use the formulation as follows to define the loss of grasp proposal net (gp).

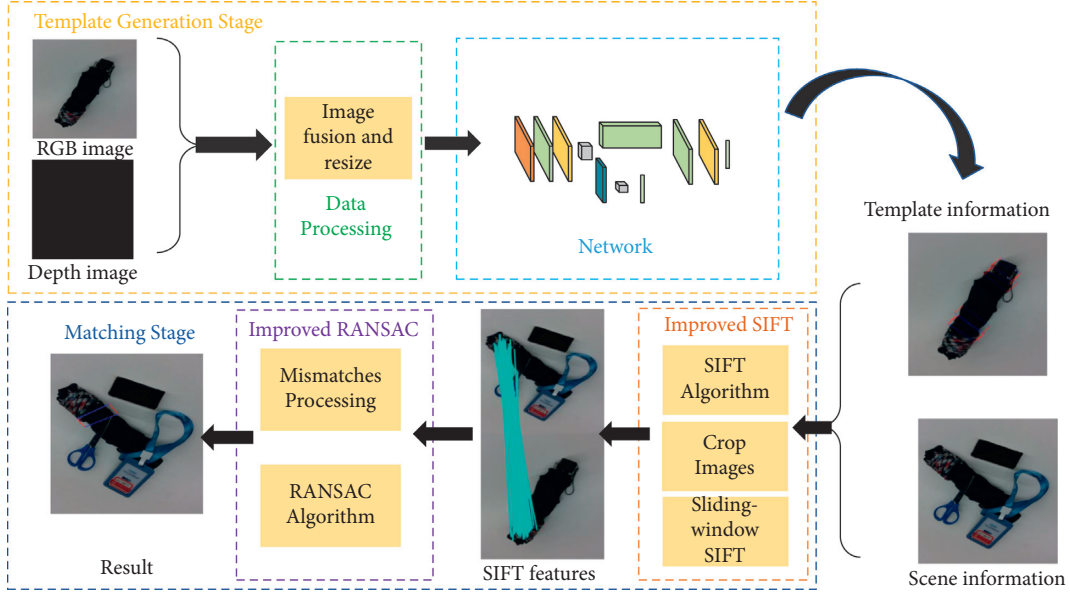


FIGURE 2: System diagram of our grasp detection algorithm. The template generation stage uses the network and template images to generate template information. For each scene image, the algorithm connects the scene image with template information in matching stage using a matching algorithm and obtains grasp rectangles for the target object in occluded condition.

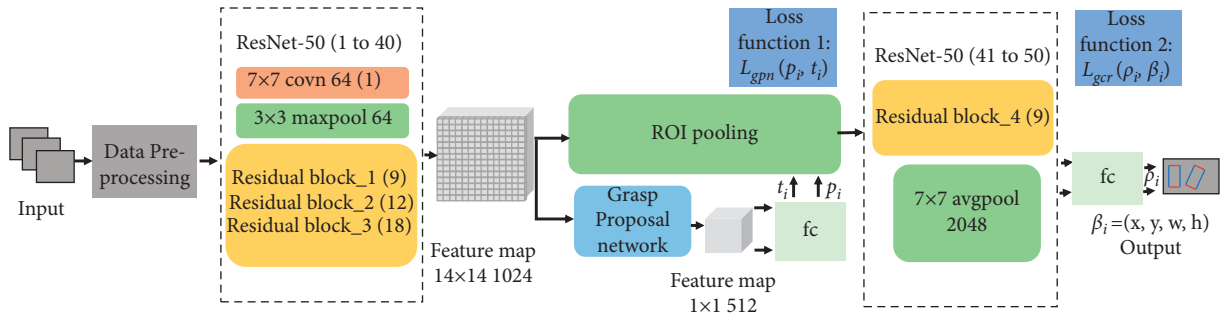


FIGURE 3: The structure of our network. The network uses RG-D images as inputs and predicts multiple grasp rectangles which contain position information, orientation information, and grasp quality score for each object. The data preprocessing part fuses the RGB image and the corresponding depth image to be the RG-D image and crops the RG-D image into a given size. The 1–40 layers of our network extract a feature map, the feature map is then fed into the Grasp Proposal Network and the ROI pooling. The rest of the network (41–50 layers) receives the output of the Grasp Proposal Network and generates several grasp rectangles.

$$L_{gp}((p_i, c_i)_{i=1}^n) = \sum_i L_{gp-c}(p_i, p_i^*) + \lambda \sum_i p_i^* L_{gp-r}(c_i, c_i^*), \quad (8)$$

where L_{gp-c} denotes the cross entropy loss of grasp proposal classification and L_{gp-r} denotes the l_1 regression loss of grasp proposal with weight λ . p_i^* is an index with only two values. $p_i^* = 0$ represents no grasp, and $p_i^* = 1$ shows that a grasp is specified. c_i^* is the coordinate of ground-truth grasp corresponding to p_i^* .

As for θ , the orientation of each grasping configuration, we consider it as a classification task. The multigrasp detection pipeline quantizes θ into R equal-length intervals and generates multiple possible grasp configuration for each possible grasp proposal using θ . If none score of the possible grasp configuration is higher than the threshold we set, then we abandon the corresponding

possible grasp proposal. In this paper, the total classes $C = R + 1$ and $R = 19$.

After the above processing, the last stage of the network classifies the grasp proposals into R regions and refines every proposal bounding box to a bounding box (x, y, w, h) without orientation. A ROI pooling layer is added into ResNet-50 and shares the common feature map extracted by intermediate convolutional layer. Thus, it reduces the recomputation of feature extraction. All the features of the proposal grasps are stacked by ROI pooling layer and then fed into two sibling fully connected layers for the classification of orientation parameter l and regression of bounding box (x, y, w, h) . The loss function of predicted grasp configuration (gc) is defined to be

$$L_{gc}((\rho_l, \beta_l)_{c=0}^C) = \sum_c L_{gc-c}(\rho_l) + \lambda_2 \sum_c L_{gc-r}(\beta_c, \beta_c^*), \quad (9)$$

where ρ_i is the probability of class l , β_l is the corresponding grasp bounding box prediction, L_{gc-c} denotes the cross entropy loss of the angle classification, L_{gc-r} denotes the l_1 regression loss grasp bounding boxes with weight λ_2 , and β_c^* is the ground-truth grasp bounding box. The total loss is defined to be

$$L_{\text{total}} = L_{\text{gp}} + L_{\text{gc}}. \quad (10)$$

The ROI layer generates grasp proposals, and grasp bounding boxes and orientations are received using the additional neurons of two sibling layers. Finally, we obtain the grasp configurations $S(g)$ of the target object on the template image. As mentioned above,

$$\begin{aligned} S(g) &= \{g_1, g_2, \dots, g_n\}, \\ g &= (x, y, w, h, \theta, s). \end{aligned} \quad (11)$$

4.2. Connect Images Using SIFT Features. Using the proposed deep network, multiple grasp bounding boxes are obtained on the template images. Every template image contains a single object, and the predicted grasp bounding boxes show the suitable grasp configurations of the object. However, as it is described earlier, grasp detection may obtain some unsuitable grasp configurations in the occluded parts. In order to abandon the unsuitable grasp bounding boxes from all predicted grasp rectangles, we try to cut the occluded parts of scene image using our matching algorithm rather than predicting grasp rectangles on scene image using an end-to-end network.

SIFT features are invariant to rotation and scale and can match robustly across affine distortion, change in 3D viewpoint, disturbance of noise, illumination variation, and even partial occlusion [29]. The original SIFT algorithm matches the key points by comparing the distance of the closest neighbor and the second-closest neighbor, and that method makes the detecting quality of the SIFT algorithm sensitive to the threshold. Correct matching happens when the ratio is less than the threshold. Thus, as the threshold raises, the matching points increase, but mismatch increases too. Usually we want to generate more correct feature points and decrease the mismatches. Only by raising the threshold cannot solve such conflicting problem. Inspired by [32], we propose a matching algorithm which combines the improved SIFT algorithm with the improved RANSAC algorithm to improve the quality of matching. Our matching strategy is shown in Figure 4.

Firstly, we extract images SIFT feature points using the improved SIFT algorithm; this algorithm contains three parts: SIFT algorithm, crop images, and sliding-window SIFT. We utilize the SIFT algorithm to each pair of images and obtain many SIFT feature points of the two images. In order to decrease the influence of occluded parts, this paper uses the original matched SIFT features to detect the occluded parts. Our method divides the scene image into some patches and judges whether a patch is the occluded part by connecting it with template image using the SIFT algorithm. Note that the original matched SIFT features have proved the

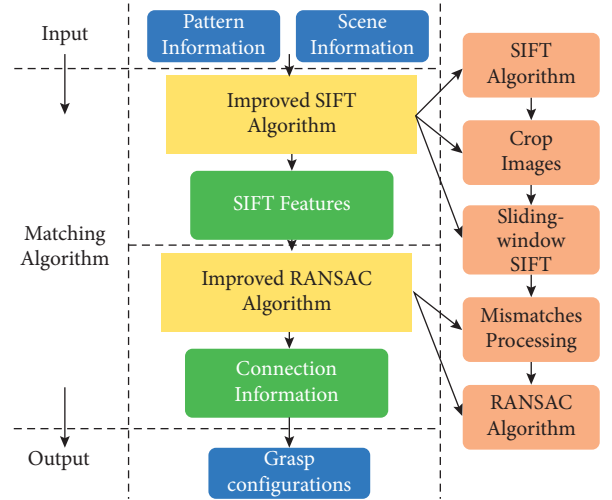


FIGURE 4: The diagram of our matching algorithm. The matching algorithm combines the improved SIFT algorithm and the improved RANSAC algorithm to connect the template information and the scene information. The connection information generated by our matching algorithm contains the transformation relationship between the matched pair of images. The output of the matching algorithm includes multiply grasp configurations of the target object in the occluded condition.

approximate position of the object on images; thus, unnecessary computation can be avoided by cropping the images. The crop image part crops images based on original matched SIFT features and obtains cropped parts of the images that contain the target object. Then, the sliding-window SIFT part slides the cropped scene image into several patches and judges whether a patch is the occluded part by the number of matched SIFT features. If a patch contains SIFT features, which are matched with template image, more than a given count (in this paper is 2), it is considered to be a part of the target object; otherwise, we classify it as occluded part and delete the corresponding SIFT features. After the improved SIFT algorithm, many matched SIFT features are obtained. The SIFT algorithm matches two images' SIFT feature points based on calculating the Euclidean distance between the two 128-dimensional key point descriptor. Such matching strategy makes the matching quality sensitive to the given threshold of the SIFT algorithm and cannot solve the trade-off between obtaining more matches and decreasing mismatches while it has to calculate the transformation matrix between two images, and mismatches may influence the accuracy of the result. In order to get a better result, we decide to eliminate some of the mismatches in advance and utilize the RANSAC algorithm to calculate a more accurate result afterwards.

Inspired by [32], this paper considers the cross points as mismatches. Generally speaking, the size of same object is a constant. The transformation of the same object in two images can be considered as rotation and scaling. Thus, there should be no crossover between two correctly matched images. So, the proposed algorithm can eliminate part of the mismatches by abandoning the feature points which cause cross line with other lines. The main function of mismatches processing part is to delete such mismatches. After the

processing of the SIFT feature points, the RANSAC algorithm is used to calculate the transformation matrix M between each pair of images using matching feature point set F . F is defined as follows:

$$\begin{aligned} F &= f_1, f_2, \dots, f_N, \\ f_k &= (t_k, s_k), \end{aligned} \quad (12)$$

where N is the number of matching point pair, f_k is the k -th matching point pair in F , k is an integer between 1 and N , and t_k and s_k are two corresponding feature points of template image and scene image, respectively.

Each pair of matching images can be connected using the corresponding transformation matrix M ; the relationship between two matching points' coordinates and transformation matrix M is defined as follows:

$$\begin{aligned} P_s &= MP_t, \\ M &= \begin{bmatrix} A_{11} & A_{12} & A_{13} \\ A_{21} & A_{22} & A_{23} \\ A_{31} & A_{32} & A_{33} \end{bmatrix}, \end{aligned} \quad (13)$$

where $P_s = [x' \ y' \ 1]^T$ is the coordinate of any feature point on scene image and $P_t = [x \ y \ 1]^T$ is the coordinate of the corresponding feature point on template image. By equation (13), we can connect two matched images at the pixel level and match each point on the template image to the pixel of the scene image. The improved RANSAC Algorithm 1 is described as follows.

4.3. Grasp Configurations Generating Strategy under Occlusions. Through the above steps, there obtains the grasp configurations $S(g)$ of the target object in the template image and uses the matching feature point pair set F to calculate the transformation matrix M between template image and scene image. Note that, the occluded parts of scene image cannot match with template image due to the specialty of the SIFT algorithm. At this step, this paper utilizes above information to generate grasp configurations for target object in the case of occlusion.

For every grasp configuration $g = (x, y, w, h, \theta, s)$ of $S(g)$, we denote $G = (x, y)$ as the grasp center point of g . Thus, we get a set $S(G)$ of grasp center point as follows:

$$S(G) = \{G_1, G_2, \dots, G_n\}. \quad (14)$$

Meanwhile, we denote $S(t)$ and $S(s)$ as the matching feature point sets of template image and scene image, respectively:

$$\begin{aligned} S(t) &= \{t_1, t_2, \dots, t_m\}, \\ S(s) &= \{s_1, s_2, \dots, s_m\}, \end{aligned} \quad (15)$$

where n is the number of grasp center points of the target object in template image and m is the number of matching pairs which satisfy the transformation matrix M .

The proposed strategy is using the points in $S(G)$ to replace the points in $S(t)$ based on the Euclidean distance

of pixels. Thus, for each $g = (G, w, h, \theta, s)$, we replace the grasp center point G with the closets SIFT feature point p' ; the closets Euclidean distance is less than a given threshold, and a new set of grasp configurations $S(g')$ is created:

$$\begin{aligned} S(g') &= \{g'_1, g'_2, \dots, g'_r\}, \\ g' &= (p', w, h, \theta, s), \end{aligned} \quad (16)$$

and then for each p' , we have a corresponding SIFT feature point s' scene image, and the parameters of s' are as follows:

$$s' = (p', w, h, \theta + \beta, s), \quad (17)$$

where β is the orientation transformation of the transformation matrix M . Finally, we obtain the grasp configurations $S(s') = \{s'_1, s'_2, \dots, s'_r\}$ of the target object in the case of occlusion.

5. Experiment

5.1. Dataset and Implementation for Network Training. In this paper, the goal is to predict grasp rectangles in occluded scenes. However, the proposed algorithm utilizes the connection between template information and scene information to obtain the grasp configurations in the multiobject, occluded cases, rather than an end-to-end deep neural network to predict grasp configurations on the scene images directly. Hence, the function of our network is to generate multiple grasp rectangles on the template image which contains only one target object. Note that, in order to increase the accuracy of detection, this paper stipulates the template image with only one object intentionally, because different matched objects between template image and scene image correspond to different transformation matrices in theory. On the basis of above condition, this paper chooses Cornell Grasp Dataset (Figure 5) as the dataset of our network.

The Cornell Grasp Dataset contains 855 images (RGB images and depth images) of 240 different objects [35]. Each image contains several ground-truth grasp rectangles with different orientations and positions. This paper takes the same procedure of data processing in [1, 8] and replaces the blue channel of each image with the corresponding depth channel. Because the data of blue channel are distributed between 0 and 255, we normalize the depth data to the same range. By combining RGB information and depth information, RG-D images are obtained. In order to generate plenty of training data and fit to the input size of ResNet-50, each image is performed extensive data augmentation by rotating randomly between 0 and 360 and resized to 227×227 .

The network is implemented on Tensorflow framework and trained end-to-end on a single GPU of GTX1660Ti. We set the initial learning rate of our network to 0.0001 and divide it by 5 every 10000 iterations. We set the training epochs as 5.

Input: Input parameters set of SIFT matches F

Output: Output transformation matrix M

- (1) Preprocessing: eliminate part of the mismatches by deleting the feature point pair that causes cross line. Denote the matching point set after preprocessing as F' .
- (2) Select 4 pairs of points from F' randomly, and calculate transformation matrix M' , create a new point set O .
- (3) Judge whether other matching pairs satisfy the transformation of M' (a matching pair belongs to O if the error less than a given threshold), record the number of satisfied matching pair (elements in O) as m .
- (4) If current m is the biggest than before, retain the current M' ; otherwise, abandon it.
- (5) Repeat 2, 3, and 4 a given times (5 in this paper), and obtain a transformation matrix M .

ALGORITHM 1: Improved RANSAC algorithm.

5.2. Evaluation Metrics of Predicted Result. In this paper, we take the metrics proposed in [21] to evaluate the grasp detection ability of our network. A grasp is considered to be a good grasp if it meets the following two criterions:

- (1) The difference of grasp orientation between predicted grasp rotation angle and the corresponding grasp rotation angle of ground-truth is less than 30° .
- (2) The Jaccard index of the predicted grasp configuration g' and the ground-truth g is more than 25%.
The Jaccard index is defined as follows:

$$J(g, g') = \frac{g_A \cap g'_A}{g_A \cup g'_A}, \quad (18)$$

where g_A and g'_A are the areas of predicted grasp rectangle and ground-truth grasp rectangle, respectively. The Jaccard index is the ratio of intersection of the two rectangles to the union of the two rectangles.

5.3. Validation Results on Cornell Grasp Dataset and Household Objects. Three main types of experiments are performed to verify the ability of the proposed grasp detection algorithm. The first experiment makes a comparison with other typical methods on Cornell Grasp Dataset. In order to prove the validity of the proposed matching algorithm, the second experiment predicts grasp rectangles for objects under occlusions using the original SIFT algorithm and the proposed matching algorithm, respectively. The last experiment predicts grasp rectangles for some household objects under occlusions. The results of all experiments prove that the proposed grasp detection algorithm can ensure the detection accuracy on Cornell Grasp Dataset and solve the problem of grasp detection under occlusions to some extent.

Experiment 1 tests the proposed grasp detection algorithm on the Cornell Grasp Dataset and makes a comparison with prior works, and the result of comparison is shown in Table 1. We compare these works in two ways: image-wise split (*IW*) and object-wise split (*OW*):

- (i) *IW*. The dataset is divided based on image randomly. Each image has an equal probability to be trained or tested. This is a common way to test the

generalization of the network to new orientation and position about objects it has seen before.

- (ii) *OW*. The dataset is divided based on object instances. Objects in training set and test set can be different. *OW* is used to test the generalization ability of a network about new object.

The performance of the proposed grasp detection algorithm on Cornell Grasp Dataset is shown at the last column of Table 1. For this grasp detection test on Cornell Grasp Dataset, we choose the best grasp rectangle from all the grasp candidates based on the corresponding output scores. Our grasp detection algorithm receives the accuracy of 97.2% on *IW* and 92.5% on *OW*, respectively. The detection accuracy is slightly inferior to the algorithm proposed in [1], the possible reason is that our matching algorithm may ignore some suitable grasp rectangles by mistake, we use the same network to generate several template images, but during calculating the transformation matrix, our matching algorithm may cut the right patch which contains the best grasp configuration, and the final result is the best of the remaining. Figure 6 shows the results of grasp detection on part of images of Cornell Grasp Dataset. We only show the grasp rectangle with the highest score.

Experiment 2 focuses on some household objects like umbrella, scissor, remote control, and so on. In order to validate the usefulness of our matching algorithm, we firstly compare our matching algorithm with the original SIFT algorithm. The result of comparison can be seen in Figure 7.

Figure 7(a) is the result of the original SIFT algorithm; the final prediction of grasp rectangle is at an occluded part. The original SIFT algorithm fails to decrease the influence of occluded parts and generates wrong grasp configurations. The reason may be that the position of grasp configuration with highest score in the template image is one of the occluded parts in the scene image; thus, without eliminating the influence of occluded parts, some SIFT feature pairs choose such grasp rectangle as the closest grasp position, and the result of matching goes wrong. Our matching algorithm deletes the occluded parts by combining the improved SIFT algorithm with the improved RANSAC algorithm and matches SIFT feature pair with the closest grasp position that is not in the occluded parts. The result is shown in Figure 7(b), and the robot can grasp the umbrella without grabbing other objects.



FIGURE 5: Several objects of Cornell Grasp Dataset.

TABLE 1: Performance of different methods on Cornell Grasp Dataset.

Approach	Algorithm	Accuracy (%)	
		IW	OW
Jiang et al. [36]	Fast search	60.5	58.3
Lenz et al. [21]	SAE, struct.	73.9	75.6
Redmon and Angelova [8]	AlexNet, MultiGrasp	88.0	87.1
Guo et al. [22]	ZF-net, hybrid network	93.2	89.1
Chu et al. [1]	ResNet-50 FCGN	97.7	94.9
Li et al. [19]	Key point-based scheme	96.05	96.5
This paper	The proposed algorithm	97.2	92.5

Bold values indicate the performance of our algorithm on Cornell Grasp Dataset. IW: image-wise. The dataset is divided based on image randomly. Each image has an equal probability to be trained or tested. This is a common way to test the generalization of the network to new orientation and position about objects it has seen before. OW: object-wise. The dataset is divided based on object instances. Objects in training set and test set can be different. OW is used to test the generalization ability of a network about new object.



FIGURE 6: The results of grasp detection on several images of Cornell Grasp Dataset.

Experiment 3 is grasping some household objects in the occluded case. Note that, our algorithm performs well when there contains plenty of SIFT features, and the degree of texture richness and occlusion of the object determine the performance of our algorithm. There are several randomly placed objects in the grasp range of the robot, our matching algorithm generates a certain number of matching points across two images, and the blue lines show the connection of each pair of matching feature points. From the matching feature pairs, we can obtain the

transformation matrix M' using the feature points' location information of matching images, and finally we can get the transformation between template images and scene images. Our grasp detection algorithm can avoid the occluded parts and predict a suitable grasp configuration for robot. The results reveal the usefulness of our algorithm (see Figure 8). Our algorithm can predict suitable grasp configurations for the target objects and help the robot to grab the target objects without grabbing other objects.



FIGURE 7: Comparison of our matching algorithm with the original SIFT algorithm on household objects: (a) the result generated by the original SIFT algorithm; (b) the result obtained by our matching algorithm. Our matching algorithm decreases the influence of occluded parts and predicts a more suitable grasp configuration than the original SIFT algorithm.

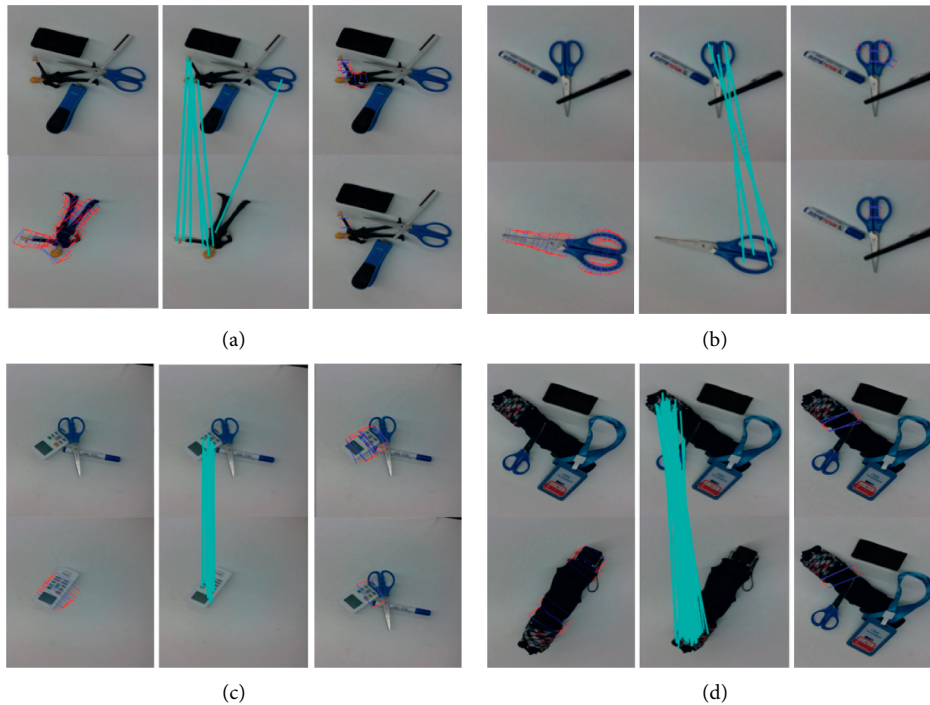


FIGURE 8: Grasp detection results on household objects under occlusions: (a) detection results of a garage kit, the first row of (a) is the input information and template information, the target object on scene image is occluded by other objects, and the template image only contains the target object and its grasp configurations; the second row shows the SIFT feature pairs obtained by our matching algorithm, and we connect each matching SIFT features using a blue line; and the last row is the detecting results with multiple-rectangle above and most suitable rectangle below, and all the results avoid the occluded parts. (b), (c), and (d) have the same layout. We connect the matching features using blue lines.

6. Conclusion

This paper proposes a grasp detection algorithm to predict grasp rectangles for objects in occluded cases, which trains the model based on Cornell Grasp Dataset and obtains grasp rectangles for scene images using our matching algorithm. Every image in the dataset contains only one object, but our algorithm can predict grasp configurations for images with multiple objects. Experiment results demonstrate the improvement of our algorithm. We evaluate our algorithm on Cornell Grasp Dataset and receive the accuracy of 97.2% on image-wise and 92.5% on object-wise, respectively. In order to verify the effect of our algorithm in occluded cases, we perform experiment in multiobject, occluded condition. The outcome shows that this is a feasible method to utilize our grasp detection algorithm to obtain grasp rectangles in

occluded condition; this is the advantage over [1]. The disadvantage of this method is that the result of the matching algorithm influences the final prediction and reduces the detection accuracy on Cornell Grasp Dataset in comparison to [1]. Future work will focus on improving the robustness of the matching algorithm while ensuring the detection accuracy of network.

Data Availability

The data used to support this study are available upon request.

Conflicts of Interest

The authors declare that they have no conflicts of interest.

Acknowledgments

This research was partially funded by the China National R&D Key Research Program (2019YFB1705703 and 2020YFB1711204).

References

- [1] F.-J. Chu, R. Xu, and P. A. Vela, "Real-world multiobject, multigrasp detection," *IEEE Robotics and Automation Letters*, vol. 3, no. 4, pp. 3355–3362, 2018.
- [2] A. Bicchi and V. Kumar, "Robotic grasping and contact: a review," in *Proceedings of the 2000 ICRA, Millennium Conference, IEEE International Conference on Robotics and Automation, Symposia Proceedings (Cat. No.00CH37065)*, vol. 1, pp. 348–353, San Francisco, CA, USA, 2000.
- [3] K. Bousmalis, A. Irpan, P. Wohlhart et al., "Using simulation and domain adaptation to improve efficiency of deep robotic grasping," in *Proceedings of the 2018 IEEE International Conference on Robotics and Automation (ICRA)*, pp. 4243–4250, Madrid, Spain, 2018.
- [4] D. Quillen, E. Jang, O. Nachum, C. Finn, J. Ibarz, and S. Levine, "Deep reinforcement learning for vision-based robotic grasping: a simulated comparative evaluation of off-policy methods," in *Proceedings of the 2018 IEEE International Conference on Robotics and Automation (ICRA)*, pp. 6284–6291, Madrid, Spain, 2018.
- [5] J. Zhang, M. Li, Y. Feng, and C. Yang, "Robotic grasp detection based on image processing and random forest," *Multimedia Tools and Applications*, vol. 79, no. 3, pp. 2427–2446, 2020.
- [6] Y. Chao, X. Chen, and N. Xiao, "Deep learning-based grasp-detection method for a five-fingered industrial robot hand," *IET Computer Vision*, vol. 13, no. 1, pp. 61–70, 2019.
- [7] S. Kumra and C. Kanan, "Robotic grasp detection using deep convolutional neural networks," in *Proceedings of the 2017 IEEE/RSJ International Conference on Intelligent Robots and Systems (IROS)*, pp. 769–776, Vancouver, Canada, September 2017.
- [8] J. Redmon and A. Angelova, "Real-time grasp detection using convolutional neural networks," in *Proceedings of the 2015 IEEE International Conference on Robotics and Automation (ICRA)*, pp. 1316–1322, IEEE, Seattle, WA, USA, 2015.
- [9] H. Lin, T. Zhang, Z. Chen, H. Song, and C. Yang, "Adaptive fuzzy Gaussian mixture models for shape approximation in robot grasping," *International Journal of Fuzzy Systems*, vol. 21, no. 4, pp. 1026–1037, 2019.
- [10] L. Bo, X. Ren, and D. Fox, "Unsupervised feature learning for rgb-d based object recognition," in *Experimental Robotics*, pp. 387–402, Springer, Berlin, Germany, 2013.
- [11] S. Levine, P. Pastor, A. Krizhevsky, J. Ibarz, and D. Quillen, "Learning hand-eye coordination for robotic grasping with deep learning and large-scale data collection," *The International Journal of Robotics Research*, vol. 37, no. 4–5, pp. 421–436, 2018.
- [12] J. Mahler and K. Goldberg, "Learning deep policies for robot bin picking by simulating robust grasping sequences," in *Proceedings of the Conference on Robot Learning, PMLR*, pp. 515–524, Mountain View, CA, USA, November 2017.
- [13] J. Zhang, C. Yang, M. Li, and Y. Feng, "Grasping novel objects with real-time obstacle avoidance," in *Proceedings of the International Conference on Social Robotics*, pp. 160–169, Springer, Qingdao, China, 2018.
- [14] D. Morrison, P. Corke, and J. Leitner, "Closing the loop for robotic grasping: a real-time, generative grasp synthesis approach," 2018, <https://arxiv.org/abs/1804.05172>.
- [15] Z. Zhou, T. Pan, S. Wu, H. Chang, and O. C. Jenkins, "Glassloc: plenoptic grasp pose detection in transparent clutter," 2019, <https://arxiv.org/abs/1909.04269>.
- [16] A. T. Miller and P. K. Allen, "Grasplit! a versatile simulator for robotic grasping," *IEEE Robotics & Automation Magazine*, vol. 11, no. 4, pp. 110–122, 2004.
- [17] R. Pelossof, A. Miller, P. Allen, and T. Jebara, "An SVM learning approach to robotic grasping," in *Proceedings of the IEEE International Conference on Robotics and Automation*, vol. 4, pp. 3512–3518, Washington, DC, USA, 2004.
- [18] J. Bohg, A. Morales, T. Asfour, and D. Kragic, "Data-driven grasp synthesis—a survey," *IEEE Transactions on Robotics*, vol. 30, no. 2, pp. 289–309, 2013.
- [19] T. Li, F. Wang, C. Ru, Y. Jiang, and J. Li, "Keypoint-based robotic grasp detection scheme in multi-object scenes," *Sensors*, vol. 21, no. 6, p. 2132, 2021.
- [20] A. Krizhevsky, I. Sutskever, and G. E. Hinton, "Imagenet classification with deep convolutional neural networks," *Advances in Neural Information Processing Systems*, vol. 25, pp. 1097–1105, 2012.
- [21] I. Lenz, H. Lee, and A. Saxena, "Deep learning for detecting robotic grasps," *The International Journal of Robotics Research*, vol. 34, no. 4–5, pp. 705–724, 2015.
- [22] D. Guo, F. Sun, H. Liu, T. Kong, B. Fang, and N. Xi, "A hybrid deep architecture for robotic grasp detection," in *Proceedings of the 2017 IEEE International Conference on Robotics and Automation (ICRA)*, pp. 1609–1614, IEEE, Marina Bay Sands, Singapore, 2017.
- [23] D. Guo, T. Kong, F. Sun, and H. Liu, "Object discovery and grasp detection with a shared convolutional neural network," in *Proceedings of the 2016 IEEE International Conference on Robotics and Automation (ICRA)*, pp. 2038–2043, IEEE, Stockholm, Sweden, 2016.
- [24] M. Vohra, R. Prakash, and L. Behera, "Real-time grasp pose estimation for novel objects in densely cluttered environment," in *Proceedings of the 2019 28th IEEE International Conference on Robot and Human Interactive Communication (RO-MAN)*, pp. 1–6, IEEE, New Delhi, India, 2019.
- [25] H. Zhang, X. Lan, S. Bai, X. Zhou, Z. Tian, and N. Zheng, "Roi-based robotic grasp detection for object overlapping scenes," in *Proceedings of the 2019 IEEE/RSJ International Conference on Intelligent Robots and Systems (IROS)*, pp. 4768–4775, IEEE, Venetian Macao, Macau, 2019.
- [26] D. G. Lowe, "Object recognition from local scale-invariant features," vol. 2, pp. 1150–1157, in *Proceedings of the Seventh IEEE International Conference on Computer Vision*, vol. 2, pp. 1150–1157, IEEE, Kerkyra, Greece, 1999.
- [27] D. G. Lowe, "Distinctive image features from scale-invariant keypoints," *International Journal of Computer Vision*, vol. 60, no. 2, pp. 91–110, 2004.
- [28] D. G. Lowe, "Local feature view clustering for 3d object recognition," in *Proceedings of the 2001 IEEE Computer Society Conference on Computer Vision and Pattern Recognition, CVPR*, Kauai, HI, USA, 2001.
- [29] X. Hu, Y. Tang, and Z. Zhang, "Video object matching based on sift algorithm," in *Proceedings of the 2008 International Conference on Neural Networks and Signal Processing*, pp. 412–415, IEEE, Zhenjiang, China, 2008.
- [30] F. Dellinger, J. Delon, Y. Gousseau, J. Michel, and F. Tupin, "Sar-sift: a sift-like algorithm for sar images," *IEEE*

- Transactions on Geoscience and Remote Sensing*, vol. 53, no. 1, pp. 453–466, 2014.
- [31] F. Alhwarin, C. Wang, D. Ristić-Durrant, and A. Gräser, “Improved sift-features matching for object recognition,” in *Proceedings of the Visions of Computer Science-BCS International Academic Conference*, pp. 179–190, London, UK, 2008.
 - [32] G. Shi, X. Xu, and Y. Dai, “Sift feature point matching based on improved RANSAC algorithm,” vol. 1, pp. 474–477, in *Proceedings of the 2013 5th International Conference on Intelligent Human-Machine Systems and Cybernetics*, vol. 1, pp. 474–477, IEEE, Hangzhou, China, 2013.
 - [33] E. Delponte, F. Isgro, F. Odone, and A. Verri, “SVD-matching using sift features,” *Graphical Models*, vol. 68, no. 5-6, pp. 415–431, 2006.
 - [34] O. Pele and M. Werman, “A linear time histogram metric for improved sift matching,” in *Proceedings of the European Conference on Computer Vision*, pp. 495–508, Springer, Marseille, France, 2008.
 - [35] R. I. Lab, Cornell Grasping Dataset, 2017, http://pr.cs.cornell.edu/grasping/rect_data/data.php/.
 - [36] Y. Jiang, S. Moseson, and A. Saxena, “Efficient grasping from RGBD images: learning using a new rectangle representation,” in *Proceedings of the 2011 IEEE International Conference on Robotics and Automation*, pp. 3304–3311, Shanghai, China, 2011.

Research Article

A Deep-Learning-Inspired Person-Job Matching Model Based on Sentence Vectors and Subject-Term Graphs

Xiaowei Wang,¹ Zhenhong Jiang,¹ and Lingxi Peng² 

¹School of Mechanical and Electrical Engineering, Guangzhou University, Guangzhou 510006, China

²Data Recovery Key Laboratory of Sichuan Province, Neijiang Normal University, Neijiang, Sichuan 641100, China

Correspondence should be addressed to Lingxi Peng; scu.peng@gmail.com

Received 20 August 2021; Accepted 7 October 2021; Published 19 October 2021

Academic Editor: Zhenyu Lu

Copyright © 2021 Xiaowei Wang et al. This is an open access article distributed under the Creative Commons Attribution License, which permits unrestricted use, distribution, and reproduction in any medium, provided the original work is properly cited.

In this study, an end-to-end person-to-job post data matching model is constructed, and the experiments for matching people with the actual recruitment data are conducted. First, the representation of the constructed knowledge in the low-dimensional space is described. Then, it is explained in the Bidirectional Encoder Representations from Transformers (BERT) pretraining language model, which is introduced as the encoding model for textual information. The structure of the person-post matching model is explained in terms of the attention mechanism and its computational layers. Finally, the experiments based on the person-post matching model are compared with a variety of person-post matching methods in the actual recruitment dataset, and the experimental results are analyzed.

1. Introduction

In the early studies of person-job fit, researchers generally focused on the relationships between the person and organization (P-O) and person and environment (P-E) [1, 2]. On this basis, some person-job fit models such as the recruitment model based on the P-O fit [3] and the weighted P-O relationship study method [4] were developed. In addition, some researchers proposed focusing on personality and job characteristics, which have an important influence on predicting a person-job fit [5]. With the development of machine learning and deep learning, an increasing number of researchers in the field of machine learning have focused on person-job fit. Some researchers use backpropagation neural networks to design end-to-end fit models, [6] whereas others input manual features and use support vector machines to measure the degree of fit [7]. These methods mostly rely on manual feature construction and require the participation of many experts in related fields. Additionally, these methods cannot fully explore potential information connections. Some advanced methods use the word2vec embedding layer to represent texts and a recurrent neural network or convolutional neural network (CNN) to serve as

the feature extractor [8, 9]. However, these advanced methods still need to truncate a large number of sentences and control the overall length of texts to avoid a large input of feature dimensions. Moreover, some researchers have used the idea of a recommendation system to fully investigate the matching between user preferences and items [10, 11] before making recommendations. Other studies have integrated optimal historical data to measure and calculate features [12]. Thus, the method of embedding a priori past resume features has been updated to investigate not only the match between the current resume and the requirements but also other information. Among the studies cited, the bidirectional recommendation system [13, 14] is an important branch in the field of personalized recommendation systems. The bidirectional talent recommendation system matches the preferences and requirements between job applicants and recruiters. This win-win strategy improves the matching accuracy. A similarity technique that combines the explicit and implicit preference data from both job applicants and recruiters has also been proposed [15]. This technique exploits the correlation between the preferences of both job applicants and recruiters and thus has a positive effect on the recommendation results.

Some researchers have also suggested incorporating a large amount of a priori information from the expert team to provide more accurate directional recommendations for some professionals [16, 17]. However, relying on a large amount of expert knowledge leads to a very high usage cost and hinders an automated construction methodology. Related tasks also include predicting the direction of talent flow [18] and investigating the network graphs of the applicant’s talent skills [19]. In these tasks, we explore the importance of the applicant’s talent skills.

Based on these previous studies, we aim to reduce the drawbacks of the word-level embedding model and fully express the correlation. Additionally, we aim to fully express the correlation between job applicants and recruiters and the subject information of texts and incorporate the idea of a recommendation system [20–24]. Therefore, we propose an end-to-end person-job fit model that uses sentence vector representations and integrates knowledge graph information, referred to as KG-DPJF. We follow the methods of Jiang et al. [25]. The model uses a multilayered attention mechanism to fully examine the information interaction between the candidate resume features and the recruitment requirement features. KG-DPJF embeds subject-term information and knowledge graph information to fully explore the relationship between candidates’ text descriptors. In addition, the translating embedding (TransE) method is used to express the resume entity information as a low-dimensional vector and then embed it into the model.

2. Knowledge Representation

Because this study is based on the knowledge-driven person-post matching model, the traditional knowledge representation methods and single-layer neural network model cannot appropriately describe the semantic relationship between entities. The use of the Trans method based on distance measurement can better describe the structural information between entities in space and bring a more accurate embedding of prior knowledge into the model. Then, we define the knowledge map, G , and all triple relationships contained in it.

$$G = \sum (h, r, t). \quad (1)$$

When G is constructed, the entities and relationships are mapped to a low-dimensional continuous vector space using TransE. Suppose h , r , and t are the vectors corresponding to the head, relation, and tail, respectively. If there is a triple relationship, it is assumed to indicate that the head entity points to the tail entity through the relationship. Then, the TransE scoring function is

$$f_r(h, t) = \|h + r - t\|_2^2. \quad (2)$$

The smaller the scoring function is, the more reliable the triple relationship of (h, r, t) in the knowledge graph is. In addition, the TransE model has few parameters and low computational complexity, and it still has good

performance and scalability in a large-scale sparse knowledge base, which is suitable for fast reasoning task scenarios.

3. BERT Coding

To make the person-post matching model learn the text information contained in the resume and recruitment requirements, it is necessary to use the word embedding matrix to spatially transform the text corpus of the resume and recruitment requirements into a low-dimensional dense spatial vector. If the one-hot representation method is used to represent each word in the sentence vectorially, for example, in the word “deep learning,” assuming that the dictionary composed of all words has only four words, the representation form of one hot is [1, 0, 0, 0]. When the number of dictionaries is very large, each word becomes a high-dimensional and sparse tensor; therefore, it is obviously unsuitable to be input to the person-post matching model. In addition, each word can be embedded into a limited low-dimensional space through word2vec. For example, deep learning can be mapped by embedding at the word level into a vector with a dimension of [200, 4]. Even if the dictionary contains far more than 1000 words, each word can be mapped to a low dimension by the word2vec embedding matrix as the input to the downstream model. However, statistics show that the number of words of long text items in each original resume is very large, which puts pressure on the model operation, and more text truncation is required during model input, resulting in a loss of matching accuracy of the person-post matching task. Based on the above considerations, the pretraining encoder of BERT is used to encode the sentences of the resume and recruitment requirements, and the powerful information learning capability of the BERT language model is used to encode the long text of the resume and the long text sentences of recruitment requirements with the BERT encoder pretrained based on large Chinese data. The model can further reduce the feature dimensions that need to be input for downstream tasks and retain text information as much as possible. Based on the representation ability of the large-scale pretraining model, all representation information in downstream tasks is fine-tuned to achieve fast and better results.

The number of sentences required by the actual resume and recruitment is not necessarily the same because the content recorded in the text itself is inconsistent, and both can reduce the input feature dimension between the matching models by only outputting the coding vector of the sentence. The coding based on the pretraining model combined with the knowledge extracted from the original corpus can provide more semantic information of the model. In this way, not only is the amount of information maintained but also the model reasoning can be accelerated to a certain extent. The sentence encoding process by BERT can be expressed as

$$C = \text{bert}([s_1, s_2, s_3, \dots, s_t]), \quad (3)$$

where bert represents the encoder based on BERT. Its pretraining model uses the 768-dimensional Chinese pretraining model, where $s_1, s_2, s_3, \dots, s_t$ is the sentence after text slicing and t represents the total number of sentences. $C \in \mathbb{R}^{dt \times de}$, where $d_e = 768$ is the fixed coding length. Through the above calculation, the sentence expression embedding matrix C can be produced, which can be input into the downstream task model to replace the word-level embedding matrix input.

4. The Person-Job Matching Model

In the actual recruitment process, the key information recorded in the resume and recruitment requirements often determines the key intention of employment in the recruitment process. The existing person-post matching model directly splices the resume features and recruitment requirements' features and inputs them into the prediction layer, resulting in low interpretability and a lack of information flow relationship between recruitment and requirements. To solve these problems, we need to fully simulate the recruitment process and build the matching model based on the attention mechanism. The model is divided into feature representation, attention interaction layer, and prediction layer, which is shown in Figure 1.

The feature representation layer must enter the graph embedding matrix, which is the information representation matrix of the graph obtained after the constructed knowledge map of supply and demand is trained by the Trans algorithm. The feature representation layer also includes the feature representation of text information, which represents the sentence-level text information by using the pretraining model BERT. The attention interaction layer uses the attention mechanism to output the set of weighting values between candidate resumes, historical best resumes, and recruitment requirements. The prediction layer accepts the set of weighting values and the feature input of the weighted resume and historical resume and outputs the prediction results through the classifier.

The design of the model is based on the construction process of a deep learning model, including preprocessing, feature representation, multilayer perceptron, and classifier. This includes the preprocessing of the model: as known from the above sections, a BERT encoder can be used to encode the segmented sentences in the input text of the resume and recruitment requirements and output sentence-level vectors. These vectors directly form an embedded sentence-level weight matrix after splicing. In addition, we use Trans to learn the structural information for all the knowledge in the map and output a low-dimensional dense entity embedding weight matrix. In the subsequent matching reasoning process, all the entity vectors of the input text segmentation sentence are extracted, and the entity embedding matrix is formed after splicing.

- (1) In the feature representation layer, the input features of the model include three modules. The first is the current input candidate resume, including the

work experience segmentation sentence, the project experience segmentation sentence, and the entity. The second is the historical best resume p_n , n representing a total of historical resumes. It also includes the work experience segmentation sentence, the project experience segmentation sentence, and the entity. Finally, the resume of recruitment requirements includes job requirements, segmentation sentences, and entities. In addition, other inputs such as entity context and matching score are included. According to the deep learning model, these features are discrete and can be transformed into a high-dimensional independent heat vector. In the construction of the deep learning model, a unique heat vector is transformed into low-dimensional dense features through the embedding layer. The feature item transformation here is sentence-level representation, so each actual resume segmentation sentence is represented by v . For example, the feature representation of the current resume is the feature of the resume to be selected j , which can be expressed as

$$j = [v_1, v_2, v_3, \dots, v_d] \in \mathbb{R}^{d_j \times d_v}, \quad (4)$$

where v is the sentence vector after each segmented sentence is encoded. d_j indicates the total number of segmented sentences, and d_v represents the vector dimension after BERT coding. The number of segmented sentences is generally limited; that is, the vector sentences of BERT coding sentences are embedded matrices, which are loaded into the model when the model diagram is running. The representation of historical recruitment characteristics p and the representation of the characteristics of recruitment requirements q can also be expressed as

$$\begin{aligned} p &= [l_1, l_2, l_3, \dots, l_d] \in \mathbb{R}^{d_p \times d_l}, \\ q &= [k_1, k_2, k_3, \dots, k_d] \in \mathbb{R}^{d_q \times d_k}, \end{aligned} \quad (5)$$

where l and k are the sentence vectors after the segmented sentences of historical recruitment and recruitment requirements are expressed by coding. d_p and d_k indicate the total number of segmented sentences, and d_v , d_p , and d_k are the same representing the vector dimension after BERT coding.

- (2) Feature interaction layer: its basic structure is an interactive computing layer based on feature extraction and attention mechanism to obtain the correlation between resume and recruitment requirements by the implicit method. The feature sentence vector matrix after the special representation layer is spliced with the entity vector, in which the entity vector contains the entity and entity context information. The feature of the spliced matrix is extracted using convolutional neural networks (K-convolutional neural networks (KCNNs)), and the output of the CV representation vector with

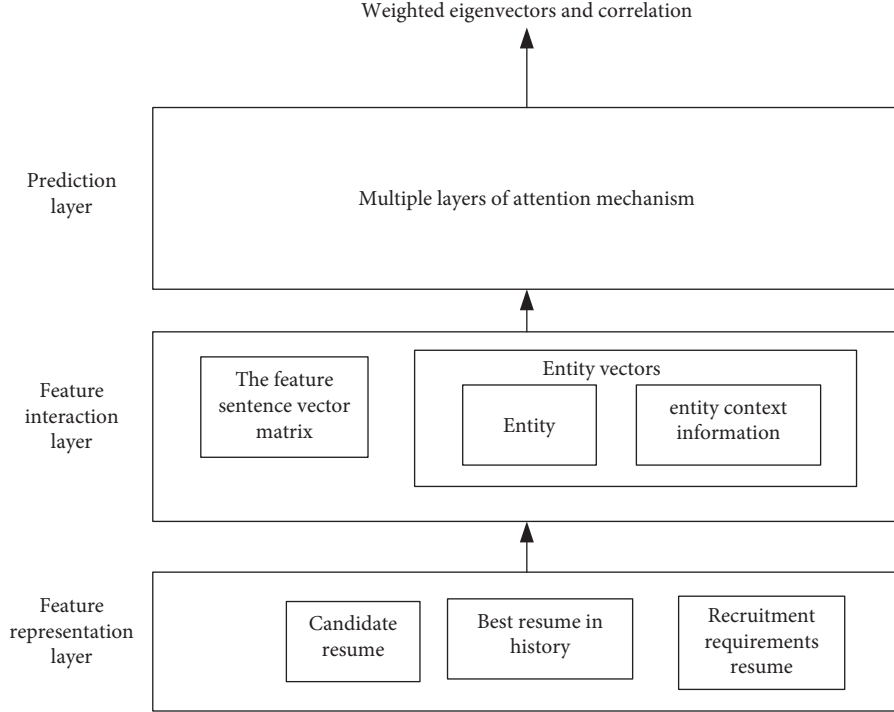


FIGURE 1: The structure of the KG-DPJF model.

a fixed dimension is c , and n is the number of historical resumes p and current recruitment requirements q . Similarly, after the embedded layer representation, it is input to the convolutional neural network for information extraction, and the historical resume representation is generated, u . The recruitment requirements are o . Among them, KCNN is a convolutional neural network which uses different convolution check features for multiple extraction and superposition. This is expressed as

$$i = [\tilde{c}^{h_1}, \tilde{c}^{h_2}, \dots, \tilde{c}^{h_m}], \quad (6)$$

where m is the number of subconvolutions and convolution kernel size is h_m . This is a preliminary feature extraction method. The parameter data between convolution layer structures are shared, which can not only reduce the memory space but also make the parameter matrix more flexible, which is convenient for attention interactive learning in the later branches. The modeling relationship between the current resume and historical resume is represented by a weighted feature interactive attention mechanism method, and the results express the representation of current resume C . And u is the correlation weight between \hat{a}_j ; this is regarded as an information enhancement between candidate resumes and historical best resumes. The two historical resume features are equally weighted and averaged here. At the same time, the same attention algorithm is used to express the correlation weight between recruitment requirements and historical resume \hat{a}_q . \hat{a}_j and \hat{a}_q can be expressed by the following formula:

$$\begin{cases} e_j = z^\top \tanh(W_j c + W_p u + b), \\ \hat{a}_j = \frac{\exp(e_j)}{\sum_{i=1}^T \exp(e_{ji})}, \end{cases} \quad (7)$$

$$\begin{cases} e'_q = z'^\top \tanh(W_q o + W'_p u + b'), \\ \hat{a}_q = \frac{\exp(e'_q)}{\sum_{i=1}^T \exp(e'_{qi})}, \end{cases}$$

where $W_j \in \mathbb{R}^{d_h \times d_c}$, $W_p \in \mathbb{R}^{d_h \times d_u}$, $b \in \mathbb{R}^{d_h}$, $z \in \mathbb{R}^{d_h}$, $W_q \in \mathbb{R}^{d_h \times d_o}$, $W'_p \in \mathbb{R}^{d_h \times d_u}$, $b' \in \mathbb{R}^{d_h}$, and $z' \in \mathbb{R}^{d_h}$ are the training parameter matrices. Then, the output weighted attention representation vectors of the current resume are c' . The weighted recruitment representation vector is o' , which can be expressed as the following formula:

$$\begin{aligned} c' &= \sum_l^T \hat{a}_j c, \\ o' &= \sum_l^T \hat{a}_q o. \end{aligned} \quad (8)$$

Here, another layer of attention layer pair is used, c' and o' , to perform correlation calculation. The output is \hat{a}_c . The attention layer is mainly used to simulate the mutual attention matching process of the actual recruitment process, fully measure the implicit correlation between the three, and

provide consideration input for the classification layer. \hat{a}_c can be expressed by the following formula:

$$\begin{cases} \hat{e}_c = \tilde{z}^\top \tanh(W'_j c' + W'_q o' + \tilde{b}), \\ \hat{a}_c = \frac{\exp(\hat{e}_c)}{\sum_{i=1}^T \exp(\hat{e}_{ci})}, \end{cases} \quad (9)$$

where $W'_j \in \mathbb{R}^{d_h \times d_{c'}}$, $W'_q \in \mathbb{R}^{d_h \times d_{o'}}$, $\tilde{b} \in \mathbb{R}^{d_h}$, and $\tilde{z} \in \mathbb{R}^{d_h}$. The final resume features after weighted calculation are \tilde{a}_c . The calculation process can be expressed as

$$\tilde{a}_c = \sum_l^T \hat{a}_c c'. \quad (10)$$

Finally, after calculation, all correlation weights are spliced into $\hat{u} = [\hat{a}_c, \hat{a}_j, \hat{a}_q]$. \hat{u} represents \tilde{a}_c and o' after splicing; the input that constitutes the prediction layer $\tilde{X} = [\tilde{a}_c, o', \hat{u}]$. The prediction layer fully takes into account the enhanced resume representation, recruitment requirements' representation, and all correlations calculated in the model and outputs the matching prediction value.

In the prediction layer, after all the feature representations have passed through the multilayer attention mechanism layer, their weighted feature vectors and related values are output. These vectors are connected through the full connection layer. The hidden layer uses the multilayer fully connected neural network layer and rectified linear unit function to activate. Finally, the output is activated using the sigmoid function. The sigmoid cross-entropy loss function is used to calculate the loss between the logic output and the label. Finally, the feature vector of the input fully connected layer is the output of the attention layer, and the classification label category is ReLU where $y \in \{0, 1\}$. Therefore, the calculation formula of the loss function is

$$L_{\text{target}} = -\frac{1}{N} \sum_{(x,y) \in D} (y \log(f(x)) + (1-y) \log(1-f(x))), \quad (11)$$

where D is the training set, with N total of samples, in which $f(x)$ is the prediction result output by the perceptron.

5. Experiments

The data used for the person-post matching experiment are the same as the data collected when the knowledge map was created. However, because of different experimental and data processing methods, the collected experimental data contain matching labels for matching control in the person-post matching experiment.

5.1. Dataset Preprocessing. The experiment uses e-resume data based on the actual recruitment process. Format and extract the desensitized data and clean the data. Referring to the construction method of the deep learning model, the person-post matching model is built using the TensorFlow platform, and the data are converted into the input format of the model. The dataset is stored in the form of resume data

corresponding to each position. At the same time, the recruitment mechanism of the recruitment platform and the enterprise employment mechanism of the company should also be considered before the experiment. Recruitment process of the enterprise: the enterprise must roughly select many candidate resumes and put them into the talent folder of the recruitment platform to store resumes or resumes submitted by job-seekers. Then, some suitable personnel are selected to invite for an interview. Finally, only some candidates will pass the interview and be officially hired. This is also the basis for classification. 0 means that the candidate only stops at the stage when the resume enters the talent folder, 1 means only completing the invitation interview stage, and 2 means they pass the invitation interview and get an offer. Note that there are only 0 and 1 labels in the training data; that is, only the data that passed the interview will be given a score of 1, and the rest of the resumes in other stages will be given a score of 0. This is meant to be close to the actual recruitment process and make the model more predictive when combined with the data.

Also, all triplet information extracted from the corpus is trained based on the Trans algorithm. Mapping dataset files of entities, relationships, and triples are constructed, and the data are transformed into a sequence. Then, the data are divided and marked as follows: 80% of the data is used as the test set, 10% of the data is used as the second test set, and the remaining 10% is used as the verification set. The output embedded model dimension is set to 50. When the training is completed, the growth is about 4 h.

After preparing the data required by the model, it starts the training stage. The whole model includes a training and adjustment stage. The two stages can carry out cyclic iteration. After enriching the knowledge map based on continuous new knowledge, it can perform continuous training to generate knowledge representation and then train the person-post matching model to form a complete model application iteration mode driven by knowledge.

During training and prediction, new knowledge is extracted from the text to be predicted. The new knowledge is mapped to the embedded space through the index relationship of the resume ID which corresponds to the entity. The skill keywords described in each resume contain the main idea of the sentence and provide information to support the matching task.

In addition, the optimal historical matching dataset is constructed based on the model design. There is no difference between the optimal historical matching dataset and the ordinary training or test dataset, but the optimal historical matching dataset stores the preset data of the best candidate for the post. The purpose of the setting is to simulate the practice of the recommendation system, embed the historical optimal matching information into the model, and let the model learn the relationship between the predicted resume and the historical optimal matching results to improve the model's matching performance.

5.2. Experimental Parameters. To realize sentence-level coding, the pretraining BERT model is adopted. So, the online BERT service based on parallel processing can be

used. The information about the service settings for BERT is described in Table 1. The number of parallel runs is set to 4. The Chinese 768 dimension is used in the pretraining model file. The number of parallel runs depends on the number of GPU (graphics processing unit) cores, and this affects the coding speed. Based on the described idea of BERT downstream tasks, the output layer of the model and the output operation of the middle layer of the model were obtained and used as the parameters of the middle layer or output layer of the model, which allows for downstream task improvement training to make the BERT model have better domain semantic expression ability. Here, we first follow the output of the original pretraining BERT code and output the sentence vector. For the person-job matching model parameters, as shown in Table 2, the length of the sentence embedding vector is 768, and the size of entity embedding is 50. In addition, the number of historical optimal recruitment records entered is 4, which depends on the average number of historical matching resumes that were collected for the position.

After explaining the setting information required for the experiment and data analysis, the final experiment is generally divided into the following four steps:

- (1) Data preprocessing: regular expressions are used to remove repeated and continuous labels, large areas of empty lines, and indentations.
- (2) Build a person-post matching model: the matching model is constructed under the framework of TensorFlow. Then, the training program is constructed, and the file address to save the training is selected.
- (3) After the hyperparameters are set according to the experimental conditions, the necessary function library is installed, the training program is started, and the model is optimized by the Adam algorithm. The computer has 4 GPUs, and 12 G memory is prepared for the experiments. The model of the graphics card is RTX2080s, and the CPU memory is 64 G.
- (4) The parameters are adjusted to achieve the best performance of the model and record the experimental data.

5.3. Baseline and Evaluation. This section refers to many existing man-post matching evaluation methods [26–30]. Therefore, in the experimental stage of verifying model performance, traditional methods including the logistic regression (LR) model and the decision tree (DT) method are used to construct the person-post matching model, as well as the existing mainstream person-job fit neural network-RNN (PJFNN-RNN) model based on the RNN. Owing to the test in the industry data, multiple baseline methods need to be created depending on the input mode. Depending on the input mode of the designed person-post matching model, the experiment also specifically constructs a model using the CNN structure to verify the importance of integrating a multilayer attention mechanism. A comparison is then performed between the model of pretraining word2vec embedding layer and the model of sentence-level embedding

after BERT coding. Then, the experiment also compares the performance of the person-post matching model using word2vec and BERT coding, and the experiment also refers to a baseline method of text semantic matching, which is measured by measuring the similarity between sentences. Finally, the performance comparison experiment of removing the knowledge map is also conducted.

The idea of constructing the baseline model based on the CNN as the feature extraction layer was inspired by the end-to-end person-post matching work in the existing literature. The model takes the feature representation vector of the text corpus that accepts the input of the resume and recruitment requirements, then uses a CNN with shared features to extract the features, and inputs them to the classification layer after averaging for activation to output the classification probability. Since the input dataset of the model is consistent with the input dataset of the person-post matching model, the BERT coding method can also be used in this experiment to encode the sentence representation, and the word2vec method can also be used to obtain the averaged sentence vector.

After the resume and the required text are represented by the embedded layer, they are input into the CNN, and the resume representation features are output, respectively, \hat{S}_j and required characteristics \hat{S}_q . These features are input into classifier D and output to the sigmoid layer for prediction through weighted activation function layer \hat{y} probability of

$$\begin{cases} D = \tanh(W_d[\hat{S}_j; \hat{S}_q; \hat{S}_j - \hat{S}_q] + b_d), \\ \hat{y} = \text{sigmoid}(W_y D + b_y). \end{cases} \quad (12)$$

In addition, it also provides a method for sentence semantic matching between long texts required by job posts compared to long texts such as work experience and project experience. The idea comes from the short sentence semantic matching method. First, the sentence is segmented, and then the previously trained word embedding matrix such as word2vec200 and Tencent embedding are used to calculate the representation vector of the text at the level of word segmentation. All the representation vectors form the sentence semantic matrix V_s , and then the dimension of the semantic matrix of the text sentence is reduced to output the sentence vector, and then the distance measurement method is used to match the sentences one by one. The purpose is to calculate the distance between the long text data of electronic resumes and the long text data in recruitment requirements listed in job postings one by one and then calculate the final matching score through the overall similarity. This allows for the measurement of the matching degree between resumes and posts. The distance can be measured by cosine similarity, and the calculation formula is as follows:

$$\cos(\theta) = \frac{\sum_{i=1}^n (x_i \times y_i)}{\sqrt{\sum_{i=1}^n (x_i)^2} \times \sqrt{\sum_{i=1}^n (y_i)^2}}, \quad (13)$$

where x_i and y_i , respectively, represent two sentence vectors that need to calculate cosine similarity. From a spatial perspective, the two sentences can be expressed as two lines

TABLE 1: The main parameters of the BERT server.

Project	Tag description	Parameter action
BERT_config	BERT_config.json	Parameter fixed setting file of the BERT model
Number of parallel services	4	Adjust the number of simultaneous tasks processed by the BERT server
BERT pretraining model parameter file	Chinese_L-12_H-768_A-12	Chinese 768-dimensional pretraining model is used
Model_dir	File address	The address where the BERT pretraining model is stored
Vocab_dir	File address	Address where vocab thesaurus is stored
Input_length	512	Maximum allowed sentence length

TABLE 2: The main parameters of the person-post matching model.

Project	Tag description	Parameter action
Num-history	4	The model loads the optimal number of resume data copies in history
Learning rate	0.001	The learning rate affects the training time and effect
Batch_sizes	8	Enter the amount of batch data for model training
Filter	[1, 2]	CNN convolution kernel step size selection
Entity_dim	50	The dimension length of the embedded vector of the entity
Epoch	500	Control the total number of training rounds

embedded in the space, taking the coordinate origin as the starting point and pointing to different directions, so that an included angle is formed between the two-line segments. If the included angle is 0 degrees, it means that the two directions of the vector space are the same and the two lines coincide. It also means that the text semantics represented by the two vectors are exactly the same. If the included angle is a 90-degree right angle, it indicates that the directions are completely different, and the semantic results are different. If the included angle is 180 degrees, it means that the direction of the vector is opposite and the semantics are not similar. Therefore, we can represent the text information of the resume and recruitment requirements according to the fully trained word embedding model and then judge the semantic similarity of the vector representation by the size of the included angle. The smaller the included angle, the more similar the sentence semantics. This is also done by segmenting sentences in the above dataset, and experiments are conducted based on the above ideas.

The experimental method is to calculate the similarity between all the sentences based on the resume and all the sentences of the recruitment post, select the highest similarity value in the recruitment requirement text one by one based on all resume sentences, then normalize according to the number of resume sentences, and finally calculate the matching degree. For example, the similarity between sentence 1 and all recruitment-required sentences is calculated in turn, and the highest similarity value is selected as the best matching semantic sentence of the resume sentence and then calculated in turn. Note that, after the sentences of recruitment requirements are matched, they cannot be matched again. Therefore, this is matching from the perspective of the resume.

When comparing the segmentation sentences between the resume and the recruitment requirements, the input data are the resume text information, and the company data are the text information required for recruitment. After

embedding space conversion and averaging is performed, this information will be calculated as described above, until all distances are calculated, and the result consistent with the number of service pairs to be matched is output, i.e., it represents the matching degree.

Finally, the performance of the model is compared with the frontier person-post matching model PJFNN-RNN under different structural data to verify the performance of the model. PJFNN-RNN is an end-to-end model based on the RNN as the feature extractor of the resume and required text. Compared with the data analysis in the previous sections, the experiment is based on industry data collected by real enterprises, and there are fixed requirements for the threshold of recruitment regulations. Therefore, in the analysis of the recruitment process, the admission pass rate is set as label 1, and a failure result is set as label 0. The accuracy, the accuracy recall rate, and the $F1$ value are used as evaluation indicators for the results. Finally, 80% of the dataset is selected as the training set, the next 10% is used to fine-tune the parameters, and the last 10% is used as the test data as the test set. It is worth noting that Table 3 also reflects the problems of data imbalance and label category imbalance. However, because of the differences between civilian posts and technical posts, the data are divided into civilian posts and technical posts. Simultaneously, some sampling methods are limited because of the actual recruitment results. Therefore, the experiment is also based on the actual production application, through cooperation with enterprises, using some of the artificial knowledge to improve some of the data. For example, the description of the CVs of low-level development posts may be closer to that of medium-level development posts, and it is noted that about 3.72% of candidates choose to apply for multiple job postings at the same time. Based on this idea, a small number of similar job postings are sampled and labeled manually, and the datasets are added to the admission and interview file categories.

TABLE 3: Analysis of experimental data.

Statistics	Value
Proportion of resumes submitted by job-seekers for two or more positions at the same time in the total number of resumes	0.0372
Average number of words in each resume of technical posts	1271
The experimental data analysis	643
Recruitment ratio of technical posts	0.3733
Civilian post recruitment ratio	0.2642

5.4. Experimental Results and Analysis. The most important and difficult points of the experiment are the processing of resume and recruitment data and the construction of a model training set. Our experiments are based on the industry corpus data collected during the actual recruitment process. The resume and post data files collected in the enterprise recruitment platform after strict desensitization measures are converted into dataset files after preprocessing the data. By analyzing the practical application requirements and related literature, the task is divided into two categories to perform a detailed experimental human work matching task.

First, as the results in Table 4 show, the built embedded knowledge map and BERT-based person-job fit are knowledge graph-based deep-learning-inspired person-job fitting model, KG-DPJF. Table 4 shows the performance of the person-post matching model based on knowledge-driven and multilayer attention mechanisms in the experiment. In addition to the comparison experiment between the model and some baseline models, including DPJF (deep-learning-inspired person-job fitting model), some ablation experiments were also performed. The designed human post matching model integrating the knowledge map and attention mechanism is better than the traditional input feature classifier, and the $F1$ value is improved by nearly 13%. At the same time, the correlation method that uses multilayer attention calculation to simulate the recruitment process also improves the performance of the model. Compared with the single use of the CNN feature extractor, the $F1$ value is improved by nearly 6%. In addition, compared with the direct use of pretraining word2vec200 coding, the use of BERT coding can increase the performance. This shows that the BERT model based on unsupervised training of a large number of Chinese corpuses can give the person-post matching model more semantic knowledge for learning, and the BERT can also be fine-tuned again based on the domain’s own data. In addition, Figure 2 also shows the analysis of the training time and also shows that using the BERT-based sentence coding method also has significant advantages in training time, while the method completely based on the word-level input feature extraction layer greatly increases the amount of calculations required, resulting in a longer training time, which can further enlighten the research idea of constructing the person-post matching model in the way of two-stage model structure. In addition, based on the above, because the knowledge is input as the entity embedding layer in the person-post matching model, the knowledge input can be removed for experiments. In the experiments, the model embedded in the knowledge map for job search has better performance than the model without

TABLE 4: Experimental performance table—no structured data.

Model	Accuracy	Precision	Recall	$F1$
Logistic regression	0.5091	0.4493	0.4473	0.4627
Decision tree	0.5369	0.4478	0.4615	0.4646
CNN and word2vec200	0.5632	0.5001	0.5385	0.5185
CNN and BERT	0.5736	0.5147	0.5465	0.5383
DPJF-word2vec200	0.5939	0.5278	0.5846	0.5548
DPJF	0.5874	0.5421	0.5974	0.5684
KG-DPJF	0.6139	0.5810	0.6047	0.5926

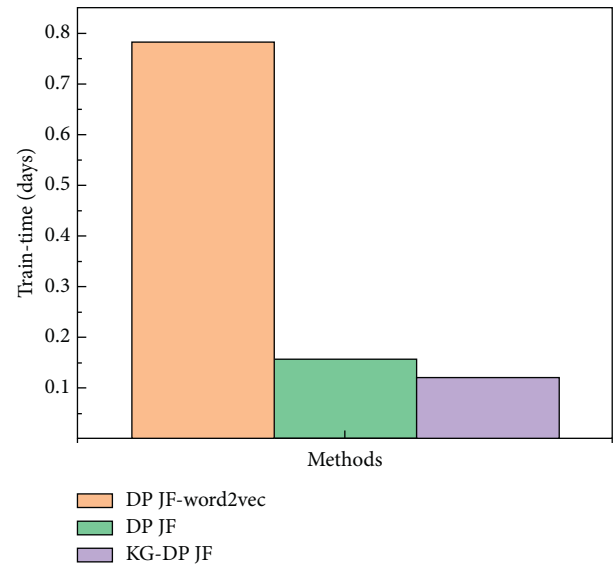


FIGURE 2: Performance comparison between word2vec and sentence-level embedding.

the embedded knowledge map for job search, which also shows that the entity knowledge method embedded with a priori person-post matching information can help the model better understand the meaning of potential skills and keywords behind sentences, express the enhanced correlation between entity words, and combine the rich semantic information of BERT. It can not only reduce the amount of calculation and increase the operation speed but also enhance the matching accuracy. This means that, during the recruitment process, the human resources department will be able to judge whether the candidate is able to meet the standard based on the key information of the text content.

However, it should be noted that only unstructured data are used for testing to match the input and output of the existing person-post matching model; that is, information inputs such as years of work and gender are removed, and

only work experience and project experience are retained as these discrete characteristics have different processing problems.

In Table 5, we can see the person-post matching model PJFNN-RNN constructed based on the RNN, which is a matching model for person-post text information perception based on the RNN. The PJFNN-RNN model is based on the cosine distance loss function. Therefore, we can compare the performance of models based on unstructured data, that is, long text as the input. From the table, we can see that the KG-DPJF model has some improvement compared to the PJFNN-RNN. The KG-DPJF model with more semantic knowledge performs better than the method that simply relies on long-distance feature extraction and multilayer CNN extraction. At the same time, these methods also have performed better than the methods based on cosine distance rearrangement and DT. It could be that they only rely on distance calculation without learning the feature information between sentence vectors and cannot fully utilize semantic information.

Table 6 begins the experiment to integrate unstructured data, i.e., age, gender, and other characteristics. At the same time, input introduces unstructured knowledge about entities. However, when constructing the input, for these discretionary data, we first use one-hot form coding to measure the performance of different models. The experimental results in Table 6 show that using one-hot coding discrete data can improve the performance of these models. In the context of analysis, it is helpful for matching because it enriches the input of some important matching information, such as gender and education. However, one-hot formal coding has its own shortcomings because it obscures some semantic information, such as the progressive relationship and the importance of educational levels.

The experimental results are shown in Table 7. For discrete data such as structured data, we tried to use BERT to uniformly encode them into a public space rich in semantic information and input them into the person-post matching model for training in combination with their entity information and the remaining unstructured data. The experimental results show that the performance of these models has been improved to a certain extent, and these models can be uniformly encoded into the shared fixed space using BERT in both unstructured data and structured data to provide some information to the language model before training. In particular, the attention mechanism matching model developed in this section based on the knowledge map and BERT can unify the coding input and coding space and learn richer information from the prior knowledge of the knowledge base and the language model. This allows us to enhance the model performance, which also enlightens the future as the performance of BERT domain representation can be adjusted in the first stage. In this manner, the performance of the two-stage person-post matching task is improved.

In this paper, a detailed person-post matching application experiment is conducted. From the above experimental results and analysis, it is found that the person-post matching model based on the attention mechanism designed

TABLE 5: The comparative experiment—no structured data.

Model	Accuracy	Precision	Recall	F1
Logistic regression	0.5091	0.4493	0.4473	0.4627
Decision tree	0.5369	0.4478	0.4615	0.4646
Cosine distance	0.5275	0.5281	0.5034	0.5169
CNN and word2vec	0.5632	0.5001	0.5385	0.5185
CNN and BERT	0.5736	0.5147	0.5465	0.5383
PJFNN-RNN	0.6023	0.5716	0.5864	0.5789
KG-DPJF	0.6169	0.5810	0.6047	0.5926

TABLE 6: The comparative experiment with structured data one hot.

Model	Accuracy	Precision	Recall	F1
Logistic regression	0.5955	0.4973	0.5034	0.5040
Decision tree	0.6247	0.5159	0.4800	0.4973
PJFNN-RNN	0.6333	0.6511	0.5689	0.6079
KG-DPJF	0.6562	0.6467	0.6018	0.6286

TABLE 7: The comparative experiment combined with structured data BERT.

Model	Accuracy	Precision	Recall	F1
Logistic regression	0.6023	0.4956	0.5177	0.5063
Decision tree	0.6274	0.5138	0.4967	0.5050
PJFNN-RNN	0.6528	0.6274	0.5953	0.6109
KG-DPJF	0.6522	0.6483	0.6125	0.6298

in this section can achieve an excellent matching effect and realize the matching degree between resumes and recruitment requirements. From the summary of the literature and the analysis of experimental results, it is found that there are still some common defects in the existing experimental tasks of person-post matching:

- (1) Inevitable text truncation: in the e-resume data of today’s actual recruitment platform, there are often many sentences in the unstructured data. The number of words displayed in the corpus statistical information map in the experiment is not consistent with the experimental data of other recent literature works. This is because other works usually use the method of truncation or fine extraction before the experiment, restricting the total number of words to a certain range, which is even less than half of the total number of words. In this way, we adapt to the method of not using a pretraining vector representation and feature extraction and hope to fully learn the semantic information in sentences. This study discusses how to make full use of pretraining sentence information, pretraining model, and prior knowledge to solve this problem.
- (2) Matching defects caused by data imbalance: in real electronic resume data, the data often consist of semistructured data, while other works usually transform items such as gender and education into discrete data. This is because their values have the ability to possibly change the perspective of the whole recruitment such as education: masters and

college degree. These ordered datasets cannot be well solved by deep learning methods in the actual recruitment data. In addition, there is also a relationship between recruitment discrimination and data samples. This usually reflects inequality in recruitment. For example, statistically, there are more men than women programmers. The model should understand and avoid these datasets. However, in the experiment in Table 7, instead of massaging the data, the data are regarded as short sentences, encoding their semantic information, embedding entity information, and transferring the expressed theme learning to the matching model. In the future, we will investigate whether the knowledge map provides effective information and internal relationship for the processing of these ordered data.

6. Conclusion

Based on the knowledge map of supply and demand, this study embeds and represents knowledge into a low-dimensional dense space. The research shows that the person-post matching model based on the knowledge-driven and linguistic model has better performance and more interpretability than the existing person-post matching methods, which can provide some clues for the future work on person-post matching.

Data Availability

All the data generated or analyzed during this study are included within this article.

Disclosure

Xiaowei Wang and Zhenhong Jiang are the co-first authors.

Conflicts of Interest

The authors declare that there are no conflicts of interest.

Acknowledgments

This work was supported by the Open Research Fund Program of Data Recovery Key Laboratory of Sichuan Province (Grant no. DRN19012).

References

- [1] S. A. Carless, "Person-job fit versus person-organization fit as predictors of organizational attraction and job acceptance intentions: a longitudinal study," *Journal of Occupational and Organizational Psychology*, vol. 78, no. 3, pp. 411–429, 2005.
- [2] J. D. Werbel and S. W. Gilliland, "Person-environment fit in the selection process," *Research in human resources management*, vol. 17, pp. 209–243, 1999.
- [3] C. Zhang and Y. Ye, "A recruitment mode based on person-organization match," *Research on Financial and Economic Issues*, vol. 3, pp. 94–98, 2006.
- [4] T. Sekiguchi and V. L. Huber, "The use of person-organization fit and person-job fit information in making selection decisions," *Organizational Behavior and Human Decision Processes*, vol. 116, no. 2, pp. 203–216, 2011.
- [5] K. H. Ehrhart, "Job characteristic beliefs and personality as antecedents of subjective person-job fit," *Journal of Business and Psychology*, vol. 21, no. 2, pp. 193–226, 2006.
- [6] Z. Yuan and S. Lu, "Application in person-job fit evaluation of BP neural network in knowledge workers," *Journal of Wuhan University of Technology*, vol. 32, no. 3, pp. 515–518, 2010.
- [7] Y. Bing and J. Fei, "Application in person-job fit evaluation of support vector machine," *Journal of Central South University of Forestry & Fechnology (Social Sciences)*, vol. 5, no. 6, pp. 92–94, 2011.
- [8] C. Qin, H. Zhu, T. Xu, C. Zhu, and L. Jiang, "Enhancing person-job fit for talent recruitment: an ability-aware neural network approach," in *Proceedings of the 41st International ACM SIGIR Conference on Research & Development in Information Retrieval*, pp. 25–34, Ann Arbor, MI, USA, 2018.
- [9] C. Zhu, H. Zhu, H. Xiong et al., "Person-job fit: adapting the right talent for the right job with joint representation learning," *ACM Transactions on Management Information Systems*, vol. 9, no. 3, pp. 12.1–12.17, 2018.
- [10] Y. Lu, S. Ingram, and D. Gillet, "A recommender system for job seeking and recruiting website," in *Proceedings of the 22nd International Conference on World Wide Web*, pp. 963–966, New York, NY, USA, 2013.
- [11] A. Gionis, D. Gunopulos, and N. Koudas, "Machine learned job recommendation," in *Proceedings of the Fifth ACM Conference on Recommender Systems*, pp. 325–328, Chicago, IL, USA, 2011.
- [12] D. Wu, L. Zhou, and H. Lin, "Design and implementation of job recommendation system for graduates based on random walk," *Journal of Guangxi Normal University*, vol. 29, no. 1, pp. 179–185, 2011.
- [13] T. Weitzel, "Matching people and jobs: a bilateral recommendation approach," in *Proceedings of the 39th Annual Hawaii International Conference on System Sciences (HICSS'06)*, 2006.
- [14] T. Chung, J. Kay, I. Koprinska, L. Pizzato, T. Rej, and K. Yacefcullum, "Reciprocal recommenders," in *Proceedings of the 8th Workshop on Intelligent Techniques for Web Personalization and Recommender Systems (UMAP'2010)*, pp. 1–12, Big Island, HI, USA, 2010.
- [15] H. Yu, C. Liu, and F. Zhang, "Reciprocal recommendation algorithm for the filed of recruitment," *Journal of Information and Computational Science*, vol. 8, no. 16, pp. 4061–4068, 2011.
- [16] S. Trewin, "Knowledge-based recommender systems," *Encyclopedia of Library and Information Science*, vol. 69, pp. 69–180, 2000.
- [17] J. D. Velásquez and V. Palade, "Building a knowledge base for implementing a webbased computerized recommendation system," *The International Journal on Artificial Intelligence Tools*, vol. 16, no. 5, pp. 793–828, 2007.
- [18] L. Zhang, H. Zhu, T. Xu et al., "Large-scale talent flow forecast with dynamic latent factor model?" in *Proceedings of the 2019 World Wide Web Conference*, pp. 2312–2322, San Francisco, CA, USA, 2019.
- [19] T. Xu, H. Zhu, C. Zhu, and H. Xiong, "Measuring the popularity of job skills in recruitment market: a multi-criteria approach," 2018, <https://arxiv.org/abs/1712.03087>.
- [20] T. Zhang, B. Liu, D. Niu, K. Lai, and Y. Xu, "Multiresolution graph attention networks for relevance matching," in *Proceedings of the 27th ACM International Conference on Information and Knowledge Management*, pp. 933–942, Turin, Italy, 2018.

- [21] Z. Lyu, Y. Dong, C. Huo, and W. Ren, "Deep match to rank model for personalized click-through rate prediction," in *Proceedings of the Thirty-Fourth AAAI Conference on Artificial Intelligence*, New York, NY, USA, 2020.
- [22] L. Peng, H. Liu, Y. Nie, Y. Xie, X. Tang, and P. Luo, "The transnational happiness study with big data technology," *ACM Transactions on Asian and Low-Resource Language Information Processing*, vol. 20, no. 1, pp. 1–12, 2021.
- [23] Z. Zhao, C. K. Ahn, and H.-X. Li, "Dead zone compensation and adaptive vibration control of uncertain spatial flexible riser systems," *IEEE*, vol. 25, no. 3, pp. 1398–1408, 2020.
- [24] Z. Zhao and Z. Liu, "Finite-time convergence disturbance rejection control for a flexible timoshenko manipulator," *IEEE/CAA Journal of Automatica Sinica*, vol. 8, no. 1, pp. 157–168, 2021.
- [25] Z. Jiang, L. Peng, and L. Shi, "Person-Job Fit model based on sentence-level representation and theme-word graph," in *Proceedings of the 2021 IEEE 5th Advanced Information Technology, Electronic and Automation Control Conference (IAEAC)*, pp. 1902–1909, Compiègne, France, 2021.
- [26] Z. Huang, W. Xu, and K. Yu, "Bidirectional LSTM-CRF models for sequence tagging," 2015, <https://arxiv.org/abs/1508.01991>.
- [27] A. Bordes, N. Usunier, A. Garcia-Duran, J. Weston, and O. Yakhnenko, "Translating embeddings for modeling multi-relational data," *Advances in Neural Information Processing Systems*, vol. 2, pp. 2787–2795, 2013.
- [28] J. Devlin, M. Chang, K. Lee, and K. Toutanova, "BERT: pre-training of deep bidirectional transformers for language understanding," 2018, <https://arxiv.org/abs/1810.04805>.
- [29] C. Qin, H. Zhu, T. Xu et al., "An enhanced neural network approach to person-job fit in talent recruitment," *ACM Transactions on Information Systems*, vol. 38, no. 2, pp. 1–33, 2020.
- [30] C. Zhu, H. Zhu, H. Xiong, and P. Ding, "Recruitment market trend analysis with sequential latent variable models," in *Proceedings of the 22nd ACM SIGKDD International Conference*, pp. 383–392, San Francisco, CA, USA, 2017.